A Quarter Century of *Wind* Spacecraft Discoveries

Lynn B. Wilson III[1], Alexandra L. Brosius[1,2], Natchimuthuk Gopalswamy[1], Teresa Nieves-Chinchilla[1], Adam Szabo[1], Kevin Hurley[3], Tai Phan[3], Justin C. Kasper[4], Noé Lugaz[5,6], Ian G. Richardson[7,1], Christopher H.K. Chen[8], Daniel Verscharen[9,5], Robert T. Wicks[10], Jason M. TenBarge[11,12]

[1]NASA Goddard Space Flight Center, Heliophysics Science Division, Greenbelt, MD 20771, USA.
[2]The Pennsylvania State University, Department of Meteorology and Atmospheric Science, University Park, PA 16802, USA.
[3]Space Sciences Laboratory, University of California, Berkeley, CA 94720-7450, USA.
[4]University of Michigan, Ann Arbor, School of Climate and Space Sciences and Engineering, Ann Arbor, MI 48109, USA.
[5]Space Science Center, Institute for the Study of Earth, Oceans, and Space, University of New Hampshire, Durham, NH, USA.
[6]Department of Physics, University of New Hampshire, Durham, NH, USA.
[7]Department of Astronomy, University of Maryland, College Park 20742, USA.
[8]School of Physics and Astronomy, Queen Mary University of London, London E1 4NS, UK.
[9]Mullard Space Science Laboratory, University College London, Holmbury St. Mary, Surrey RH5 6NT, UK.
[10]Department: Mathematics, Physics and Electrical Engineering, Northumbria University: Newcastle upon Tyne, Tyne and Wear, NE1 8ST, UK.
[11]IREAP, University of Maryland, College Park, MD 20742, USA.
[12]Princeton University, Princeton, NJ 08544, USA.

Key Points:

- *Wind* has made seminal advances to the fields of astrophysics, turbulence, kinetic physics, magnetic reconnection, and the radiation belts
- *Wind* pioneered the study of the source and evolution solar radio emissions below 15 MHz
- *Wind* revolutionized our understanding of coronal mass ejections, their internal magnetic structure, and evolution

Corresponding author: Lynn B. Wilson III, `lynn.b.wilsoniii@gmail.com`

Abstract

The *Wind* spacecraft is a critical element in NASA's Heliophysics System Observatory (HSO) – a fleet of spacecraft created to understand the dynamics of the sun-Earth system – owing to the combination of its longevity (>25 years in service), its diverse compliment of instrumentation, and high resolution and accurate measurements. *Wind* has over 55 selectable public data products with over ∼1100 total data variables (including OMNI data products) on SPDF/CDAWeb alone. These data have led to paradigm shifting results in studies of statistical solar wind trends, magnetic reconnection, large-scale solar wind structures, kinetic physics, electromagnetic turbulence, the Van Allen radiation belts, coronal mass ejection topology, interplanetary and interstellar dust, the lunar wake, solar radio bursts, solar energetic particles, and extreme astrophysical phenomena such as gamma-ray bursts. This review introduces the mission and instrument suites then discusses examples of the contributions by *Wind* to these scientific topics that emphasize its importance to both the fields of heliophysics and astrophysics.

Plain Language Summary

The *Wind* spacecraft is a south ecliptic pointed spinning spacecraft. It is equipped with an array of instrument suites that measure electric and magnetic fields, electrons from thermal to relativistic energies, protons and alpha-particles from thermal to suprathermal energies, and energetic ions from hydrogen to trans-iron elements. *Wind* can also observe remote sources of electromagnetic radiation in the radio and gamma-ray frequency ranges. This diverse array of instrumentation has allowed researchers to examine such a broad range of research topics including astrophysics, turbulence, kinetic physics, magnetic reconnection, interplanetary and interstellar dust, transient solar phenomena, and the radiation belts. Examples of the contributions of *Wind* to the fields of heliophysics and astrophysics are reviewed.

1 The *Wind* Mission

1.1 Wind Mission Overview

NASA launched the *Wind* spacecraft on November 1, 1994. *Wind* and *Polar* (Harten & Clark, 1995) were part of the stand-alone Global Geospace Science (GGS) Program (Acuña et al., 1995), a subset of the International Solar Terrestrial Physics (ISTP) Program (Whipple & Lancaster, 1995). The ISTP Program included the additional missions *Geotail* (Nishida, 1994), the SOlar and Heliospheric Observatory or *SoHO* (Domingo et al., 1995), and *Cluster* (Escoubet et al., 1997). The objective of the ISTP program was to study the origin of solar variability and activity, the transport of manifestations of that activity to the Earth via plasma processes, and the cause-and-effect relationships between that time varying energy transport and the near-earth environment.

Wind is a spin stabilized spacecraft – spin axis aligned with ecliptic south – with a spin period of ∼3 seconds. Prior to May 2004, *Wind* performed a series of orbital maneuvers (H. Franz et al., 1998), as shown in Figure 1, that led to the spacecraft visiting numerous regions of the near-Earth enviroment. For instance, between launch and late 2002 *Wind* completed ∼67 petal orbits through the magnetosphere and two out of the ecliptic plane lunar rolls in April and May of 1999. Between August 2000 and June 2002 *Wind* completed four east-west prograde 1:3–Lissajous orbits reaching $\gtrsim$300 R_E along the ±Y-GSE direction (Fränz & Harper, 2002). From November 2003 to February 2004

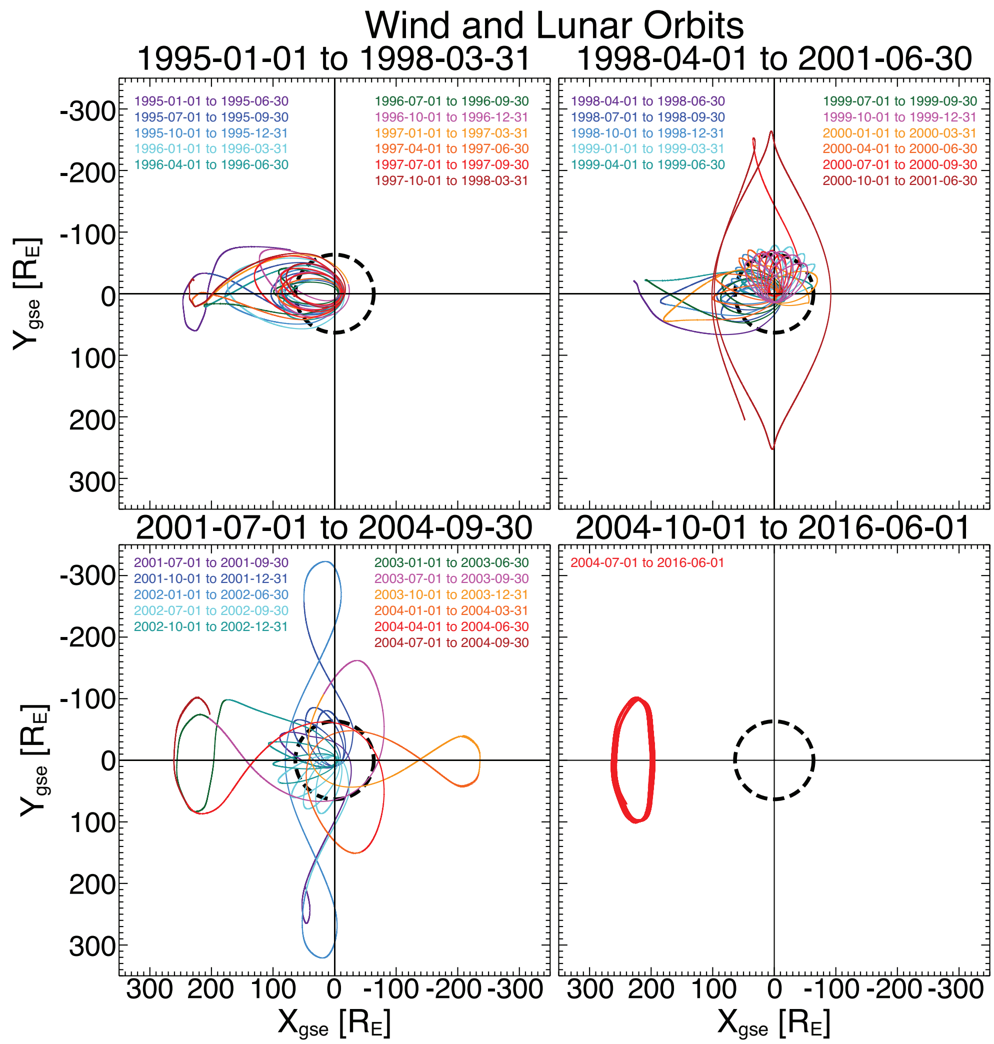

Figure 1: *Orbital trajectories of the* Wind *spacecraft in the GSE XY plane from 1 November 1994 to 1 June 2016. Colors denote time ranges as indicated. The dashed black circle indicates the Moon's orbit (Adapted from Figure 1 in Malaspina & Wilson III, 2016). Note that the orbit has not noticeably changed since 1 June 2016.*

Wind performed an excursion to the second Earth-Sun libration point, or Lagrange point, called L2[1].

In May 2004, *Wind* made its final major orbital maneuver using a lunar gravitational assist to insert it into a Lissajous orbit[2] about the first Earth-Sun libration point, labeled L1 by late June 2004. On June 26, 2020, the *Wind* flight operations team (FOT)

[1] Note that L2 is located >220 R_E downstream of Earth and ∼500 R_E downstream of the Advanced Composition Explorer (ACE) (Stone et al., 1998). For reference, ACE launched in 1997 and was designed to study energetic particles and their composition. Unlike *Wind*, ACE was not designed to study kinetic physics or remote solar and astrophysical phenomena using electric fields.

[2] Note that *Wind*'s L1 orbit has a ±Y-GSE displacement about the sun-Earth line of ∼100 R_E, much larger than the other two current L1 missions ACE and Deep Space Climate Observatory (DSCOVR). For more details, see the *Wind* Senior Review reports provided at: `https://wind.nasa.gov`.

successfully completed the first halo orbit insertion maneuver and the second was successfully completed on August 31, 2020. The third maneuver is currently scheduled for November 9, 2020. This orbital change was necessary to prevent the spacecraft trajectory from entering the solar exclusion zone – region around the solar disk where solar radio emissions cause sufficient interference with spacecraft communications to prevent telemetry signal locks. The projection of the orbit in the ecliptic plane will not noticeably change, however the out-of-ecliptic projection will now be a stationary ellipse centered on the solar disk.

The mission has amassed >5380 refereed publications using *Wind* data between launch and December 31, 2019 with a NASA ADS h-index of 142, an i10-index of 3038, >145,450 citations, and >984,100 reads as of Sep. 08, 2020. Despite being 25+ years old, the *Wind* mission still remains active and *Wind* data continue to be relevant as evidenced by the >1065 refereed publications between January 1, 2017 and December 31, 2019. Further, *Wind* data access requests were >10,291,900 between January 1, 2017 and December 31, 2019 on NASA's SPDF/CDAWeb or ∼9400 per day. Thus, *Wind* is one of the longest running and most productive missions in the Heliophysics System Observatory (HSO).

1.2 *Wind* Instrument Suites

The *Wind* instruments can be divided into two categories: field and particle suites. The field instruments measure γ-rays, radio waves, electric fields, and magnetic fields. The particle instruments measure thermal protons, alpha-particles, and electrons in addition to heavy ions (e.g., carbon-nitrogen-oxygen, iron, trans-iron). All of the particle instruments measure particles as functions of energy and solid angle which allows researchers to construct velocity distribution functions (VDFs) – particle probability density functions in velocity space. The full 3D VDF measurements also allow researchers to calculate velocity moments of the distribution such as number density, bulk flow velocity, thermal pressure/temperature, and heat flux. The *Wind* instrument names and acronyms are listed below in Table 1.

Table 1: *Wind* Instrument Names

Abbrev.	Instrument name	Reference
TGRS	Transient Gamma-Ray Spectrometer	A. Owens et al. (1995)
KONUS	Gamma-Ray Spectrometer	Aptekar et al. (1995)
EPACT	Energetic Particles: Acceleration, Composition, and Transport	von Rosenvinge et al. (1995)
SMS	Solar Wind and Suprathermal Ion Composition Experiment	Gloeckler et al. (1995)
MFI	Magnetic Field Investigation	Lepping et al. (1995)
WAVES	The Radio and Plasma Wave Investigation	Bougeret et al. (1995)
3DP	Three-Dimensional Plasma and Energetic Particle Investigation	Lin et al. (1995)
SWE	Solar Wind Experiment	Ogilvie et al. (1995)

It is important to note that unlike most other missions, *Wind* had significant redundancy in its measurements. For instance, there are at least five possible measurements of the solar wind number density (two from 3DP, two from SWE, one from WAVES, and one from SMS under certain conditions) and prior to 2000 there were two different gamma ray instruments. The MFI is comprised of two fluxgate magnetometers at different locations on a 12 meter boom (one closer at ~8 m, the other at 12 m) which improves spacecraft noise/artifact removal (one from 3DP, one from SMS, and one from EPACT). There are three separate measurements of protons with energies >50 keV. Finally, there are at least three separate measurements of heavy ions (i.e., ions more massive than alpha-particles). The instrument capabilities and current status are shown in Table 2.

Most of the instruments continue to be fully functional, aside from temporary complete or partial data losses due to a command and attitude processor (CAP) and tape unit anomaly (both issues were resolved or mitigated). The dates of significant spacecraft and instrumental issues are listed below for reference in chronological order:

- **January 19, 1995:** GTM1[3] failure
- **October 1995:** APE-A/APE-B/IT HVPS[4] suffered a loss of gain
- **April 30, 1997:** CAP1[5] Reed-Solomon encoder failure
- **December 13, 1997:** DTR2[6] power supply failure
- **January 2000:** TGRS γ-ray instrument turned off (planned coolant outage)
- **May 2000:** SMS-SWICS solar wind composition sensor turned off
- **June 2001:** SWE-VEIS thermal electron detectors HVPS failure
- **August 2002:** SWE-Strahl reconfigured to recover VEIS functionality
- **June 2009:** SMS DPU experienced a latch-up reset – MASS acceleration/deceleration power supply in fixed voltage mode
- **2010:** SMS-MASS experienced a small degradation in the acceleration/deceleration power supply
- **May 19, 2014:** 3DP-PESA Low suffered an anomaly that affected only the telemetry HK data
- **October 27, 2014:** CAP1 anomaly at ~21:59:38 GMT
- **November 7, 2014:** CAP2 set to primary while recovery starts on CAP1
- **November 26, 2014:** full reset of SWE instrument due to CAP1 anomaly
- **January 30, 2015:** CAP1 fully recovered
- **April 11, 2016:** DTR1 TUA began experiencing read/write errors (~1% bit errors)
- **May 6, 2016:** FOT switches to DTR1 TUB for primary recorder

1.3 Solar Wind 25-year Mission Statistics

In this review, we present *Wind* results for a variety of environments and durations in an effort to highlight a reasonable fraction of *Wind*'s publications. For a broad overview of *Wind* particles and field observations, Figure 2 shows 25+ years of observations from MFI and SWE instruments across more than two solar cycles (late cycle 22–cycle 24) indicated by the background color. The temporal resolutions for MFI and SWE are ~1 minute (averages) and ~92 seconds, respectively. A 2D histogram was constructed from one week bins on the horizontal axis while the vertical axis is split up into 300 bins for each panel. The color bars show the number of counts in each bin where white space represents no counts and red [represents] saturation. These calculations include solar wind and magnetospheric intervals. The fluxgate magnetometer had few data gaps during mag-

[3] two GGS telemetry modules, GTM1 and GTM2
[4] high voltage power supply
[5] two command and attitude processors, CAP1 and CAP2
[6] two digital tape recorders, DTR1 and DTR2, each with independent tape units, TUA and TUB

Table 2: Operational Instruments on *Wind*

Name	Type	Cadence	Range	Status & Notes
MFI				**Nominal**
	3 $B_{o,j}$[a]	∼11–22 sps[b]	±4 – ±65,536 nT	±0.001 – ±16 nT
WAVES				**Nominal**
TDS Fast	2 δE_j	1.8–120 ksps	∼0.1–300 mV/m	∼80 μV rms
TDS Slow	1 or 3 δE_j	0.1–7.5 ksps	∼0.5–300 mV/m	∼300 μV rms
	1 or 3 δB_j	0.1–7.5 ksps	∼0.25 – $\gtrsim$30 nT	∼10^{-9} nT^2 Hz^{-1} @ 100 Hz
TNR	1 δE_j	∼1 min	∼4–256 kHz	∼7 nV Hz$^{-1/2}$
RAD1	2 δE_j	∼1 min	∼20–1040 kHz	∼7 nV Hz$^{-1/2}$
RAD2	2 δE_j	∼1 min	∼1.1–14 MHz	∼7 nV Hz$^{-1/2}$
3DP				**Nominal**
EESA	e^-	∼3–22 s	∼0.003–30 keV	∼20% $\Delta E/E$[c], ∼5.6–22.5°
PESA	H^+, He^{2+}	∼3–75 s	∼0.003–30 keV	∼20% $\Delta E/E$, ∼5.6–22.5°
SST Foil	e^-	∼12 s	∼25–400 keV	∼30% $\Delta E/E$, $\gtrsim$22.5°
SST Open	H^+	∼12 s	∼25–6000 keV	∼30% $\Delta E/E$, $\gtrsim$22.5°
SWE				**VEIS Off, Strahl Reconf.**
FCs	H^+, He^{2+}	∼92 s	∼0.15–8 keV	∼6.5% $\Delta E/E$
Strahl	e^-	∼12 s	∼0.005–5 keV	∼3% $\Delta E/E$
				∼3° × 30°
SMS				**SWICS Off, MASS Reduced**
STICS	H – Fe	$\gtrsim$3 min	∼8–226 keV/e	∼5% $\Delta E/E$, ∼4° × 150°
			1–60 amu/e	∼12% $\Delta M/M$[d]
EPACT				**IT off, APE Reduced**
LEMT	He – Fe	$\gtrsim$5–60 min	∼2–12 MeV/n	$\gtrsim$20% $\Delta E/E$
			∼2–90 Z	$\gtrsim$2% $\Delta Q/Q$[e]
STEP	H – Fe	$\gtrsim$10 min	∼0.02–2.56 MeV/n	$\gtrsim$30% $\Delta E/E$
				∼17° × 44°
				Nominal
KONUS	photons	$\gtrsim$2 ms	∼0.02–15 MeV	$\gtrsim$5% $\Delta E/E$
		$\gtrsim$3 s	∼0.02–1.5 MeV	Background Mode
				Off (out of coolant)
TGRS	photons	$\gtrsim$62 μs	∼0.025–8.2 MeV	∼3 keV @ 1 MeV
				eff. ∼43% @ 511 keV

[a] three magnetic field vector components [b] samples per second [c] normalized energy resolution
[d] normalized mass resolution [e] normalized charge resolution

netospheric passes. The SWE Faraday cups could not track the bulk ion population within the magnetosphere and exhibit sparser coverage than MFI prior to May 2004.

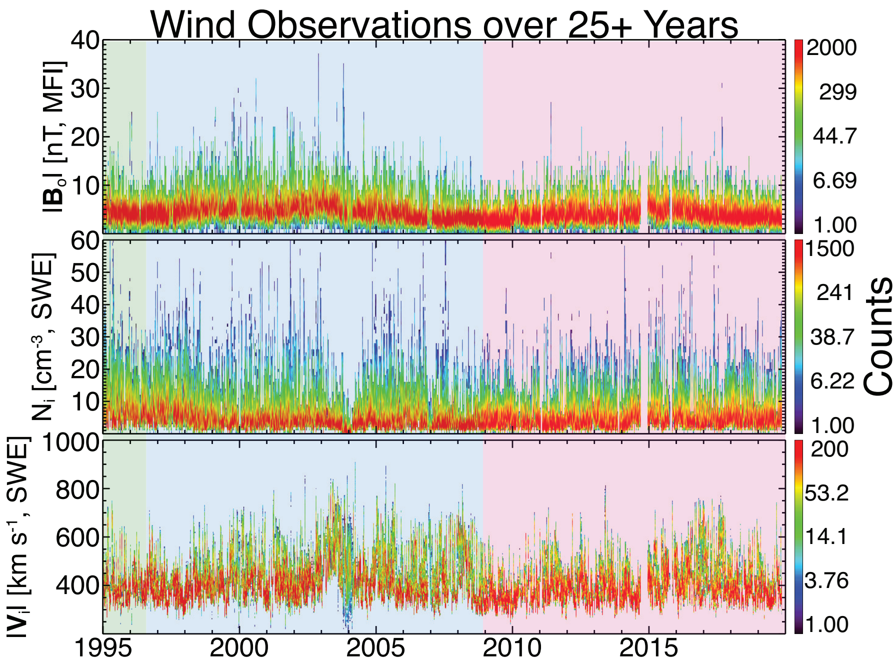

Figure 2: *A 2D histogram representation of 25+ years of* Wind *observations. The panels are as follows from top to bottom: quasi-static magnetic field magnitude [nT], total ion number density [cm^{-3}], and total ion bulk flow speed [km/s]. The shading corresponds to solar cycles 22 (green), 23 (blue), and 24 (magenta). The color bars indicate the counts in each bin (see text for details).*

Table 3: Solar wind statistics

Solar Cycle	n_i $[cm^{-3}]$[a]	V_i $[km\ s^{-1}]$	B_o $[nT]$
Overall[b]	1.70–16.8, ∼5.24	304–633, ∼405	2.42–12.0, ∼5.04
22 End	2.65–20.2, ∼7.42	310–637, ∼398	2.45–11.3, ∼5.01
23 All	1.57–17.0, ∼5.11	309–652, ∼418	2.55–13.7, ∼5.46
24 All	1.75–15.5, ∼5.11	299–605, ∼392	2.30–10.2, ∼4.62

[a] $X_{5\%}$–$X_{95\%}$, $\tilde{X}$ (where $X_{y\%}$ is the yth percentile and $\tilde{X}$ is the median).
[b] Magnetospheric data are not included in the particle stats as SWE cannot measure magnetospheric ions

Section 2 traces *Wind*'s science journey through time and different regions of space. We begin in Section 2.1 with gamma ray detections of energetic events both within and beyond our own galaxy. We then discuss interstellar and interplanetary dust in Section 2.2. Section 2.3 focuses on *Wind*'s contribution to our understanding of the lunar wake. Section 2.4 introduces magnetic reconnection and discusses *Wind* observations in Earth's magnetotail. Section 2.5 highlights some discoveries and advances made in our understanding of the Earth's radiation belts. Section 2.6 discusses the numerous contributions *Wind* has made to our understanding of the terrestrial foreshock. Section 2.7 includes multiple subsections that discuss studies in the solar wind of large scale structures and magnetic reconnection (Section 2.7.1), kinetic instabilities and waves (Section 2.7.2), turbulence (Section 2.7.3), and long-term statistical studies (Section 2.7.4). Section 2.8 discusses the *Wind*'s contribution to our understanding of interplanetary shocks (Section 2.8.1), interplanetary coronal mass ejections (Section 2.8.2), and corotating interaction regions (Section 2.8.3). Section 2.9 highlights a selection of *Wind* discoveries involving solar energetic particles. Section 2.10 illustrates *Wind*'s critical contributions to our understanding of solar radio bursts. Finally, Section 3 provides a brief summary of the review. We also include two Appendices where Appendix A provides symbol/parameter definitions and Appendix B provides a review of several plasma instabilities and their properties. We also provide a Glossary of terms and a list of acronyms/initialisms for the reader.

2 Selected Science Results from *Wind*

In this section we highlight and review some of the major scientific work that was either enabled by or directly resulted from *Wind* studies. The purpose is to illustrate both the breadth and importance of *Wind* in heliophysics and astrophysics. This section will also illustrate one of *Wind*'s greatest assets; the redundancies of some of its instruments which greatly improves the calibration and accuracy of the data products.

Wind was designed to examine space plasmas, therefore we must define what is a plasma and the environments through which *Wind* has flown. A plasma is an ionized gas exhibiting a collective behavior that is found in nearly all regions of space. Plasmas are mediated by long-range forces (i.e., electromagnetic) as well. Many plasmas, like that of the solar wind, are not in thermodynamic or even thermal equilibrium. That is, the temperatures of species s' and s are not equal or $(T_{s'}/T_{s})_{tot} \neq 1$ for $s' \neq s$ (see Appendix A for symbol definitions) and there is an ubiquitous presence of finite heat fluxes, i.e., nonequilibrium particle distributions. The former negates thermal equilibrium and both the former and latter negate thermodynamic equilibrium.

The near-Earth environment (see cartoon in Figure 3) is comprised of a neutral atmosphere surrounded by a plasma. The transition between the two is not abrupt. The neutral atmosphere consists of the troposphere, the stratosphere, the mesosphere, and a portion of the thermosphere. In the thermosphere, temperature increases as a function of altitude and as a function of extreme ultraviolet radiation. The ultraviolet radiation ionizes neutral constituents and gives rise to the ionosphere, a collisionally mediated, weakly ionized plasma. Above the ionosphere is the plasmasphere surrounded by the magnetosphere which is bounded by the magnetopause. Within the magnetosphere are the Van Allen radiation belts, magnetotail, and several other regions. The magnetosheath separates the magnetopause from the bow shock, the largest feature of the near-Earth environment. The bow shock is the outermost boundary between the magnetosphere and the interplanetary medium (IPM) and solar wind. The magnetopause forms due to the Earth's magnetic field acting as an obstacle to the supersonic flow of the solar wind. The plasma compresses on the sunward side, piling up leading to a nonlinearly steepening fast/magnetosonic wave. Eventually this steepening wave reaches a balance between nonlinear steepening and energy dissipation, at which point the bow shock forms.

Plasmas are ordered as collisionless, weakly collisional, collisional, and strongly collisional. A weakly collisional system is one in which the collision rate is small but not completely negligible compared to other relevant time scales (e.g., cyclotron frequency). The solar wind is an example of a weakly collisional, magnetized plasma that is constantly emitted from the sun with variable speeds from $\sim$280 km/s to >800 km/s (e.g., see Figure 2) and comprised of $\sim$95% protons, $\gtrsim$4% alpha-particles, and electrons (e.g., Alterman & Kasper, 2019; Kasper et al., 2012). In the solar wind near Earth, one Debye length is $\sim$9 meters while the scattering cross-sectional radius for neutral particles can be roughly six orders of magnitude smaller. Further, the transit time from the sun to the Earth for a typical solar wind parcel is $\sim$3-4 days while the Coulomb collision period between particles is typically $\gtrsim$0.5–1.0 days (e.g., Wilson III et al., 2018). Thus, the solar wind is a weakly collisional medium near Earth, for example.

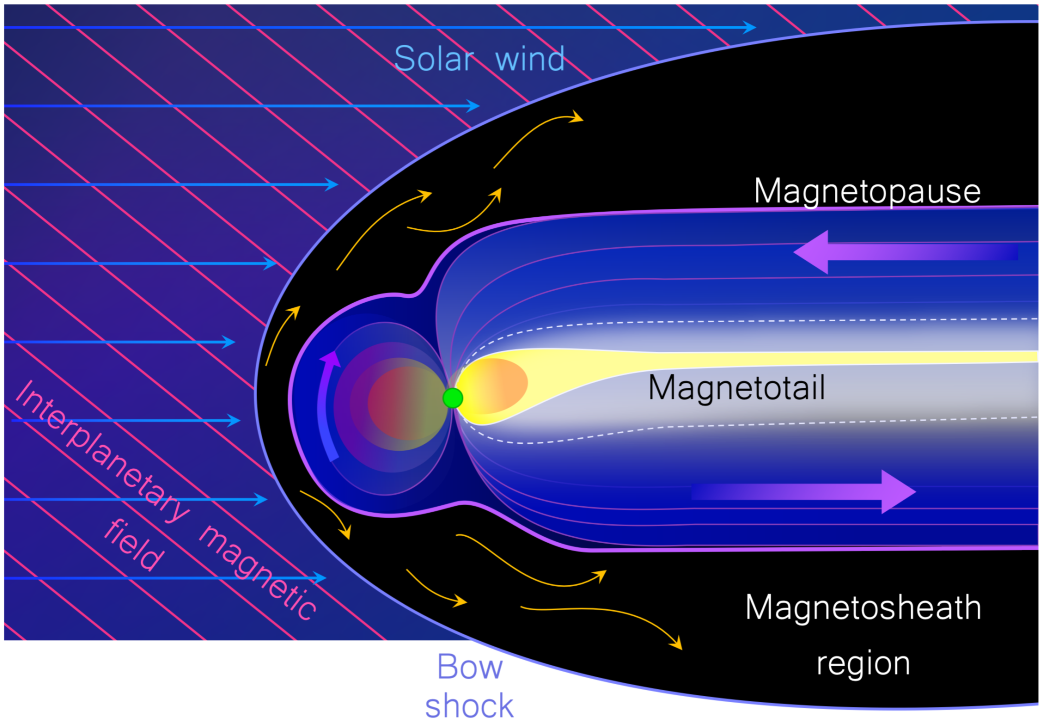

Figure 3: *Cartoon of the Earth's global geospace environment (not to scale) shown in the plane orthogonal to the ecliptic.*

The collisionless limit is obviously that which ignores all Coulomb collisions on the time scales of interest. Shock waves are considered collisionless because the gradient scale length of the ramp tends to fall between the electron and ion inertial lengths (i.e., ∼1-100 km near Earth) while the Coulomb collision mean free path of protons can be ∼1 AU[7] (e.g., Wilson III et al., 2018). Thus they are called collisionless shocks.

Collisionless shock waves are distinguished by their Mach number (M_f), shock normal angle[8], θ_{Bn} (e.g., quasi-perpendicular shocks satisfy $\theta_{Bn} \geq 45°$), and upstream averaged plasma beta ($\langle\beta_{tot}\rangle_{up}$). The asymmetric ram pressure/forces due to the supersonic solar wind combined with plasma coupling to the fields causes the Earth's magnetic dipole field to be "dragged out" into a tail with the appearance of something akin to a wind sock. On the sunward (upstream) side of the bow shock, the region upstream of the quasi-parallel portion of the bow shock is called the ion foreshock (see Section 2.6 and Figure 7) and is filled with multiple backstreaming ion populations and energetic electrons (Wilson III, 2016; Wilson III et al., 2016). The interplanetary magnetic field (IMF) can be visualized as open solar magnetic field lines approaching Earth at approximately 45 degrees to the Earth-Sun direction. The radial Sun-Earth line is along the horizontal in Figure 3.

A unique attribute of *Wind* for solar wind studies is that it is the only near-Earth spacecraft that consistently measures the "plasma line" in the solar wind. The plasma line (or upper hybrid line) is a thermal emission that occurs at the upper hybrid frequency, f_{uh} (see Appendix A for symbol definitions), and can be measured because the WAVES

[7] The Coulomb collision mean free path of protons near 1 AU is also on the order of ∼1 AU.
[8] the angle between upstream average magnetic field vector and shock normal unit vector

antenna are longer than the local Debye length, λ_{De} (see Table 5). The plasma frequency is so much larger than the cyclotron frequency in the solar wind, i.e., $f_{pe} \gg f_{ce}$, that the upper hybrid line is often called the plasma line because $f_{uh} \sim f_{pe}$. Even without this approximation, the spacecraft accurately measures the magnetic field so one can invert the observed upper hybrid line frequency to solve for the total electron density. This gives the only unambiguous measurement of the total electron density from any instrument and is used to calibrate the thermal particle detectors not just on *Wind*, but other spacecraft as well (e.g., THEMIS plasma instruments McFadden, Phan, et al., 2008; McFadden, Carlson, et al., 2008).

In the following subsections we highlight selected scientific discoveries and/or advances made using *Wind* observations.

2.1 Remote Astrophysics

2.1.1 Gamma Ray Bursts

Cosmic gamma ray bursts (GRBs) are the brightest electromagnetic events known to occur in the universe and are triggered by the collapse of massive stars or the coalescence of compact objects. Even though the call for proposals to the International Solar-Terrestrial Physics program had already taken place, the discovery of gamma ray bursts in the 1970s by Klebesadel et al. (1973) prompted the addition of two gamma ray detectors to the *Wind* instrument payload. The KONUS instrument (Aptekar et al., 1995), also called KONUS-W, is the first Russian instrument to fly on a US spacecraft.

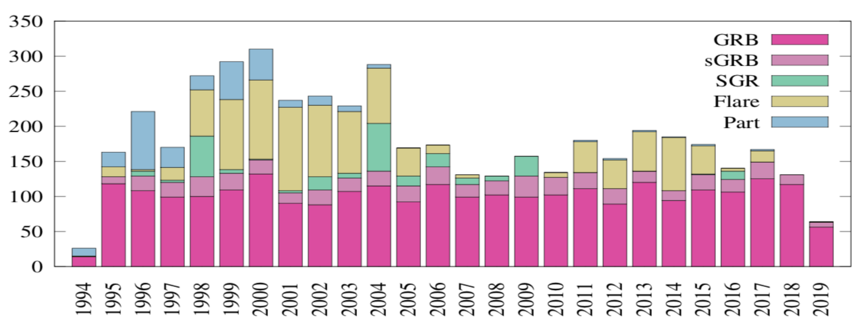

Statistic of ~4700 KW triggers from November 1994 to mid-2019.

Figure 4: *KONUS statistics of various astrophysical events emitting gamma rays. The color code corresponds to the type of burst trigger for the instrument, which are defined as: GRB is gamma ray burst ($\gtrsim$2740, magenta); sGRB is short gamma ray burst ($\sim$500, purple); SGR is soft gamma repeater ($\sim$270, green); Flare is solar flare ($\gtrsim$1040, yellow); and Part is particle event-induced (taken from Figure 1 in D. Frederiks et al., 2019).*

By studying GRBs, we can learn about the formation of large-scale structures in the early universe and present-day processes (Fishman & Meegan, 1995; Fishman, 1995). GRBs consist of an initial flash of gamma-rays lasting from tens of milliseconds to minutes followed by a longer duration afterglow at radio and optical wavelengths. For a particularly bright event, (Guiriec et al., 2017) find evidence of a photospheric jet by comparing simultaneous KONUS[9,10] and *Fermi* observations. In 2019, the gravitational wave facilities Advanced LIGO and Virgo provided evidence of short GRBs associated with both binary neutron star mergers and the emission of gravitational radiation (Abbott et al., 2019)[11]. As of 2020, 300 bursts per year are detected by KONUS (roughly 6000 to date). Figure 4 shows the gamma ray bursts detected by KONUS between 1994 and 2019 (D. Frederiks et al., 2019).

2.1.2 Soft Gamma Repeaters (Magnetars)

Soft gamma repeaters (SGRs), also called magnetars, are strongly magnetized Galactic neutron stars with surface magnetic fields up to 10^{14} G. Magnetars emit large bursts of X-rays and gamma-rays at irregular intervals (Aptekar et al., 2002; Kouveliotou et al., 1999). Approximately two dozen magnetars have been identified. When these sources become active, they emit several up to several hundreds of bursts within a timeframe of days to months.

Magnetar giant flares (GFs) are of greater apparent intensity than GRBs with an average occurrence rate of once per decade (D. D. Frederiks et al., 2007; Hurley et al., 2010). Only a handful of GFs have been detected. The intensity of a single event is sufficient to create ionospheric disturbances. KONUS has detected extragalactic GFs from the Andromeda and the M81 group (Mazets et al., 2008; D. D. Frederiks et al., 2007) and more recently the discovery of a GF from the Sculptor galaxy (D. Svinkin, Golenetskii, et al., 2020; D. Svinkin, Hurley, et al., 2020).

2.1.3 Solar Flares

During its more than 25 year-long history, the KONUS instrument onboard *Wind* has accumulated an unique volume of solar flare observations in the hard X-ray and gamma ray range. Data on solar flares recorded by KONUS in the triggered mode are published online (`http://www.ioffe.ru/LEA/kwsun/`) from 1994 to the present along with their GOES classification. This database (see Table 6) provides light curves with high temporal resolution (up to 16 ms) and energy spectra over a wide energy range (now $\sim$20 keV to $\sim$15 MeV). The high time resolution of KONUS allows for the study of fine temporal structure in solar flares. The KONUS energy band covers the region of nonthermal emission due to accelerated electrons and ions in solar flares, which allows probing the source of their acceleration. Thus, the *Wind* KONUS solar flare observations provide researchers with an additional, high time resolution data product with which to examine solar flare phenomenon.

2.2 Interstellar and Interplanetary Dust

This section gives a broad overview of the heliosphere via interplanetary and interstellar dust. Dust in the interplanetary and interstellar media can be studied in situ using dedicated mass spectrometers or, as on *Wind*, electric field measurements. While *Wind* mission objectives did not include the detection of dust, it was realized that a certain type of impulsive, “spiky” waveform, electric field signal observed by the *Wind*/WAVES time domain sampler (TDS) receiver was the product of hypervelocity dust impacts. The

[9] KONUS is the most prolific detector in the Interplanetary Network (IPN, `http://ssl.berkeley.edu/ipn3/index.html`), which contains gamma-ray detectors from a variety of telescopes, including *Swift* and *Fermi* (Cline et al., 2001; Hurley, Cline, et al., 2003; Hurley, Atteia, et al., 2003; Hurley et al., 2011), maintained by Dr. Kevin Hurley at UC Berkeley.

[10] KONUS is also a member of the Gamma-ray Burst Coordinates Network or GCN (`https://gcn.gsfc.nasa.gov`), maintained by Dr. Scott Barthelmy at NASA's Goddard Space Flight Center

[11] The authors also cite *Wind* data from the Interplanetary Network in their study.

electric field pulse is caused by short-lived clouds of plasma due to the ablation of spacecraft material during the impact.

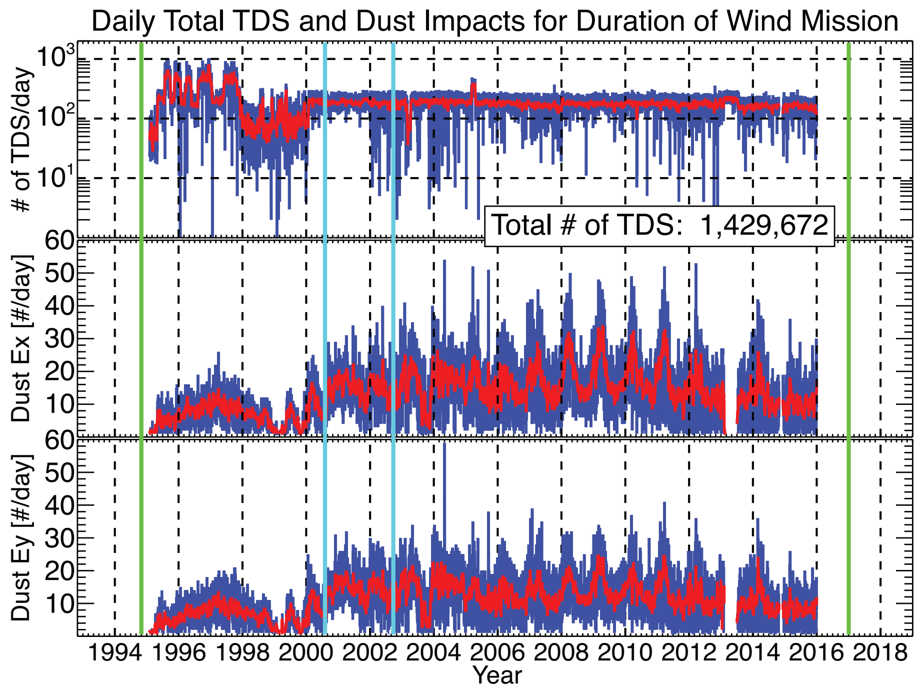

Figure 5: *Plot of the entire* Wind *mission showing the daily totals. In each panel the dark blue and red lines represent the actual and 10-day smoothed counts, respectively. The panels shown are the following (in order from top-to-bottom): daily total number of TDS events; number of dust impacts observed on the x-antenna; and number of dust impacts observed on the y-antenna. The two vertical green lines define the duration of the Wind mission at the time of creation of this figure (i.e., Jan. 2017). The two vertical cyan lines define the times when the x-antenna was cut apparently by dust impacts (Adapted from Figures 5 and 6 in Malaspina & Wilson III, 2016).*

Researchers determined that the signals corresponded to micron-sized (i.e., dust grains approximately $\sim$1 μm in size) interplanetary dust (IPD) and interstellar dust (ISD) (Malaspina et al., 2014; Sterken et al., 2019). S. R. Wood et al. (2015) then determined the longitudinal direction of ISD using spectroscopic measurements from *Ulysses*, which was orbiting the solar poles. Although dust had been detected previously using the same method on other spacecraft (Malaspina et al., 2015; Sterken et al., 2019; I. Mann et al., 2019), S. R. Wood et al. (2015) presented the first antenna triangulations of ISD with the *Wind* and *Ulysses* spacecraft across an entire solar cycle. They utilized the yearly modulation of dust count rates to separate ISD from IPD. The authors show an unexplained source of variability in 2005 on a timescale of less than a year. This temporal variability is interesting because it deviates fromthe expected temporal variability of the dust count rates and remains unexplained.

Subsequent work led to the creation of a *Wind* dust impact database (Malaspina & Wilson III, 2016), comprised of >107,000 impacts, which is publicly available through SPDF CDAWeb (see Table 6). The large statistics allowed researchers to determine that *Wind* does not respond to dust grains with sizes $\ll$0.1 μm, the so called nanodust (Kellogg et al., 2016; Kellogg, 2017; Kellogg et al., 2018; Malaspina et al., 2014; Malaspina & Wilson III, 2016; Sterken et al., 2019).

Figure 5 shows the counting statistics for TDS events and dust impacts observed by the *Wind* TDS receiver. The obvious annual variation in dust impacts seen in the bottom two panels is primarily due to ISD. The reason is that for half of the year, *Wind* is moving approximately anti-parallel to the flow of ISD through the solar system. The difference in flow speed of the ISD in *Wind*'s reference frame varies from ∼4–56 km/s, thus leading to an annual variation in the counting rates (i.e., higher impact speeds produces larger electric field amplitudes and thus more dust observations). This annual variation has been reported in multiple studies (Kellogg et al., 2016; Malaspina et al., 2014; Malaspina & Wilson III, 2016; S. R. Wood et al., 2015).

The *Wind* dust impact database presents exciting opportunities for heliospheric dust dynamics (Sterken et al., 2019) and statistical studies of the dependence on large-scale, transient magnetic phenomenon (see Sections 2.8.2 and 2.8.3). The relevance of dust to the heliospheric community has increased in recent years with the recognition that it plays an important role in numerous ways from mass, momentum, and energy transport to physical damage to spacecraft (e.g., cutting of wire antenna). For instance, one of the wire antennas, that form the electric field probes for *Wind*/WAVES, was cut twice by what is suspected to be dust impacts. The first occurrence happened on August 3, 2000 and the second time on September 24, 2002.

Finally, a more recent development arose when an Earth-observing spacecraft, Aeronomy of Ice in the Mesosphere (AIM) (Russell et al., 2009). Although the mission is cloud-focused, cloud science overlaps with studies of dust, geomagnetic activity, and solar cycles (Hervig et al., 2017, 2019; X. Liu et al., 2018). For instance, researchers have recently found some variations in meteoric smoke – the product of meteoroid ablation (at ∼75–110 km altitude) in Earth's mesosphere. These observations were made by the Solar Occultation For Ice Experiment (SOFIE) (Gordley et al., 2009). Interestingly, the temporal variations in meteoric smoke are consistent with the dust count rates observed by *Wind*, providing a new avenue of research and future collaborations.

2.3 Lunar Wake Studies

Wind offered the first modern[12] glimpses into the lunar wake in 1994 and completed 10 wake crossings before entering a Lissajous orbit at L1 in 2004. Table 4 lists all crossings of the lunar optical wake (Ogilvie & Desch, 1997).

Table 4: Optical Lunar Wake Transits by *Wind*

Start time [UTC]	End time [UTC]
1994-12-01/15:04:07	1994-12-01/15:29:10
1994-12-27/14:36:30	1994-12-27/15:22:36
1996-03-24/05:19:43	1996-03-24/06:24:50
1996-11-13/01:43:16	1996-11-13/03:07:25
1999-04-01/20:38:02	1999-04-01/20:53:04
1999-05-12/20:52:12	1999-05-12/21:04:14
2000-08-19/15:35:45	2000-08-19/16:51:53
2001-12-05/16:48:53	2001-12-05/17:54:00
2002-07-18/17:46:39	2002-07-18/18:42:45
2002-11-30/11:30:28	2002-11-30/12:16:33

[12] the first lunar wake observations by the *Explorer 35* and *Apollo* missions occurred at around 2 lunar radii from the lunar surface (Ness, 1972)

The lunar environment is an exciting laboratory for plasma physics (Halekas, Angelopoulos, et al., 2011; Halekas, Saito, et al., 2011; Halekas et al., 2015), comparative planetology, solar system formation, and astrochemistry. Because the moon is relatively nonconducting, the interplanetary magnetic field passes through the obstacle while solar wind ions and electrons only interact with the lunar surface. As a result, the near-moon plasma environment has a low-density downstream cavity called a wake. *Wind* contributed the first wake measurements more than 2 lunar radii or R_L from the surface (Bosqued et al., 1996; Farrell et al., 1998; Owen et al., 1996). Ogilvie et al. (1996) presented wake field and particle observations which contradicted the previously accepted theory of a magnetohydrodynamic wake flow. In the lunar wake, *Wind* observed oppositely directed ion beam distributions (Farrell et al., 1997; Ogilvie et al., 1996). These beams are a response to asymmetric ambipolar diffusion.

According to the magnetohydrodynamic (MHD) paradigm, the spatial scale of magnetic field perturbations near the wake should be much larger than an electron orbit while the ions are on a ballistic trajectory interacting with an unmagnetized body. Therefore, the ions and electrons should behave like a fluid around such an obstacle. This MHD model predicted that the lunar wake would extend to no more than four lunar radii or $\sim$4 R_L (Bosqued et al., 1996; Farrell et al., 1998; Owen et al., 1996). However, *Wind* still observed a wake at $\sim$6 R_L (Bosqued et al., 1996; Farrell et al., 1996; Kellogg, Goetz, et al., 1996; Ogilvie et al., 1996; Owen et al., 1996). The alignment of the lunar wake with respect to the moon's optical shadow helps us understand the complex ion and electron flow patterns which act to replenish the low-density cavity (Clack et al., 2004).

2.4 Reconnection in the Magnetotail

This section and the following Section 2.5 describe several studies which draw upon *Wind* observations within Earth's magnetic environment.

Magnetic reconnection is the process by which a change in the magnetic field topology results in the destruction of magnetic flux and the conversion of electromagnetic energy to particle kinetic energy (see Hesse & Cassak, 2020, for a detailed review). The process of magnetic reconnection is universal in space plasmas and occurs in response to stretching and/or compression of regions with oppositely directed magnetic fields. As the oppositely directed magnetic fields slowly converge, a current sheet begins to form creating a spatially thin region called the diffusion region (Sonnerup, 1979). Traditionally this is associated with a so called "X-line" or place where the magnetic field lines trace out an X (e.g., see the gray boxes in the cartoon in Figure 6). The diffusion region is where magnetic flux is destroyed and electromagnetic energy starts to convert to particle kinetic energy forming two oppositely directed, outflowing jets, sometimes called "reconnection exhausts." Magnetic reconnection has been known to be an important particle energization mechanism in astrophysical plasmas for decades. This section describes magnetic reconnection discoveries made using *Wind* data in Earth's geomagnetic tail or magnetotail – region anti-sunward of Earth where Earth's magnetic dipole field lines are stretched and compressed due to asymmetric pressure/forces from the solar wind. Section 2.7 discusses conditions and processes relevant to reconnection in the solar wind.

When the magnetic field changes on shorter spatial scales than the particles can respond (i.e., they can no longer follow a single magnetic field line), they are said to be demagnetized. The magnetic reconnection process starts in the diffusion region, which is characterized by the presence of dissipative electric fields on small length scales (i.e., smaller than the particle gyroradii and/or inertial length). There are in fact two diffusion regions, one for the electrons and one for the ions. When inside of the ion diffusion region, thermal ions become demagnetized but electrons can still remain magnetized. However, inside the electron diffusion region, both particle populations become demagnetized. The presence of dissipative fields allows changes in magnetic field topology by redistributing energy between fields and particles resulting in large scale (much larger than ion gyroradii and/or inertial lengths) consequences.

Although early observations associated with reconnection in space provided evidence of the reconnection process through downstream outflows identified as exhausts, the diffusion region was not observed directly (e.g., Paschmann et al., 1979). The observational discovery of the magnetic reconnection (ion) diffusion region was made in Earth's magnetotail at ∼60 R_E by *Wind* (Øieroset et al., 2001). The primary evidence of reconnection presented in this study was the quadrupolar (Hall) magnetic field around an X-line crossing (see Figure 6), which caused the ions to become demagnetized as they enter the diffusion region. In the same reconnection event, *Wind* found direct evidence that reconnection can accelerate electrons to suprathermal energies, up to 300 keV (Øieroset et al., 2002). Later studies sought to explain the electron energization. In particular, Drake et al. (2006) suggested that the contraction of magnetic islands was involved, leading to new ideas of particle energization in magnetic reconnection.

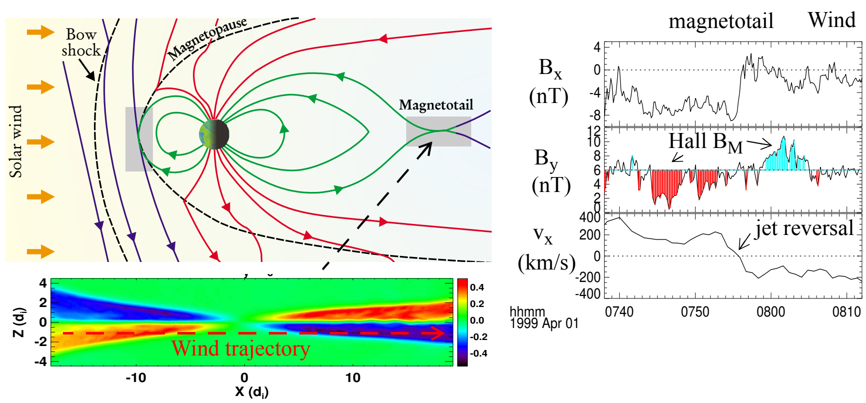

Figure 6: Wind *encounter with the magnetic reconnection ion diffusion region in Earth's magnetotail, showing (right) the out-of-plane Hall magnetic field B_y and the reversal of the reconnection outflow jets across the reconnection region. The simulation panel shows the normalized Hall B_y with* Wind*'s trajectory overlaid (red dashed line). Note that the polarity in the simulation is different from the* Wind *data, which is a consequence of the coordinate basis (Modified from Figures 1 and 2 in Øieroset et al., 2001).*

Raj et al. (2002) found a clear dawn-dusk asymmetry in the occurrence of asymmetric magnetic reconnection in *Wind* observations in Earth's magnetotail. Reconnection occurred preferentially on the dusk side, which links tail reconnection to nightside auroral intensifications[13]. The *Wind* discovery led to a number of studies trying to explain the source of the asymmetry, including ionospheric control of tail reconnection Lotko et al. (2014).

[13] Auroral intensifications are known to be strongly skewed toward the dusk/pre-midnight sector.

2.5 The Radiation Belts

In this section, we describe the large amplitude whistler mode waves[14] observed in the radiation belts (note these were originally discovered by C. Cattell et al., 2008, using STEREO observations). The peak-to-peak electric and magnetic field amplitudes of these waves can exceed 200 mV/m and 8 nT, respectively (Kellogg et al., 2011; Wilson III et al., 2011). These values are >10 times the magnitude of previous observations and call into question the assumptions required in quasi-linear diffusion models that are based upon much smaller wave amplitudes (C. A. Cattell et al., 2012). For each magnetospheric pass examined that traversed the radiation belts, Wilson III et al. (2011) found that large amplitude waves were present in the radiation belts. Kellogg et al. (2011) used *Wind* to provide some of the first evidence that these waves were being excited by electrons with energies below ∼30 keV – previous work suggested that energies of at least 100 keV were necessary to excite whistler mode waves in the radiation belts. Kellogg et al. (2011) also showed evidence of electron beam-driven electrostatic solitary waves in conjunction with large amplitude whistler mode waves. This result suggested that the energy budget and particle dynamics of the radiation belts are not as well understood as previously thought.

Wilson III et al. (2011) showed that the whistler mode wave amplitudes had a weak positive correlation with the auroral electrojet index or AE-index[15]. The large amplitude whistler mode waves in this study were concurrent with earthward injections of ∼30–300 keV electrons from the geomagnetic tail. Wilson III et al. (2011) also obtained a lower bound on the Poynting flux of one wave, which was $\gtrsim$300 μW m^{-2}, or nearly four orders of magnitude larger than any previous measurement for radiation belt whistler mode waves. A previous statistical survey of whistler mode chorus Poynting flux found typical amplitudes of ∼0.05 μW m^{-2} (Santolík et al., 2010). The authors used this value to estimate the time scale for filling a ∼3 R_E long, field-aligned column flux tube in the radiation belt with ∼1 MeV electrons energized from typical plasma sheet energies (i.e., ∼200–10^4 eV). Assuming a 1% efficiency Santolík et al. (2010) estimated that chorus could fill the outer radiation belt in a matter of days, consistent with the then standard assumption of the radiation belt refilling time scale of ∼1 day (Horne et al., 2005). For comparison, using the $\gtrsim$300 μW m^{-2} *Wind* observation and a 1% efficiency, the time scale decreases to ∼33 seconds providing further evidence that the energy budget and particle dynamics of the radiation belts were not as well understood as previously thought.

These *Wind* studies also helped to define some of the primary science goals for the electromagnetic fields instruments (Wygant et al., 2013) on NASA's *Van Allen Probes*, which were launched in 2012. The *Wind*-estimated timescale of sub-minute energization was considered much too short at the time of publication but later studies using *Van Allen Probes* (O. Agapitov et al., 2019) reduced the upper limit to less than ∼3 hours from the previous ∼12-24 hour time scales[16]. *Wind* also serves as an upstream monitor for radiation belt studies by the *Van Allen Probes* and other magnetospheric missions (Borovsky & Denton, 2009; Halford et al., 2015; Jaynes et al., 2015; W. Li et al., 2015; I. R. Mann et al., 2016; Schiller et al., 2014; Turner et al., 2014).

Wind studies of large amplitude whistler waves have led to a series of new theoretical analyses based upon the new, much larger wave amplitude estimates. A compre-

[14] Note that both chorus-like and hiss-like emissions were observed in these studies but because of most events exhibiting a relatively narrow, constant frequency peak, Kellogg et al. (2011), Kersten et al. (2011), and Wilson III et al. (2011) use the words *whistler mode wave*.

[15] a set space weather numerical values designed to provide a global, quantitative measure of auroral zone magnetic activity produced by enhanced ionospheric currents

[16] Note these time scales are for electrons below ∼1 MeV. Changes in electrons at or above ∼1 MeV are still in the ∼12 hour time range.

hensive review of large amplitude whistler mode waves in the radiation belts can be found in C. A. Cattell et al. (2012).

2.6 The Ion Foreshock

In this section, we discuss *Wind* measurements upstream of Earth's bow shock in the region magnetically connected to the quasi-parallel shock called the foreshock, where the shock can communicate with the unperturbed solar wind. Figure 7 shows a cartoon example of a possible foreshock scenario illustrating the multiple particle population regions and the presence of large amplitude electromagnetic fluctuations/disturbances (see Wilson III, 2016, for detailed review of the foreshock).

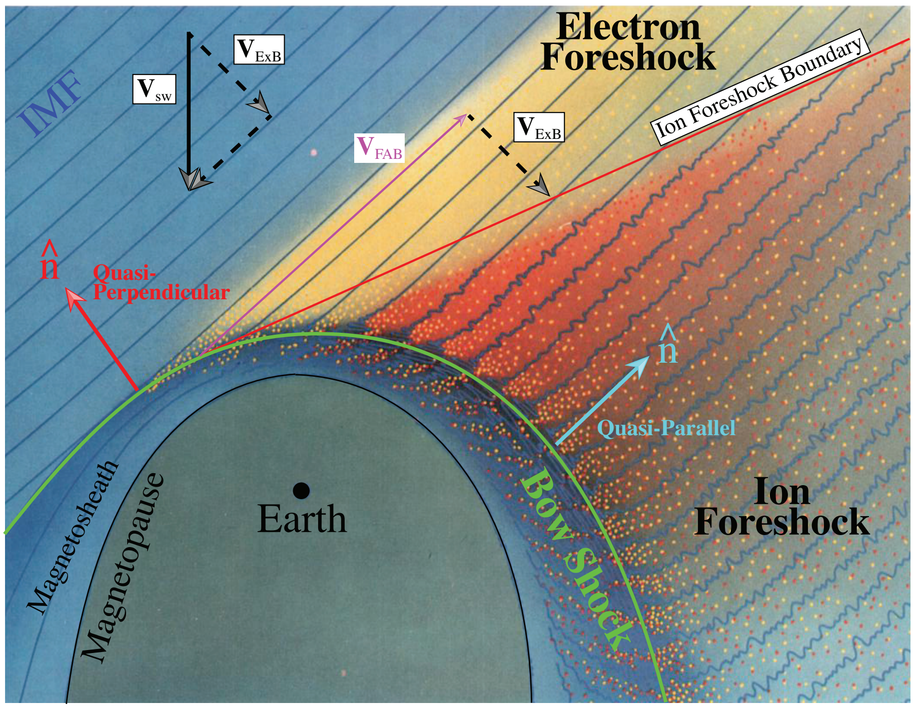

Figure 7: *A cartoon example of a possible terrestrial foreshock configuration. The interplanetary magnetic field (IMF) is represented by the dark blue lines,* $\mathbf{V}_{sw}$ *represents the bulk solar wind velocity,* $\mathbf{V}_{ExB}$ *is the* $(E \times B)$*-drift velocity due to the solar wind convection electric field, and* $\mathbf{V}_{FAB}$ *is the reflected field-aligned ion beam velocity (Adapted from Figure 1 of Wilson III, 2016).*

The spatial extent of shock-reflected ions defines the foreshock boundaries. Prior to *Wind*, the most distant foreshock measurement was made by ISEE-3 at 200 R_E, *Wind*'s predecessor (Scholer et al., 1980). Using *Wind*, Berdichevsky et al. (1999) discovered that the ion foreshock could extend to $\sim$250 R_E from Earth. Using a combination of *Wind* and STEREO observations, Desai et al. (2008) subsequently found ion foreshock particles $>$3000 R_E upstream.

In addition to redefining the extent of the foreshock, *Wind* observations also showed that the high energy cutoff for energetic ions is higher upstream of the quasi-perpendicular bow shock (Meziane et al., 1999, 2002, 2003) rather than the quasi-parallel bow shock, in contrast with theory (Caprioli & Spitkovsky, 2014; Park et al., 2015). Upstream of the quasi-parallel bow shock the highest energy ions only reach $\sim$330 keV while upstream of the quasi-perpendicular bow shock the highest energy ions can reach ∼2 MeV. These energetic ions were observed to be "gyrophase-bunched"[17] due to their single, adiabatic reflection off of the bow shock.

At lower energies below ∼30 keV, *Wind* observations revealed that magnetic field-aligned ion beams could become disrupted by waves (Meziane et al., 1997; Mazelle et al., 2000; Meziane et al., 2001). These three studies presented the first *in situ* evidence that ion-generated foreshock waves can modify foreshock ion velocity distributions by scattering and trapping the particles.

Wind has also played a pivotal role in our understanding of transient ion foreshock phenomena (TIFP) – large-scale (∼1000 to >30,000 km), solitary [∼5–10 per day and transient] structures with durations of tens of seconds to several minutes (D. G. Sibeck et al., 2002; D. Sibeck et al., 2004; Wilson III, Koval, Sibeck, et al., 2013; Zesta & Sibeck, 2004). For instance, D. G. Sibeck et al. (2002) used *Wind* to identify a new transient ion foreshock phenomenon, called a foreshock cavity, which is driven by a diamagnetic effect due to shock-accelerated ions. More recently, Wilson III, Koval, Sibeck, et al. (2013) used *Wind* to show that transient ion foreshock phenomena can locally reflect ions, generating their own miniature foreshocks. This discovery was completely unexpected because it showed that a collisionless shock can self-consistently energize particles through a multi-step process:

- shock reflects ions,
- reflected ions generate TIFP,
- TIFP locally energize particles,
- these pre-energized particles interact with bow shock and gain even more energy.

In an adjacent region of space called the electron foreshock (see Figure 7), *Wind* provided the some of the first determinations of the source of radio emissions near twice the plasma frequency (see Section 2.10 for more discussion of radio measurements (Reiner et al., 1996)). *Wind* measurements also allowed researchers to examine some of the first time series electric fields of Langmuir waves (Kellogg, Monson, et al., 1996). Electron and ion foreshock processes are relevant to a range of space plasma phenomena, including waves in the lunar wake (see Section 2.3), waves in the solar wind (see Section 2.7.2, magnetotail reconnection (see Section 2.4), and waves upstream interplanetary shocks (see Section 2.8.1).

2.7 Solar Wind Studies

This section involves studies conducting primarily in the solar wind including those of large-scale magnetic phenomena (Section 2.7.1), kinetic instabilities and waves (Section 2.7.2), plasma turbulence (Section 2.7.3), and long-term statistical studies (Section 2.7.4).

2.7.1 Large-scale and Reconnection Investigations

As shown in Figure 1, the *Wind* mission has sampled many different regions in the vicinity of Earth. In combination with spacecraft in Earth orbit and at L1, this has allowed *Wind* to investigate structures on a variety of distance scales. In particular, the prograde orbits extending tangentially in the east/west direction and separated from Earth by up to 1 degree in heliolongitude provided an opportunity for observations separated by much larger distances from Earth than is possible using spacecraft at L1. In fact, *Wind* holds the record for the most time spent at 65-500 R_E (2.5×10^{-3} - 0.02 AU) tangentially from Earth (similar distances were reached by the STEREO spacecraft in March-April

[17] a beam localized in velocity space and not symmetric about $\mathbf{B}_o$

2007). Investigations using observations from *Wind* and other spacecraft allowed researchers to test theories of very large scale turbulence (Ogilvie et al., 2007; Wicks et al., 2009, also see Section 2.7.3), solar energetic particles and energetic storm particles (Neugebauer & Giacalone, 2005; Neugebauer et al., 2006, see Section 2.9), the curvature/shape of interplanetary shocks (Koval & Szabo, 2010), and the spatial coherence of interplanetary coronal mass ejections or ICMEs (Farrugia et al., 2005; Möstl et al., 2008; Lugaz et al., 2018, see Section 2.8.2).

Energetic storm particles (ESPs) are particles locally accelerated by an IP shock and have typical energies between 100 keV and 10 MeV. ESP events are typically classified into the following types depending on their temporal profile: spike, rise, step, flat and complex (Lario et al., 2003; Tsurutani & Lin, 1985). There is no simple relationship between the presence/absence and type of ESP events and shock parameters, such as speed, Mach number, or shock normal angle (Cohen, 2006). To understand how the acceleration of particles varies along the shock front, ESP measurements made by *Wind* and ACE of the same events were compared, when *Wind* was in prograde or petal orbits. The analyses of 86 ESP events measured for small longitudinal separations ($< 0.7\circ$) revealed that the measurements become less correlated as the spacecraft separation increases (Neugebauer & Giacalone, 2005; Neugebauer et al., 2006).

The global radius of curvature of CME-driven shocks (Janvier et al., 2015) is thought to be 0.2-1 AU. It is one of the fundamental quantities that describes shocks since it characterizes the variation of the large-scale shock normal angle (the angle between the shock normal and the magnetic field) along the shock front. However, for smaller spacecraft separations ($< 0.5°$), Koval and Szabo (2010) examined 62 shocks measured by *Wind* and at least one other spacecraft (e.g., ACE, DSCOVR, etc.) to determine the shock radius of curvature. The largest shock curvature that could be determined was 0.04 AU, i.e. it reflects the "large-scale local" not global properties of the shock.

Taking advantage of *Wind*'s visit to Earth's magnetotail while ACE remained in an orbit at L1 in October-November 2003, Farrugia et al. (2005) calculated the radial correlation length inside ICMEs (see Section 2.8.2) using observations from the two spacecraft radially separated by 0.02 AU, while Möstl et al. (2008) performed one of the first two-spacecraft reconstructions of a magnetic cloud. *Wind* underwent distant prograde orbits during the maximum phase of solar cycle 23 (2000 – 2002), i.e., *Wind* moved up to 0.01 AU tangentially (east-west in GSE coordinates) of the Sun-Earth line while measuring more than two dozen ICMEs. Lugaz et al. (2018) used these periods to calculate the non-radial correlation length inside ICMEs. Later Ala-Mathi et al. (2020) used the same observations to calculate the correlation length inside the sheath regions of ICMEs. Combined with measurements of the correlation lengths in the IP space, a picture of the coherence of ICMEs near 1 AU has emerged as shown in Figure 8.

Wind's high time resolution plasma and magnetic field measurements led to numerous studies of reconnection in solar wind current sheets (Gosling, Eriksson, Phan, et al., 2007; Gosling, Phan, et al., 2007; Gosling, 2007; Gosling & Szabo, 2008; Gosling, 2010, 2011). Widely-spaced multi-spacecraft in-situ observations revealed that the reconnection X-line in the solar wind can extend to millions of kilometers (or tens of thousands of ion inertial lengths) and persist for hours (or thousands of Alfvèn transit times). An X-line extending at least 390 Earth radii was discovered using observations from *Wind*, ACE and *Cluster* (Phan et al., 2006). Later, even more extreme events, with X-lines extending 660–1800 Earth radii, were reported using in-situ data from *Wind*, ACE, *Geotail*, and both STEREO spacecraft (Gosling, Eriksson, Blush, et al., 2007; Lavraud et al., 2009). These discoveries involving *Wind* could not have been made in Earth's spatially-limited magnetosphere, and have revealed the solar wind as a colloquial laboratory for studying the large-scale properties of reconnection.

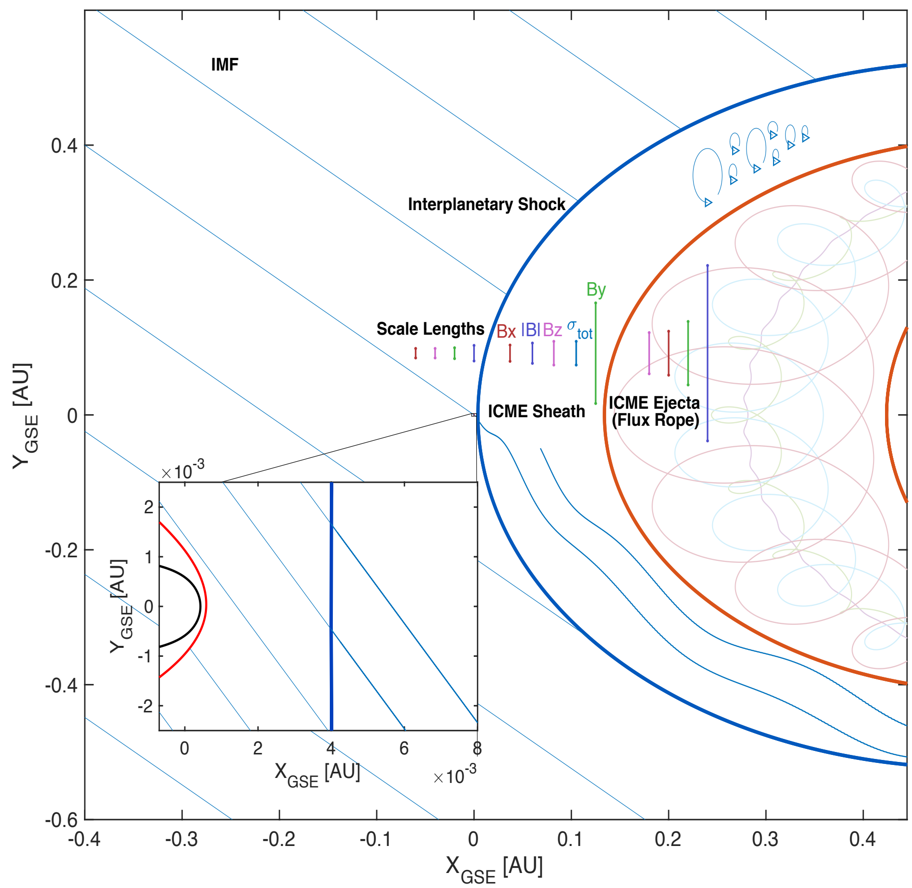

Figure 8: *Sketch of an ICME in Earth-centered interplanetary space in the ecliptic plane with scale lengths. The ICME sheath is preceded by an interplanetary shock (dark blue curve) and driven by the ICME ejecta, bounded by orange curves. The ICME is modeled as arcs of a circle by taking the average angular width of the ICME ejecta given by (X. H. Zhao et al., 2017) and the average radial width reported by (E. Kilpua et al., 2017) for the sheath. Blue lines show and IMF with a 45° Parker spiral angle at the Earth's distance from the Sun. Scale lengths of the solar wind (J. D. Richardson & Paularena, 2001), ICME sheath (Ala-Mathi et al., 2020), and ICME ejecta (Lugaz et al., 2018) are illustrated in the y-direction (Adapted from Figure 6 in Ala-Mathi et al., 2020).*

2.7.2 Kinetic Instabilities and Waves

Small-scale phenomena play a critical role in the evolution of the solar wind (Marsch, 2006; Verscharen, Klein, & Maruca, 2019). As previously discussed, *Wind*'s longevity and redundant thermal particle measurement capabilities (i.e., 3DP, SWE, and WAVES) provide researchers with a highly accurate set of calibrated data. Only with this capacity have researchers been able to examine the particle VDFs in sufficient detail to investigate one of the more elusive topics in plasma physics, plasma instabilities. In this section we discuss kinetic instabilities and waves.

To understand charged particle motion, free energy, and instabilities we first introduce the concepts of particle velocity distribution functions (VDFs). A VDF is a seven dimensional function of three spatial components, three velocity (or momentum) components, and one temporal component. Generally, spacecraft measure a VDF at a given time and location, so the VDF reduces to a three dimensional function of the 3-vector velocity (or momentum). Generically speaking, the VDF is a probability density function of velocity for a particle ensemble. An example VDF is the well known Maxwell-Boltzmann distribution, or Maxwellian (for more examples see Wilson III et al., 2019b).

Free energy in the context of space plasmas refers to non-Maxwellian features in a VDF such as temperature anisotropies, secondary beams, excess skewness (i.e., heat flux), etc. In general, any deviation from an isotropic Maxwellian is a form of free energy but the magnitude of the deviation is critical for determining whether or how that energy will be transformed. This definition of free energy derives from the assumption that an isotropic Maxwellian is the global, maximum entropy distribution.

A plasma instability[18] is the mechanism through which a plasma converts some particle free energy source into electromagnetic fluctuations. All thermal plasmas contain pre-existing thermal fluctuations at the natural frequencies of the system, often called normal modes (Navarro, Moya, et al., 2014; Navarro, Araneda, et al., 2014; Valdivia et al., 2016; Viñas et al., 2014). The properties of these normal modes depend on the background plasma parameters (e.g., magnetic field strength, density, temperature, etc.). The normal modes determine which possible thermal fluctuations can absorb the free energy from the particle populations, if present, and grow over time above the thermal amplitude level. In some ways, an instability is like a "walkie talkie" between the source (particle free energy) and receiver (electromagnetic fluctuations). In this analogy, the transmitting walkie talkie channel frequency is analogous to the pre-existing normal modes of the system while the receiving walkie talkie is analogous to the electromagnetic modes. For more details and specific examples of instabilities, see Appendix B.

The solar wind does not behave like an adiabatic fluid, a thermodynamic, or an equilibrium fluid. The solar wind behaves like a nonequilibrium, weakly collisional plasma controlled by the interplanetary magnetic field (IMF). Therefore, free energy in the solar wind cannot be regulated by collisions or the normal fluid/thermodynamic processes. If a particle VDF were to evolve adiabatically as it moved away from the sun it would quickly become very anisotropic due to the differing forces parallel versus perpendicular to $\mathbf{B}_o$ (Schwartz & Marsch, 1983). Under such assumptions, the VDF near Earth should resemble a narrow beam, focused along the direction of the magnetic field streaming away from the sun but this is not observed. Further, the total temperature would also be much lower than is observed for both ions and electrons (Marsch, 2006; Verscharen, Klein, & Maruca, 2019). Kinetic instabilities in the solar wind may help explain departures from adiabatic conditions.

Some of the more heavily examined instabilities are those involving temperature anisotropies in both electrons and ions. The long baseline of observations provided by *Wind* allowed researchers to perform a series of long-term statistical evaluations of the stability of particle VDFs in the solar wind (Adrian et al., 2016; Bale et al., 2009; C. H. K. Chen et al., 2016; Hellinger & Trávníček, 2006; Hellinger et al., 2006; Hellinger & Trávníček, 2014; Kasper et al., 2002, 2003, 2006, 2008, 2013; Maruca et al., 2011, 2012; Maruca & Kasper, 2013). *Wind*'s results showed that the firehose, mirror, and ion cyclotron modes (see Appendix B for details) are relevant to limiting the ion temperature anisotropy in the solar wind for protons and alpha-particles. Furthermore, theories of parallel and obliquely propagating firehose instabilities could be compared, which was only possible due to the large statistics and accuracy of the data. The critical takeaway is that some of these results help explain why the ion VDFs deviate from adiabatic approximations as they propagate away from the sun.

[18] Note that the use of both kinetic and plasma instability will occur throughout. The former specifically refers to features in the VDFs while the latter also encompasses fluid-like instabilities.

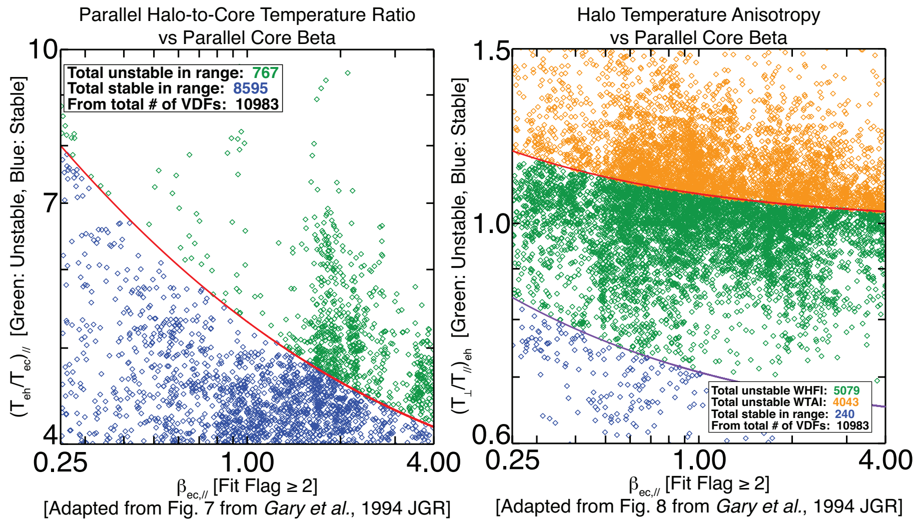

Figure 9: *Adaptations of Figures 7 and 8 from Gary et al. (1994) showing the observed data from Wilson III et al. (2020a). The left panel shows the parallal halo-to-core electron temperature ratios,* $(T_{eh}/T_{ec})_{\|}$*, versus parallel core electron beta,* $\beta_{ec,\|}$ *(see Appendix A for symbol definitions) while the right panel shows halo temperature anisotropy,* $\left(T_{\perp}/T_{\|}\right)_{eh}$*, versus* $\beta_{ec,\|}$*. The left panel is a proxy for heat flux instability while the right for temperature anisotropy instability. In each panel are curves indicating an instability thresholds (corresponding to maximum growth rates satisfying* $\gamma_{max} > 10^{-1}\ \Omega_{cp}$*), below(above) which the observed VDF is stable(unstable). Diamonds shown in green and orange are unstable while blue are stable. The green diamonds show data unstable to the whistler heat flux instability (WHFI) while the orange diamonds are unstable to the whistler temperature anisotropy instability (WTAI). This figure illustrates that most electron VDFs are unstable near IP shocks (Taken from Figure 6 in Wilson III et al., 2020a). Note these data are publicly available, e.g., see Table 6.*

Another free energy source of great interest are secondary beams[19] (secondary to the core population). Interestingly, the presence of a differential flow between the proton and alpha-particles was found to reduce the instability thresholds for the temperature anisotropy instabilities of the Alfvèn ion cyclotron and fast/magnetosonic-whistler modes (Bourouaine et al., 2013; Verscharen et al., 2013; Wicks et al., 2016). Another study showed electromagnetic ion cyclotron waves were unstable to secondary proton beams in the solar wind (Wicks et al., 2016) suggesting ion cyclotron wave storms may be locally generated. While the influence of this secondary proton beam reduces the thresholds for the temperature anisotropy instability, others have found it also introduces a new beam instability that radiates fast/magnetosonic-whistler modes (Alterman et al., 2018; C. H. K. Chen et al., 2016; Gary et al., 2016).

Electron-driven instabilities are also of great interest as they help regulate the partition of energy among the multiple electron populations[20] in the solar wind. Specifically, electron VDFs have been compared with electromagnetic wave observations to test theoretical instability thresholds for the whistler mode (Moullard et al., 2001; Wilson III,

[19] Note that the source of a second proton beam (in addition to the main solar wind proton beam) is still not well established.

[20] Solar wind electrons are comprised of a cold, dense core, hot tenuous halo, and a warm, magnetic field-aligned beam streaming away from the sun called the strahl (Wilson III et al., 2019b, 2019a, 2020a).

Koval, Szabo, et al., 2013; Wilson III et al., 2020a), fast/magnetosonic modes (Kellogg et al., 2011; Verscharen, Chandran, et al., 2019; Wilson III et al., 2009; Wilson III, Koval, Szabo, et al., 2013), electrostatic solitary modes (Bale, Kellogg, Larson, et al., 1998; Bale et al., 2002; Kellogg et al., 2011), ion acoustic modes near interplanetary (IP) shocks (Wilson III et al., 2007; Wilson III, 2010; Wilson III et al., 2020a), Langmuir-like modes (Ergun et al., 1998; Moullard et al., 2001; Pulupa & Bale, 2008), and electron cyclotron drift instability modes near IP shocks (Wilson III, 2010).

The studies mentioned above have focused on measurements of ions or electrons separately, however the stability of a plasma depends on all species simultaneously. In recent years, data from *Wind*'s multiple particle instruments have been combined to investigate the total plasma stability. C. H. K. Chen et al. (2016) combined data from SWE and 3DP, including all major solar wind species (protons, alphas, and electrons) to compare the stability of the solar wind to the long-wavelength firehose and mirror instabilities, for which analytical thresholds exist. For both instabilities, the dominant contribution ($\sim$2/3) was found to be from the protons, but there were also significant contributions ($\sim$1/3) from the other species. When a proton beam was present, drifts between species contributed 57% to the firehose instability. In this combined analysis, both instabilities were found to provide good constraints to the data with <1% unstable, suggesting that these long-wavelength multi-species instabilities act to provide a robust limit the evolution of the solar wind. K. G. Klein et al. (2018) then used a method involving Nyquist's instability criterion to search for the presence of unstable plasma using ion (proton and alpha) data from SWE and assuming isotropic electrons. They found the majority (53.7%) of solar wind intervals to be unstable, with the vast majority of these being kinetic (no long-wavelength counterpart), with growth rates satisfying $\sim$0–0.2 Ω_{cp}. However, the majority of growth rates were found to be slow compared to other dynamical timescales, such as the turbulence timescale, making it unclear whether these kinetic instabilities could be dynamically relevant or constrain the solar wind, and may explain why the majority of the plasma was found to be unstable. Further, examination of $\sim$10 years of data found that $(T_e/T_p)_{tot} \gtrsim 3$ was satisfied for $\sim$12.4% of $\sim$446,000 intervals (Wilson III et al., 2018). This temperature ratio is a threshold often used to determine the separation between strong and weak damping of ion acoustic waves. Wilson III et al. (2020a) examined electron VDFs near IP shocks finding only $\sim$3% were stable to either the whistler heat flux or whistler temperature anisotropy instabilities, as shown in the right-hand panel of Figure 9. They also found $\sim$28.6% of all VDFs examined satisfied $(T_e/T_p)_{tot} \gtrsim 3$ and $\sim$42.8% of upstream-only VDFs satisfied the same criteria, i.e., conducive for ion acoustic wave growth. To compare with ambient solar wind studies, Wilson III et al. (2020a) examined the rate of instability of the firehose and mirror modes finding $\sim$1.3% and $\sim$13.5% were unstable, respectively. These rates are $\sim$10 and $\sim$20 times higher than those found by C. H. K. Chen et al. (2016) in the ambient solar wind for the same instability criteria. Thus, these studies illustrate that the solar wind VDFs are likely strongly shaped by plasma instabilities as they propagate away from the sun to the Earth and beyond.

2.7.3 Turbulence

In this section, we discuss *Wind*'s contribution to our understanding of plasma turbulence. Turbulence can be described as fluctuations in properties of the plasma (e.g., density) that are chaotic in nature (Bruno & Carbone, 2013; Verscharen, Klein, & Maruca, 2019). Turbulence is an intrinsically multi-scale phenomenon where energy enters at large spatial scales and cascades to much smaller scales. Although the individual realizations cannot be predicted, the statistical properties of the energy cascade rate can be derived and in plasmas it changes at different temporal and spatial scales. Unlike in neutral fluid turbulence, turbulence in magnetized plasmas is generally anisotropic. That is, the distribution of power in wave vector ($\mathbf{k}$) space is not equal in all directions relative to $\mathbf{B}_o$, i.e., $k_\perp \neq k_\parallel \neq k$. Often turbulence is examined by use of Fourier transforms in frequency or wavenumber space. In the solar wind, for instance, the magnetic fluctuation power spectrum has the form of multiple broken power-laws where each power-law corresponds to a different type of cascade. The range with the largest scales and lowest frequencies in the spacecraft frame is referred to as the injection range or outer scale. The next range is called the MHD inertial range and it extends up to slightly larger than the relevant ion scales (e.g., ion inertial length or ion thermal gyroradius). Beyond this is the kinetic range, also sometimes known as the dissipation range[21] since this is where fluctuations can transfer energy to the medium through heat. For more details, see Appendix A and the Glossary for definitions.

Wind has enabled significant advances in our understanding of plasma turbulence. These were made possible due to the continuous 3 second resolution plasma moments from 3DP together with magnetic field vectors at up to 22 samples per second, allowing the full inertial range to be studied with all MHD variables for the first time, and the start of the kinetic range to begin being probed in detail. These high-resolution data are supported by measurements of the ion temperature anisotropy from SWE allowing a detailed examination of the interaction of electromagnetic fields and particles as a result of turbulence. The many years of data in the free solar wind also allow the study of the dependence of the turbulence properties on important parameters, such as plasma beta and cross-helicity.

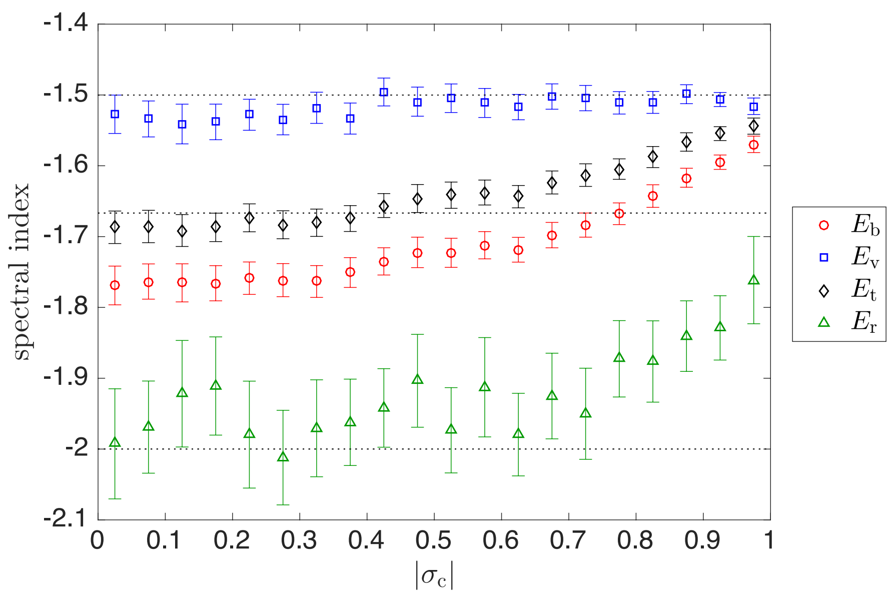

Figure 10: *Variation of the wavenumber power spectral indices of magnetic field (E_b), velocity (E_v), total ($E_t = E_b + E_v$), and residual energy ($E_r = E_v - E_b$) with the level of imbalance $|\sigma_c|$. Note that $|\sigma_c| \approx 0$ corresponds to balanced turbulence and $|\sigma_c| \approx 1$ to highly imbalanced turbulence (Adapted from Figure 4 in C. H. K. Chen, 2016).*

An important achievement of *Wind* has been to establish the MHD inertial range scaling properties. Mangeney (2001) investigated the scaling of the magnetic and veloc-

[21] Note that this term has become less relevant and been replaced by "kinetic range."

ity fluctuations through conditioned structure functions, finding the velocity to have a shallower scaling, consistent with a wavenumber spectrum $k^{-3/2}$, compared to $k^{-5/3}$ for the magnetic field. This finding was confirmed by later studies (Podesta et al., 2006, 2007; Salem et al., 2009). Podesta and Borovsky (2010) showed that both Elsasser spectra[22] scale as $k^{-5/3}$, but that the magnetic field and total[23] energy spectra scale as $k^{-3/2}$ when the cross-helicity is large, which has since been confirmed by others (Boldyrev et al., 2011; C. H. K. Chen et al., 2013). These differences are significant since leading models of plasma turbulence predict these scalings, e.g., a total energy spectrum ${k_\perp}^{-5/3}$ by Goldreich and Sridhar (1995) and ${k_\perp}^{-3/2}$ by Boldyrev (2006). Boldyrev et al. (2011); Boldyrev and Perez (2012), based on previous work by Grappin et al. (1983), proposed that the difference between magnetic and velocity fluctuation spectra is due to turbulence-generated residual energy, which is predicted to scale as ${k_\perp}^{-2}$ and this steep scaling was confirmed by C. H. K. Chen et al. (2013). The large dataset provided by *Wind* allows conditional statistics to be used to separate solar wind with different properties and this has allowed the measurement of the impact of cross helicity and residual energy on the turbulent cascade to be measured simultaneously (Bowen et al. (2018), Bruno et al. (2007), and Wicks, Mallet, et al. (2013) following Bavassano et al. (1998)). The current state of knowledge is summarized in Figure 10 which shows the inertial range spectral indices of the MHD fields as functions of cross-helicity, $|\sigma_c|$, which is a quantitative measure of imbalance[24]. While not every aspect of this figure is explained (notably the cross-helicity dependence of the total energy spectrum), we are tantalizingly close to understanding these spectra and the MHD turbulence cascade, and *Wind* has played a dominant role in enabling this.

Wind has also allowed us to measure the anisotropy of the turbulence to further determine the physics of the cascade. Wicks et al. (2011) used a wavelet technique (based on Horbury et al. (2008)) to measure the spectrum of the Alfvénic turbulence variables with respect to the local mean field direction. Deep in the inertial range, all fields were shown to be anisotropic, $k_\perp \gg k_\parallel$, with velocity, magnetic, and the dominant Elsasser field having ${k_\parallel}^{-2}$ scaling parallel to the local mean field. This ${k_\parallel}^{-2}$ spectrum is one the key predictions of critical balance, the conjecture at the heart of modern turbulence theories, implying that the turbulence becomes increasingly anisotropic towards smaller scales. Verdini et al. (2018) took this further by using a structure function technique (based on C. H. K. Chen et al., 2012) to measure the 3D anisotropy of the turbulent eddies, concluding that under conditions of weak solar wind expansion the turbulence spectrum is different in all 3 directions resulting in "ribbon" rather than "tube" shaped eddies at small scales, consistent with the Boldyrev (2006) picture. Verdini et al. (2019) then showed that this is also true for the velocity fluctuations, although they maintain overall their shallower scaling compared to the magnetic fluctuations. Figure 11 shows an example of the 3D magnetic eddy shapes measured by *Wind*.

While the dominant fluctuation power in the solar wind is in the Alfvénic fluctuations, there is also a subdominant compressive component to the turbulence, which presents some interesting, but quite different physics. While it has long been known that the solar wind compressive components are broadly pressure-balanced, Howes et al. (2012) and K. G. Klein et al. (2012) performed a statistical analysis on the density and magnetic field strength correlation as a function of plasma β using 10 years of *Wind* data. They concluded a compressive component is consistent with being almost entirely in the kinetic slow mode, implying very little or no transfer of energy to whistler turbulence at smaller scales. Later, Verscharen et al. (2017) compared a larger variety of compressive quantities to linear predictions for both kinetic and MHD slow modes, finding the MHD

[22] spectra of the Elsasser variables $\mathbf{z}^{\pm}$ defined in Appendix A

[23] i.e., magnetic plus velocity fluctuation energies

[24] imbalance here refers to the different fluxes of turbulent fluctuations propagating toward or away from the sun

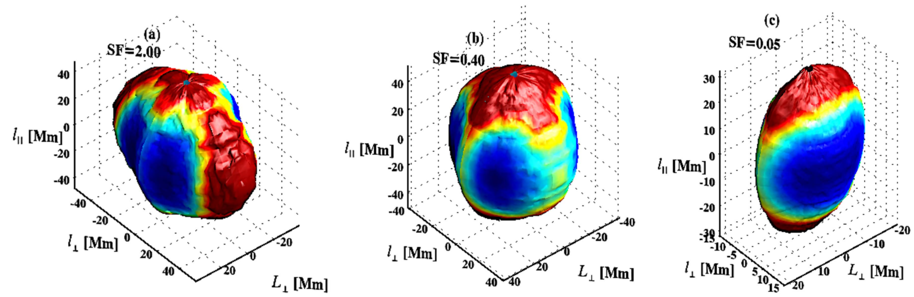

Figure 11: *Statistical 3D eddy shapes of magnetic fluctuations at three different scales in the MHD inertial range, from large scales (left) to small scales (right), for the case of weak expansion. Colors represent distance from the origin (Adapted from Figure 11 in Verdini et al., 2018).*

polarizations to be a good match. This unexpected[25] finding raises interesting possibilities about what may be causing such fluid-like behavior in the weakly-collisional solar wind, with possibilities including wave-particle scattering and anti-phase-mixing; both topics have much broader implications for weakly-collisional plasma physics in general.

It is well known that plasma turbulence is not a completely random process but generates correlated intermittent structures. However, an open question in solar wind physics is exactly how much of the structure in the solar wind is generated in situ by turbulence vs remnant structure from processes at the Sun (Borovsky, 2008; M. J. Owens et al., 2010). One view is that large angle magnetic field rotations represent flux tubes or other structures from the Sun, while the turbulence is responsible for the small-amplitude fluctuations of these structures. However, Zhdankin et al. (2012) presented an analysis to suggest that turbulence can account for the full distribution of angle rotations, large and small. They compared 5 years of *Wind* observations to an MHD turbulence simulation to show a very good match for this distribution, concluding that the majority of solar wind discontinuities arise as intermittent structures from the turbulent cascade. Osman et al. (2012) investigated these structures further, finding the plasma near the discontinuities to be hotter and the temperature more anisotropic and often marginal to the mirror and firehose instabilities, suggesting a link between the structures, turbulent heating and kinetic instabilities. Although the debate on the nature of the structures continues, these results from *Wind* have changed the way we view solar wind structure.

At the large-scale end of the cascade, the correlation length of turbulence is linked to the energy containing scales that feed the cascade. When measuring such large-scale fluctuations in the solar wind, one significant problem is that plasma travels quickly over the spacecraft, meaning that at long timescales the stream structure dominates the signature, rather than the low-frequency fluctuations that might be present within streams. The extensive *Wind* dataset allowed Bruno et al. (2019) to measure the low-frequency spectrum within extended intervals of slow solar wind, showing for the first time that slow solar wind, like the fast wind, is also able to support a "1/f" range, in addition to this well-known result in fast wind. Long time series of fast wind data from *Wind* were also used by Wicks, Roberts, et al. (2013) to show that the scale at which the 1/f range transitions to the inertial range of turbulence depends on the correlation properties of the fluctuations at the spectral break. Intervals with less aligned velocity and magnetic

[25] It was not expected that MHD would do so well at predicting the polarizations since the solar wind is a weakly collisional plasma.

field fluctuations become turbulent at larger scales, even within a single stream. The realization of this property of turbulence is significant since it indicates that the turbulence spectrum may extend to larger scales than previously thought.

Data from *Wind* MFI and SWE have been used in combination with data from other spacecraft to achieve multi-point measurements of the turbulence in the solar wind. Such a multi-point analysis allows the study of the space-time structure of the turbulent fluctuations without having to rely on Taylor's frozen-in hypothesis, which is usually employed in single-point measurements (Verscharen, Klein, & Maruca, 2019). By combining plasma and magnetic-field data from IMP8 and *Wind*, J. D. Richardson and Paularena (2001) calculated multiple correlation coefficients for solar wind turbulence. The scale sizes for changes in the magnetic-field components perpendicular to the flow direction were found to be about 0.002 AU, while the plasma velocity and density scale lengths were found to be larger by a factor of more than two. The same study found a radial scale length of order 0.017 AU. These results were supported by a later study using the amplitude ratio, coherence, and phase lag of field and plasma measurements from *Wind* and ACE (Matsui et al., 2002), although the radial scale was somewhat smaller than in the earlier estimate.

The combination of magnetic-field data from *Wind* with quasi-simultaneous measurements from ACE and *Cluster* facilitated the determination of the Eulerian correlation scale and the Taylor microscale in the solar-wind plasma frame near Earth (Matthaeus et al., 2005). This multi-spacecraft comparison gives an estimate for the omni-directional correlation length of 0.0082 AU. The combination of this result with *Cluster*'s simultaneous measurement of the Taylor microscale of 1.6×10^{-5} AU provides an estimate for the effective Reynolds number of about 230,000 in the measured solar-wind interval. The same method also reveals a Eulerian decorrelation time of about 2.9 hours in the solar wind near 1 AU (Matthaeus et al., 2010). Later combinations of ACE, *Geotail*, and IMP8 data with *Wind* data refined this picture, finding slightly smaller correlation lengths and different correlation lengths in fast and slow solar-wind streams (Matthaeus et al., 2016; Wicks et al., 2009, 2010). *Wind* also supported other turbulence studies through, for example, cross-calibrations with ACE measurements for the OMNI datasets (King & Papitashvili, 2005) or as a source of magnetic-field measurements for spacecraft without a working magnetometer (Pitňa et al., 2019; Šafránková et al., 2019).

Leamon et al. (1998) attempted to distinguish between wave and turbulence paradigms at the dissipation scale using *Wind* MFI solar wind data. The authors observed steepening of the magnetic field spectrum at ~ 1 Hz with an associated increase in compressibility and non-zero magnetic helicity. Further, the turbulence was measured to be significantly oblique, interpreted as a combination of kinetic Alfvén waves and 2D ($k_\parallel = 0$) modes. A reinterpretation of these results has contributed to our current understanding of a critically balanced dispersive cascade of kinetic Alfvén turbulence (with some damping at ion and electron scales).

Another way to understand the processes occurring in the kinetic range is to investigate the scale at which the spectral break occurs. Leamon et al. (2000) compared the measured power spectral break point – the frequency or wavenumber where the power spectral density power-law profile changes exponent – to the cyclotron frequency, parallel resonant wavenumber, and inertial scale, finding the latter to have the best correlation, and suggested this could be related to current sheets of the break point thickness. Bruno and Trenchi (2014) used *Wind* in combination with MESSENGER and *Ulysses* observations to show that the break point evolves linearly with distance from the Sun, similarly to the ion gyroscale, inertial length, and cyclotron resonance scale. The authors concluded that the scale of cyclotron resonance controls the linear evolution. The difficulty, however, in distinguishing these scales (and therefore processes) is that at $\beta \sim 1$ they are essentially the same, so C. H. K. Chen et al. (2014) examined intervals of very high and low β, showing the break point to be at the gyroscale at high β and inertial scale at low β. Woodham et al. (2018) came to a similar conclusion using the large *Wind* data archive and examining the full range of β. The high β result matches expectations for a transition to dispersive kinetic Alfvén turbulence, but a fully consistent explanation for the low β result has yet to be identified and remains an open question. Boldyrev et al. (2015) suggested that the result could be explained by a significant field-parallel wavenumber component at low β. Vech et al. (2018) used *Wind* data at low electron β to suggest the break to be related to the disruption scale at which reconnection could dominate the cascade dynamics. We still have much to learn about kinetic range turbulence, but *Wind*'s early pioneering results have certainly given key valuable insights.

The early Leamon et al. (1998) results were followed up by statistical studies of the high-frequency magnetic field data, identifying key features of coherent waves with distinct left-handed and right-handed rotations (Markovskii et al., 2015). Woodham et al. (2019) linked these helical waves to the SWE proton temperature anisotropy data and showed that field-parallel propagating modes at the spectral break scale are dominated by ion cyclotron waves driven by temperature anisotropy and proton and alpha particle beams (Wicks et al., 2016) but the background of oblique modes are kinetic Alfvén waves with no particular dependence on proton temperature anisotropy. These statistical studies, only possible with *Wind*, demonstrate the link between particle temperature and the inertial range energy cascade, and provide the current best knowledge of energy transfer in turbulent space plasmas.

These are just a selection of results that *Wind* has enabled in solar wind turbulence, but they illustrate the diverse aspects of the physics that have been revealed. Hopefully *Wind* will continue contributing to our understanding of this important and widespread plasma process over the coming years, in particular in combination with new missions such as *Parker Solar Probe* and *Solar Orbiter*, where the multi-point measurements will likely prove to be invaluable (e.g., Velli et al., 2020).

2.7.4 Long-term Solar Wind Studies

Due to *Wind*'s longevity and accurate measurements, it is an ideal mission for investigating long-term statistical properties of various phenomena in space plasmas. This section highlights some of these results from in situ observations in the solar wind.

Surprisingly, the first long-term statistical study of the electron-to-ion scalar temperature ratio, $(T_e/T_s)_{tot}$ ($s = p$ for protons, α for alpha-particles) was only recently performed using *Wind* observations (Wilson III et al., 2018). The study used $\sim$10 years of solar wind data[26]. A summary of the results for all solar wind conditions from Wilson III et al. (2018) are shown in Table 5, where n_s is the number density [cm^{-3}] of species s, $T_{s,tot}$ is the scalar temperature [eV] of species s, $V_{Ts,tot}$ is the most probable thermal speed [km/s] of species s with mass m_s (see Equation A1b), $\beta_{s,tot}$ is the total plasma beta of species s (see Equation A1h), f_{cs} is the cyclotron frequency [Hz] of species s (see Equation A1c), f_{ps} is the plasma frequency [Hz] of species s (see Equation A1d), ρ_{cs} is the thermal gyroradius [km] of species s (see Equation A1f), λ_e is the inertial length [km] of species s (see Equation A1g), and λ_{De} is the electron Debye length [m] (see Equation A1e). See Appendix A for further symbol definitions.

Wilson III et al. (2018) showed, however, that not only is the solar wind plasma not in thermodynamic equilibrium, the plasma isn't in thermal equilibrium either. The authors illustrated that because the particle-particle Coulomb collision rates are so low in the IP medium, an interaction with just one small-amplitude wave packet can cause a greater effect than the cumulative effect of collisions between the sun and Earth. This begs the question of why we actually see any evidence of particle-particle collisions in

[26] from January 1995 to December 2004, publicly available at SPDF CDAWeb

Table 5: Long-term Solar Wind Statistics

Parameter	$X_{25\%}$[a]	$X_{75\%}$	$\tilde{X}$[b]
Densities			
n_e $[cm^{-3}]$	5.71	13.0	8.57
n_p $[cm^{-3}]$	5.05	11.7	7.61
n_α $[cm^{-3}]$	0.13	0.32	0.21
Temperatures and Thermal Speeds			
$T_{e,tot}$ [eV]	9.41	13.1	11.1
$T_{p,tot}$ [eV]	4.80	15.1	8.45
$T_{\alpha,tot}$ [eV]	5.43	34.0	12.2
$V_{Te,tot}$ [km/s]	1579	2411	1975
$V_{Tp,tot}$ [km/s]	21.9	76.9	40.2
$(T_e/T_p)_{tot}$	0.78	2.14	1.28
$(T_e/T_\alpha)_{tot}$	0.32	1.78	0.82
$(T_\alpha/T_p)_{tot}$	1.39	3.62	2.01
Plasma Betas			
$\beta_{e,tot}$	0.83	2.64	1.45
$\beta_{p,tot}$	0.67	1.90	1.16
$\beta_{\alpha,tot}$	0.02	0.19	0.07
Frequencies and Lengths			
f_{cp} [Hz]	0.04	0.22	0.09
f_{ce} [Hz]	80.2	409	162
f_{pp} [Hz]	371	944	578
f_{pe} [Hz]	17.2	42.5	26.3
ρ_{ce} [km]	1.03	4.62	2.28
ρ_{cp} [km]	32.5	186	88.8
λ_e [km]	1.12	2.77	1.82
λ_p [km]	50.5	129	82.5
λ_{De} [m]	4.74	13.8	8.58

[a] $X_{y\%}$ is the yth percentile [b] $\tilde{X}$ is the median

the solar wind since we consistently observe, directly or indirectly, numerous different types of electromagnetic fluctuations in the solar wind (O. V. Agapitov et al., 2020; Bale et al., 2009; He, Wang, et al., 2015; He, Pei, et al., 2015; He et al., 2019; Kasper et al., 2013; Malaspina et al., 2020; Maruca et al., 2012; Vasko et al., 2020; Wicks et al., 2016). That is, the ubiquitous electromagnetic waves should wash out any particle-particle collision signatures much faster than particle-particle collisions can relax the distributions[27].

In contrast researchers have traced a preferential ion heating source back to the solar corona and even placed limits on the heliocentric distance below which this heating

[27] Note that the result of wave-particle interactions is not to reduce a particle distribution to an isotropic Maxwellian. Rather, wave-particle interactions tend to produce power-laws or plateaus and sometimes even introduce anisotropies (e.g., see discussion in Wilson III et al., 2020a). So there are clear differences between the effect of waves versus particle-particle collisions on the particle distribution functions.

occurs (Kasper et al., 2017; Kasper & Klein, 2019). That is, the ions appear to be heated below some altitude near the sun and then negligible changes occurr as the particles propagate to Earth. The conflict between the preferential coronal ion heating observations and the expected plasma evolution due to interactions with ubiquitous waves between the sun and Earth still remains an unanswered and fundamentally critical question in studies of the solar wind.

Further, numerous studies that examine the limits of the collisionality in the solar wind (Adrian et al., 2016; Bale et al., 2013; Horaites et al., 2015, 2019; Kasper et al., 2017; Maruca et al., 2013; Salem et al., 2003; Wilson III et al., 2018, 2019a) have found the collision rates to be very small (i.e., ∼1 Coulomb collision per day). Despite the solar wind's weakly collisional nature, researchers have found that collisional effects can be observed in particle data near Earth. The ability to observe collisional effects near Earth is interesting because the collision rate is so low compared to other effects due to phenomenon like waves and/or turbulence (e.g., recall discussion about the study by Wilson III et al., 2018). The observation of collisional effects despite its weak/slow nature on the particle distributions compared to other effects (e.g., waves and/or turbulence) remains an outstanding question.

Finally, *Wind* studies of the relative abundance between protons and alpha-particles have shown solar cycle and other effects (Alterman et al., 2018; Alterman & Kasper, 2019; Kasper et al., 2007, 2012). The authors showed that the alpha-particle-to-proton abundance varies with solar cycle and is a function of solar wind speed (Alterman & Kasper, 2019; Kasper et al., 2007, 2012). That is, higher speed solar wind has a higher alpha-particle abundance than slower wind and the abundances peak near solar maximum. In fact, when binned by solar wind speed, Kasper et al. (2007) showed a consistent six month periodicity in the alpha-particle abundance. Later, Alterman and Kasper (2019) showed that there is a phase delay between the rise in sunspot numbers and the rise in alpha-particle abundance, which turns out to be a monotonic function of the solar wind speed. The authors found that changes in the sunspot number precede changes in alpha-particle abundance with the smallest lag time, ∼150 days, corresponding to the lowest solar wind speed. Such a relationship could allow researchers to predict forecast solar minimum or maximum by nearly half a year or more.

The above contributions to our understanding of the solar wind almost entirely rely upon the longevity of *Wind*. That is, the use of data from a single mission improves the accuracy of the data by removing the uncertainties introduced when cross-calibrating between different sets of instrumentation. Given that many of these nuanced results are relatively small in magnitude and/or difficult to measure, it is unlikely many could have been obtained using multiple missions over similar periods of time.

2.8 Transient Large-scale Magnetic Phenomena

The high-cadence, high-resolution measurements of *Wind* and the connection with *Polar* through the Global Geospace Science (GCS) program made it possible to investigate large-and small-scale interplanetary (IP) transients in the solar wind and their effects on the magnetospheric system. Large-scale transient structures in the solar wind have been a focus of attention in numerous studies since the advent of the space era. Some of these large structures originate in the solar atmosphere, such as coronal mass ejections (CMEs), while others are a result of dynamic processes in the IP medium, such as corotating interaction regions (CIRs) or IP shock waves. The *Wind* mission has provided numerous opportunities to identify, characterize, and model such structures. This section summarizes the results of investigations that have improved our understanding of these structures and their importance for Sun-earth connections.

2.8.1 Interplanetary Shock Waves

A shock is a sudden transition between supersonic and subsonic flows and is characterized by an abrupt change in pressure, temperature, and density in the medium (Krasnoselskikh et al., 2002; Wilson III, 2016; Wilson III et al., 2017). Shock waves can arise from the nonlinear steepening of compressional waves when the steepening is balanced by some form of irreversible energy dissipation. In Earth's neutral atmosphere, energy dissipation is mediated by binary particle collisions. In the solar wind, the mean free path of particles is around 1 AU (Wilson III et al., 2018, 2019a, 2020a). Shock waves can and do form in the solar wind. The energy dissipation mechanism(s) that govern shock dynamics in astrophysical plasmas are still not well understood because they are not mediated by particle-particle collisions. Thus, shocks in the solar wind, and most other space plasma environments are called collisionless shock waves.

In the interplanetary medium (IPM), shocks are mainly caused by ICMEs (see Section 2.8.2), when they reach a supersonic velocity, propagating and expanding through the IPM (Lepping et al., 2007; Lepping, Wu, Berdichevsky, & Ferguson, 2008; Vandas et al., 2009). Such IP shocks can also be generated by interaction regions between slow and high speed solar streams (G. Mann et al., 2002; Mason et al., 2009), often referred to as corotating interaction regions or CIRs, or stream interaction regions or SIRs (see Section 2.8.3).

Wind has made several critical contributions to understand phenomena related to IP shocks, many of which are discussed in other sections of this review. These phenomenon include radio emissions such as type II solar radio bursts (e.g., Bale et al., 1999; Pulupa & Bale, 2008, and discussed in Section 2.10), acceleration and transport of solar energetic particles events (SEPs) (e.g., Reames, 2017, and discussed in Section 2.9), ion foreshocks (e.g., Wilson III et al., 2009, and discussed in Section 2.6), electron VDF evolution across the shock (e.g., Fitzenreiter et al., 2003; Wilson III et al., 2019b, 2019a, 2020a, and discussed in Section 2.7.2), large amplitude electrostatic waves and dissipation (e.g., Wilson III et al., 2007; Wilson III, 2010, and discussed in Section 2.7.2), nonlinear wave-particle interactions (e.g., Wilson III et al., 2012, and discussed in Section 2.7.2), shock-shock acceleration with the terrestrial bow shock (e.g., Hietala et al., 2011, 2012), and the nonplanar structure of IP shock fronts (e.g., Neugebauer & Giacalone, 2005, and discussed in Section 2.7.1).

Below we discuss *Wind*'s contribution to understanding the phenomenon associated with ICMEs and CIRs.

2.8.2 Interplanetary Coronal Mass Ejections

Interplanetary coronal mass ejections (ICMEs) are the manifestations in the solar wind of CMEs at the Sun and are identified in the solar wind by a number of characteristic signatures that differ from those in the ambient solar wind (e.g., Table 1 of Zurbuchen & Richardson, 2006). These signatures include abnormally low proton temperatures, unusual composition (e.g., enhanced alpha-to-proton ratio) and high ion charge states resulting from heating during the eruption at the Sun; low charge states may also be present. Some ICMEs show an enhanced magnetic field that slowly rotates through a large angle, as well as low plasma beta, and are termed "magnetic clouds" (MCs) (L. Burlaga et al., 1981). Another characteristic feature of many ICMEs is the presence of bidirectional field-aligned flows of suprathermal electrons from the hot corona. The presence of the suprathermal electrons suggests that field lines in the ICME may be looped and rooted at the Sun at both ends. A fast ICME may drive a shock which is separated from the ICME by a sheath of compressed, turbulent, heated solar wind. ICMEs are of interest for several reasons: they provide direct measurements of CME plasma, and diagnostics of the conditions during the eruption at the Sun. ICMEs are also the major drivers of geomagnetic storms (Zhang et al., 2007). In particular, occasionally, the slowly-rotating magnetic field of a magnetic cloud may remain southward for an extended period, resulting in favorable conditions for reconnection at the dayside magnetopause (see cartoon in Figure 6) and energy transfer into the magnetosphere, eventually leading to a major geomagnetic storm; southward fields in the sheath can also contribute to geomagnetic storms (E. K. J. Kilpua et al., 2017). Particles accelerated at ICME-driven shocks also contribute to SEP events (e.g., Reames, 2012). Although ICMEs and their signatures were largely discovered in early in-situ observations (often being referred to as "shock drivers","pistons" and "ejecta"), *Wind* continues to contribute to the study of ICMEs and MCs (e.g., Hidalgo & Nieves-Chinchilla, 2012; Lepping, Wu, Berdichevsky, & Szabo, 2018).

The launch of *Wind* closely preceded the launch of SoHO carrying the LASCO coronagraphs which made near-continuous observations of the corona and CMEs. The combination of *Wind* in situ measurements from MFI, SMS, 3DP, and SWE, SoHO LASCO CME observations and Yokhoh X-ray observations resulted in the confirmation of the connection between CMEs in the corona and MCs subsequently observed near-Earth. In particular, MCs were shown to be associated with the dark, magnetically-dominated, cavity of the three-part CME structure (bright front, cavity, prominence) rather than with the prominence (L. Burlaga et al., 1998; Gopalswamy, Hanaoka, et al., 1998).

Another important contribution to understanding the origin to the CMEs is the observation of enhanced solar wind $^3He^{2+}$ within ICMEs. Ho et al. (2000) identified six enhanced $^3He^{2+}/^4He^{2+}$ periods from January 1995 to May 1998, using data from the MASS high resolution solar wind spectrometer on *Wind*. The ratios observed in these events are four to ten times higher than previously reported average solar wind values. It was suggested that these enhancements originated in the prominence core embedded within the CME. In a separate event, the high-resolution measurements of helium ions, including their number density, velocity and temperature revealed the presence of short-duration cold prominence material within MC (L. F. Burlaga, 1988).

The 3DP instrument's ability to measure thermal, suprathermal and energetic electrons allowed *Wind* to provide some of the first measurements of extremely cold (temperature down to below 1 eV) electrons inside MCs (Larson et al., 2000). Because *Wind* is a spinning platform, careful analysis of the spacecraft potential with similar measurements of proton temperatures allowed Larson et al. (2000) to presented the first experimental observation of collisionally-coupled electrons and protons in interplanetary space.

To probe the internal structure of MCs, Shodhan et al. (2000) used observations of suprathermal electrons from *Wind* and several other spacecraft to assess the fraction of time when bidirectional vs. unidirectional electron flows were present during the passage of MCs. This classification indicates the presence of looped field lines rooted at the Sun at both ends vs. open field lines, respectively. The fraction of bidirectional flows was found to vary widely from no bidirectional streaming to $\sim$100%, with the largest MCs being the most closed. The different flows were also distributed randomly within the MCs. These results suggest that although MCs are large-scale coherent structures, reconnection, either near the Sun or with the IMF, sporadically alters the field topology from closed to open. A separate analysis technique was also used to investigate the open/closed field line nature of MCs. By measuring the arrival time and velocity dispersion of suprathermal and energetic electrons (100 eV – 100 keV) associated with a series of impulsive solar flares that fortuitously were injected into the footpoints of a MC as it passed over *Wind* in October 1995, Larson et al. (1997) estimated the path lengths traveled by these electrons at different locations within the MC. These were overall found to be consistent with a low-twist core and a more highly twisted outer shell, as expected for a flux rope configuration as shown in Figure 12. On the other hand, Kahler et al. (2011) applied a similar method to eight MCs and found a poor correlation between the inferred electron path lengths and those expected from MC field models, with the exception of the event studied by Larson et al. (1997).

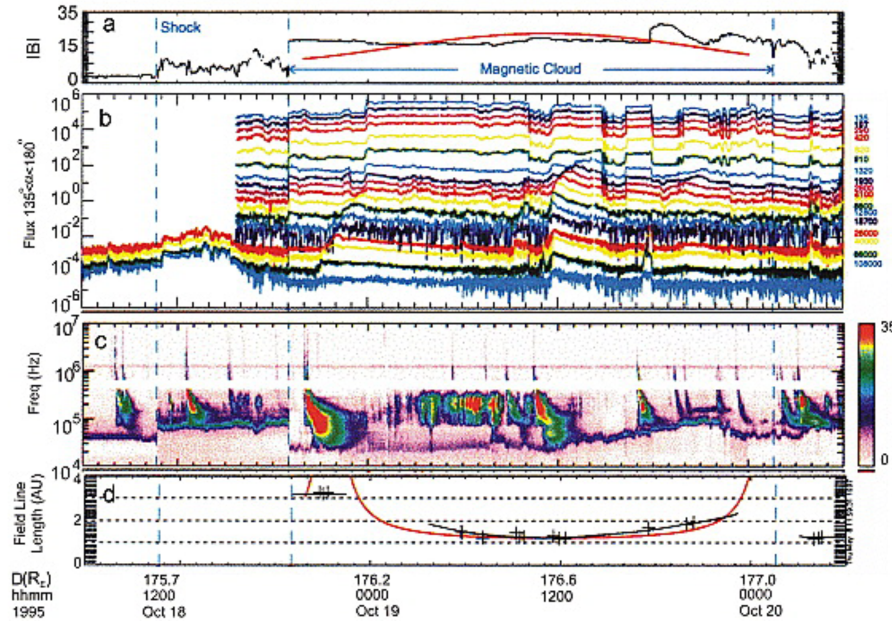

Figure 12: *Analysis of the length of magnetic field lines inside an MC measured by* Wind *for the 1995 October 18-20 ICME (Larson et al., 1997). The figure is taken from Kahler et al. (2011), which was adapted from the Larson et al. (1997) study. The panels show from top to bottom, the magnetic field strength with results from the force-free model in red (a), the flux of suprathermal electrons for various energies between 135 eV and 100 keV propagating anti-parallel to the magnetic field from 3DP (b), the wave power of solar radio emissions observed by WAVES (c) including multiple type III bursts, some associated with the electron injections in (b), and the derived field line length in AU for each of these bursts with the modeled length from the force-free model of panel (a) in red (d).*

Fitting and reconstruction techniques are needed to determine the global structure of ICMEs and MCs from single-spacecraft crossings. In the best cases, MCs are well-ordered (single flux ropes) and they can be readily modeled by a variety of techniques. Although spheromak-like plasmoid models have been proposed for MCs (Vandas et al., 1993), work has focused on flux rope models of various levels of sophistication (Marubashi, 1986; L. F. Burlaga, 1988; Lepping et al., 1990; Farrugia et al., 1993; Hidalgo et al., 2002). Frequently, MC are reconstructed by neglecting expansion or cross-section distortion. In particular, Lepping et al. (1990) developed the most commonly used in situ reconstruction technique in which the magnetic structure is assumed to be a static, axially symmetric cylinder that can be approximated by a linear force-free magnetic configuration (L. F. Burlaga, 1988; Lundquist, 1951). Following the same geometrical assumptions, but relaxing the force-free requirement, Hidalgo et al. (2000) derived a family of models that attempt to reproduce the varying physical and geometrical characteristics of MCs found in in situ data (Hidalgo et al., 2002; Hidalgo & Nieves-Chinchilla, 2012; Nieves-Chinchilla et al., 2012, 2016). However, it is not yet clear whether any one of these models is sufficiently realistic to describe the observed variety of MC signatures. *Wind* measurements of the magnetic field and plasma pressure have resulted in the development of MC analysis techniques that go beyond force-free approximations to extend to magneto-hydrostatic equilibrium through the Grad-Shafranov technique. This was first applied to *Wind* measurements of magnetic clouds by Hu and Sonnerup (2002) and has been used extensively since. However, recent comparisons of various fitting and reconstruction models, both for general (Al-Haddad et al., 2013) and simple ICMEs (Al-Haddad et al., 2018), have highlighted that different techniques do not return consistent results for the ICME orientation.

Gopalswamy, Yashiro, et al. (2015) and Nieves-Chinchilla et al. (2018) use *Wind* data to elucidate properties of MCs during solar cycles 23 and 24 (e.g., see Table 6). Of particular importance is the relation between ICMEs or MCs measured at L1 and the solar activity, which was weaker in cycle 24 than cycle 23 with an extended deep minimum in 2007–2009. Although the average sunspot number declined by ∼40% between solar cycles 23 and 24, there was no decline in the number of MCs in cycle 24 compared with cycle 23 (see Figure 13). This reduction in geo-effectiveness may be diminished in solar cycle 24 as compared to 23. Some of this may be related to the 22-year cycle in bipolar MCs (Y. Li et al., 2018) and also associated with the weaker magnetic fields inside MCs, and the shorter MC duration, during solar cycle 24 (Lepping et al., 2011). B. E. Wood et al. (2017) used *Wind* in situ observations of MCs in conjunction with observations from the coronagraphs and Heliospheric Imagers on the STEREO spacecraft to track 31 MCs from the Sun to near 1 AU and compare the properties of the MCs with the associated erupting flux ropes at the Sun. They found that the flux rope orientations and sizes inferred from imaging near the Sun were not well correlated with those of the in situ MCs, but the arrival times at 1 AU were well predicted.

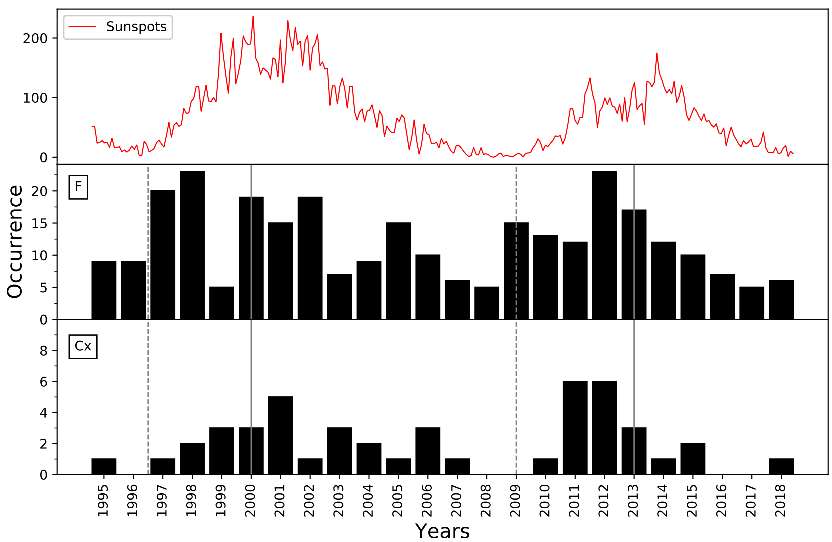

Figure 13: *Occurrence of magnetic ejecta (e.g., MCs) per year near 1 AU as compared to sunspot number. Top panel: sunspot number showing the weaker solar maximum in 2012–2014 as compared to 2000–2002. Middle and bottom panels: number of flux-rope like ICME (F, middle) and complex ICMEs (Cx, bottom) from* Wind.

Estimates in the literature of the fraction of ICMEs that include MCs vary from ∼15–80% (Gosling et al., 1990; Bothmer & Schwenn, 1996; Marubashi, 2000; Mulligan et al., 1999; I. G. Richardson & Cane, 2004). Long-term statistical studies including observations during the *Wind* mission make it possible to reconcile these various studies by recognizing that the fraction of MCs varies with with the solar cycle (I. G. Richardson & Cane, 2004; Lepping, Wu, Berdichevsky, & Kay, 2018; Lepping et al., 2020).

The several hundred ICMEs measured by Wind also allow the characteristics that distinguish MCs from those with more complex magnetic structures to be better defined (Nieves-Chinchilla et al., 2018). Non-MC-like configurations may arise in several circumstances: the ICME may result from the interaction of several individual ICMEs on their way to Earth (L. F. Burlaga et al., 2002; Lugaz et al., 2007), or if the magnetic field configuration of the original CME was more complex than a simple flux rope. For example, a MC may be a substructure of a more extended ICME region (I. G. Richardson & Cane, 2010) and not encounter the observing spacecraft. The absence of the flux rope signatures can be explained by the spacecraft encountering the MC far from the center axis or in the flux rope leg. Magnetic flux erosion by reconnection at the front of the magnetic ejecta may also erase the clear flux rope signature (Dasso et al., 2007; E. K. J. Kilpua et al., 2011; Ruffenach et al., 2012). Some studies classify a subset of ICMEs that meet some but not all the magnetic and plasma signature of MCs as "MC-like" or "flux rope like" (Gopalswamy, Yashiro, et al., 2015; Lepping et al., 2005; C.-C. Wu & Lepping, 2015) that meet some but not all the magnetic and plasma signature of MCs. One of the first detailed studies of an ICME with signatures of complexity was made by Lepping et al. (1997). *Wind* instruments measured a coherent structure with an embedded shock in the back half of the structure. This complex event triggered an intense geomagnetic storm for which the joint measurements by *Wind* and *Polar* provided a new coupling function between the solar wind and the magnetosphere (Farrugia et al., 1998; Takeuchi et al., 2000).

The Lepping et al. (2003) catalog of MCs has been central for numerous statistical studies (Démoulin et al., 2013, 2016; Janvier et al., 2019; Lepping, Wu, Gopalswamy, & Berdichevsky, 2008; Lepping et al., 2017, among others) and is based on the approximation of MCs as simple, circular flux rope in force-free equilibrium[28]. Results from these catalogs include data-driven models of typical MCs and shocks (Démoulin et al., 2016), studies of the importance of expansion to understand MC measurements (Lepping, Wu, Gopalswamy, & Berdichevsky, 2008) as well as investigations of the impact of the distance of closest approach on the spacecraft measurements (Démoulin et al., 2013; Lepping et al., 2017). These studies revealed that the cross-section of MCs is in fact non-circular (Démoulin et al., 2013, 2019) and the distribution of magnetic field line twist may be more complex than that derived from a force-free model (Lanabere et al., 2020). These results have led to the development of several new models which incorporate more complex magnetic field structures and cross-sections.

The Nieves-Chinchilla et al. (2018) catalog also provides the internal flux-rope physical properties as well as the orientation and closest approach based on the model and reconstruction technique described in Nieves-Chinchilla et al. (2016). The statistical study published by Nieves-Chinchilla et al. (2019) revealed remarkable spatial complexity of ICMEs. Figure 13 displays the occurrence of ICMEs with complex topology (bottom), with clear flux rope signatures (middle) and both populations compared with the sunspot number over the *Wind* mission. The orientation of ICME flux ropes during the Wind mission shows solar cycle trends that follow the orientation of the heliospheric current sheet (Y. Li et al., 2018), confirming the results of previous studies based on visual inspection that found a Hale cycle dependence of the reversal in the flux rope poloidal field.

In combination with measurements from *Wind*, in situ measurements from STEREO, *Parker Solar Probe*, MESSENGER, *Venus Express*, and *Solar Orbiter* reveal the heliospheric evolution of the internal structure of MCs. The evolutionary signatures of evolution include distortions, deformations, rotations, deflections, and deviations from self-

[28] The results from the analyses have shaped two different MC catalogs, both included on the *Wind* webpage `https://wind.nasa.gov/ICMEindex.php`. These catalogs provide fitting parameters for most entries. These parameters include magnetic field strength, closest approach (or impact parameters), orientation as well as measures of the goodness of the fit for all *Wind* MC measurements.

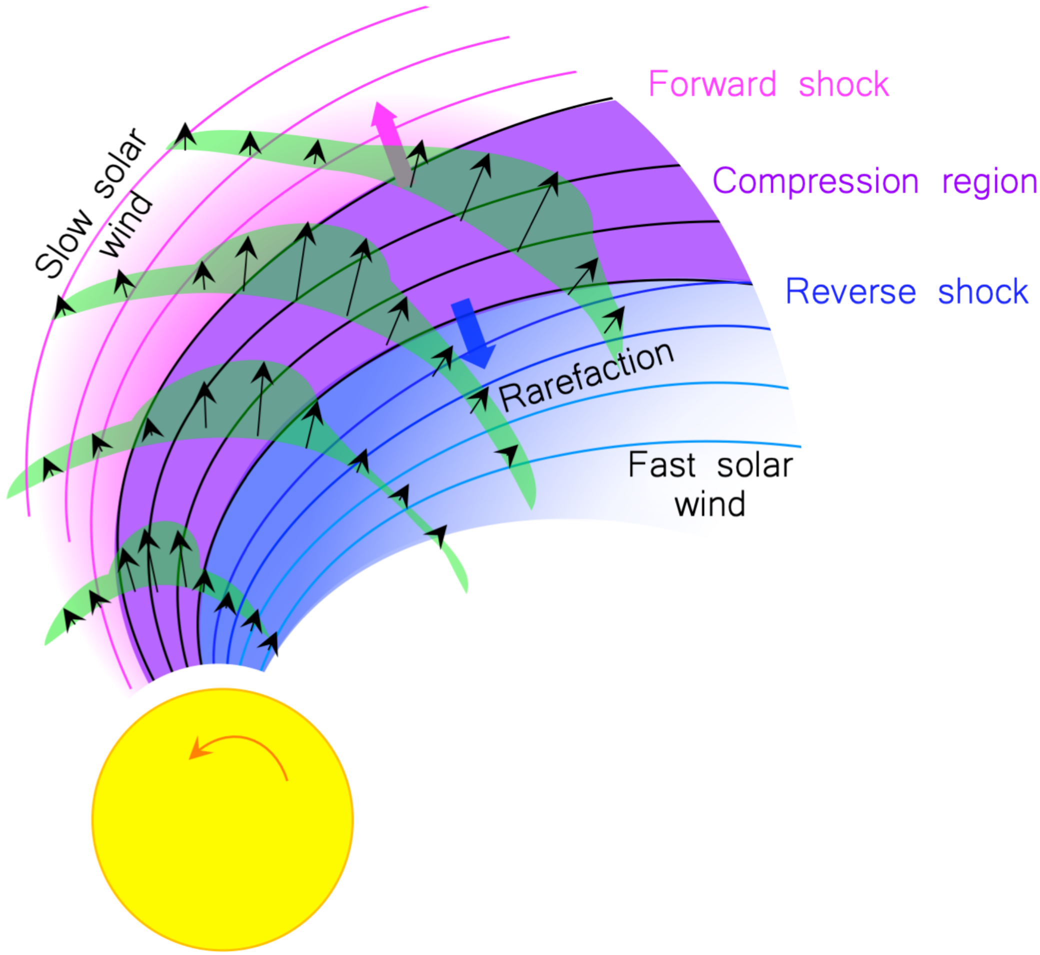

Figure 14: *Cartoon of stream interaction region (SIR) and/or corotating interaction region (CIR). The black arrows indicate velocity and the solid lines represent magnetic field lines. The thick magenta and blue arrows indicate the local, outward normals of the expanding compression region that can form a forward and reverse shock, respectively, as the SIR/CIR propagates further away from the sun.*

similar expansion or radial propagation (Good et al., 2019; Kubicka et al., 2016; Lugaz et al., 2020; Nakwacki et al., 2011; Nieves-Chinchilla et al., 2012; Salman et al., 2020; Vršnak et al., 2019; Y. Wang et al., 2018; Winslow et al., 2016). These analyses use data from spacecraft that are radially aligned or in quadrature, giving multi-point or multi-view observations of the evolving MC, respectively.

2.8.3 Corotating Interaction Regions

A corotating interaction region or CIR (e.g., see I. G. Richardson et al., 2018, for recent review) is formed by the interaction of a high-speed solar wind stream (HSS) originating in a coronal hole at the Sun with the preceding slower solar wind (e.g., see Figure 14 for illustration). This interaction forms a region of compressed solar wind – the CIR – that lies along the leading edge of the high-speed stream and has an approximately spiral configuration. CIRs/HSSs corotate with the Sun and may recur for several solar rotations. They occasionally drive intense geomagnetic storms (Alves et al., 2006; Zhang et al., 2007) and generate extended periods of enhanced geomagnetic activity as they pass over Earth (Tsurutani et al., 2006). Expansion of the CIR may lead to the formation of a corotating forward (reverse) shock at the CIR leading (trailing) edge. These shocks usually form beyond 1 AU (Smith & Wolfe, 1976) but occasionally are found at 1 AU.

L. Jian et al. (2006) summarize the properties of 365 "stream interaction regions" (SIRs) at 1 AU during 1995 to 2004 using *Wind* and ACE data, and provide a catalog of these events and their properties. They reserve the term "corotating" interaction region to designate those streams that recur on two or more solar rotations, though SIR and CIR are often used interchangeably. They emphasize the use of the total (magnetic and plasma) pressure perpendicular to the magnetic field direction as an aid to identifying CIRs, with a local pressure peak being a characteristic feature of the stream interface (Forsyth & Marsch, 1999) separating slow and fast solar wind plasma. They found that ∼17% (5.75%) of interaction regions at 1 AU had only a forward (reverse) shock, and 1.37% had a forward-reverse shock pair. An extended catalog of 588 CIR/HSS during 1995–2017 has been compiled by Grandin et al. (2019) using a detection algorithm applied to OMNI data which incorporates *Wind* observations. They also show superposed-epoch analyses of the solar wind parameters and geomagnetic activity associated with these structures for different phases of solar cycles 22–24, noting for example, cycle to cycle variations in their occurrence and properties, such as the lower geoeffectiveness of CIRs/HSS in cycle 24 due to lower magnetic field strengths and lower stream speeds (e.g., see Figure 15).

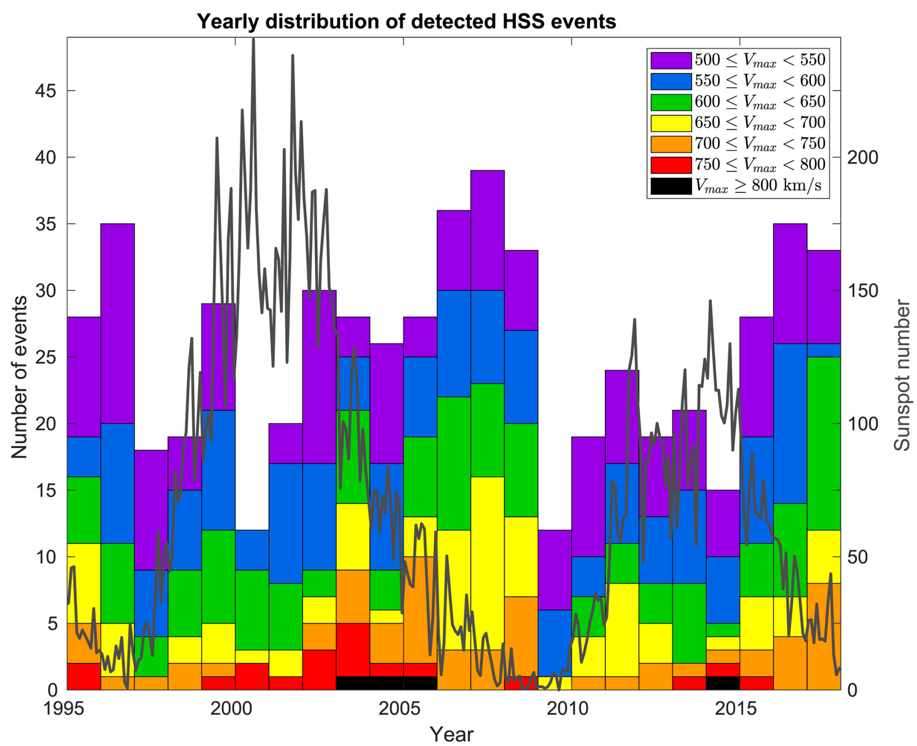

Figure 15: *Yearly number of high speed streams in various peak speed ranges (minimum 500 km/s) with the sunspot number for solar cycles 23 and 24 superposed, showing the tendency for HSS to be most frequent during the declining phase of the cycle and the generally lower peak speeds in cycle 24 vs. 23 (Adapted from Grandin et al., 2019).*

Although CIRs and HSSs are long-lived structures corotating with the Sun, they do evolve on shorter time-scales, for example due to changes in the configuration of the source coronal holes and development of the stream interaction. Several studies have used data from *Wind* and other spacecraft separated from Earth to study this evolution. For example, L. K. Jian et al. (2009) examined a CIR in August 2007 that was observed in succession by STEREO B, 10° east of *Wind*, then by *Wind*, and by STEREO A, 15° to the west; the spacecraft were only separated by 2° in heliolatitude. Figure 16 shows the differences in the profiles of various solar wind parameters at each spacecraft (the CIR is indicated by enhanced magnetic fields and plasma densities on the leading edge of the HSS) and the varying locations of a crossing of the heliospheric current sheet[29] (HCS) ahead of the CIR, the stream interface (SI), and a forward shock forming at the CIR leading edge, which was only present at *Wind*, and a reverse shock forming at the CIR trailing edge, only evident at STEREO B. Occasionally, a MC interacts with a CIR, as in the example discussed by Farrugia et al. (2011). Observations from *Wind* and both STEREO spacecraft, separated by ∼40° in heliolongitude, illustrate the distortion and rotation of the MC that resulted from this interaction.

Broiles et al. (2012) used observations from *Wind* and ACE to search for planar magnetic structures in 153 CIRs and, from their orientation, inferred the tilt of the CIR, which might be expected to reflect the orientation of the fast-slow stream interaction. The mean azimuthal tilt was found to be consistent with the average Parker spiral direction. Average out-of-the-ecliptic tilts were ∼20° both north or south, but these values often changed significantly between successive recurrences of the same stream.

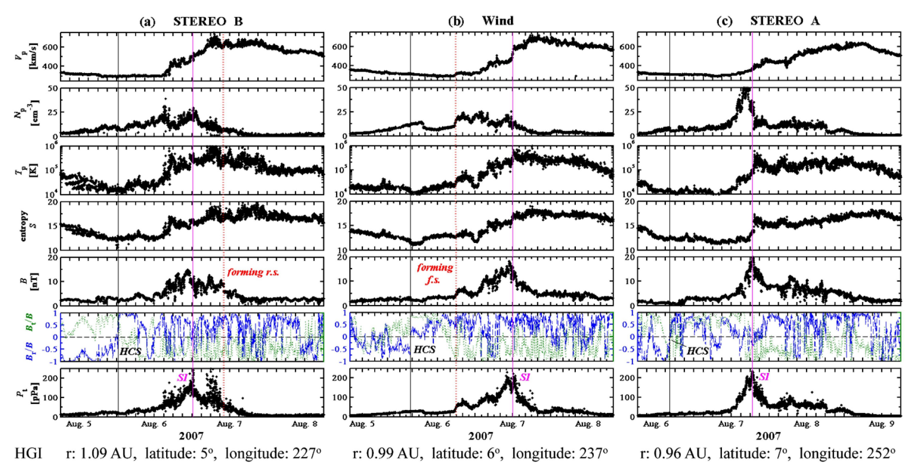

Figure 16: *A CIR and HSS observed in turn by STEREO B (left),* Wind *(center) and STEREO A (right), illustrating the differences in various solar wind parameters observed over a heliolongitude range of only 25°. The parameters shown are (from top) the solar wind speed (V_p), proton density (n_p) and temperature (T_p), entropy ($S = \ln |{T_p}^{3/2}\ n_p|$), magnetic field intensity (B_o), the ratios of the radial and transverse components of the magnetic field to B_y, and the total perpendicular pressure (P_t) (Adapted from L. K. Jian et al., 2009).*

Several studies of energetic particles associated with CIRs have been made with *Wind*/EPACT. For example, Mason et al. (1997) and Mason et al. (1999) used measurements from *Wind*/EPACT to show that the spectra of energetic particles do not show the low-energy turndown expected (Fisk & Lee, 1980) if the particles were accelerated

[29] the boundary that separates the two magnetic polarities or hemispheres of the heliosphere

at CIR shocks at several AU (Barnes & Simpson, 1976). That is, the particles would lose energy due to adiabatic deceleration in the expanding solar wind whilst propagating sunward to the spacecraft. Instead, observations suggest the particles are accelerated closer to the spacecraft. Chotoo et al. (2000) found that the spectra of energetic particles in the vicinity of CIRs merged with the suprathermal tail of the solar wind ion distribution, also suggesting that the particles were accelerated relatively local to the spacecraft, possibly out of the solar wind distribution. Ebert et al. (2012) use EPACT/STEP observations of suprathermal He ions to show that acceleration occurred near the trailing edges of two well-developed CIRs. One of the CIRs is associated with a reverse shock, and the other CIR is not associated with a reverse shock. This surprising result suggests that particle acceleration at CIRs does not require the presence of a shock. Filwett et al. (2017) investigate suprathermal heavy ion abundances at 41 CIRs using STEP. The authors conclude that the upper limit on the distance traveled from the source to the spacecraft was 1 AU, which is consistent with a relatively local source. Filwett et al. (2017) also found evidence for enhanced Fe abundances in CIR-associated particles at higher solar activity levels. Their result suggests that Fe-rich particles from impulsive solar events contribute to the source of CIR particles. Interstellar pick up ions, interstellar neutrals that are ionized near the Sun, such as He^{+} (Chotoo et al., 2000), may also be accelerated at CIRs (J. H. Chen et al., 2015). Reames (2018), using EPACT/LEMT data, concludes that the element abundances of CIR-accelerated ions mirror the solar wind abundances with a modification depending on the mass to charge ratio of the ions.

2.9 Solar Energetic Particles

The *Wind* EPACT instrument has made observations of solar energetic particles or SEPs throughout the mission lifetime (e.g., see Reames, 2017, and references therein). First, we highlight one result that illustrates the ability of the EPACT/LEMT instrument to detect, for the first time, ultra-heavy ($34 \leq Z \leq 82$) ions in impulsive solar particle events accelerated by solar flares and jets. With a large collecting geometry, a large dynamic range above ∼2 MeV amu^{-1}, and a pulse-height analysis scheme that prioritizes $Z > 33$ particles, LEMT is ideal for heavy element detection. It was well-established by previous missions that smaller and shorter duration "impulsive" SEP events accelerated by solar flares exhibit remarkable enhancements in the abundances of ^{3}He and heavy ions compared to coronal abundances. LEMT observations (Reames, 2000; Reames & Ng, 2004) demonstrate that these abundance enhancements extend to ultra-heavy ions.

Figure 17 from Reames and Ng (2004) shows the increase in the ion abundance enhancement relative to coronal abundances with increasing Z. Clearly, the ultra-heavy ions continue the trend evident for ions lighter than iron (filled circles are LEMT data, open circles are from previous missions). Figure 17 (right) shows that the abundance enhancements decrease with increasing Q/A, where a coronal temperature of 3 MK is assumed to estimate the charge states. Note that the enhanced but low charge state ^{3}He does not fit these trends, suggesting that the ^{3}He enhancement arises from a separate process. Remarkably, the strongest heavy ion enhancements are associated with the smallest impulsive events associated with the weakest solar flares and softest particle spectra (Reames & Ng, 2004).

The reason for these heavy and ultra-heavy ion abundance enhancements is still under discussion, but they may occur if the ions interact with a turbulent region where there is more power at larger length scales, which favors the acceleration of heavier ions with larger gyroradii. A promising candidate is the formation of islands by reconnection (Drake et al., 2009; Drake & Swisdak, 2012), where the island size distribution may lead to a strong Q/A-dependence in the particle abundances. However, such a process could not account for the enhancement of ^{3}He over ^{4}He. This may result instead from acceleration through a resonance with ion cyclotron waves generated by streaming electrons (Roth & Temerin, 1997; Temerin & Roth, 1992).

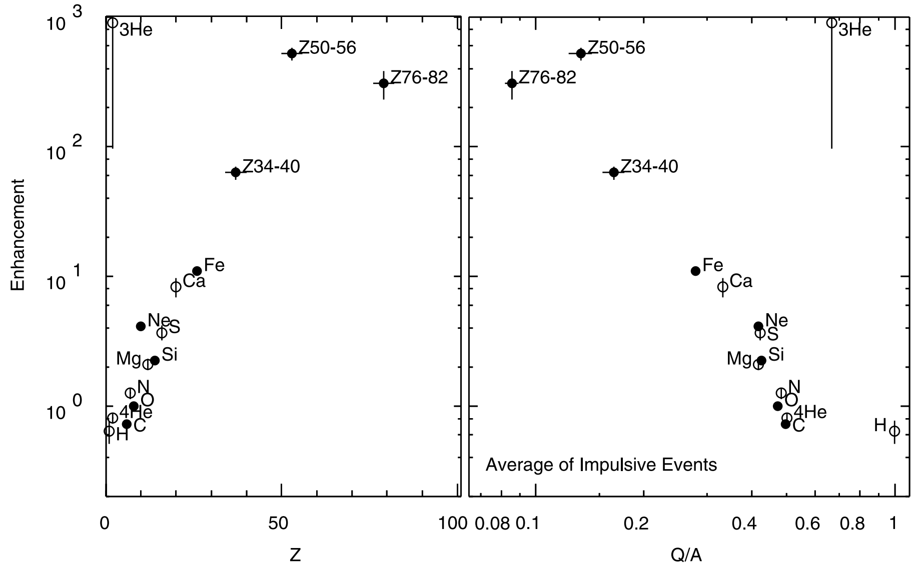

Figure 17: *Abundance enhancements in average large impulsive events relative to coronal abundances, shown as a function of Z and of Q/A at ∼3 MK. Here Z denotes the element/proton number and Q/A is the charge per mass ratio. The solid circles are from the study by Reames and Ng (2004) and open circles are from previous studies (Adapted from Figure 4 in Reames & Ng, 2004).*

The *Wind* mission has also allowed SEP abundances at lower masses to be compared over an extended time period. For example, Reames et al. (2014) show, for 8 hour intervals during a 19 year period, a range of values of Ne/O and Fe/O (both normalized to typical values in large SEP events) at ∼3 MeV/nucleon. The observations show evidence for a bimodal distribution, with a group of periods with enhanced Fe and Ne abundances likely to be associated with impulsive SEP events and another, larger, group with abundances similar to those in large SEP events, associated with gradual events. However, intervals with intermediate values are also present.

Considering particles accelerated by interplanetary shocks, Reames (2012) studied the spectra of ∼1-10 MeV/nucleon ^{4}He at 258 shocks in the CfA Wind shock database[30] with the aim of determining which shock parameters are more important to produce particle acceleration. Only 39 (∼15%) of these shocks had significant particle acceleration to these energies, and the shock speed was found to be the strongest determinant of the particle intensity at the shock followed by the shock compression ratio; quasi-perpendicular shocks were also favored.

2.10 Solar Radio Bursts

Before the launch of *Wind*, type II bursts were known in only two domains: metric (> 15 MHz) from ground-based observations, and hectometric-kilometric (< 2 MHz) from space-based observations. These frequencies correspond to spatial domains of <2 R_s and >10 R_s from the Sun center. The *Wind*/WAVES experiment is capable of observing radio emission in ∼2–14 MHz range, filling the previous observational frequency gap and thereby resulting in a number of new discoveries that will be highlighted in this

[30] `https://www.cfa.harvard.edu/shocks/wi_data/`

section. The coronal domain sampled by *Wind*/WAVES overlaps with that imaged by space-borne coronagraphs. A quarter century of *Wind*/WAVES observations and white-light observations from the Solar and Heliospheric Observatory (SOHO) mission have contributed enormously to our understanding of solar eruptions and their heliospheric consequences. The combined radio and coronal imagery were enhanced with the addition of STEREO in 2006, which greatly advanced our understanding of inner heliospheric nonthermal processes associated with solar magnetic active regions. All radio emissions are due to nonthermal electrons of various energies, so the radio bursts provide key information not only on the particle energization process but also on the ambient medium in which the electrons propagate and produce the radio signatures. Note that in this section, we intentionally refer to both coronal mass ejections (CMEs) and interplanetary coronal mass ejections (ICMEs). The former refers to CMEs observed using coronal imagers and the later to those observed with in situ plasma measurements.

Nonthermal radio signatures in the interplanetary medium (IPM) are simple compared to those in the corona ($<2\ R_s$). Most of the IP radio emissions arise from the plasma emission mechanism[31], whereas near the Sun additional mechanisms such as cyclotron emission, gyrosynchrotron emission, and bremsstrahlung emission operate. Early *Wind* studies showed that nearly all the known radio burst types (e.g., type II, type III, and type IV and see review by Wild et al., 1963) were observed[32] by the WAVES radio receivers (Bale et al., 1999; Gopalswamy, Kaiser, et al., 1998; Gopalswamy et al., 2001; Gopalswamy, 2004a, 2004b; Gopalswamy & Mäkelä, 2010; Kaiser, 2003; Reiner et al., 1998, 2001).

Type III bursts occur as regular, frequency-drifting radio emissions and as type III storms. Type III storms typically start in the metric domain (around 80 MHz) in association with type I storms at higher frequencies but extend down to sub-MHz frequencies. Type III storms are characterized by broadband (>few MHz), very short duration (i.e., $\lesssim$1–2 minutes) emissions that occur in rapid succession (typically >10 per hour). Type III bursts are characterized by their fast frequency drift (i.e., MHz per minute) versus time, which is a tracer of the gradient in the IP electron number density. Type III storms are caused by nonthermal processes taking place in active regions outside of eruptions. Both type III storm bursts and regular type III bursts result from emissions due to nonthermal electrons propagating along open magnetic field lines. Type II bursts are caused by nonthermal electrons accelerated by CME-driven shocks. Type II bursts are characterized by their slow frequency drift (i.e., few 100s of kHz per hour) versus time, which is a tracer of the shock speed and electron number density upstream of the shock. Type IV bursts are thought to be due to nonthermal electrons trapped in post-eruption arcades (i.e., half-loop-like arches of intense magnetic field connecting to active regions on the solar surface) in the eruption site. Type IV bursts are characterized by a broadband frequency emission in the several to >10 MHz range, sometimes showing a U-shaped profile.

Figure 18 shows a solar eruption that exhibits all the IP burst types: type III storm, type III burst, type IV burst, and type II burst. All the burst types are associated with complex magnetic regions on the Sun. All but the type III storm are associated with solar eruptions involving CMEs and solar flares.

[31] i.e., nonthermal electron beams excite Langmuir-like waves which nonlinearly mode convert to free electromagnetic radio emissions at frequencies near the plasma frequency of their source region

[32] Type I radio bursts occur at higher frequencies than can be resolved by *Wind*/WAVES, so they will not be discussed herein.

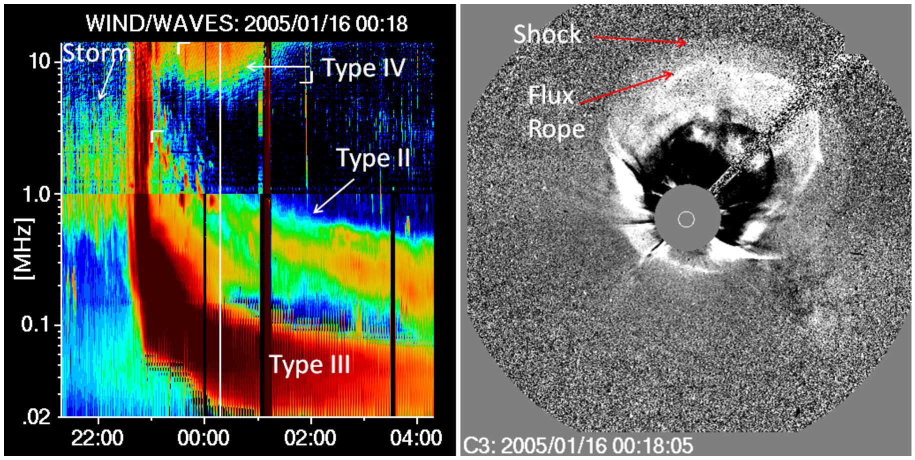

Figure 18: *Four types of radio bursts observed by* Wind*/WAVES on 2005 January 15 toward the end of the day: type III storm was in progress when the eruption occurred. The eruption is marked by the regular type III burst, followed by a type II burst and a type IV burst. (right) The associated CME observed by SOHO/LASCO. The CME has a flux rope driving a shock as indicated. The shock is at a heliocentric distance of ∼25 R_s in sky-plane projection (Adapted from Gopalswamy, 2016).*

2.10.1 Type II Bursts

As previously stated, type II bursts result from nonthermal electrons accelerated by CME-driven shock waves. Thus, they are a tracer of the shock speed/position versus time and of the electron number density immediately upstream of the shock front. Remotely tracking shocks using radio waves is an important element of our space weather forecasting infrastructure. It also provides information on the radial gradient of the IP electron number density, critical for heliospheric models. Therefore, it is important to understand the origin and evolution of the frequency drifts of type II bursts.

Type II bursts can exist in the decametric-hectometric (DH), metric (m), and km wavelength range. Interestingly, there are type II bursts that start in the m range and evolve to the DH range (i.e., meter to DH or m-DH range) while other DH type II bursts are not continuations of m type II bursts. Some type II bursts start in the DH range and end there as well, called pure DH type II bursts. Some type II bursts occur in the m and DH ranges simultaneously while others start in the m range and evolve to the DH and onto the km range. Finally, there can be purely km type II radio bursts (Gopalswamy et al., 2000; Gopalswamy, 2004a; Kaiser et al., 1998; Reiner & Kaiser, 1999). Thus, initially there was a mystery as to the source of the diversity in type II radio bursts.

The mystery was resolved in a subsequent investigation by Gopalswamy et al. (2005) who found that the wavelength extent of type II bursts depends on CME kinematics, i.e., their speed and acceleration/deceleration. The authors showed that the frequency/wavelength of the radio emissions depends upon the CME speeds where the emission ranges and speeds (averages from multiple events) were: ∼610 km/s (m), 1068 km/s (m-DH, DH, and DH-km combined), 1490 km/s (m-to-km), and 540 km/s (purely km). When examining coronal images using the SOHO coronagraphs, Gopalswamy et al. (2005) observed all CMEs decelerated in the coronagraph FOV except those associated purely km type II bursts. These accelerated to super Alfvénic speeds at tens of R_s from the Sun.

Simultaneous type II bursts at different frequencies

Further investigation after the accumulation of numerous type II bursts showed the simultaneous occurrence of two type II bursts: one in the DH domain that evolved from the m domain and one starting in the DH domain and continuing to the km domain. Gopalswamy (2011) reported on one such CME-associated event on 2003 June 17 where the inferred source height of the m-DH component (from the Sun center) was $\sim$2.4 R_s and the DH-km type II was at $\sim$7 R_s. A possible explanation proposed was a curved shock front where the nose was at $\sim$7 R_s and the flanks at $\sim$2.4 R_s (e.g., see the shock surrounding the flux rope in Figure 18). The CME was very fast ($\sim$1800 km/s), so the flanks are also fast enough to drive shocks and accelerate electrons. The flanks are at lower altitudes (where the higher electron density corresponds to higher emission frequency), while the nose is at higher altitudes (lower electron density corresponds to lower emission frequency). The Gopalswamy (2011) study is supported by an earlier study by Raymond et al. (2000) of a slower CME (only $\sim$1300 km/s, thus without flank shocks), only showing type II bursts in the m domain.

Wind/WAVES is also capable of determining the direction from which a radio emission propagated to the spacecraft (Hoang et al., 1998). This analysis has been applied to another fast CME ($\sim$1900 km/s) on 2012 July 6 with both m-DH and DH-km domain type II bursts (Mäkelä et al., 2018). The authors also used the same technique using STEREO to confirm the source regions to be near the nose of the CME shock. Thus, these studies support the nose-flank emission source regions, in contrast to another model that invokes a second shock – the flare blast wave – to explain the metric emission.

Type II burst dependence on ICME properties

Another curiosity is that not all CMEs have an associated type II burst. By the end of 2019, *Wind*/WAVES has observed more than 500 bursts at frequencies below 14 MHz. Even so, early work of $\sim$100 events revealed that type II bursts are associated with fast (>900 km/s) and wide (>60°) CMEs (Gopalswamy et al., 2000, 2001). Later work noted that the average CME speed in the sky plane of coronagraphs has increased to $\sim$1164 km/s due to the energetic CMEs during the maxima of cycles 23 and 24 (Gopalswamy, Mäkelä, & Yashiro, 2019).

An interesting correlation was observed between the initial deceleration and initial speed of CMEs associated with type II bursts. The CMEs are found to decelerate in the coronagraph FOV at $\sim$0–100 m s^{-2}, where the deceleration is correlated with initial speed (Gopalswamy et al., 2001). Later work confirmed the correlation between initial deceleration and initial speed using the frequency drift rate of the observed type II bursts (Reiner, Kaiser, & Bougeret, 2007; X. Zhao et al., 2019).

Given that CMEs are strongly coupled to the solar cycle, examinations of DH type II bursts showed a solar cycle variation with maximum rates of $\sim$10 bursts per Carrington rotation ($\sim$27.3 days) – the approximate rotation period of low solar latitudes – during solar maximum. However, no DH type II bursts were observed in the lowest part of solar minimum. Interestingly, the occurrence rate of type II bursts depends upon the CME properties (i.e., fast and wide CMEs produce type II bursts) rather than the sunspot number (SSN). Gopalswamy et al. (2020) showed that the decrease in SSN between solar cycles 23 and 24 was $\sim$39% while the decrease in type II bursts was $\sim$48%. The authors argued the decrease in fast and wide CMEs was also $\sim$48%, illustrating the connection between the CMEs and type II bursts.

Shock arrival prediction using type II bursts

Recall that type II bursts are a tracer of the shock speed/position versus time and of the electron number density immediately upstream of the shock front. Thus, researchers can use the frequency drift rate, $\frac{df}{dt}$, as a function of time to examine the evolution of the associated ICMEs and the density gradients in the interplanetary medium (IPM). Aguilar-Rodriguez et al. (2005) showed that the drift rate followed a power law of the form $|\frac{df}{dt}| \sim f^{-\varepsilon}$, where the exponent $\varepsilon \sim 1.8$ for the entire wavelength domain (m to km)

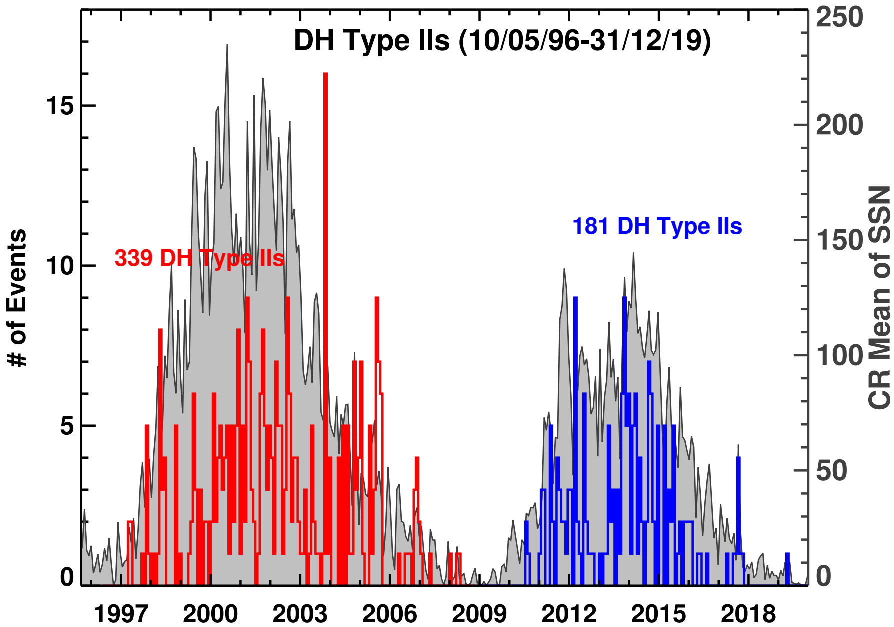

Figure 19: *Occurrence rate of DH type II bursts 1996 May 10 to 2019 December 31 (red: cycle 23; blue: cycle 24) summed over Carrington rotation periods. The sunspot number is shown for comparison. Gopalswamy, Mäkelä, and Yashiro (2019) found that the drop in the number of events in cycle 24 is similar to the drop in the number of fast and wide CMEs (figure updated from Gopalswamy, Mäkelä, & Yashiro, 2019).*

and was higher in the km domain (2.7 at $f < 1$ MHz), and lower at m-DH domain (1.5 at $f > 1$ MHz). The different exponents in the different spectral domains reflect the CME/ICME evolution at different distances from the Sun (Gopalswamy & Mäkelä, 2011; Vršnak et al., 2001). Initially ICMEs accelerate into a more and more tenuous region which results in a smaller ε. Further from the Sun, ICMEs decelerate which increases ε. The evolution of the ICME shocks and influence on ε have been supported by numerous case studies (Gopalswamy, Mäkelä, Akiyama, et al., 2018; Y. D. Liu et al., 2013).

After type II bursts reach the km range their evolution is more consistent with a constant IP shock speed, thus allowing researchers to predict the shock arrival time at Earth. Cremades et al. (2015) combined coronagraph images of CMEs, type II radio emissions in the km range, and in situ information on shocks to investigate the height-time history of 71 IP shocks. The authors were able to predict the shock arrival time within ~6 hr for 85% of the events. Other studies (Corona-Romero et al., 2013) attempted to approximate the shock evolution as that of a blast wave. However, the speeds of magnetic clouds (MCs) and the associated shocks have been shown to be highly correlated (95%) (Gopalswamy, 2006). Thus, ICMEs and their shocks remain coupled at 1 AU, even though both have undergone significant decelerations, which is inconsistent with a blast wave scenario.

Type II bursts and SEPs

Type II bursts are the earliest indicators of CME-driven shocks, and can also serve as an indicator of solar energetic particle (SEP) events because the same shock accelerates electrons and ions (see Section 2.9 for more discussion of SEPs). Recall that the observed frequency of type II bursts is strongly related to the CME speed. For instance, purely m type II bursts are associated with average speed CMEs satisfying ~600 km/s while m-DH type II bursts are associated with >1000 km/s CMEs. Faster CMEs tend to result in stronger (higher Mach number) IP shocks, which are known to be more efficient accelerators of particles. Therefore, investigating the relationship between type II bursts and SEPs was an obvious avenue for improving space weather forecasting.

Cliver et al. (2004) found that only ∼25% of purely m type II bursts are associated with >20 MeV SEP events but the rate almost quadrupled to 90% when a m type II had a DH counterpart. Gopalswamy et al. (2005) found that CMEs producing type II bursts in the m-to-km range also had high energy SEPs. Further, all SEPs strong enough to generate a ground level enhancement (GLE) – solar particles observed by ground-based instruments – are associated with m-to-km type II bursts (Gopalswamy et al., 2012).

Later work (Cliver et al., 2019; Gopalswamy, Mäkelä, et al., 2015; Gopalswamy, Yashiro, et al., 2016) found that the initial frequency of type II bursts correlated with the spectral slope of the SEP number flux versus energy power-law relationship. Shocks forming closer to the solar surface (i.e., with a higher initial type II burst frequency) had harder spectra[33] than those forming at higher altitudes. The harder spectra SEP events are often also GLE events. The reason for the shock formation altitude dependence on spectral slope relates to the background plasma parameters in which the shock formed. At lower altitudes, the magnetic field magnitude is much larger and the geometry is more complicated, both of which make for more efficient particle scattering and acceleration (Cliver et al., 2019; Gopalswamy et al., 2017).

Finally, the examination of type II bursts have helped us understand the source of the >300 MeV protons required for producing the pion-decay continuum observed as sustained gamma-ray emission (SGRE) from the Sun (Gopalswamy, Mäkelä, Yashiro, et al., 2018; Share et al., 2018). Gopalswamy, Mäkelä, Yashiro, et al. (2018) and Gopalswamy, Mäkelä, Yashiro, Lara, et al. (2019) demonstrated a close linear relationship between the SGRE and type II burst durations, in every SGRE event with duration >3 hr, supporting the hypothesis that the >300 MeV protons continue to be accelerated at the shock as it moves away from the Sun, and then propagate back to the Sun, generating the SGRE. However, other studies (de Nolfo et al., 2019; K.-L. Klein et al., 2018; Malandraki & Crosby, 2018) may not support this hypothesis for the origin of SGRE.

2.10.2 Type III Bursts

Type III bursts result from nonthermal electrons accelerated in solar magnetic active regions exciting plasma waves as they stream along the magnetic field away from the Sun. Early work using triangulation between *Ulysses* and *Wind* identified the electron beam source of type III bursts, finding that the electrons were traveling at a speed of ∼0.3 c (Reiner et al., 1998). When the radio emission of a type III burst reaches the local plasma frequency of the observing spacecraft, the emission is occurring locally. Reiner and MacDowall (2015) analyzed five in-situ type III radio bursts observed by *Wind* and STEREO, finding that the electron beam speed ranged from 0.2 c to 0.38 c near the Sun but was only ∼0.2 c near 1 AU. The reduction in beam speed corresponded to a deceleration of ∼30 km s^{-2}. That is, the primary electrons exciting type III bursts near the sun correspond to energies of 20–30 keV while they drop to ≤10 keV near 1 AU. The reduction in energy is consistent with the beam losing energy as it converts kinetic energy to electromagnetic energy to generate the initial Langmuir waves.

Type III bursts generally accompany SEP events (e.g., Cane et al., 2002; MacDowall et al., 2003, 2009; Miteva et al., 2017; I. G. Richardson et al., 2018; Winter & Ledbetter, 2015, and see Section 2.9). In particular, large SEP events are usually associated with bright, long duration, complex type IIIs such as that shown in Figure 19. These long-

[33] i.e., indicates a flatter or less-steep drop in number flux with increasing energy

duration emissions were originally thought to result from electrons accelerated at or associated with CME-driven shocks (Bougeret et al., 1998; Cane et al., 1981). Based on *Wind*/WAVES observations, which as discussed above, closed a frequency gap between ground and previous space-based instruments, these complex type III emissions can appear to extend from the associated type II bursts (Gopalswamy et al., 2000), they are now thought to result from electron acceleration in magnetic reconnection below CMEs (Cairns et al., 2018; Cane et al., 2002; Reiner et al., 2000). Characteristics such as correlations between the burst duration or intensity and SEP peak intensity, and their rapid onset and frequency drift following solar flares, have led to the inclusion of type IIIs in proposed SEP prediction schemes (e.g., Laurenza et al., 2009; I. G. Richardson et al., 2018; Winter & Ledbetter, 2015). However, these require real-time radio observations that are not available from *Wind*. The largest SEP events are usually associated with type III burst durations of $\gtrsim$15 min at $\sim$1 MHz (Cane et al., 2002; MacDowall et al., 2003, 2009; I. G. Richardson et al., 2018; Winter & Ledbetter, 2015). Krucker et al. (1999) examined the relationship between type III bursts and energetic electrons observed in situ using *Wind* 3DP electron and WAVES observations. They found that while some near-relativistic electron events are released at the Sun at the time of the type III burst, others are apparently released up to half an hour later, suggesting that they originate from a different population than the type III-producing electrons. Similar conclusions were reached by Haggerty and Roelof (2002), Klassen et al. (2002), and L. Wang et al. (2006, 2016). An alternative interpretation is that the energetic electrons may be delayed during propagation through the interplanetary medium (Cane, 2003; Cane & Erickson, 2003; L. Wang et al., 2011).

2.10.3 Type III Storms

Solar noise storms are nonthermal radio emission due to electrons accelerated in a non-eruptive energy release in active regions. At metric wavelengths, noise storms manifest as type I bursts, which transition into type III storms in the outer corona. Thus, type III storms are the low-frequency extensions of type I storms (Fainberg & Stone, 1970). Type III storms can last for several days and can be observed at heliocentric distances of up to 170 R_s (Bougeret et al., 1984). Interestingly the rate of type III storm and their intensity increase as the source active region crosses the central meridian (Gopalswamy, 2004b; Morioka et al., 2007, 2015; Reiner et al., 2001; Reiner, Fainberg, et al., 2007). Further work indicated that type III bursts and storms have different energization processes based upon differences in occurrence frequency and emitted power flux (Morioka et al., 2007).

The source regions of type III storms were later identified to be solar active regions accompanied by coronal holes. These are regions in which the magnetic field lines do not connect back to the solar surface but rather are directed outward into the IPM. The suggested mechanism (Del Zanna et al., 2011) is a type of magnetic reconnection called interchange reconnection – magnetic reconnection between coronal hole and adjacent, closed magnetic field lines that leads to the energization of low energy electrons (see Section 2.4 for details on magnetic reconnection). These sustain the type III storm on closed magnetic field loops and give rise to weak type III emission on open field lines.

Type III storms can be disrupted by CMEs for upwards of $\sim$10 hr (see Figure 18). Gopalswamy (2016) reported on a type III storm starting on 2005 January 14 that was disrupted by five CMEs (including that in Figure 18), with the last one being an extreme event that occurred on 2005 January 20. Following the final CME the type III storm did not reappear suggesting a possible reconfiguration of the active region or a change in the directivity of the storm or the active region complexity.

Type III storms also exhibit an interesting change in degree of polarization with radial distance. In the metric range, type III storms have a degree of circular polarization of up to ∼25%. In the IPM, type III storms have much smaller degrees of circular polarization (<5%) at frequencies near 1 MHz (Reiner, Fainberg, et al., 2007). Reiner, Fainberg, et al. (2007) used the change in the degree of circular polarization to determine the magnitude and radial projection of the magnetic fields above solar active regions. Typical magnetic field strengths of ∼50 mG (or ∼5000 nT) at a heliocentric distance of 25 R_s were calculated and the field strength decreased faster than the inverse-square of the radial distance. Thus, type III storms can be used to remotely probe the magnetic structure and strength of solar active regions.

2.10.4 Type IV Bursts

Type IV bursts are another phenomenon that has been better understood through observations of their lower frequency range by WAVES in the DH frequency range. The type IV burst on 1998 May 2 studied by Leblanc et al. (2000) was one of the first observed down to 7.5 MHz (e.g., similar to the one shown in Figure 18). Gopalswamy (2004b) studied a dozen DH type IV bursts finding they are extensions of the emissions in the metric range. The type IV bursts lasted typically for ∼2 hours at 14 MHz with a typical ending frequency of ∼7.7 MHz. The type IV bursts in the DH frequency range are associated with very energetic CMEs (average speed ∼1200 km/s). Further, the average speed of CMEs (∼1500 km/s) associated with DH type IV bursts is similar to that in large SEP events (Gopalswamy, 2011, 2016; Hillaris et al., 2016). The most likely source of type IV bursts is electrons accelerated in a solar flare site that become trapped in the closed magnetic fields of the post eruption arcades.

More recent studies discovered that DH type IV bursts have a relatively narrow emission cone. That is, DH type IV bursts associated with eruptions in the middle of the solar disk show a symmetric time profile about their lowest frequency (i.e., the lowest frequency boundary of the emission is U shaped). In contrast, DH type IV bursts associated with eruptions on the limb of the solar disk show an asymmetric time profile. Gopalswamy, Akiyama, et al. (2016) concluded that the type IV emission cone is less than ∼60° in full width and that this narrow cone results from the small angular extent of the source region, the post eruption solar arcades. Another proposed explanation is that the shock-compressed, high-density plasmas in the foreground of the emission attenuate the intensity of the type IV bursts more on the shock flanks than the center (i.e., due to larger line of sight integration) (Pohjolainen & Talebpour Sheshvan, 2020; Talebpour Sheshvan & Pohjolainen, 2018). The reason for the narrow type IV emission cone continues to be an active area of research.

3 Summary

3.1 Science Overview

Wind launched on November 1, 1994 and immediately began detecting gamma ray burst signatures with KONUS and TGRS. In 2020, KONUS detected a magnetar superflare in the Sculptor galaxy (D. Svinkin, Golenetskii, et al., 2020; D. Svinkin, Hurley, et al., 2020). *Wind* also contributes to remote astrophysics via observations of interstellar dust (ISD). Malaspina and Wilson III (2016) provided a database (see Table 6) of IPD and ISD which provides researchers an opportunity to examine if a link exists between large-scale magnetic structures in the IPM and dust detections near 1 AU.

Wind provided the first complete set of plasma particle and field measurements of the lunar wake in 1994 (Farrell et al., 1997, 1998; Ogilvie et al., 1996; Owen et al., 1996). Between 1997 and 1999, *Wind* made the first partial orbit of L2 with modern instrumentation and provided the first in situ measurements of an ion diffusion region during a magnetotail reconnection event. Petal orbits through Earth's dayside magnetosphere revealed that large-amplitude radiation belt whistler-mode waves have amplitudes much larger than previously thought possible. *Wind* provided some of the first non-spectral observations of Langmuir waves in Earth's electron foreshock (Eastwood et al., 2005) and helped define Earth's ion foreshock boundaries. *Wind* foreshock data was used to discover the foreshock cavity, a new transient phenomenon of the ion foreshock (D. G. Sibeck et al., 2002).

Wind measurements provided insight into the structure of ICMEs, in particular MCs, and CIRs. *Wind* also redefined the wave structure of quasi-perpendicular interplanetary shocks by showing that whistler-mode waves are present where flows were expected to be laminar (Wilson III et al., 2017). *Wind* STICS observations of suprathermal particles helped refine the arrival time estimates of CME-driven interplanetary shocks (Posner et al., 2004). Long-term measurements in the solar wind provided the first opportunity to perform statistics across multiple solar cycles. *Wind* also helped discover many solar wind turbulence features, including the evolution of the spectral break point as a function of β (Woodham et al., 2018; C. H. K. Chen et al., 2014) and the ability of the slow solar wind to support a "1/f" range (Bruno et al., 2019).

The solar radio data provided by *Wind*/WAVES contributed enormously to the understanding of nonthermal radio emission from the inner heliosphere associated with both eruptive and non-eruptive energy releases. The radio phenomena observed by *Wind*/WAVES provided a detailed picture of the interconnection among plasmas, magnetic structures, and energetic particle populations. The complex behavior of type II bursts simultaneously observed at multiple frequencies is now understood to result from a single curved ICME-driven shock that intersects regions of differing density, magnetic field strength, and Alfvén speed. Sustatined solar gamma ray emissions with a close connection to IP type II bursts and SEP events, may provide new insight into the particle transport toward and away from the Sun in the inner heliosphere. Studies of type III bursts continue to provide detailed information on the evolution of electron beams between the Sun and earth. The combination of STEREO/WAVES and *Wind*/WAVES provide longitudinal coverage of type III storms and their evolution. Type III storms are the low-frequency extension of type I storms and are caused by nonthermal electrons trapped in the magnetic arcades of active regions. Type III storms help us understand high-altitude coronal structures overlying solar active regions and their interaction with neighboring open magnetic field structures. They are used to remotely probe the magnetic field structure of the corona. Observations of Type IV bursts have opened a window to study their source and the environment overlying active regions that causes variablity in these emissions. Their narrow emission cone angle helps to confine the source regions to better understand the phenomena.

3.2 *Wind*'s relevance to Parker Solar Probe

Wind's broad contributions to solar and heliospheric physics can be viewed through the lens of Parker Solar Probe's mission objectives. *Parker Solar Probe* (PSP) was launched in August, 2018 to study the origin and acceleration of the solar wind in the upper solar corona. PSP will not reach its minimum perihelion of $\sim$10 solar radii (R_s) until 2026, but PSP is already significantly closer to the sun than any previous mission. One method of understanding the evolution of the solar wind in the inner heliosphere is to compare the near-sun PSP in situ observations with *Wind* observations at 1 AU. Although these studies may require specific spacecraft alignments and are still in their early phase, PSP and *Wind* have already provided insight into the heliospheric current sheet, stream interaction regions, and radio remote sensing as detailed in the following.

The Heliospheric Current Sheet (HCS) varies significantly from its formation in the solar corona to its interaction with Earth at 1 AU. PSP observations of HCS crossings during the first solar orbit were successfully mapped to *Wind* observations at 1 (Szabo et al., 2020). The authors found that during solar minimum years, the HCS shows remarkable stability and can be successfully traced over full solar rotations. However, earlier work showed that the internal structure of the HCS exhibits a marked difference between solar minimum and solar maximum. Although magnetic reconnection-induced magnetic structures appear to be present near PSP as well as near 1 AU, the characteristics of individual structures differ. Magnetic signatures are stronger and more pronounced at PSP, and more pronounced density enhancements occur at 1 AU. SIRs can also be traced from PSP to *Wind* (Allen et al., 2020). This study, though investigating only the first PSP solar orbit, demonstrated that SIRs can form well within 0.5 AU. Allen et al. (2020) also determined that the associated and locally accelerated suprathermal particles penetrate deeper into the fast stream further away from the sun.

Supplemented with data from STEREO and *Wind*, PSP radio observations of Type III radio bursts confirmed they are associated with energetic electron beams (Krupar et al., 2020). The radio beams showed significant scattering due to solar wind density fluctuations in the inner heliosphere. The predicted density fluctuation levels from the radio data was compared to the in-situ PSP observations and yielded the same 6–7% level.

3.3 Space Weather and Space Climate

The *Wind* mission is perhaps best known as a solar wind monitor but it also has one of the most diverse arrays of instrument suites. For a majority of the mission, *Wind* provided the only observations of kinetic phenomena in the solar wind, and *Wind* is still the only mission to provide comprehensive, high-cadence plasma measurements across multiple solar cycles. *Wind* continues to provide continuous low-frequency solar radio observations, which are a critical part of space weather monitoring.

The duration, resolution, and also well calibrated solar wind measurements that *Wind* provides enables the study of small-scale and rapid processes on a solar climate timescale (i.e., solar cycle). Finally, *Wind* data are used in multiple databases (see Table 6) for gamma ray bursts, dust, particle distribution fits, electric field waveform captures, IP shocks, SEPs, and radio bursts provide improved accessibility to researchers studying diverse phenomena at multiple temporal and spatial scales.

Appendix A Definitions and Notation

This appendix lists the symbols/notation used throughout.

one-variable statistics
- $X_{min} \equiv$ minimum
- $X_{max} \equiv$ maximum
- $\bar{X} \equiv$ mean
- $\tilde{X} \equiv$ median
- $X_{5\%} \equiv 5^{th}$ percentile
- $X_{25\%} \equiv 25^{th}$ percentile
- $X_{75\%} \equiv 75^{th}$ percentile
- $X_{95\%} \equiv 95^{th}$ percentile
- $\sigma \equiv$ standard deviation
- $\sigma^2 \equiv$ variance

fundamental parameters
- $\varepsilon_o \equiv$ permittivity of free space
- $\mu_o \equiv$ permeability of free space
- $c \equiv$ speed of light in vacuum $[km\ s^{-1}] = (\varepsilon_o\ \mu_o)^{-1/2}$
- $k_B \equiv$ the Boltzmann constant $[J\ K^{-1}]$
- $e \equiv$ the fundamental charge $[C]$

plasma parameters
- $\mathbf{B}_o \equiv$ quasi-static magnetic field vector $[nT]$ with magnitude B_o

[H]

Table 6: A selection of *Wind* databases first published between 2013 and 2020

Year	Title	Citation & URL
2020	*Wind* WAVES TDSF Dataset	Wilson III (2020) https://doi.org/10.5281/zenodo.3911205
2020	Supplement to: Electron energy partition across interplanetary shocks: III. Analysis	Wilson III et al. (2020b) https://doi.org/10.5281/zenodo.3627284
2020	Radial Evolution of Coronal Mass Ejections Between MESSENGER, & Venus Express, STEREO, and L1: Catalog and Analysis	Salman et al. (2020) https://doi.org/10.1029/2019JA027084
2019	Supplement to: Electron energy partition across interplanetary shocks	Wilson III et al. (2019c) https://doi.org/10.5281/zenodo.2875806
2019	A Catalog of Type II radio bursts observed by *Wind*/WAVES and their Statistical Properties	Gopalswamy, Mäkelä, and Yashiro (2019) https://cdaw.gsfc.nasa.gov/CME_list/radio/waves_type2.html
2018	A database of small-scale magnetic flux ropes in the solar wind from *Wind* spacecraft measurements	Hu et al. (2018) https://doi.org/10.1088/1742-6596/1100/1/012012
2018	*Wind* ICME Catalogue	Nieves-Chinchilla et al. (2018) https://wind.nasa.gov/ICMEindex.php
2018	The *Wind*/EPACT Proton Event Catalogue	Miteva et al. (2018) http://www.stil.bas.bg/SEPcatalog/
2017	The KONUS-*Wind* GRB Catalogue with known Redshifts	Tsvetkova et al. (2017) http://www.ioffe.ru/LEA/zGRBs/triggered/
2017	Interactive Multi-instrument Database of Solar Flares	Sadykov et al. (2017) https://solarflare.njit.edu
2016	The 2nd KONUS-*Wind* Catalogue of sGRBs	D. S. Svinkin et al. (2016) http://www.ioffe.ru/LEA/shortGRBs/Catalog/
2016	*Wind* Dust Impact Database	Malaspina and Wilson III (2016) https://cdaweb.gsfc.nasa.gov/index.html/
2014	Catalogue of High-Speed Solar Wind Streams during Solar Cycle 23	Xystouris et al. (2014) https://doi.org/10.1007/s11207-013-0355-z
2014	KONUS-*Wind* Solar Flares	Pal'shin et al. (2014) http://www.ioffe.ru/LEA/Solar/
2013	Interplanetary Network Localizations of sGRBs	Pal'shin et al. (2013) https://doi.org/10.1088/0067-0049/207/2/38

- $n_s \equiv$ the number density $[cm^{-3}]$ of species s
- $m_s \equiv$ the mass $[kg]$ of species s
- $Z_s \equiv$ the charge state of species s
- $q_s = Z_s\ e \equiv$ the charge $[C]$ of species s
- $\rho_m = \sum_s m_s n_s \equiv$ total mass density $[kgcm^{-3}]$
- $\gamma_s \equiv$ polytropic index or ratio of specific heats $[N/A]$ of species s
- $T_{s,j} \equiv$ the scalar temperature $[eV]$ of the jth component of species s, j = $\|$, $\perp$, or tot where $\|(\perp)$ is parallel(perpendicular) with respect to $\mathbf{B}_o$ (see Equation A1a)
- $P_{s,j} = n_s\ k_B\ T_{s,j} \equiv$ the partial thermal pressure $[eV\ cm^{-3}]$ of the jth component of species s
- $P_{t,j} = \sum_s\ P_{s,j} \equiv$ the total pressure $[eV\ cm^{-3}]$ of the jth component, summed over all species
- $V_{Ts,j} \equiv$ the most probable thermal speed $[km\ s^{-1}]$ of a one-dimensional velocity distribution (see Equation A1b)
- $\Omega_{cs} = 2\ \pi f_{cs} \equiv$ the angular cyclotron frequency $[rad\ s^{-1}]$ (see Equation A1c)
- $\omega_{ps} = 2\ \pi f_{ps} \equiv$ the angular plasma frequency $[rad\ s^{-1}]$ (see Equation A1d)
- $\Omega_{lh} = 2\ \pi\sqrt{f_{ce}\ f_{ci}} \equiv$ the angular lower hybrid resonance frequency $[rad\ s^{-1}]$
- $\Omega_{uh} = 2\ \pi\sqrt{{f_{ce}}^2 + {f_{pe}}^2} \equiv$ the angular upper hybrid resonance frequency $[rad\ s^{-1}]$
- $\lambda_{De} \equiv$ the electron Debye length $[m]$ (see Equation A1e)
- $\rho_{cs} \equiv$ the thermal gyroradius $[km]$ (see Equation A1f)
- $\lambda_s \equiv$ the inertial length $[km]$ (see Equation A1g)
- $\beta_{s,j} \equiv$ the plasma beta [N/A] of the jth component of species s (see Equation A1h)
- $V_A \equiv$ the Alfvén speed $[km\ s^{-1}]$ (see Equation A1i)
- $C_s \equiv$ the sound or ion-acoustic sound speed $[km\ s^{-1}]$ (see Equation A1j)
- $V_f \equiv$ the fast mode speed $[km\ s^{-1}]$ (see Equation A1l)
- $\theta_{Bn} \equiv$ the shock normal angle, i.e., the acute reference angle between $\langle \mathbf{B}_o \rangle_{up}$ and the shock normal unit vector [deg]
- $\langle |U_{shn}| \rangle_j \equiv$ the j^{th} region average shock normal speed $[km\ s^{-1}]$ in the shock rest frame (i.e., the speed of the flow relative to the shock)
- $\langle M_A \rangle_j = \langle |U_{shn}| \rangle_j / \langle V_A \rangle_j \equiv$ the j^{th} region average Alfvénic Mach number [N/A]
- $\langle M_f \rangle_j = \langle |U_{shn}| \rangle_j / \langle V_f \rangle_j \equiv$ the j^{th} region average fast mode Mach number [N/A]
- $R_E \equiv$ mean equatorial radius of Earth ($\sim$6378 km)
- $R_L \equiv$ mean equatorial radius of Earth's moon ($\sim$1737 km)
- $R_s \equiv$ mean solar radius ($\sim$695,700 km)
- $\sigma_c \equiv$ normalized cross-helicity, a quantified measure of the imbalance in plasma turbulence (see Equation A1m)
- $\mathbf{z}^{\pm} = \delta\mathbf{v} \pm \delta\mathbf{b} \equiv$ Elsasser variables $[km\ s^{-1}]$, where $\delta\mathbf{v}$ and $\delta\mathbf{b}$ are the velocity and magnetic field fluctuations, the latter being normalized by $\sqrt{\mu_o n_i M_i}$ to make it akin to an Alfvénic fluctuation speed

where multiple parameters are given in the following equations:

$$T_{s,tot} = \frac{1}{3}\left(T_{s,\parallel} + 2\ T_{s,\perp}\right) \tag{A1a}$$

$$V_{Ts,j} = \sqrt{\frac{2\ k_B\ T_{s,j}}{m_s}} \tag{A1b}$$

$$\Omega_{cs} = \frac{q_s\ B_o}{m_s} \tag{A1c}$$

$$\omega_{ps} = \sqrt{\frac{n_s\ {q_s}^2}{\varepsilon_o\ m_s}} \tag{A1d}$$

$$\lambda_{De} = \frac{V_{Te,tot}}{\sqrt{2}\ \omega_{pe}} = \sqrt{\frac{\varepsilon_o\ k_B\ T_{e,tot}}{n_e\ e^2}} \tag{A1e}$$

$$\rho_{cs} = \frac{V_{Ts,tot}}{\Omega_{cs}} \tag{A1f}$$

$$\lambda_s = \frac{c}{\omega_{ps}} \tag{A1g}$$

$$\beta_{s,j} = \frac{2\mu_o n_s k_B T_{s,j}}{{B_o}^2} \tag{A1h}$$

$$V_A = \frac{B_o}{\sqrt{\mu_o n_i M_i}} \tag{A1i}$$

$${C_s}^2 = \frac{\partial P}{\partial \rho_m} = \frac{\sum_s \gamma_s P_s}{\rho_m} \tag{A1j}$$

$$2{V_f}^2 = \left({C_s}^2 + {V_A}^2\right) \tag{A1k}$$

$$+ \sqrt{\left({C_s}^2 - {V_A}^2\right)^2 + 4{C_s}^2{V_A}^2 \sin^2\theta_{Bn}} \tag{A1l}$$

$$\sigma_c = 2\frac{\langle \delta\mathbf{v}\cdot\delta\mathbf{b}\rangle}{\langle \delta\mathbf{v}^2 + \delta\mathbf{b}^2\rangle} \tag{A1m}$$

Appendix B Instability and Wave Definitions and Summary

In this appendix we briefly summarize some of the most commonly investigated kinetic plasma instabilities and waves in the interplanetary medium to provide context and reference for the reader. The role *Wind* has played in our understanding of many of these phenomena is discussed in Section 2.7.2. We use the phrase “driven unstable” to mean the free energy was sufficiently above the growth threshold for the electric or magnetic fluctuations to grow in amplitude. The instabilities and/or waves are as follows in no particular order:

- **Firehose Instability:** The firehose mode can be driven unstable by temperature anisotropies (i.e., $T_{s,\perp} < T_{s,\parallel}$) in both electrons (Gary & Nishimura, 2003) and ions (Bale et al., 2009; Gary et al., 1976; Hellinger et al., 2006; Maruca et al., 2012). These are not typically observed with in situ time series data but more so inferred by statistical trends limiting $T_{s,\perp}/T_{s,\parallel}$.
  - **Electron Firehose Instability:** The electron firehose mode can be both resonant and non-resonant with the electrons (Gary & Nishimura, 2003). It either propagates along $\mathbf{B}_o$ and is left-hand polarized (with respect to $\mathbf{B}_o$), or it is non-propagating[34] with $\mathbf{k}$ oblique to $\mathbf{B}_o$ and nearly linearly polarized.
  - **Ion Firehose Instability:** The ion firehose mode can be both resonant and non-resonant with the ions but can only experience a non-resonant, cyclotron-like interaction with the electrons (Gary et al., 1998). The mode is right-hand polarized (with respect to $\mathbf{B}_o$) and the wave vector is oriented nearly along $\mathbf{B}_o$ in the linear regime but can become oblique when nonlinear.

[34] i.e., the real part of its frequency is zero

- **Mirror Modes:** The mirror mode can be driven unstable by temperature anisotropies (i.e., $T_{s,\perp} > T_{s,\parallel}$) in both electrons (Gary & Karimabadi, 2006) and ions (C. H. K. Chen et al., 2016; Gary et al., 1976; Hellinger et al., 2006). In the linear stage mirror modes are purely growing modes, i.e., the real part of their frequency is zero so they do not propagate. They also show an anti-correlation between δB and δB. In the nonlinear regime, the mirror mode can propagate and $\mathbf{k}$ can be obliquely[35] oriented with respect to $\mathbf{B}_o$. In time series they are usually seen as local decreases in the magnitude of $\mathbf{B}_o$ and less commonly as enhancements.
  - **Electron Mirror Mode:** The electron mirror mode is a non-propagating mode with wave vector oriented obliquely to $\mathbf{B}_o$ and has $k\ c/\omega_{pe} < 1$.
  - **Ion Mirror Mode:** The ion mirror mode is a non-propagating mode with wave vector oriented obliquely to $\mathbf{B}_o$ and has $k\ \rho_{cp} < 1$.
- **ICWs:** Electromagnetic ion cyclotron waves (EMIC), ion cyclotron waves (ICWs), proton cyclotron waves (PCWs), or Alfvén/ion cyclotron (AIC) waves are linear or left-hand polarized (with respect to $\mathbf{B}_o$) modes that propagate small angles to $\mathbf{B}_o$. They have rest frame frequencies below the local f_{cp} in the solar wind and typically satisfy $k\ c/\omega_{pp} \sim$ 0.2–0.6 (He, Wang, et al., 2015; He, Pei, et al., 2015; Wicks et al., 2016). They can be driven unstable by temperature anisotropies (Gary et al., 1976) or ion beams (Gary et al., 1981; Wicks et al., 2016). These waves can reach amplitudes in excess of >10 mV/m and >2 nT in the solar wind.
- **LHWs:** Electrostatic (or electromagnetic) lower hybrid waves (or lower hybrid drift or lower hybrid drift instability) are typically linearly polarized electrostatic (i.e., $\mathbf{k}\times\mathbf{B}_o = 0$) waves propagating perpendicular to $\mathbf{B}_o$. When obliquely propagating, they become a right-hand circularly polarized electromagnetic mode and lie on the same branch of the dispersion relation as fast/magnetosonic-whistler mode waves (Davidson & Gladd, 1975; Huba & Wu, 1976; Lemons & Gary, 1978; Marsch & Chang, 1983; C. S. Wu et al., 1983, 1984). The typical free energy sources include but are not limited to electric currents (Lemons & Gary, 1978), gradient drifts (Davidson & Gladd, 1975; Huba & Wu, 1976; Lemons & Gary, 1978), the modified two-stream instability (C. S. Wu et al., 1983, 1984), and/or heat flux carrying electrons (Marsch & Chang, 1983). In time series in situ data these waves look like modulated sine waves in the perpendicular electric field for the electrostatic version and much less well defined electric and magnetic fluctuations when electromagnetic (Walker et al., 2008; Wilson III, Koval, Szabo, et al., 2013). The electrostatic fluctuations tend to remain below the local lower hybrid resonance frequency, $f_{lh} = \sqrt{f_{ce}\ f_{ci}}$, while the electromagnetic fluctuations can extend to well above f_{lh} (Walker et al., 2008; Wilson III, Koval, Szabo, et al., 2013). These waves can reach amplitudes in excess of >30 mV/m and >20 nT in space plasmas.
- **Magnetosonic-whistler Waves:** These are the electromagnetic version of electrostatic LHWs discussed above and are sometimes called electromagnetic lower hybrid waves, whistler precursors, "1 Hz waves" and/or ULF waves in the terrestrial foreshock. They are part of the MHD fast mode branch of the dispersion relation. They are right-hand polarized (with respect to $\mathbf{B}_o$), obliquely propagating modes with wave normal angles satisfying $10° \lesssim \theta_{kB} \lesssim 60°$, wavenumbers satisfying $0.02 \lesssim k\ \rho_{ce} \lesssim 3.0$, spacecraft frame frequencies near 1 AU satisfying 0.01 Hz $\lesssim f_{sc} \lesssim$ 7.0 Hz, and rest frame frequencies near 1 AU satisfying $0.01 \lesssim \frac{f_{rest}}{f_{cp}} \lesssim 38$ (Wilson III, Koval, Szabo, et al., 2013; Wilson III, 2016; Wilson III et al., 2017). The instabilities responsible for radiating these modes can be driven unstable by shock-reflected ions (Wilson III et al., 2012; C. S. Wu et al., 1983) and/or heat heat flux carrying electrons (Verscharen, Chandran, et al., 2019; Marsch & Chang, 1983). These modes can also be directly radiated through a process called

[35] In linear kinetic theory, mirror modes are always oblique and only in fluid theories is $\mathbf{k}$ exactly orthogonal to $\mathbf{B}_o$.

dispersive radiation (Tidman & Northrop, 1968; Krasnoselskikh et al., 2002; Wilson III et al., 2009, 2017), whereby the temporally and spatially varying magnetic fields and currents in the nonlinearly steepening collisionless shock ramp radiate electromagnetic fluctuations on the fast/magnetosonic-whistler branch of the dispersion relation. They are observed with in situ time series data as modulated sine waves at low amplitudes and can exhibit soliton-like pulsations at large amplitudes (Wilson III et al., 2012; Wilson III, Koval, Szabo, et al., 2013; Wilson III, Koval, Sibeck, et al., 2013; Wilson III et al., 2017). These waves can reach amplitudes in excess of >30 mV/m and >20 nT in space plasmas.

- **Whistler Waves:** Electromagnetic whistler mode waves (or whistler waves or whistlers or lion roars or chorus or hiss) are right-hand polarized with respect to $\mathbf{B}_o$ and dispersive (i.e., phase speed depends upon the wavenumber) (Hull et al., 2012; Santolík et al., 2003, 2014). They are radiated by instabilities driven unstable by the temperature anisotropy of hot electrons or heat flux carrying electrons (Tong et al., 2019; Vasko et al., 2019; Verscharen, Chandran, et al., 2019; Wilson III et al., 2009; Wilson III, Koval, Szabo, et al., 2013; Wilson III et al., 2020a). They tend to have rest frame frequencies satisfying $\omega_{lh} \ll \omega < \omega_{ce}$ and wavenumbers satisfying $k\ c/\omega_{pe} \sim 0.2$–$1.0$ or $k\ \rho_{ce} \sim 0.2$–0.8 (Stansby et al., 2016; Wilson III, Koval, Szabo, et al., 2013). These waves can reach amplitudes in excess of >300 mV/m and >8 nT in space plasmas.
- **ESWs:** Electrostatic solitary waves (or BGK phase space holes or electron/ion holes or solitary waves) are linearly polarized electrostatic structures that exhibit a bipolar(unipolar) electric field pulse parallel(perpendicular) to $\mathbf{B}_o$ with $\lambda \gtrsim 2\ \pi\ \lambda_{De}$ (Bale, Kellogg, Larson, et al., 1998; C. Cattell et al., 2003, 2005; Breneman et al., 2013; J. R. Franz et al., 2005; Malaspina et al., 2013; Vasko et al., 2018; Wilson III et al., 2007, 2010). They can propagate along the quasi-static magnetic field at fractions of V_{Te} (C. Cattell et al., 2005; J. R. Franz et al., 2005) or obliquely to the field and at much lower speeds (Vasko et al., 2018). These waves can reach amplitudes in excess of >1000 mV/m in space plasmas.
- **IAWs:** Electrostatic ion acoustic waves (or ion sound waves) are linearly polarized (parallel to $\mathbf{B}_o$) electrostatic (i.e., $\mathbf{k}\times\mathbf{B}_o = 0$) waves with $\lambda \gtrsim 2\ \pi\ \lambda_{De}$ (Breneman et al., 2013; Fuselier & Gurnett, 1984; Gurnett, Neubauer, & Schwenn, 1979; Gurnett, Marsch, et al., 1979; Wilson III et al., 2007, 2010). The time series present as symmetric (about zero) electric field oscillations in the form of modulated sine waves with spacecraft frame frequencies near 1 AU satisfying few 100 Hz $\lesssim f_{sc} \lesssim$ 10 kHz. Near collisionless shock waves in space plasmas, these waves can reach amplitudes in excess of >300 mV/m.
- **ECDI:** The electron cyclotron drift instability (D. W. Forslund et al., 1970; D. Forslund et al., 1972) or beam cyclotron instability (Lampe, Manheimer, et al., 1971; Lampe, McBride, et al., 1971) or electrostatic electron-ion streaming instability (Wong, 1970) occurs upstream of collisionless shocks due to the relative drift between incident electrons and shock-reflected ions (D. W. Forslund et al., 1970; Muschietti & Lembège, 2013, 2017). They are observed as electrostatic fluctuations with mixtures of IAW and electron cyclotron harmonics. That is, the power spectrum shows a broad acoustic spectrum expected for IAWs and superposed are integer and/or half-integer harmonics of f_{ce}. The polarizations shown in hodogram plots can look like "tadpoles" or "tear drops." The time series present as asymmetric (about zero) electric field oscillations in both the parallel and perpendicular (with respect to $\mathbf{B}_o$) components (Breneman et al., 2013; Wilson III et al., 2010). These waves can reach amplitudes in excess of >300 mV/m in space plasmas.
- **Langmuir Waves:** Langmuir waves can be both linearly (electrostatic) and elliptically (electromagnetic) polarized and are driven unstable by electron beams (e.g., "bump-on-tail" instability). The time series signature is a modulated sine wave with spacecraft frame frequencies near f_{pe} (Bale et al., 1996, 1997; Bale, Kellogg, Goetz, & Monson, 1998; Kellogg, Monson, et al., 1996; Malaspina & Ergun,

2008; Malaspina et al., 2011). In space plasmas, they are often large amplitude with some in excess of >500 mV/m.

Glossary

AE-Index An index designed to provide a global, quantitative measure of auroral zone magnetic activity produced by enhanced ionospheric currents.

Alpha-particle A doubly-charged ion that is the nucleus of a ^{4}He atom.

Astronomical Unit Roughly the distance between the Earth and sun called 1 AU. Originally it was defined as the average distance between the two bodies but was defined as exactly 149,597,870,700 meters (or ∼149.6 million kilometers or ∼92.96 million miles) in 2012.

Bow Shock Shock wave standing upstream of a obstacle/piston in an incident, supersonic flow. In a plasma, this only occurs upstream of magnetized planetary bodies.

Carrington rotation An approximate time scale over which the photosphere (i.e., optical surface of the Sun) at low latitudes rotates through 2π radians. Richard C. Carrington determined this rate watching sun spots in the 1850s and arrived at a sidereal rotation period of ∼23.38 days (1 day = 86400 seconds). Since sidereal rotation is relative to fixed stars and Earth orbits the sun, a Carrington rotation observed from Earth is ∼27.2753 days.

Collisionless Shock A shock wave where the ramp region, or region of sharpest parameter gradients, spatial scale is orders of magnitude smaller than the mean free Coulomb collisional path. Anecdotally, the mean free path of a thermal proton near Earth is roughly 1 AU while the typical shock ramp thickness only several kilometers to a few tens of kilometers.

Coronal Hole Regions in which the magnetic field lines do not connect back to the solar surface but rather are directed outward into the interplanetary medium.

Coronal Mass Ejection Eruptions of plasma from the solar corona that are some of the largest (energetically) phenomena in the solar system. When moving out though the interplanetary medium, they are called interplanetary coronal mass ejections or ICMEs.

Corotating Interaction Region The compressed plasma region that corotates with the Sun formed along the leading edge of a fast solar wind stream from a coronal hole as it interacts with preceding slower solar wind. Some reseachers require that the CIR is observed at least twice to distinguish it from a "stream interaction region" (SIR). Shock waves can develop along the CIR boundaries, usually beyond 1 AU, mostly due to the expansion speed of the CIR relative to the ambient plasma. This becomes more favorable at larger heliocentric distances.

Cyclotron Frequency The rate at which a charged particle orbits a magnetic field. It is also called the gyrofrequency.

Cyclotron Resonance Condition where an electric field oscillates at the same rate as the particle gyrofrequency in the particle guiding center rest frame resulting in energy gain/loss, depending upon whether the oscillations are damping/growing.

Critical Balance A conjecture of turbulence models in which the linear and nonlinear timescales of the system remain comparable at all scales in the inertial range.

Debye Length The maximum distance any single charged particle's electric field can influence other charged particles in a plasma. This is often referred to in terms of the electrostatic screening or shielding because for scales larger than the Debye length, only wave and convective electric fields tend to persist.

Dispersion Relation The function that defines the relationship between the frequency and wavenumber, i.e., $\omega = \omega\left(\mathbf{k}\right)$.

Dispersive Radiation The process through which an electromagnetic emission is generated due to temporally and spatially varying currents with the fluctuation frequencies having an explicit dependence upon the wavenumber. This phenomena typically occurs in the magnetic ramp of collisionless shocks, which are nonlinearly steepened fast/magnetosonic-whistler waves. Thus, the radiated waves are on the fast/magnetosonic-whistler branch of the dispersion relation.

Dispersive Wave Any fluctuation that has an explicit wavenumber dependence in its frequency, i.e., $\omega = \omega(\mathbf{k})$.

Disruption Scale The spatial scale at which the reconnection timescale becomes faster than the turbulent eddy timescale resulting in a reconnection dominated cascade range.

Dissipation Range The range of scales in a turbulent medium where dissipation dominates over the energy cascade, usually at the smallest scales. Note that this term has become less relevant and been replaced by just kinetic range.

Dust Dust here refers to particles ranging in size from nanometers to several micrometers (microns) originating either with the interplanetary medium (IPD) or from the interstellar medium (ISD).

Eddy Turnover Time Approximate time scale necessary for a fluid vortex, or eddy, to rotate about its axis of symmetry.

Energetic Storm Particles An enhancement in the energetic particle intensity, typically at energies of tens of keV to $\sim$10 MeV, in the vicinity of an interplanetary shock, usually attributed to local particle acceleration by the shock.

Eulerian Decorrelation Time Timescale over which turbulent fluctuations remain correlated in the Eulerian frame of reference.

Foreshock Region upstream of a shock wave in communication with the shock wave through electromagnetic waves and/or backstreaming particles.

Gamma Rays These are photons with energies $>$100 keV. There is no distinct cutoff between gamma rays and x-rays, but they are typically distinguished by their source. X-rays are emitted by electrons and gamma rays from nuclear processes.

Gamma Ray Burst The brightest electromagnetic events known to occur in the universe, occurring transiently from the collapse of massive stars or coalescence of compact objects (e.g., two neutron stars or a neutron star-black hole merger). They consist of an initial flash of gamma-rays lasting from tens of milliseconds to minutes followed by a longer duration "afterglow" at radio and optical wavelengths.

Giant Flare These are of greater apparent intensity than gamma ray bursts and are very rare, averaging once per decade.

Ground Level Enhancement Solar particle events that extend to sufficiently high ($\sim$GeV) energies that they produce secondary particles in the atmosphere that are detected by ground-based neutron monitors.

Gyrophase The angular description of a particle's gyro orbit about the magnetic field.

Gyroradius The orbital distance of a charged particle's motion about a magnetic field. It is also called the Larmor radius.

Halo Orbit A periodic trajectory around a gravitational Lagrange point that consists of a subset of Lissajous orbits where all three components share the same periodicity.

Heliosphere Region of space dominated by the sun's solar wind bounded by its interaction with the interstellar medium.

Heliospheric Current Sheet The surface that separates the two solar magnetic polarities or hemispheres of the heliosphere.

Inertial Length The distance covered by the speed of light in vacuum during one plasma oscillation. This is also called the skin depth.

Inertial Range The range of scales in a turbulent medium in which the inertial forces dominate resulting in the proposed cascade of energy from larger to smaller scales.

Interplanetary Coronal Mass Ejection A structure in the solar wind observed remotely or in situ formed of material associated with a coronal mass ejection.

Interplanetary Magnetic Field The magnetic field permeating the interplanetary medium.

Interplanetary Shock Shock wave propagating in the interplanetary medium are generated by either corotating/stream interaction regions or interplanetary coronal mass ejections.

Kinetic Instability Similar to plasma instability defined below, it is a mechanism through which a plasma converts some free energy source into electromagnetic fluctuations. The difference between kinetic and plasma instabilities is that the former specifically refers to features in the VDFs while the latter also encompasses fluid-like instabilities.

Kinetic Range The range of scales in a turbulent plasma comparable to or smaller than the plasma kinetic scales, e.g. particle gyroradii, inertial lengths, etc.

Lagrange Point Region of space with a local minimum in the gravitational potential caused between at least two large masses (e.g., Earth and sun).

Landau Resonance Condition where a longitudinal electric field oscillates along the same direction as a particle's velocity at such a rate as to allow the particle to gain/lose energy by effectively "surfing" on the electric potential gradients of the oscillating field. The gain/loss depends upon whether the oscillations are damping/growing much like cyclotron resonance.

Lissajous Orbit A quasi-periodic trajectory around a gravitational Lagrange point. Often, two of the three spatial coordinates of the orbit are stable and coupled to each other while the third is periodically independent.

Magnetic Cloud A structure in an interplanetary coronal mass ejection characterized by an enhanced magnetic field that rotates through a large angle, usually interpreted as evidence for a magnetic flux rope, and low plasma beta.

Magnetic Island Region of space wherein all magnetic field lines are closed either in two- or three-dimensions.

Magnetic Reconnection The process of of a change in the topology of a magnetic field through the destruction of magnetic flux and subsequent conversion to particle kinetic energy.

Magnetohydrodynamics The approximation that the plasma can be represented as a single species fluid model which is scale-invariant. It is often abbreviated as MHD.

Magnetosheath Region between the bow shock and magnetosphere where plasma flow is decelerated and deflected around the magnetosphere of the planetary body.

Magnetosphere Region of space surrounding a magnetized planetary body separated/protected from the incident solar wind by the body's magnetic field.

Magnetotail Region of magnetosphere on opposite side of solar wind incident flow, where the field has been stretched due to the asymmetric pressure (i.e., ram pressure) exerted on the planetary body's magnetic field combined with dayside reconnecting field lines being dragged into the nightside region.

Normal Mode The natural or preferred frequency and wavelength of fluctuations/oscillations of a medium/system.

Phase Space The region in which all possible states of a system can be expressed. In plasma physics and/or kinetic theory, this is usually limited to position and momentum coordinates.

Plasma An ionized gas that exhibits a collective behavior similar to a fluid and is governed by long-range interactions/forces.

Plasma Frequency The fastest rate at which a collection of charged particles can oscillate in the absence of an external driving force. The oscillation is typically considered in the absence of a magnetic field because the frequency only depends upon the charged species density and charge state.

Plasma Instability The mechanism through which a plasma converts some free energy source into electromagnetic fluctuations.

Quasi-perpendicular(parallel) Shock Denoting collisionless shock waves with shock normal angles often considered to be $\geq 45°(<45°)$.

Radiation Belts A region of space surrounding magnetized planetary bodies that contains particles that are much more energetic than in the surrounding medium. The particles are trapped and perform three types of orbital motions: gyration about the magnetic field, bouncing between the two magnetic poles, and drifting around the magnetized planetary body. At Earth, these regions are sometimes called the Van Allen radiation belts or Van Allen belts after their discoverer James Van Allen.

Shock Normal Angle The angle between the upstream magnetic field vector and the outward shock normal unit vector.

Shock Wave A stable discontinuity arising from a nonlinearly steepened compressional wave that has reached a balance between steepening and energy dissipation.

Solar Energetic Particles Temporary enhancements of suprathermal ($\gtrsim$10 keV) to relativistic ($\sim$few GeV) particles following energetic solar events (e.g., flares and coronal mass ejections) that last from hours to several days and include protons, electrons and heavy ions.

Soft Gamma Repeater These are strongly magnetized Galactic neutron stars that emit large bursts of X-rays and gamma-rays at irregular intervals.

Solar Exclusion Zone Region of sky about solar disk where solar radio emissions cause sufficient interference with spacecraft communications to prevent telemetry signal locks.

Solar Flare An abrupt and intense enhancement in ultraviolet to gamma ray electromagnetic radiation from a localized region on the sun. On rare occasions for strong flares, the enhanced, localized emission can occur in the visible frequency range too.

Solar Wind A stream of plasma propagating away from the Sun. It is primarily comprised of electrons, protons, and alpha-particles (and heavier ions), is not in thermal or thermodynamic equilibrium, and flows supersonically.

Stream Interaction Region A corotating interaction region (CIR) that need not be observed on two solar rotations. Also used interchangably with CIR.

Structure Function A statistical measure to describe the typical fluctuation amplitudes as a function of scale in a turbulent medium; a conditioned structure function is a structure function constructed from a selected subset of the turbulent fluctuations.

Suprathermal Particles with kinetic energies above the thermal energy of the medium.

Sustained Gamma Ray Emission A continuum at gamma ray frequencies caused by pion-decay due to interaction with >300 MeV protons.

Taylor's Hypothesis The assumption that any variation in a moving flow is propagating at a speed much slower than the bulk flow of the fluid, thus allowing one to convert time series data into spatial scales.

Taylor Microscale A fundamental scale in a turbulent medium characterizing the spatial size of fluctuation gradients.

Thermal Equilibrium Condition where the particle constituents of a medium are in equipartition of energy (i.e., all have the same temperature) but there can be finite heat fluxes present.

Thermodynamic Equilibrium Condition where the particle constituents of a medium are in equipartition of energy (i.e., all have the same temperature) and there are no heat fluxes present.

Transient Ion Foreshock Phenomena These are large-scale ($\sim$1000 to >30,000 km), solitary [$\sim$5–10 per day and transient] structures with durations of tens of seconds to several minutes. They are driven by instabilities caused by the backstreaming particles forming the foreshock.

Trans-iron Elements These are elements on the periodic table at higher proton number than iron, i.e., more than 26 protons.

Turbulence A process in fluids or plasmas characterized by chaotic broadband fluctuations which is modelled by a cascade of energy, usually from large injection scales to small dissipation scales.

Type II Burst A class of solar radio emissions caused by nonthermal electrons accelerated by CME-driven shock waves. They are characterized by their slow frequency drift (i.e., few 100s of kHz per hour) versus time, which is a tracer of the shock speed and the electron number density upstream of the shock.

Type III Burst A class of solar radio emissions caused by nonthermal electrons accelerated during a solar eruption streaming out along the IMF. They are characterized by their fast frequency drift (i.e., MHz per minute) versus time, which is a tracer of the gradient in the interplanetary electron number density.

Type III Storm A class of solar radio emissions caused by nonthermal electrons streaming along local magnetic fields in active regions, but outside of flare or CME eruption sites. They are characterized by broadband (>few MHz), very short duration (i.e., $\lesssim$1–2 minutes) emissions that occur in rapid succession (typically >10 per hour).

Type IV Burst A class of solar radio emissions caused by nonthermal electrons trapped in the post-eruption arcades (i.e., half-loop-like arches of intense magnetic field connecting to active regions on the solar surface) in/around a solar flare or CME eruption site. They are characterized by a broadband frequency emission in the several to >10 MHz range, sometimes showing a U-shaped frequency-time profile.

Velocity Distribution Function A function that defines the probability density of particles in phase space. An example is the Maxwell-Boltzmann velocity distribution function.

X-line The region within a magnetic reconnection site of an intense current sheet where magnetic flux is being destroyed, changing the field topology.

X-rays Photons with energies in the range ∼124 eV to ∼124 keV. These are split into hard and soft ranges, with hard being photons with energies $\gtrsim$5–10 keV.

Acronyms

ACE Advanced Composition Explorer

ADS Astrophysics Data System

AE-Index Auroral Electrojet Index

AIM Aeronomy of Ice in the Mesosphere

APE Alpha-Proton-Electron telescope, part of *Wind* EPACT/ELITE

ARTEMIS Acceleration, Reconnection, Turbulence, and Electrodynamics of the Moon's Interaction with the Sun

AU Astronomical Unit

CAP Command and Attitude Processor

CDAWeb Coordinated Data Analysis Web

CIR Corotating Interaction Region

CME Coronal Mass Ejection

DH Decametric-hectometer

DSCOVR Deep Space Climate Observatory

DTR Digital Tape Recorder

EESA Electron Electrostatic Analyzer, part of *Wind* 3DP

ECDI Electron Cyclotron Drift Instability

ELITE Electron-Isotope Telescope system, part of *Wind* EPACT

EPACT Energetic Particles: Acceleration, Composition, and Transport, the APE-ELITE-IT-LEMT-STEP instrument suite on *Wind* known as EPACT

ESA ElectroStatic Analyzer

ESP Energetic Storm Particle
ESW Electrostatic Solitary Wave
eV electron volt
FC Faraday Cup, e.g., *Wind*/SWE
FOT Flight Operations Team
GCN Gamma-ray Coordinates Network
GeV Giga-electron volt
GF SGR Giant Flare
GGS Global Geospace Science
GLE Ground Level Enhancement
GRB Gamma Ray Burst
GSE Geocentric Solar Ecliptic
GSFC Goddard Space Flight Center
HCS Heliospheric Current Sheet
HK House Keeping, i.e., type of engineering data for spacecraft and instruments
HSO Heliophysics System Observatory
IAW electrostatic Ion Acoustic Wave
ICME Interplanetary Coronal Mass Ejection
ICW Ion Cyclotron Wave
IMF Interplanetary Magnetic Field
INTEGRAL INTErnational Gamma-Ray Astrophysics Laboratory
IP Interplanetary
IPD Interplanetary Dust
IPM Interplanetary Medium
IPN Interplanetary GRB Network
ISD Interstellar Dust
ISTP International Solar-Terrestrial Physics
IT Isotope Telescope, part of *Wind* EPACT/ELITE
keV kilo-electron volt
KONUS Gamma-Ray Spectrometer, i.e., the *Wind* KONUS instrument
LEMT Low Energy Matrix Telescopes, part of *Wind* EPACT
LHW Lower Hybrid Wave
LIGO Laser Interferometer Gravitational-Wave Observatory
MASS high-resolution MASS spectrometer, part of *Wind* SMS
MeV Mega-electron volt
MFI Magnetic Field Investigation, *Wind* MFI
NASA National Aeronautics and Space Administration
PESA Ion (Proton) ESA, part of *Wind* 3DP
PSP *Parker Solar Probe*
SEP Solar Energetic Particle
SGR Soft Gamma Repeater
SGRE Sustained Gamma-ray Emission
SIR Stream Interaction Region
SMS Solar Wind and Suprathermal Ion Composition Experiment, i.e., the SWICS-MASS-STICS instrument suite on *Wind* known as SMS
SOFIE Solar Occultation For Ice Experiment
SPDF Space Physics Data Facility
sps samples per second
SSN Sunspot number
SST Solid-State (semi-conductor detector) Telescope
STEP SupraThermal Energetic Particle Telescope, part of *Wind* EPACT

STICS SupraThermal Ion Composition Spectrometer, part of *Wind* SMS
Strahl (detector) electron strahl sensor in *Wind* SWE instrument suite
SWE Solar Wind Experiment, i.e., the VEIS-Strahl-FC instrument suite on *Wind* known as SWE
SWICS Solar Wind Ion Composition Spectrometer, part of *Wind* SMS
STEREO Solar Terrestrial Relations Observatory
THEMIS Time History of Events and Macroscale Interactions during Substorms
TDS Time Domain Sampler, part of *Wind* WAVES
TGRS Transient Gamma-Ray Spectrometer, i.e., the *Wind* TGRS experiment
TIFP Transient Ion Foreshock Phenomena
TNR Thermal Noise Receiver, part of *Wind* WAVES
TUA Tape Unit A
TUB Tape Unit B
VDF Velocity Distribution Function
VEIS Vector Ion-Electron Spectrometers, part of *Wind* SWE

Acknowledgments

L.B.W. is partially supported by *Wind* MO&DA grants and a Heliophysics Innovation Fund (HIF) grant. A.L.B. is supported by NASA grant 80NSSC20M0189. C.H.K.C. is supported by STFC Ernest Rutherford Fellowship ST/N003748/2 and STFC Consolidated Grant ST/T00018X/1. D.V. is supported by STFC Ernest Rutherford Fellowship ST/P003826/1 and STFC Consolidated Grant ST/S000240/1. I.G.R. is partially supported by NASA grants NNH17ZDA001N-LWS and NNH18ZDA001N-2HSWO2R. N.L. is partially supported by NASA grant 80NSSC19K0831. The authors thank D.L. Turner, M. Henderson, and G. Reeves for useful discussions of the radiation belts. A.L.B. is grateful to Robert Candey for insightful discussions about the OPEN program and the GSFC Laboratory for Extraterrestrial Physics. The authors thank the Harvard Smithsonian Center for Astrophysics and the NASA SPDF/CDAWeb team for the interplanetary shock analysis and the *Wind* plasma and magnetic field data, respectively. The authors thank Carlos A. Perez Alanis for providing Figure 13. The authors thank Andrea Verdini for providing Figure 11. The authors thank Don V. Reames for providing Figure 17. The *Wind* shock database can be found at:
`https://www.cfa.harvard.edu/shocks/wi_data/`.
Analysis software for *Wind* data can be found at:
`https://github.com/lynnbwilsoniii/wind_3dp_pros`, and
`https://github.com/lynnbwilsoniii/Wind_Decom_Code`.
Nearly all *Wind* data is publicly available at:
`https://cdaweb.gsfc.nasa.gov`.
If not directly available through SPDF/CDAWeb, then data can be accessed indirectly from the *Wind* webpage at:
`https://wind.nasa.gov`.

References

Abbott, B. P., Abbott, R., Abbott, T. D., Abraham, S., Acernese, F., Ackley, K., ... others (2019, November). Search for Gravitational-wave Signals Associated with Gamma-Ray Bursts during the Second Observing Run of Advanced LIGO and Advanced Virgo. *Astrophys. J.*, *886*(1), 75. doi: 10.3847/1538-4357/ab4b48

Acuña, M. H., Ogilvie, K. W., Baker, D. N., Curtis, S. A., Fairfield, D. H., & Mish, W. H. (1995, February). The Global Geospace Science Program and Its Investigations. *Space Sci. Rev.*, *71*, 5–21. doi: 10.1007/BF00751323

Adrian, M. L., Viñas, A. F., Moya, P. S., & Wendel, D. E. (2016, December). Solar Wind Magnetic Fluctuations and Electron Non-thermal Temperature Anisotropy: Survey of Wind-SWE-VEIS Observations. *Astrophys. J.*, *833*, 49. doi: 10.3847/1538-4357/833/1/49

Agapitov, O., Mourenas, D., Artemyev, A., Hospodarsky, G., & Bonnell, J. W. (2019, June). Time Scales for Electron Quasi-linear Diffusion by Lower-Band Chorus Waves: The Effects of ω_{pe}/Ω_{ce} Dependence on Geomagnetic Activity. *Geophys. Res. Lett.*, *46*(12), 6178–6187. doi: 10.1029/2019GL083446

Agapitov, O. V., Dudok de Wit, T., Mozer, F. S., Bonnell, J. W., Drake, J. F., Malaspina, D., ... Wygant, J. R. (2020, March). Sunward-propagating Whistler Waves Collocated with Localized Magnetic Field Holes in the Solar Wind: Parker Solar Probe Observations at 35.7 R_s Radii. *Astrophys. J. Lett.*, *891*(1), L20. doi: 10.3847/2041-8213/ab799c

Aguilar-Rodriguez, E., Gopalswamy, N., MacDowall, R., Yashiro, S., & Kaiser, M. I. (2005, September). A Study of the Drift Rate of Type II Radio Bursts at Different Wavelengths. In B. Fleck, T. H. Zurbuchen, & H. Lacoste (Ed.), *Solar wind 11/soho 16, connecting sun and heliosphere* (Vol. 592, p. 393-+).

Al-Haddad, N., Nieves-Chinchilla, T., Savani, N. P., Lugaz, N., & Roussev, I. I. (2018, May). Fitting and Reconstruction of Thirteen Simple Coronal Mass Ejections. *Solar Phys.*, *293*, 73. doi: 10.1007/s11207-018-1288-3

Al-Haddad, N., Nieves-Chinchilla, T., Savani, N. P., Möstl, C., Marubashi, K., Hidalgo, M. A., ... Farrugia, C. J. (2013, May). Magnetic Field Configuration Models and Reconstruction Methods for Interplanetary Coronal Mass Ejections. *Solar Phys.*, *284*, 129–149. doi: 10.1007/s11207-013-0244-5

Ala-Mathi, M., Ruohotie, J., Good, S. W., Kilpua, E. K. J., & Lugaz, N. (2020). Spatial coherence of interplanetary coronal mass ejection sheaths at 1 AU. *J. Geophys. Res.*, *125*. doi: 10.1029/2020JA28002

Allen, R. C., Lario, D., Odstrcil, D., Ho, G. C., Jian, L. K., Cohen, C. M. S., ... Wiedenbeck, M. (2020, February). Solar Wind Streams and Stream Interaction Regions Observed by the Parker Solar Probe with Corresponding Observations at 1 au. *Astrophys. J. Suppl.*, *246*(2), 36. doi: 10.3847/1538-4365/ab578f

Alterman, B. L., & Kasper, J. C. (2019, July). Helium Variation across Two Solar Cycles Reveals a Speed-dependent Phase Lag. *Astrophys. J. Lett.*, *879*(1), L6. doi: 10.3847/2041-8213/ab2391

Alterman, B. L., Kasper, J. C., Stevens, M. L., & Koval, A. (2018, September). A Comparison of Alpha Particle and Proton Beam Differential Flows in Collisionally Young Solar Wind. *Astrophys. J.*, *864*, 112. doi: 10.3847/1538-4357/aad23f

Alves, M. V., Echer, E., & Gonzalez, W. D. (2006, July). Geoeffectiveness of corotating interaction regions as measured by Dst index. *J. Geophys. Res.*, *111*, 7. doi: 10.1029/2005JA011379

Aptekar, R. L., Butterworth, P. S., Cline, T. L., Frederiks, D. D., Golenetskii, S. V., Il'Inskii, V. N., ... Pal'Shin, V. D. (2002). General properties of recurrent bursts from SGRs. *Mem. Soc. Astron. It.*, *73*, 485–490.

Aptekar, R. L., Frederiks, D. D., Golenetskii, S. V., Ilynskii, V. N., Mazets, E. P., Panov, V. N., ... Stilwell, D. E. (1995, February). Konus-W Gamma-Ray Burst Experiment for the GGS Wind Spacecraft. *Space Sci. Rev.*, *71*, 265–272. doi: 10.1007/BF00751332

Bale, S. D., Burgess, D., Kellogg, P. J., Goetz, K., Howard, R. L., & Monson, S. J. (1996). Phase coupling in Langmuir wave packets: Possible evidence of three-wave interactions in the upstream solar wind. *Geophys. Res. Lett.*, *23*, 109–112. doi: 10.1029/95GL03595

Bale, S. D., Burgess, D., Kellogg, P. J., Goetz, K., & Monson, S. J. (1997, June). On the amplitude of intense Langmuir waves in the terrestrial electron foreshock. *J. Geophys. Res.*, *102*, 11281–11286. doi: 10.1029/97JA00938

Bale, S. D., Hull, A., Larson, D. E., Lin, R. P., Muschietti, L., Kellogg, P. J., … Monson, S. J. (2002, August). Electrostatic Turbulence and Debye-Scale Structures Associated with Electron Thermalization at Collisionless Shocks. *Astrophys. J.*, *575*, L25-L28. doi: 10.1086/342609

Bale, S. D., Kasper, J. C., Howes, G. G., Quataert, E., Salem, C., & Sundkvist, D. (2009, November). Magnetic Fluctuation Power Near Proton Temperature Anisotropy Instability Thresholds in the Solar Wind. *Phys. Rev. Lett.*, *103*, 211101-+. doi: 10.1103/PhysRevLett.103.211101

Bale, S. D., Kellogg, P. J., Goetz, K., & Monson, S. J. (1998). Transverse z-mode waves in the terrestrial electron foreshock. *Geophys. Res. Lett.*, *25*, 9–12. doi: 10.1029/97GL03493

Bale, S. D., Kellogg, P. J., Larson, D. E., Lin, R. P., Goetz, K., & Lepping, R. P. (1998). Bipolar electrostatic structures in the shock transition region: Evidence of electron phase space holes. *Geophys. Res. Lett.*, *25*, 2929–2932. doi: 10.1029/98GL02111

Bale, S. D., Pulupa, M., Salem, C., Chen, C. H. K., & Quataert, E. (2013, June). Electron Heat Conduction in the Solar Wind: Transition from Spitzer-Härm to the Collisionless Limit. *Astrophys. J. Lett.*, *769*, L22. doi: 10.1088/2041-8205/769/2/L22

Bale, S. D., Reiner, M. J., Bougeret, J.-L., Kaiser, M. L., Krucker, S., Larson, D. E., & Lin, R. P. (1999, June). The source region of an interplanetary type II radio burst. *Geophys. Res. Lett.*, *26*, 1573–1576. doi: 10.1029/1999GL900293

Barnes, C. W., & Simpson, J. A. (1976, December). Evidence for interplanetary acceleration of nucleons in corotating interaction regions. *Astrophys. J. Lett.*, *210*, L91–L96. doi: 10.1086/182311

Bavassano, B., Pietropaolo, E., & Bruno, R. (1998, April). Cross-helicity and residual energy in solar wind turbulence: Radial evolution and latitudinal dependence in the region from 1 to 5 AU. *J. Geophys. Res.*, *103*(A4), 6521–6530. doi: 10.1029/97JA03029

Berdichevsky, D., Thejappa, G., Fitzenreiter, R. J., Lepping, R. L., Yamamoto, T., Kokubun, S., … Lin, R. P. (1999, January). Widely spaced wave-particle observations during GEOTAIL and wind magnetic conjunctions in the Eearth's ion foreshock with near-radial interplanetary magnetic field. *J. Geophys. Res.*, *104*(1), 463–482. doi: 10.1029/1998JA900018

Boldyrev, S. (2006, March). Spectrum of Magnetohydrodynamic Turbulence. *Phys. Rev. Lett.*, *96*(11), 115002. doi: 10.1103/PhysRevLett.96.115002

Boldyrev, S., Chen, C. H. K., Xia, Q., & Zhdankin, V. (2015, June). Spectral Breaks of Alfvénic Turbulence in a Collisionless Plasma. *Astrophys. J.*, *806*, 238. doi: 10.1088/0004-637X/806/2/238

Boldyrev, S., & Perez, J. C. (2012, October). Spectrum of Kinetic-Alfvén Turbulence. *Astrophys. J. Lett.*, *758*(2), L44. doi: 10.1088/2041-8205/758/2/L44

Boldyrev, S., Perez, J. C., Borovsky, J. E., & Podesta, J. J. (2011, November). Spectral Scaling Laws in Magnetohydrodynamic Turbulence Simulations and in the Solar Wind. *Astrophys. J. Lett.*, *741*, L19. doi: 10.1088/2041-8205/741/1/L19

Borovsky, J. E. (2008, August). Flux tube texture of the solar wind: Strands of the magnetic carpet at 1 AU? *J. Geophys. Res.*, *113*(A8), A08110. doi: 10.1029/2007JA012684

Borovsky, J. E., & Denton, M. H. (2009, February). Relativistic-electron dropouts and recovery: A superposed epoch study of the magnetosphere and the solar wind. *J. Geophys. Res.*, *114*, 2201. doi: 10.1029/2008JA013128

Bosqued, J. M., Lormant, N., Rème, H., d'Uston, C., Lin, R. P., Anderson, K. A., … Wenzel, K.-P. (1996). Moon-solar wind interaction: First results from the WIND/3DP experiment. *Geophys. Res. Lett.*, *23*, 1259–1262. doi: 10.1029/96GL00303

Bothmer, V., & Schwenn, R. (1996, January). Signatures of fast CMEs in interplanetary space. *Adv. Space Res.*, *17*(4-5), 319–322. doi: 10.1016/0273-1177(95)00593-4

Bougeret, J. L., Fainberg, J., & Stone, R. G. (1984, July). Interplanetary radio storms. I - Extension of solar active regions through the interplanetary medium. *Astron. & Astrophys.*, *136*(2), 255–262.

Bougeret, J.-L., Kaiser, M. L., Kellogg, P. J., Manning, R., Goetz, K., Monson, S. J., ... Hoang, S. (1995, February). Waves: The Radio and Plasma Wave Investigation on the Wind Spacecraft. *Space Sci. Rev.*, *71*, 231–263. doi: 10.1007/BF00751331

Bougeret, J.-L., Zarka, P., Caroubalos, C., Karlický, M., Leblanc, Y., Maroulis, D., ... Perche, C. (1998). A shock associated (SA) radio event and related phenomena observed from the base of the solar corona to 1 AU. *Geophys. Res. Lett.*, *25*, 2513–2516. doi: 10.1029/98GL50563

Bourouaine, S., Verscharen, D., Chandran, B. D. G., Maruca, B. A., & Kasper, J. C. (2013, November). Limits on Alpha Particle Temperature Anisotropy and Differential Flow from Kinetic Instabilities: Solar Wind Observations. *Astrophys. J. Lett.*, *777*, L3. doi: 10.1088/2041-8205/777/1/L3

Bowen, T. A., Badman, S., Hellinger, P., & Bale, S. D. (2018, February). Density Fluctuations in the Solar Wind Driven by Alfvén Wave Parametric Decay. *Astrophys. J. Lett.*, *854*, L33. doi: 10.3847/2041-8213/aaabbe

Breneman, A. W., Cattell, C. A., Kersten, K., Paradise, A., Schreiner, S., Kellogg, P. J., ... Wilson, L. B. (2013, December). STEREO and Wind observations of intense cyclotron harmonic waves at the Earth's bow shock and inside the magnetosheath. *J. Geophys. Res.*, *118*, 7654–7664. doi: 10.1002/2013JA019372

Broiles, T. W., Desai, M. I., & McComas, D. J. (2012, March). Formation, shape, and evolution of magnetic structures in CIRs at 1 AU. *J. Geophys. Res.*, *117*, 3102. doi: 10.1029/2011JA017288

Bruno, R., & Carbone, V. (2013, May). The Solar Wind as a Turbulence Laboratory. *Living Rev. Solar Phys.*, *10*, 2. doi: 10.12942/lrsp-2013-2

Bruno, R., D'Amicis, R., Bavassano, B., Carbone, V., & Sorriso-Valvo, L. (2007, August). Magnetically dominated structures as an important component of the solar wind turbulence. *Ann. Geophys.*, *25*, 1913–1927. doi: 10.5194/angeo-25-1913-2007

Bruno, R., Telloni, D., Sorriso-Valvo, L., Marino, R., De Marco, R., & D'Amicis, R. (2019, July). The low-frequency break observed in the slow solar wind magnetic spectra. *Astron. & Astrophys.*, *627*, A96. doi: 10.1051/0004-6361/201935841

Bruno, R., & Trenchi, L. (2014, June). Radial Dependence of the Frequency Break between Fluid and Kinetic Scales in the Solar Wind Fluctuations. *Astrophys. J. Lett.*, *787*(2), L24. doi: 10.1088/2041-8205/787/2/L24

Burlaga, L., Fitzenreiter, R., Lepping, R., Ogilvie, K., Szabo, A., Lazarus, A., ... Larson, D. E. (1998, January). A magnetic cloud containing prominence material - January 1997. *J. Geophys. Res.*, *103*, 277-+. doi: 10.1029/97JA02768

Burlaga, L., Sittler, E., Mariani, F., & Schwenn, R. (1981, August). Magnetic loop behind an interplanetary shock: Voyager, Helios, and IMP 8 observations. *J. Geophys. Res.*, *86*(8), 6673–6684. doi: 10.1029/JA086iA08p06673

Burlaga, L. F. (1988, July). Magnetic clouds and force-free fields with constant alpha. *J. Geophys. Res.*, *93*(7), 7217–7224. doi: 10.1029/JA093iA07p07217

Burlaga, L. F., Plunkett, S. P., & St. Cyr, O. C. (2002, October). Successive CMEs and complex ejecta. *J. Geophys. Res.*, *107*(A10), 1266. doi: 10.1029/2001JA000255

Cairns, I. H., Lobzin, V. V., Donea, A., Tingay, S. J., McCauley, P. I., Oberoi, D., ... Williams, C. L. (2018, January). Low Altitude Solar Magnetic Reconnection, Type III Solar Radio Bursts, and X-ray Emissions. *Sci. Rep.*, *8*, 1676. doi: 10.1038/s41598-018-19195-3

Cane, H. V. (2003, December). Near-Relativistic Solar Electrons and Type III Radio Bursts. *Astrophys. J.*, *598*, 1403–1408. doi: 10.1086/379007

Cane, H. V., & Erickson, W. C. (2003, May). Energetic particle propagation in the inner heliosphere as deduced from low-frequency (¡100 kHz) observations of type III radio bursts. *J. Geophys. Res.*, *108*(A5), 1203. doi: 10.1029/2002JA009488

Cane, H. V., Erickson, W. C., & Prestage, N. P. (2002, October). Solar flares, type III radio bursts, coronal mass ejections, and energetic particles. *J. Geophys. Res.*, *107*(A10), 1315. doi: 10.1029/2001JA000320

Cane, H. V., Stone, R. G., Fainberg, J., Stewart, R. T., Steinberg, J. L., & Hoang, S. (1981, December). Radio evidence for shock acceleration of electrons in the solar corona. *Geophys. Res. Lett.*, *8*(12), 1285–1288. doi: 10.1029/GL008i012p01285

Caprioli, D., & Spitkovsky, A. (2014, March). Simulations of Ion Acceleration at Non-relativistic Shocks. I. Acceleration Efficiency. *Astrophys. J.*, *783*, 91. doi: 10.1088/0004-637X/783/2/91

Cattell, C., Dombeck, J., Wygant, J., Drake, J. F., Swisdak, M., Goldstein, M. L., ... Balogh, A. (2005, January). Cluster observations of electron holes in association with magnetotail reconnection and comparison to simulations. *J. Geophys. Res.*, *110*, 1211. doi: 10.1029/2004JA010519

Cattell, C., Neiman, C., Dombeck, J., Crumley, J., Wygant, J., Kletzing, C. A., ... André, M. (2003). Large amplitude solitary waves in and near the Earth's magnetosphere, magnetopause and bow shock: Polar and Cluster observations. *Nonlin. Proc. Geophys.*, *10*, 13–26.

Cattell, C., Wygant, J. R., Goetz, K., Kersten, K., Kellogg, P. J., von Rosenvinge, T., ... Russell, C. T. (2008, January). Discovery of very large amplitude whistler-mode waves in Earth's radiation belts. *Geophys. Res. Lett.*, *35*, 1105. doi: 10.1029/2007GL032009

Cattell, C. A., Breneman, A., Goetz, K., Kellogg, P. J., Kersten, K., Wygant, J. R., ... Roth, I. (2012, December). Large-Amplitude Whistler Waves and Electron Acceleration in the Earth's Radiation Belts: A Review of STEREO and Wind Observations. In D. Summers, I. R. Mann, D. N. Baker, & M. Schulz (Eds.), *Dynamics of the Earth's Radiation Belts and Inner Magnetosphere* (Vol. 199, pp. 41–51). Washington, D.C.: American Geophysical Union. doi: 10.1029/2012GM001322

Chen, C. H. K. (2016, December). Recent progress in astrophysical plasma turbulence from solar wind observations. *J. Plasma Phys.*, *82*(6), 535820602. doi: 10.1017/S0022377816001124

Chen, C. H. K., Bale, S. D., Salem, C. S., & Maruca, B. A. (2013, June). Residual Energy Spectrum of Solar Wind Turbulence. *Astrophys. J.*, *770*, 125. doi: 10.1088/0004-637X/770/2/125

Chen, C. H. K., Leung, L., Boldyrev, S., Maruca, B. A., & Bale, S. D. (2014, November). Ion-scale spectral break of solar wind turbulence at high and low beta. *Geophys. Res. Lett.*, *41*, 8081–8088. doi: 10.1002/2014GL062009

Chen, C. H. K., Mallet, A., Schekochihin, A. A., Horbury, T. S., Wicks, R. T., & Bale, S. D. (2012, October). Three-dimensional Structure of Solar Wind Turbulence. *Astrophys. J.*, *758*(2), 120. doi: 10.1088/0004-637X/758/2/120

Chen, C. H. K., Matteini, L., Schekochihin, A. A., Stevens, M. L., Salem, C. S., Maruca, B. A., ... Bale, S. D. (2016, July). Multi-species Measurements of the Firehose and Mirror Instability Thresholds in the Solar Wind. *Astrophys. J. Lett.*, *825*, L26. doi: 10.3847/2041-8205/825/2/L26

Chen, J. H., Schwadron, N. A., Möbius, E., & Gorby, M. (2015, November). Modeling interstellar pickup ion distributions in corotating interaction regions inside

1 AU. *J. Geophys. Res.*, *120*(11), 9269–9280. doi: 10.1002/2014JA020939
Chotoo, K., Schwadron, N. A., Mason, G. M., Zurbuchen, T. H., Gloeckler, G., Posner, A., ... Collier, M. R. (2000, October). The suprathermal seed population for corotating interaction region ions at 1 AU deduced from composition and spectra of H^+, He^{++}, and He^+ observed on Wind. *J. Geophys. Res.*, *105*, 23107–23122. doi: 10.1029/1998JA000015
Clack, D., Kasper, J. C., Lazarus, A. J., Steinberg, J. T., & Farrell, W. M. (2004, March). Wind observations of extreme ion temperature anisotropies in the lunar wake. *Geophys. Res. Lett.*, *310*, L06812. doi: 10.1029/2003GL018298
Cline, T. L., Hurley, K. C., Barthelmy, S., Butterworth, P., Feroci, M., Frontera, F., ... Trombka, J. (2001). The IPN I: From the Past to the Future. In E. Costa, F. Frontera, & J. Hjorth (Ed.), *Gamma-ray bursts in the afterglow era* (p. 375-+). doi: 10.1007/10853853_102
Cliver, E. W., Kahler, S. W., Kazachenko, M., & Shimojo, M. (2019, May). The Disappearing Solar Filament of 2013 September 29 and Its Large Associated Proton Event: Implications for Particle Acceleration at the Sun. *Astrophys. J.*, *877*(1), 11. doi: 10.3847/1538-4357/ab0e03
Cliver, E. W., Nitta, N. V., Thompson, B. J., & Zhang, J. (2004, November). Coronal Shocks of November 1997 Revisited: The Cme Type II Timing Problem. *Solar Phys.*, *225*, 105–139. doi: 10.1007/s11207-004-3258-1
Cohen, C. M. S. (2006, October). Observations of Energetic Storm Particles: An Overview. *Washington DC American Geophysical Union Geophysical Monograph Series*, *165*, 275–282. doi: 10.1029/165GM26
Corona-Romero, P., Gonzalez-Esparza, J. A., & Aguilar-Rodriguez, E. (2013, July). Propagation of Fast Coronal Mass Ejections and Shock Waves Associated with Type II Radio-Burst Emission: An Analytic Study. *Solar Phys.*, *285*, 391–410. doi: 10.1007/s11207-012-0103-9
Cremades, H., Iglesias, F. A., St. Cyr, O. C., Xie, H., Kaiser, M. L., & Gopalswamy, N. (2015, September). Low-Frequency Type-II Radio Detections and Coronagraph Data Employed to Describe and Forecast the Propagation of 71 CMEs/Shocks. *Solar Phys.*, *290*, 2455–2478. doi: 10.1007/s11207-015-0776-y
Dasso, S., Nakwacki, M. S., Démoulin, P., & Mandrini, C. H. (2007, August). Progressive Transformation of a Flux Rope to an ICME. Comparative Analysis Using the Direct and Fitted Expansion Methods. *Solar Phys.*, *244*, 115–137. doi: 10.1007/s11207-007-9034-2
Davidson, R. C., & Gladd, N. T. (1975, October). Anomalous transport properties associated with the lower-hybrid-drift instability. *Phys. Fluids*, *18*, 1327–1335. doi: 10.1063/1.861021
de Nolfo, G. A., Bruno, A., Ryan, J. M., Dalla, S., Giacalone, J., Richardson, I. G., ... Munini, R. (2019, July). Comparing Long-duration Gamma-Ray Flares and High-energy Solar Energetic Particles. *Astrophys. J.*, *879*(2), 90. doi: 10.3847/1538-4357/ab258f
Del Zanna, G., Aulanier, G., Klein, K. L., & Török, T. (2011, February). A single picture for solar coronal outflows and radio noise storms. *Astron. & Astrophys.*, *526*, A137. doi: 10.1051/0004-6361/201015231
Démoulin, P., Dasso, S., & Janvier, M. (2013, February). Does spacecraft trajectory strongly affect detection of magnetic clouds? *Astron. & Astrophys.*, *550*, A3. doi: 10.1051/0004-6361/201220535
Démoulin, P., Dasso, S., Janvier, M., & Lanabere, V. (2019, December). Re-analysis of Lepping's Fitting Method for Magnetic Clouds: Lundquist Fit Reloaded. *Solar Phys.*, *294*(12), 172. doi: 10.1007/s11207-019-1564-x
Démoulin, P., Janvier, M., & Dasso, S. (2016, February). Magnetic Flux and Helicity of Magnetic Clouds. *Solar Phys.*, *291*, 531–557. doi: 10.1007/s11207-015-0836-3
Desai, M. I., Mason, G. M., Müller-Mellin, R., Korth, A., Mall, U., Dwyer, J. R.,

& von Rosenvinge, T. T. (2008, August). The spatial distribution of upstream ion events from the Earth's bow shock measured by ACE, Wind, and STEREO. *J. Geophys. Res.*, *113*(8), A08103. doi: 10.1029/2007JA012909

Domingo, V., Fleck, B., & Poland, A. I. (1995, December). The SOHO Mission: an Overview. *Solar Phys.*, *162*(1-2), 1–37. doi: 10.1007/BF00733425

Drake, J. F., Cassak, P. A., Shay, M. A., Swisdak, M., & Quataert, E. (2009, July). A Magnetic Reconnection Mechanism for Ion Acceleration and Abundance Enhancements in Impulsive Flares. *Astrophys. J. Lett.*, *700*, L16–L20. doi: 10.1088/0004-637X/700/1/L16

Drake, J. F., & Swisdak, M. (2012, November). Ion Heating and Acceleration During Magnetic Reconnection Relevant to the Corona. *Space Sci. Rev.*, *172*(1-4), 227–240. doi: 10.1007/s11214-012-9903-3

Drake, J. F., Swisdak, M., Che, H., & Shay, M. A. (2006, October). Electron acceleration from contracting magnetic islands during reconnection. *Nature*, *443*, 553–556. doi: 10.1038/nature05116

Eastwood, J. P., Lucek, E. A., Mazelle, C., Meziane, K., Narita, Y., Pickett, J., & Treumann, R. A. (2005, June). The Foreshock. *Space Sci. Rev.*, *118*, 41–94. doi: 10.1007/s11214-005-3824-3

Ebert, R. W., Desai, M. I., Dayeh, M. A., & Mason, G. M. (2012, August). Helium Ion Anisotropies in Corotating Interaction Regions at 1 AU. *Astrophys. J. Lett.*, *754*, L30. doi: 10.1088/2041-8205/754/2/L30

Ergun, R. E., Larson, D., Lin, R. P., McFadden, J. P., Carlson, C. W., Anderson, K. A., ... Bougeret, J.-L. (1998, August). Wind Spacecraft Observations of Solar Impulsive Electron Events Associated with Solar Type III Radio Bursts. *Astrophys. J.*, *503*, 435-+. doi: 10.1086/305954

Escoubet, C. P., Schmidt, R., & Goldstein, M. L. (1997, January). Cluster - Science and Mission Overview. *Space Sci. Rev.*, *79*, 11–32. doi: 10.1023/A:1004923124586

Fainberg, J., & Stone, R. G. (1970, November). Type III Solar Radio Burst Storms Observed at Low Frequencies. *Solar Phys.*, *15*(1), 222–233. doi: 10.1007/BF00149487

Farrell, W. M., Fitzenreiter, R. J., Owen, C. J., Byrnes, J. B., Lepping, R. P., Ogilvie, K. W., & Neubauer, F. (1996). Upstream ULF waves and energetic electrons associated with the lunar wake: Detection of precursor activity. *Geophys. Res. Lett.*, *23*, 1271–1274. doi: 10.1029/96GL01355

Farrell, W. M., Kaiser, M. L., & Steinberg, J. T. (1997, May). Electrostatic instability in the central lunar wake: A process for replenishing the plasma void? *Geophys. Res. Lett.*, *24*, 1135–1138. doi: 10.1029/97GL00878

Farrell, W. M., Kaiser, M. L., Steinberg, J. T., & Bale, S. D. (1998, October). A simple simulation of a plasma void: Applications to Wind observations of the lunar wake. *J. Geophys. Res.*, *1032*, 23653–23660. doi: 10.1029/97JA03717

Farrugia, C. J., Berdichevsky, D. B., Möstl, C., Galvin, A. B., Leitner, M., Popecki, M. A., ... Sauvaud, J. A. (2011, June). Multiple, distant (40°) in situ observations of a magnetic cloud and a corotating interaction region complex. *J. Atmos. Solar-Terr. Phys.*, *73*, 1254–1269. doi: 10.1016/j.jastp.2010.09.011

Farrugia, C. J., Burlaga, L. F., Osherovich, V. A., Richardson, I. G., Freeman, M. P., Lepping, R. P., & Lazarus, A. J. (1993, May). A study of an expanding interplanetary magnetic cloud and its interaction with the Earth's magnetosphere: The interplanetary aspect. *J. Geophys. Res.*, *98*(A5), 7621–7632. doi: 10.1029/92JA02349

Farrugia, C. J., Matsui, H., Kucharek, H., Torbert, R. B., Smith, C. W., Jordanova, V. K., ... Skoug, R. (2005, September). Interplanetary coronal mass ejection and ambient interplanetary magnetic field correlations during the Sun-Earth connection events of October-November 2003. *J. Geophys. Res.*, *110*, A09S13. doi: 10.1029/2004JA010968

Farrugia, C. J., Sandholt, P. E., Moen, J., & Arnoldy, R. L. (1998). Unusual features of the January 1997 magnetic cloud and their effect on optical dayside auroral signatures. *Geophys. Res. Lett.*, *25*, 3051–3054. doi: 10.1029/98GL01226

Filwett, R. J., Desai, M. I., Dayeh, M. A., & Broiles, T. W. (2017, March). Source Population and Acceleration Location of Suprathermal Heavy Ions in Corotating Interaction Regions. *Astrophys. J.*, *838*, 23. doi: 10.3847/1538-4357/aa5ca9

Fishman, G. J. (1995, December). Gamma-Ray Bursts: an Overview. *Publ. Astron. Soc. Pacific*, *107*, 1145-+. doi: 10.1086/133672

Fishman, G. J., & Meegan, C. A. (1995). Gamma-Ray Bursts. *Ann. Rev. Astron. Astrophys.*, *33*, 415–458. doi: 10.1146/annurev.aa.33.090195.002215

Fisk, L. A., & Lee, M. A. (1980, April). Shock acceleration of energetic particles in corotating interaction regions in the solar wind. *Astrophys. J.*, *237*, 620–626. doi: 10.1086/157907

Fitzenreiter, R. J., Ogilvie, K. W., Bale, S. D., & Viñas, A. F. (2003, December). Modification of the solar wind electron velocity distribution at interplanetary shocks. *J. Geophys. Res.*, *108*, 1415. doi: 10.1029/2003JA009865

Forslund, D., Morse, R., Nielson, C., & Fu, J. (1972, July). Electron Cyclotron Drift Instability and Turbulence. *Phys. Fluids*, *15*, 1303–1318. doi: 10.1063/1.1694082

Forslund, D. W., Morse, R. L., & Nielson, C. W. (1970, November). Electron Cyclotron Drift Instability. *Phys. Rev. Lett.*, *25*, 1266–1270. doi: 10.1103/PhysRevLett.25.1266

Forsyth, R. J., & Marsch, E. (1999, July). Solar Origin and Interplanetary Evolution of Stream Interfaces. *Space Sci. Rev.*, *89*, 7–20. doi: 10.1023/A:1005235626013

Franz, H., Sharer, P., Ogilvie, K., & Desch, M. (1998). Wind nominal mission performance and extended mission design. In *Aiaa/aas astrodynamics specialist conference and exhibit.* Retrieved from `https://arc.aiaa.org/doi/abs/10.2514/6.1998-4467` doi: 10.2514/6.1998-4467

Franz, J. R., Kintner, P. M., Pickett, J. S., & Chen, L.-J. (2005, September). Properties of small-amplitude electron phase-space holes observed by Polar. *J. Geophys. Res.*, *110*, 9212. doi: 10.1029/2005JA011095

Fränz, M., & Harper, D. (2002, February). Heliospheric coordinate systems. *Planet. Space Sci.*, *50*(2), 217–233. doi: 10.1016/S0032-0633(01)00119-2

Frederiks, D., Svinkin, D., Tsvetkova, A., Aptekar, R., Golenetskii, S., Kozlova, A., … Ulanov, M. (2019, February). GRB observations with Konus-WIND experiment. *Mem. Soc. Astron. Ital.*, *90*(1–2), 67–70. Retrieved from `http://sait.oat.ts.astro.it/MSAIt9001-0219/`

Frederiks, D. D., Golenetskii, S. V., Palshin, V. D., Aptekar, R. L., Ilyinskii, V. N., Oleinik, F. P., … Cline, T. L. (2007, January). Giant flare in SGR 1806-20 and its Compton reflection from the Moon. *Astron. Lett.*, *33*, 1–18. doi: 10.1134/S106377370701001X

Fuselier, S. A., & Gurnett, D. A. (1984, January). Short wavelength ion waves upstream of the earth's bow shock. *J. Geophys. Res.*, *89*, 91–103. doi: 10.1029/JA089iA01p00091

Gary, S. P., Gosling, J. T., & Forslund, D. W. (1981, August). The electromagnetic ion beam instability upstream of the earth's bow shock. *J. Geophys. Res.*, *86*, 6691–6696. doi: 10.1029/JA086iA08p06691

Gary, S. P., Jian, L. K., Broiles, T. W., Stevens, M. L., Podesta, J. J., & Kasper, J. C. (2016, January). Ion-driven instabilities in the solar wind: Wind observations of 19 March 2005. *J. Geophys. Res.*, *121*, 30–41. doi: 10.1002/2015JA021935

Gary, S. P., & Karimabadi, H. (2006, November). Linear theory of electron temperature anisotropy instabilities: Whistler, mirror, and Weibel. *J. Geophys. Res.*, *111*, 11224. doi: 10.1029/2006JA011764

Gary, S. P., Li, H., O'Rourke, S., & Winske, D. (1998, July). Proton resonant firehose instability: Temperature anisotropy and fluctuating field constraints. *J. Geophys. Res.*, *103*, 14567–14574. doi: 10.1029/98JA01174

Gary, S. P., Montgomery, M. D., Feldman, W. C., & Forslund, D. W. (1976, March). Proton temperature anisotropy instabilities in the solar wind. *J. Geophys. Res.*, *81*, 1241–1246. doi: 10.1029/JA081i007p01241

Gary, S. P., & Nishimura, K. (2003, September). Resonant electron firehose instability: Particle-in-cell simulations. *Phys. Plasmas*, *10*, 3571–3576. doi: 10.1063/1.1590982

Gary, S. P., Scime, E. E., Phillips, J. L., & Feldman, W. C. (1994, December). The whistler heat flux instability: Threshold conditions in the solar wind. *J. Geophys. Res.*, *99*(12), 23391–23399. doi: 10.1029/94JA02067

Gloeckler, G., Balsiger, H., Bürgi, A., Bochsler, P., Fisk, L. A., Galvin, A. B., ... Wilken, B. (1995, February). The Solar Wind and Suprathermal Ion Composition Investigation on the Wind Spacecraft. *Space Sci. Rev.*, *71*, 79–124. doi: 10.1007/BF00751327

Goldreich, P., & Sridhar, S. (1995, January). Toward a Theory of Interstellar Turbulence. II. Strong Alfvenic Turbulence. *Astrophys. J.*, *438*, 763. doi: 10.1086/175121

Good, S. W., Kilpua, E. K. J., LaMoury, A. T., Forsyth, R. J., Eastwood, J. P., & Möstl, C. (2019, July). Self-Similarity of ICME Flux Ropes: Observations by Radially Aligned Spacecraft in the Inner Heliosphere. *J. Geophys. Res.*, *124*(7), 4960–4982. doi: 10.1029/2019JA026475

Gopalswamy, N. (2004a, September). Interplanetary Radio Bursts. In D. E. Gary & C. U. Keller (Ed.), *Astrophysics and space science library* (Vol. 314, p. 305-+). doi: 10.1007/1-4020-2814-8_15

Gopalswamy, N. (2004b, December). Recent advances in the long-wavelength radio physics of the Sun. *Planet. Space Sci.*, *52*, 1399–1413. doi: 10.1016/j.pss.2004.09.016

Gopalswamy, N. (2006, June). Properties of Interplanetary Coronal Mass Ejections. *Space Sci. Rev.*, *124*(1-4), 145–168. doi: 10.1007/s11214-006-9102-1

Gopalswamy, N. (2011, January). Coronal Mass Ejections and Solar Radio Emissions. In H. O. Rucker, W. S. Kurth, P. Louarn, & G. Fischer (Eds.), *Planetary, solar and heliospheric radio emissions (pre vii)* (pp. 325–342).

Gopalswamy, N. (2016, May). Low-Frequency Radio Bursts and Space Weather. *arXiv e-prints*, arXiv:1605.02218.

Gopalswamy, N., Aguilar-Rodriguez, E., Yashiro, S., Nunes, S., Kaiser, M. L., & Howard, R. A. (2005, October). Type II radio bursts and energetic solar eruptions. *J. Geophys. Res.*, *110*, A12S07. doi: 10.1029/2005JA011158

Gopalswamy, N., Akiyama, S., Mäkelä, P., Yashiro, S., & Cairns, I. H. (2016, May). On the Directivity of Low-Frequency Type IV Radio Bursts. *arXiv e-prints*, arXiv:1605.02223.

Gopalswamy, N., Akiyama, S., Yashiro, S., Michalek, G., Xie, H., & Mäkelä, P. (2020, July). Effect of the Weakened Heliosphere in Solar Cycle 24 on the Properties of Coronal Mass Ejections. *arXiv e-prints*, arXiv:2007.08291.

Gopalswamy, N., Hanaoka, Y., Kosugi, T., Lepping, R. P., Steinberg, J. T., Plunkett, S., ... Hudson, H. S. (1998). On the relationship between coronal mass ejections and magnetic clouds. *Geophys. Res. Lett.*, *25*, 2485–2488. doi: 10.1029/98GL50757

Gopalswamy, N., Kaiser, M. L., Lepping, R. P., Kahler, S. W., Ogilvie, K., Berdichevsky, D., ... Akioka, M. (1998, January). Origin of coronal and interplanetary shocks - A new look with WIND spacecraft data. *J. Geophys. Res.*, *103*, 307-+. doi: 10.1029/97JA02634

Gopalswamy, N., Kaiser, M. L., Thompson, B. J., Burlaga, L. F., Szabo, A., Vourlidas, A., ... Bougeret, J.-L. (2000, May). Radio-rich Solar Eruptive Events. *Geophys. Res. Lett.*, *27*, 1427-+. doi: 10.1029/1999GL003665

Gopalswamy, N., & Mäkelä, P. (2010, September). Long-duration Low-frequency Type III Bursts and Solar Energetic Particle Events. *Astrophys. J.*, *721*, L62-L66. doi: 10.1088/2041-8205/721/1/L62

Gopalswamy, N., & Mäkelä, P. (2011). Low-frequency type III radio bursts and solar energetic particle events. *Central European Astrophys. Bull.*, *35*, 71–82.

Gopalswamy, N., Mäkelä, P., Akiyama, S., Yashiro, S., Xie, H., & Thakur, N. (2018, November). Sun-to-earth propagation of the 2015 June 21 coronal mass ejection revealed by optical, EUV, and radio observations. *J. Atmos. Solar-Terr. Phys.*, *179*, 225–238. doi: 10.1016/j.jastp.2018.07.013

Gopalswamy, N., Mäkelä, P., Akiyama, S., Yashiro, S., Xie, H., Thakur, N., & Kahler, S. W. (2015, June). Large Solar Energetic Particle Events Associated with Filament Eruptions Outside of Active Regions. *Astrophys. J.*, *806*, 8. doi: 10.1088/0004-637X/806/1/8

Gopalswamy, N., Mäkelä, P., & Yashiro, S. (2019, January). A Catalog of Type II radio bursts observed by Wind/WAVES and their Statistical Properties. *Sun and Geosphere*, *14*, 111–121. doi: 10.31401/SunGeo.2019.02.03

Gopalswamy, N., Mäkelä, P., Yashiro, S., Lara, A., Akiyama, S., & Xie, H. (2019, November). On the Shock Source of Sustained Gamma-Ray Emission from the Sun. In *J. phys. conf. ser.* (Vol. 1332, p. 012004). doi: 10.1088/1742-6596/1332/1/012004

Gopalswamy, N., Mäkelä, P., Yashiro, S., Lara, A., Xie, H., Akiyama, S., & MacDowall, R. J. (2018, December). Interplanetary Type II Radio Bursts from Wind/WAVES and Sustained Gamma-Ray Emission from Fermi/LAT: Evidence for Shock Source. *Astrophys. J. Lett.*, *868*, L19. doi: 10.3847/2041-8213/aaef36

Gopalswamy, N., Mäkelä, P., Yashiro, S., Thakur, N., Akiyama, S., & Xie, H. (2017, September). A Hierarchical Relationship between the Fluence Spectra and CME Kinematics in Large Solar Energetic Particle Events: A Radio Perspective. In *Journal of physics conference series* (Vol. 900, p. 012009). doi: 10.1088/1742-6596/900/1/012009

Gopalswamy, N., Xie, H., Yashiro, S., Akiyama, S., Mäkelä, P., & Usoskin, I. G. (2012, October). Properties of Ground Level Enhancement Events and the Associated Solar Eruptions During Solar Cycle 23. *Space Sci. Rev.*, *171*, 23–60. doi: 10.1007/s11214-012-9890-4

Gopalswamy, N., Yashiro, S., Kaiser, M. L., Howard, R. A., & Bougeret, J. L. (2001, December). Characteristics of coronal mass ejections associated with long-wavelength type II radio bursts. *J. Geophys. Res.*, *106*(A12), 29219–29230. doi: 10.1029/2001JA000234

Gopalswamy, N., Yashiro, S., Thakur, N., Mäkelä, P., Xie, H., & Akiyama, S. (2016, December). The 2012 July 23 Backside Eruption: An Extreme Energetic Particle Event? *Astrophys. J.*, *833*, 216. doi: 10.3847/1538-4357/833/2/216

Gopalswamy, N., Yashiro, S., Xie, H., Akiyama, S., & Mäkelä, P. (2015, November). Properties and geoeffectiveness of magnetic clouds during solar cycles 23 and 24. *J. Geophys. Res.*, *120*, 9221–9245. doi: 10.1002/2015JA021446

Gordley, L. L., Hervig, M. E., Fish, C., Russell, I., James M., Bailey, S., Cook, J., ... Kemp, J. (2009, March). The solar occultation for ice experiment. *J. Atmos. Solar-Terr. Phys.*, *71*(3-4), 300–315. doi: 10.1016/j.jastp.2008.07.012

Gosling, J. T. (2007, December). Observations of Magnetic Reconnection in the Turbulent High-Speed Solar Wind. *Astrophys. J.*, *671*, L73-L76. doi: 10.1086/524842

Gosling, J. T. (2010, March). Magnetic Reconnection in the Solar Wind: An Update. *Twelfth International Solar Wind Conference*, *1216*, 188–193. doi: 10

.1063/1.3395833
Gosling, J. T. (2011, February). Magnetic Reconnection in the Solar Wind. *Space Sci. Rev.*, 104. doi: 10.1007/s11214-011-9747-2
Gosling, J. T., Bame, S. J., McComas, D. J., & Phillips, J. L. (1990, June). Coronal mass ejections and large geomagnetic storms. *Geophys. Res. Lett.*, *17*(7), 901–904. doi: 10.1029/GL017i007p00901
Gosling, J. T., Eriksson, S., Blush, L. M., Phan, T. D., Luhmann, J. G., McComas, D. J., ... Simunac, K. D. (2007, October). Five spacecraft observations of oppositely directed exhaust jets from a magnetic reconnection X-line extending $>4.26 \times 10^6$ km in the solar wind at 1 AU. *Geophys. Res. Lett.*, *342*, L20108. doi: 10.1029/2007GL031492
Gosling, J. T., Eriksson, S., Phan, T. D., Larson, D. E., Skoug, R. M., & McComas, D. J. (2007, March). Direct evidence for prolonged magnetic reconnection at a continuous x-line within the heliospheric current sheet. *Geophys. Res. Lett.*, *340*, 6102. doi: 10.1029/2006GL029033
Gosling, J. T., Phan, T. D., Lin, R. P., & Szabo, A. (2007, August). Prevalence of magnetic reconnection at small field shear angles in the solar wind. *Geophys. Res. Lett.*, *341*, 15110. doi: 10.1029/2007GL030706
Gosling, J. T., & Szabo, A. (2008, October). Bifurcated current sheets produced by magnetic reconnection in the solar wind. *J. Geophys. Res.*, *113*, A10103. doi: 10.1029/2008JA013473
Grandin, M., Aikio, A. T., & Kozlovsky, A. (2019, June). Properties and Geoeffectiveness of Solar Wind High-Speed Streams and Stream Interaction Regions During Solar Cycles 23 and 24. *J. Geophys. Res.*, *124*(6), 3871–3892. doi: 10.1029/2018JA026396
Grappin, R., Leorat, J., & Pouquet, A. (1983, September). Dependence of MHD turbulence spectra on the velocity field-magnetic field correlation. *Astron. & Astrophys.*, *126*(1), 51–58.
Guiriec, S., Gehrels, N., McEnery, J., Kouveliotou, C., & Hartmann, D. H. (2017, September). Photospheric Emission in the Joint GBM and Konus Prompt Spectra of GRB 120323A. *Astrophys. J.*, *846*, 138. doi: 10.3847/1538-4357/aa81c2
Gurnett, D. A., Marsch, E., Pilipp, W., Schwenn, R., & Rosenbauer, H. (1979, May). Ion acoustic waves and related plasma observations in the solar wind. *J. Geophys. Res.*, *84*, 2029–2038. doi: 10.1029/JA084iA05p02029
Gurnett, D. A., Neubauer, F. M., & Schwenn, R. (1979, February). Plasma wave turbulence associated with an interplanetary shock. *J. Geophys. Res.*, *84*, 541–552. doi: 10.1029/JA084iA02p00541
Haggerty, D. K., & Roelof, E. C. (2002, November). Impulsive Near-relativistic Solar Electron Events: Delayed Injection with Respect to Solar Electromagnetic Emission. *Astrophys. J.*, *579*, 841–853. doi: 10.1086/342870
Halekas, J. S., Angelopoulos, V., Sibeck, D. G., Khurana, K. K., Russell, C. T., Delory, G. T., ... Glassmeier, K. H. (2011, January). First Results from ARTEMIS, a New Two-Spacecraft Lunar Mission: Counter-Streaming Plasma Populations in the Lunar Wake. *Space Sci. Rev.*, 95. doi: 10.1007/s11214-010-9738-8
Halekas, J. S., Brain, D. A., & Holmström, M. (2015, January). Moon's Plasma Wake. In *Magnetotails in the solar system* (Vol. 207, pp. 149–167). doi: 10.1002/9781118842324.ch9
Halekas, J. S., Saito, Y., Delory, G. T., & Farrell, W. M. (2011, November). New views of the lunar plasma environment. *Planet. Space Sci.*, *59*(14), 1681–1694. doi: 10.1016/j.pss.2010.08.011
Halford, A. J., McGregor, S. L., Murphy, K. R., Millan, R. M., Hudson, M. K., Woodger, L. A., ... Fennell, J. F. (2015, April). BARREL observations of an ICME-shock impact with the magnetosphere and the resultant radiation belt

electron loss. *J. Geophys. Res.*, *120*, 2557–2570. doi: 10.1002/2014JA020873
Harten, R., & Clark, K. (1995, February). The Design Features of the GGS Wind and Polar Spacecraft. *Space Sci. Rev.*, *71*, 23–40. doi: 10.1007/BF00751324
He, J., Pei, Z., Wang, L., Tu, C., Marsch, E., Zhang, L., & Salem, C. (2015, June). Sunward Propagating Alfvén Waves in Association with Sunward Drifting Proton Beams in the Solar Wind. *Astrophys. J.*, *805*, 176. doi: 10.1088/0004-637X/805/2/176
He, J., Wang, L., Tu, C., Marsch, E., & Zong, Q. (2015, February). Evidence of Landau and Cyclotron Resonance between Protons and Kinetic Waves in Solar Wind Turbulence. *Astrophys. J. Lett.*, *800*, L31. doi: 10.1088/2041-8205/800/2/L31
He, J., Wang, Y., & Sorriso-Valvo, L. (2019, March). Unified Quantitative Description of Solar Wind Turbulence Intermittency in Both Inertial and Kinetic Ranges. *Astrophys. J.*, *873*(1), 80. doi: 10.3847/1538-4357/ab03d0
Hellinger, P., & Trávníček, P. (2006, January). Parallel and oblique proton fire hose instabilities in the presence of alpha/proton drift: Hybrid simulations. *J. Geophys. Res.*, *111*, A01107. doi: 10.1029/2005JA011318
Hellinger, P., Trávníček, P., Kasper, J. C., & Lazarus, A. J. (2006, May). Solar wind proton temperature anisotropy: Linear theory and WIND/SWE observations. *Geophys. Res. Lett.*, *330*, L09101. doi: 10.1029/2006GL025925
Hellinger, P., & Trávníček, P. M. (2014, March). Solar Wind Protons at 1 AU: Trends and Bounds, Constraints and Correlations. *Astrophys. J. Lett.*, *784*, L15. doi: 10.1088/2041-8205/784/1/L15
Hervig, M. E., Brooke, J. S. A., Feng, W., Bardeen, C. G., & Plane, J. M. C. (2017, December). Constraints on Meteoric Smoke Composition and Meteoric Influx Using SOFIE Observations With Models. *J. Geophys. Res.*, *122*(24), 13495–13505. doi: 10.1002/2017JD027657
Hervig, M. E., Siskind, D. E., Bailey, S. M., Merkel, A. W., DeLand, M. T., & Russell, J. M. (2019, August). The Missing Solar Cycle Response of the Polar Summer Mesosphere. *Geophys. Res. Lett.*, *46*(16), 10132–10139. doi: 10.1029/2019GL083485
Hesse, M., & Cassak, P. A. (2020, January). Magnetic Reconnection in the Space Sciences: Past, Present, and Future. *J. Geophys. Res.*, *125*(2), e2018JA025935. doi: 10.1029/2018JA025935
Hidalgo, M. A., Cid, C., Medina, J., & Viñas, A. F. (2000, May). A new model for the topology of magnetic clouds in the solar wind. *Solar Phys.*, *194*, 165–174.
Hidalgo, M. A., & Nieves-Chinchilla, T. (2012, April). A Global Magnetic Topology Model for Magnetic Clouds. I. *Astrophys. J.*, *748*, 109. doi: 10.1088/0004-637X/748/2/109
Hidalgo, M. A., Nieves-Chinchilla, T., & Cid, C. (2002, July). Elliptical cross-section model for the magnetic topology of magnetic clouds. *Geophys. Res. Lett.*, *29*(13), 1637. doi: 10.1029/2001GL013875
Hietala, H., Agueda, N., Andréeová, K., Vainio, R., Nylund, S., Kilpua, E. K. J., & Koskinen, H. E. J. (2011, October). In situ observations of particle acceleration in shock-shock interaction. *J. Geophys. Res.*, *116*, 10105. doi: 10.1029/2011JA016669
Hietala, H., Sandroos, A., & Vainio, R. (2012, May). Particle Acceleration in Shock-Shock Interaction: Model to Data Comparison. *Astrophys. J. Lett.*, *751*, L14. doi: 10.1088/2041-8205/751/1/L14
Hillaris, A., Bouratzis, C., & Nindos, A. (2016, August). Interplanetary Type IV Bursts. *Solar Phys.*, *291*, 2049–2069. doi: 10.1007/s11207-016-0946-6
Ho, G. C., Hamilton, D. C., Gloeckler, G., & Bochsler, P. (2000). Enhanced solar wind $^{3}He^{2+}$ associated with coronal mass ejections. *Geophys. Res. Lett.*, *27*, 309–312. doi: 10.1029/1999GL003660
Hoang, S., Maksimovic, M., Bougeret, J.-L., Reiner, M. J., & Kaiser, M. L. (1998).

Wind-Ulysses source location of radio emissions associated with the January 1997 Coronal Mass Ejection. *Geophys. Res. Lett.*, *25*, 2497–2500. doi: 10.1029/98GL00571

Horaites, K., Boldyrev, S., Krasheninnikov, S. I., Salem, C., Bale, S. D., & Pulupa, M. (2015, June). Self-Similar Theory of Thermal Conduction and Application to the Solar Wind. *Physical Review Letters*, *114*(24), 245003. doi: 10.1103/PhysRevLett.114.245003

Horaites, K., Boldyrev, S., & Medvedev, M. V. (2019, April). Electron strahl and halo formation in the solar wind. *Mon. Not. Roy. Astron. Soc.*, *484*, 2474–2481. doi: 10.1093/mnras/sty3504

Horbury, T. S., Forman, M., & Oughton, S. (2008, October). Anisotropic Scaling of Magnetohydrodynamic Turbulence. *Phys. Rev. Lett.*, *101*(17), 175005. doi: 10.1103/PhysRevLett.101.175005

Horne, R. B., Thorne, R. M., Glauert, S. A., Albert, J. M., Meredith, N. P., & Anderson, R. R. (2005, March). Timescale for radiation belt electron acceleration by whistler mode chorus waves. *J. Geophys. Res.*, *110*(A3), A03225. doi: 10.1029/2004JA010811

Howes, G. G., Bale, S. D., Klein, K. G., Chen, C. H. K., Salem, C. S., & TenBarge, J. M. (2012, July). The Slow-mode Nature of Compressible Wave Power in Solar Wind Turbulence. *Astrophys. J. Lett.*, *753*, L19. doi: 10.1088/2041-8205/753/1/L19

Hu, Q., & Sonnerup, B. U. Ö. (2002, July). Reconstruction of magnetic clouds in the solar wind: Orientations and configurations. *J. Geophys. Res.*, *107*, 1142. doi: 10.1029/2001JA000293

Hu, Q., Zheng, J., & Chen, Y. (2018, October). A database of small-scale magnetic flux ropes in the solar wind from Wind spacecraft measurements. In *Journal of physics conference series* (Vol. 1100, p. 012012). doi: 10.1088/1742-6596/1100/1/012012

Huba, J. D., & Wu, C. S. (1976, July). Effects of a magnetic field gradient on the lower hybrid drift instability. *Phys. Fluids*, *19*, 988–994. doi: 10.1063/1.861594

Hull, A. J., Muschietti, L., Oka, M., Larson, D. E., Mozer, F. S., Chaston, C. C., ... Hospodarsky, G. B. (2012, December). Multiscale whistler waves within Earth's perpendicular bow shock. *J. Geophys. Res.*, *117*, 12104. doi: 10.1029/2012JA017870

Hurley, K., Atteia, J.-L., Crew, G., Ricker, G., Doty, J., Monnelly, G., ... Cline, T. (2003, April). HETE-II and the Interplanetary Network. In G. R. Ricker & R. K. Vanderspek (Ed.), *Gamma-ray burst and afterglow astronomy 2001: A workshop celebrating the first year of the hete mission* (Vol. 662, pp. 42–44). doi: 10.1063/1.1579296

Hurley, K., Cline, T., Mitrofanov, I., Mazets, E., Golenetskii, S., Frontera, F., ... Feroci, M. (2003, April). The Current Performance of the Third Interplanetary Network. In G. R. Ricker & R. K. Vanderspek (Eds.), *Gamma-ray burst and afterglow astronomy 2001: A workshop celebrating the first year of the hete mission* (Vol. 662, pp. 473–476). doi: 10.1063/1.1579405

Hurley, K., Golenetskii, S., Aptekar, R., Mazets, E., Pal'Shin, V., Frederiks, D., ... Hajdas, W. (2011, August). The Third Interplanetary Network. In J. E. McEnery, J. L. Racusin, & N. Gehrels (Eds.), *American institute of physics conference series* (Vol. 1358, pp. 385–388). doi: 10.1063/1.3621810

Hurley, K., Rowlinson, A., Bellm, E., Perley, D., Mitrofanov, I. G., Golovin, D. V., ... von Kienlin, A. (2010, March). A new analysis of the short-duration, hard-spectrum GRB 051103, a possible extragalactic soft gamma repeater giant flare. *Mon. Not. Roy. Astron. Soc.*, *403*, 342–352. doi: 10.1111/j.1365-2966.2009.16118.x

Janvier, M., Dasso, S., Démoulin, P., Masías-Meza, J. J., & Lugaz, N. (2015, May).

Comparing generic models for interplanetary shocks and magnetic clouds axis configurations at 1 AU. *J. Geophys. Res.*, *120*(5), 3328–3349. doi: 10.1002/2014JA020836

Janvier, M., Winslow, R. M., Good, S., Bonhomme, E., Démoulin, P., Dasso, S., ... Boakes, P. D. (2019, February). Generic Magnetic Field Intensity Profiles of Interplanetary Coronal Mass Ejections at Mercury, Venus, and Earth From Superposed Epoch Analyses. *J. Geophys. Res.*, *124*(2), 812–836. doi: 10.1029/2018JA025949

Jaynes, A. N., Baker, D. N., Singer, H. J., Rodriguez, J. V., Loto'aniu, T. M., Ali, A. F., ... Reeves, G. D. (2015, September). Source and seed populations for relativistic electrons: Their roles in radiation belt changes. *J. Geophys. Res.*, *120*, 7240–7254. doi: 10.1002/2015JA021234

Jian, L., Russell, C. T., Luhmann, J. G., & Skoug, R. M. (2006, December). Properties of Stream Interactions at One AU During 1995–2004. *Solar Phys.*, *239*, 337–392. doi: 10.1007/s11207-006-0132-3

Jian, L. K., Russell, C. T., Luhmann, J. G., Galvin, A. B., & MacNeice, P. J. (2009, October). Multi-Spacecraft Observations: Stream Interactions and Associated Structures. *Solar Phys.*, *259*, 345–360. doi: 10.1007/s11207-009-9445-3

Kahler, S. W., Krucker, S., & Szabo, A. (2011, January). Solar energetic electron probes of magnetic cloud field line lengths. *J. Geophys. Res.*, *116*, 1104. doi: 10.1029/2010JA015328

Kaiser, M. L. (2003, August). Solar radio emissions at solar maximum: Interplanetary perspective. *Adv. Space Res.*, *32*, 461–465. doi: 10.1016/S0273-1177(03)00330-2

Kaiser, M. L., Reiner, M. J., Gopalswamy, N., Howard, R. A., St. Cyr, O. C., Thompson, B. J., & Bougeret, J.-L. (1998). Type II radio emissions in the frequency range from 1-14 MHz associated with the April 7, 1997 solar event. *Geophys. Res. Lett.*, *25*, 2501–2504. doi: 10.1029/98GL00706

Kasper, J. C., & Klein, K. G. (2019, June). Strong Preferential Ion Heating is Limited to within the Solar Alfvén Surface. *Astrophys. J. Lett.*, *877*(2), L35. doi: 10.3847/2041-8213/ab1de5

Kasper, J. C., Klein, K. G., Weber, T., Maksimovic, M., Zaslavsky, A., Bale, S. D., ... Case, A. W. (2017, November). A Zone of Preferential Ion Heating Extends Tens of Solar Radii from the Sun. *Astrophys. J.*, *849*, 126. doi: 10.3847/1538-4357/aa84b1

Kasper, J. C., Lazarus, A. J., & Gary, S. P. (2002, September). Wind/SWE observations of firehose constraint on solar wind proton temperature anisotropy. *Geophys. Res. Lett.*, *29*, 1839. doi: 10.1029/2002GL015128

Kasper, J. C., Lazarus, A. J., & Gary, S. P. (2008, December). Hot Solar-Wind Helium: Direct Evidence for Local Heating by Alfvén-Cyclotron Dissipation. *Phys. Rev. Lett.*, *101*, 261103-+. doi: 10.1103/PhysRevLett.101.261103

Kasper, J. C., Lazarus, A. J., Gary, S. P., & Szabo, A. (2003, September). Solar Wind Temperature Anisotropies. In M. Velli, R. Bruno, F. Malara, & B. Bucci (Ed.), *Solar wind ten* (Vol. 679, pp. 538–541). doi: 10.1063/1.1618653

Kasper, J. C., Lazarus, A. J., Steinberg, J. T., Ogilvie, K. W., & Szabo, A. (2006, March). Physics-based tests to identify the accuracy of solar wind ion measurements: A case study with the Wind Faraday Cups. *J. Geophys. Res.*, *111*, A03105. doi: 10.1029/2005JA011442

Kasper, J. C., Maruca, B. A., Stevens, M. L., & Zaslavsky, A. (2013, March). Sensitive Test for Ion-Cyclotron Resonant Heating in the Solar Wind. *Phys. Rev. Lett.*, *110*(9), 091102. doi: 10.1103/PhysRevLett.110.091102

Kasper, J. C., Stevens, M. L., Korreck, K. E., Maruca, B. A., Kiefer, K. K., Schwadron, N. A., & Lepri, S. T. (2012, February). Evolution of the Relationships between Helium Abundance, Minor Ion Charge State, and Solar Wind Speed over the Solar Cycle. *Astrophys. J.*, *745*, 162. doi:

10.1088/0004-637X/745/2/162

Kasper, J. C., Stevens, M. L., Lazarus, A. J., Steinberg, J. T., & Ogilvie, K. W. (2007, May). Solar Wind Helium Abundance as a Function of Speed and Heliographic Latitude: Variation through a Solar Cycle. *Astrophys. J.*, *660*, 901–910. doi: 10.1086/510842

Kellogg, P. J. (2017, January). Note on the Pantellini et al. process for dust impact signals on spacecraft. *J. Geophys. Res.*, *122*, 63–70. doi: 10.1002/2016JA023073

Kellogg, P. J., Cattell, C. A., Goetz, K., Monson, S. J., & Wilson, L. B., III. (2011, September). Large amplitude whistlers in the magnetosphere observed with Wind-Waves. *J. Geophys. Res.*, *116*, 9224. doi: 10.1029/2010JA015919

Kellogg, P. J., Goetz, K., & Monson, S. J. (2016, February). Dust impact signals on the wind spacecraft. *J. Geophys. Res.*, *121*, 966–991. doi: 10.1002/2015JA021124

Kellogg, P. J., Goetz, K., & Monson, S. J. (2018, May). Sign of the Dust Impact-Antenna Coupling Cloud. *J. Geophys. Res.*, *123*(5), 3273–3276. doi: 10.1029/2017JA025173

Kellogg, P. J., Goetz, K., Monson, S. J., Bougeret, J.-L., Manning, R., & Kaiser, M. L. (1996). Observations of plasma waves during a traversal of the moon's wake. *Geophys. Res. Lett.*, *23*, 1267–1270. doi: 10.1029/96GL00376

Kellogg, P. J., Monson, S. J., Goetz, K., Howard, R. L., Bougeret, J.-L., & Kaiser, M. L. (1996). Early wind observations of bow shock and foreshock waves. *Geophys. Res. Lett.*, *23*, 1243–1246. doi: 10.1029/96GL01067

Kersten, K., Cattell, C. A., Breneman, A., Goetz, K., Kellogg, P. J., Wygant, J. R., … Roth, I. (2011, April). Observation of relativistic electron microbursts in conjunction with intense radiation belt whistler-mode waves. *Geophys. Res. Lett.*, *38*, 8107.

Kilpua, E., Koskinen, H. E. J., & Pulkkinen, T. I. (2017, November). Coronal mass ejections and their sheath regions in interplanetary space. *Living Reviews in Solar Physics*, *14*, 5. doi: 10.1007/s41116-017-0009-6

Kilpua, E. K. J., Balogh, A., von Steiger, R., & Liu, Y. D. (2017, November). Geo-effective Properties of Solar Transients and Stream Interaction Regions. *Space Sci. Rev.*, *212*, 1271–1314. doi: 10.1007/s11214-017-0411-3

Kilpua, E. K. J., Lee, C. O., Luhmann, J. G., & Li, Y. (2011, August). Interplanetary coronal mass ejections in the near-Earth solar wind during the minimum periods following solar cycles 22 and 23. *Ann. Geophys.*, *29*, 1455–1467. doi: 10.5194/angeo-29-1455-2011

King, J. H., & Papitashvili, N. E. (2005, February). Solar wind spatial scales in and comparisons of hourly Wind and ACE plasma and magnetic field data. *J. Geophys. Res.*, *110*, A02104. doi: 10.1029/2004JA010649

Klassen, A., Bothmer, V., Mann, G., Reiner, M. J., Krucker, S., Vourlidas, A., & Kunow, H. (2002, April). Solar energetic electron events and coronal shocks. *Astron. & Astrophys.*, *385*, 1078–1088. doi: 10.1051/0004-6361:20020205

Klebesadel, R. W., Strong, I. B., & Olson, R. A. (1973, June). Observations of Gamma-Ray Bursts of Cosmic Origin. *Astrophys. J. Lett.*, *182*, L85. doi: 10.1086/181225

Klein, K. G., Alterman, B. L., Stevens, M. L., Vech, D., & Kasper, J. C. (2018, May). Majority of Solar Wind Intervals Support Ion-Driven Instabilities. *Phys. Rev. Lett.*, *120*(20), 205102. doi: 10.1103/PhysRevLett.120.205102

Klein, K. G., Howes, G. G., TenBarge, J. M., Bale, S. D., Chen, C. H. K., & Salem, C. S. (2012, August). Using Synthetic Spacecraft Data to Interpret Compressible Fluctuations in Solar Wind Turbulence. *Astrophys. J.*, *755*, 159. doi: 10.1088/0004-637X/755/2/159

Klein, K.-L., Tziotziou, K., Zucca, P., Valtonen, E., Vilmer, N., Malandraki, O. E., … Kiener, J. (2018). X-Ray, Radio and SEP Observations of Relativistic

Gamma-Ray Events. In O. E. Malandraki & N. B. Crosby (Eds.), *Solar particle radiation storms forecasting and analysis* (Vol. 444, pp. 133–155). doi: 10.1007/978-3-319-60051-2_8

Kouveliotou, C., Strohmayer, T., Hurley, K., van Paradijs, J., Finger, M. H., Dieters, S., ... Duncan, R. C. (1999, January). Discovery of a Magnetar Associated with the Soft Gamma Repeater SGR 1900+14. *Astrophys. J.*, *510*, L115-L118. doi: 10.1086/311813

Koval, A., & Szabo, A. (2010, December). Multispacecraft observations of interplanetary shock shapes on the scales of the Earth's magnetosphere. *J. Geophys. Res.*, *115*, 12105. doi: 10.1029/2010JA015373

Krasnoselskikh, V. V., Lembège, B., Savoini, P., & Lobzin, V. V. (2002, April). Nonstationarity of strong collisionless quasiperpendicular shocks: Theory and full particle numerical simulations. *Phys. Plasmas*, *9*, 1192–1209. doi: 10.1063/1.1457465

Krucker, S., Larson, D. E., Lin, R. P., & Thompson, B. J. (1999, July). On the Origin of Impulsive Electron Events Observed at 1 AU. *Astrophys. J.*, *519*, 864–875. doi: 10.1086/307415

Krupar, V., Szabo, A., Maksimovic, M., Kruparova, O., Kontar, E. P., Balmaceda, L. A., ... Hegedus, A. M. (2020, February). Density Fluctuations in the Solar Wind Based on Type III Radio Bursts Observed by Parker Solar Probe. *Astrophys. J. Suppl.*, *246*(2), 57. doi: 10.3847/1538-4365/ab65bd

Kubicka, M., Möstl, C., Amerstorfer, T., Boakes, P. D., Feng, L., Eastwood, J. P., & Törmänen, O. (2016, December). Prediction of Geomagnetic Storm Strength from Inner Heliospheric In Situ Observations. *Astrophys. J.*, *833*(2), 255. doi: 10.3847/1538-4357/833/2/255

Lampe, M., Manheimer, W. M., McBride, J. B., Orens, J. H., Shanny, R., & Sudan, R. N. (1971, May). Nonlinear Development of the Beam-Cyclotron Instability. *Phys. Rev. Lett.*, *26*, 1221–1225. doi: 10.1103/PhysRevLett.26.1221

Lampe, M., McBride, J. B., Orens, J. H., & Sudan, R. N. (1971, May). On the theory of the beam cyclotron instability in plasmas. *Phys. Lett. A*, *35*, 129–130. doi: 10.1016/0375-9601(71)90583-4

Lanabere, V., Dasso, S., Démoulin, P., Janvier, M., Rodriguez, L., & Masías-Meza, J. J. (2020, March). Magnetic twist profile inside magnetic clouds derived with a superposed epoch analysis. *Astron. & Astrophys.*, *635*, A85. doi: 10.1051/0004-6361/201937404

Lario, D., Ho, G. C., Decker, R. B., Roelof, E. C., Desai, M. I., & Smith, C. W. (2003, September). ACE Observations of Energetic Particles Associated with Transient Interplanetary Shocks. In M. Velli, R. Bruno, F. Malara, & B. Bucci (Eds.), *Proc. 10th intl. solar wind conf.* (Vol. 679, pp. 640–643). doi: 10.1063/1.1618676

Larson, D. E., Lin, R. P., McTiernan, J. M., McFadden, J. P., Ergun, R. E., McCarthy, M., ... Mazur, J. (1997). Tracing the topology of the October 18-20, 1995, magnetic cloud with ~0.1-10^2 keV electrons. *Geophys. Res. Lett.*, *24*, 1911–1914. doi: 10.1029/97GL01878

Larson, D. E., Lin, R. P., & Steinberg, J. (2000). Extremely cold electrons in the January 1997 magnetic cloud. *Geophys. Res. Lett.*, *27*, 157–160. doi: 10.1029/1999GL003632

Laurenza, M., Cliver, E. W., Hewitt, J., Storini, M., Ling, A. G., Balch, C. C., & Kaiser, M. L. (2009, April). A technique for short-term warning of solar energetic particle events based on flare location, flare size, and evidence of particle escape. *Space Weather*, *70*, S04008. doi: 10.1029/2007SW000379

Lavraud, B., Gosling, J. T., Rouillard, A. P., Fedorov, A., Opitz, A., Sauvaud, J.-A., ... Russell, C. T. (2009, May). Observation of a Complex Solar Wind Reconnection Exhaust from Spacecraft Separated by over 1800 R_E. *Solar Phys.*, *256*, 379–392. doi: 10.1007/s11207-009-9341-x

Leamon, R. J., Matthaeus, W. H., Smith, C. W., Zank, G. P., Mullan, D. J., & Oughton, S. (2000, July). MHD-driven Kinetic Dissipation in the Solar Wind and Corona. *Astrophys. J.*, *537*(2), 1054–1062. doi: 10.1086/309059

Leamon, R. J., Smith, C. W., Ness, N. F., Matthaeus, W. H., & Wong, H. K. (1998, March). Observational constraints on the dynamics of the interplanetary magnetic field dissipation range. *J. Geophys. Res.*, *103*, 4775-+. doi: 10.1029/97JA03394

Leblanc, Y., Dulk, G. A., Cairns, I. H., & Bougeret, J.-L. (2000, August). Type II fixed on boards flare continuum in the corona and solar wind. *J. Geophys. Res.*, *105*, 18215–18224. doi: 10.1029/1999JA000429

Lemons, D. S., & Gary, S. P. (1978, April). Current-driven instabilities in a laminar perpendicular shock. *J. Geophys. Res.*, *83*, 1625–1632. doi: 10.1029/JA083iA04p01625

Lepping, R. P., Acũna, M. H., Burlaga, L. F., Farrell, W. M., Slavin, J. A., Schatten, K. H., ... Worley, E. M. (1995, February). The Wind Magnetic Field Investigation. *Space Sci. Rev.*, *71*, 207–229. doi: 10.1007/BF00751330

Lepping, R. P., Berdichevsky, D. B., Szabo, A., Arqueros, C., & Lazarus, A. J. (2003, February). Profile of an Average Magnetic Cloud at 1 au for the Quiet Solar Phase: Wind Observations. *Solar Phys.*, *212*, 425–444.

Lepping, R. P., Berdichevsky, D. B., & Wu, C.-C. (2017, February). Average Magnetic Field Magnitude Profiles of Wind Magnetic Clouds as a Function of Closest Approach to the Clouds' Axes and Comparison to Model. *Solar Phys.*, *292*, 27. doi: 10.1007/s11207-016-1040-9

Lepping, R. P., Burlaga, L. F., Szabo, A., Ogilvie, K. W., Mish, W. H., Vassiliadis, D., ... Mariani, F. (1997, July). The Wind magnetic cloud and events of October 18-20, 1995: Interplanetary properties and as triggers for geomagnetic activity. *J. Geophys. Res.*, *102*, 14049–14064. doi: 10.1029/97JA00272

Lepping, R. P., Jones, J. A., & Burlaga, L. F. (1990, August). Magnetic field structure of interplanetary magnetic clouds at 1 AU. *J. Geophys. Res.*, *95*(A8), 11957–11965. doi: 10.1029/JA095iA08p11957

Lepping, R. P., Narock, T. W., & Chen, H. (2007, January). Comparison of magnetic field observations of an average magnetic cloud with a simple force free model: the importance of field compression and expansion. *Ann. Geophys.*, *25*, 2641–2648.

Lepping, R. P., Wu, C.-C., & Berdichevsky, D. B. (2005, October). Automatic identification of magnetic clouds and cloud-like regions at 1 AU: occurrence rate and other properties. *Ann. Geophys.*, *23*, 2687–2704. doi: 10.5194/angeo-23-2687-2005

Lepping, R. P., Wu, C.-C., Berdichevsky, D. B., & Ferguson, T. (2008, July). Estimates of magnetic cloud expansion at 1 AU. *Ann. Geophys.*, *26*, 1919–1933. doi: 10.5194/angeo-26-1919-2008

Lepping, R. P., Wu, C.-C., Berdichevsky, D. B., & Kay, C. (2018, December). Magnetic Field Magnitude Modification for a Force-free Magnetic Cloud Model. *Solar Phys.*, *293*, 162. doi: 10.1007/s11207-018-1383-5

Lepping, R. P., Wu, C. C., Berdichevsky, D. B., & Szabo, A. (2011, December). Magnetic Clouds at/near the 2007 - 2009 Solar Minimum: Frequency of Occurrence and Some Unusual Properties. *Solar Phys.*, *274*(1-2), 345–360. doi: 10.1007/s11207-010-9646-9

Lepping, R. P., Wu, C.-C., Berdichevsky, D. B., & Szabo, A. (2018, April). Wind Magnetic Clouds for the Period 2013 - 2015: Model Fitting, Types, Associated Shock Waves, and Comparisons to Other Periods. *Solar Phys.*, *293*, 65. doi: 10.1007/s11207-018-1273-x

Lepping, R. P., Wu, C. C., Berdichevsky, D. B., & Szabo, A. (2020, June). Model Fitting of Wind Magnetic Clouds for the Period 2004 - 2006. *Solar Phys.*, *295*(6), 83. doi: 10.1007/s11207-020-01630-2

Lepping, R. P., Wu, C.-C., Gopalswamy, N., & Berdichevsky, D. B. (2008, March). Average Thickness of Magnetosheath Upstream of Magnetic Clouds at 1 AU versus Solar Longitude of Source. *Solar Phys.*, *248*, 125–139. doi: 10.1007/s11207-007-9111-6

Li, W., Thorne, R. M., Bortnik, J., Baker, D. N., Reeves, G. D., Kanekal, S. G., … Green, J. C. (2015, September). Solar wind conditions leading to efficient radiation belt electron acceleration: A superposed epoch analysis. *Geophys. Res. Lett.*, *42*, 6906–6915. doi: 10.1002/2015GL065342

Li, Y., Luhmann, J. G., & Lynch, B. J. (2018, October). Magnetic Clouds: Solar Cycle Dependence, Sources, and Geomagnetic Impacts. *Solar Phys.*, *293*, 135. doi: 10.1007/s11207-018-1356-8

Lin, R. P., Anderson, K. A., Ashford, S., Carlson, C., Curtis, D., Ergun, R., … Paschmann, G. (1995, February). A Three-Dimensional Plasma and Energetic Particle Investigation for the Wind Spacecraft. *Space Sci. Rev.*, *71*, 125–153. doi: 10.1007/BF00751328

Liu, X., Yue, J., Wang, W., Xu, J., Zhang, Y., Li, J., … Nakamura, T. (2018, May). Responses of Lower Thermospheric Temperature to the 2013 St. Patrick's Day Geomagnetic Storm. *Geophys. Res. Lett.*, *45*(10), 4656–4664. doi: 10.1029/2018GL078039

Liu, Y. D., Luhmann, J. G., Lugaz, N., Möstl, C., Davies, J. A., Bale, S. D., & Lin, R. P. (2013, May). On Sun-to-Earth Propagation of Coronal Mass Ejections. *Astrophys. J.*, *769*(1), 45. doi: 10.1088/0004-637X/769/1/45

Lotko, W., Smith, R. H., Zhang, B., Ouellette, J. E., Brambles, O. J., & Lyon, J. G. (2014, July). Ionospheric control of magnetotail reconnection. *Science*, *345*, 184–187. doi: 10.1126/science.1252907

Lugaz, N., Farrugia, C. J., Winslow, R. M., Al-Haddad, N., Galvin, A. B., Nieves-Chinchilla, T., … Janvier, M. (2018, September). On the Spatial Coherence of Magnetic Ejecta: Measurements of Coronal Mass Ejections by Multiple Spacecraft Longitudinally Separated by 0.01 au. *Astrophys. J. Lett.*, *864*, L7. doi: 10.3847/2041-8213/aad9f4

Lugaz, N., Manchester, W. B., IV, Roussev, I. I., Tóth, G., & Gombosi, T. I. (2007, April). Numerical Investigation of the Homologous Coronal Mass Ejection Events from Active Region 9236. *Astrophys. J.*, *659*, 788–800. doi: 10.1086/512005

Lugaz, N., Winslow, R. M., & Farrugia, C. J. (2020, January). Evolution of a Long-Duration Coronal Mass Ejection and Its Sheath Region Between Mercury and Earth on 9-14 July 2013. *J. Geophys. Res.*, *125*(1), e27213. doi: 10.1029/2019JA027213

Lundquist, S. (1951, July). On the Stability of Magneto-Hydrostatic Fields. *Phys. Rev.*, *83*(2), 307–311. doi: 10.1103/PhysRev.83.307

MacDowall, R. J., Lara, A., Manoharan, P. K., Nitta, N. V., Rosas, A. M., & Bougeret, J. L. (2003, May). Long-duration hectometric type III radio bursts and their association with solar energetic particle (SEP) events. *Geophys. Res. Lett.*, *30*, 8018. doi: 10.1029/2002GL016624

MacDowall, R. J., Richardson, I. G., Hess, R. A., & Thejappa, G. (2009, March). Re-examining the correlation of complex solar type III radio bursts and solar energetic particles. In N. Gopalswamy & D. F. Webb (Ed.), *Iau symposium* (Vol. 257, pp. 335–340). doi: 10.1017/S1743921309029512

Mäkelä, P., Gopalswamy, N., & Akiyama, S. (2018, November). Direction-finding Analysis of the 2012 July 6 Type II Solar Radio Burst at Low Frequencies. *Astrophys. J.*, *867*, 40. doi: 10.3847/1538-4357/aae2b6

Malandraki, O. E., & Crosby, N. B. (2018). Solar Energetic Particles and Space Weather: Science and Applications. In O. E. Malandraki & N. B. Crosby (Eds.), *Solar particle radiation storms forecasting and analysis* (Vol. 444, p. 1-26). doi: 10.1007/978-3-319-60051-2_1

Malaspina, D. M., Cairns, I. H., & Ergun, R. E. (2011, July). Dependence of Langmuir wave polarization on electron beam speed in type III solar radio bursts. *Geophys. Res. Lett.*, *38*, L13101. doi: 10.1029/2011GL047642

Malaspina, D. M., & Ergun, R. E. (2008, December). Observations of three-dimensional Langmuir wave structure. *J. Geophys. Res.*, *113*, 12108. doi: 10.1029/2008JA013656

Malaspina, D. M., Halekas, J., Berčič, L., Larson, D., Whittlesey, P., Bale, S. D., … Stevens, M. L. (2020, February). Plasma Waves near the Electron Cyclotron Frequency in the Near-Sun Solar Wind. *Astrophys. J. Suppl.*, *246*(2), 21. doi: 10.3847/1538-4365/ab4c3b

Malaspina, D. M., Horányi, M., Zaslavsky, A., Goetz, K., Wilson, L. B., & Kersten, K. (2014, January). Interplanetary and interstellar dust observed by the Wind/WAVES electric field instrument. *Geophys. Res. Lett.*, *41*, 266–272. doi: 10.1002/2013GL058786

Malaspina, D. M., Newman, D. L., Wilson, L. B., III, Goetz, K., Kellogg, P. J., & Kersten, K. (2013, February). Electrostatic Solitary Waves in the Solar Wind: Evidence for Instability at Solar Wind Current Sheets. *J. Geophys. Res.*, *118*, 591–599.

Malaspina, D. M., O'Brien, L. E., Thayer, F., Sternovsky, Z., & Collette, A. (2015, August). Revisiting STEREO interplanetary and interstellar dust flux and mass estimates. *J. Geophys. Res.*, *120*, 6085–6100. doi: 10.1002/2015JA021352

Malaspina, D. M., & Wilson III, L. B. (2016, November). A database of interplanetary and interstellar dust detected by the Wind spacecraft. *J. Geophys. Res.*, *121*, 9369–9377. doi: 10.1002/2016JA023209

Mangeney, A. (2001, January). Intermittency in the Solar Wind Turbulence and the Haar Wavelet Transform. In B. Warmbein (Ed.), *Sheffield space plasma meeting: Multipoint measurements versus theory* (Vol. 492, p. 53-+).

Mann, G., Classen, H. T., Keppler, E., & Roelof, E. C. (2002, August). On electron acceleration at CIR related shock waves. *Astron. & Astrophys.*, *391*, 749–756. doi: 10.1051/0004-6361:20020866

Mann, I., Nouzák, L., Vaverka, J., Antonsen, T., Fredriksen, Å., Issautier, K., … Zaslavsky, A. (2019, December). Dust observations with antenna measurements and its prospects for observations with Parker Solar Probe and Solar Orbiter. *Ann. Geophys.*, *37*(6), 1121–1140. doi: 10.5194/angeo-37-1121-2019

Mann, I. R., Ozeke, L. G., Murphy, K. R., Claudepierre, S. G., Turner, D. L., Baker, D. N., … Honary, F. (2016, October). Explaining the dynamics of the ultra-relativistic third Van Allen radiation belt. *Nature Phys.*, *12*, 978–983. doi: 10.1038/nphys3799

Markovskii, S. A., Vasquez, B. J., & Smith, C. W. (2015, June). Statistical Analysis of the Magnetic Helicity Signature of the Solar Wind Turbulence at 1 AU. *Astrophys. J.*, *806*, 78. doi: 10.1088/0004-637X/806/1/78

Marsch, E. (2006, July). Kinetic Physics of the Solar Corona and Solar Wind. *Living Reviews in Solar Physics*, *3*, 1-+.

Marsch, E., & Chang, T. (1983, September). Electromagnetic lower hybrid waves in the solar wind. *J. Geophys. Res.*, *88*, 6869–6880. doi: 10.1029/JA088iA09p06869

Marubashi, K. (1986, January). Structure of the interplanetary magnetic clouds and their solar origins. *Adv. Space Res.*, *6*(6), 335–338. doi: 10.1016/0273-1177(86)90172-9

Marubashi, K. (2000, January). Physics of Interplanetary Magnetic Flux Ropes: Toward Prediction of Geomagnetic Storms. *Adv. Space Res.*, *26*(1), 55–66. doi: 10.1016/S0273-1177(99)01026-1

Maruca, B. A., Bale, S. D., Sorriso-Valvo, L., Kasper, J. C., & Stevens, M. L. (2013, December). Collisional Thermalization of Hydrogen and Helium in Solar-Wind

Plasma. *Phys. Rev. Lett.*, *111*(24), 241101. doi: 10.1103/PhysRevLett.111.241101
Maruca, B. A., & Kasper, J. C. (2013, August). Improved interpretation of solar wind ion measurements via high-resolution magnetic field data. *Adv. Space Res.*, *52*, 723–731. doi: 10.1016/j.asr.2013.04.006
Maruca, B. A., Kasper, J. C., & Bale, S. D. (2011, November). What Are the Relative Roles of Heating and Cooling in Generating Solar Wind Temperature Anisotropies? *Phys. Rev. Lett.*, *107*, 201101. doi: 10.1103/PhysRevLett.107.201101
Maruca, B. A., Kasper, J. C., & Gary, S. P. (2012, April). Instability-driven Limits on Helium Temperature Anisotropy in the Solar Wind: Observations and Linear Vlasov Analysis. *Astrophys. J.*, *748*, 137. doi: 10.1088/0004-637X/748/2/137
Mason, G. M., Desai, M. I., Mall, U., Korth, A., Bucik, R., von Rosenvinge, T. T., & Simunac, K. D. (2009, May). In situ Observations of CIRs on STEREO, Wind, and ACE During 2007 - 2008. *Solar Phys.*, *256*, 393–408. doi: 10.1007/s11207-009-9367-0
Mason, G. M., Mazur, J. E., Dwyer, J. R., Reames, D. V., & von Rosenvinge, T. T. (1997, September). New Spectral and Abundance Features of Interplantary Heavy Ions in Corotating Interaction Regions. *Astrophys. J.*, *486*, L149+. doi: 10.1086/310845
Mason, G. M., von Steiger, R., Decker, R. B., Desai, M. I., Dwyer, J. R., Fisk, L. A., ... Mazur, J. E. (1999, July). Origin, Injection, and Acceleration of CIR Particles: Observations Report of Working Group 6. *Space Sci. Rev.*, *89*, 327–367. doi: 10.1023/A:1005278214143
Matsui, H., Farrugia, C. J., & Torbert, R. B. (2002, November). Wind-ACE solar wind correlations, 1999: An approach through spectral analysis. *J. Geophys. Res.*, *107*, 1355. doi: 10.1029/2002JA009251
Matthaeus, W. H., Dasso, S., Weygand, J. M., Kivelson, M. G., & Osman, K. T. (2010, September). Eulerian Decorrelation of Fluctuations in the Interplanetary Magnetic Field. *Astrophys. J.*, *721*, L10-L13. doi: 10.1088/2041-8205/721/1/L10
Matthaeus, W. H., Dasso, S., Weygand, J. M., Milano, L. J., Smith, C. W., & Kivelson, M. G. (2005, December). Spatial Correlation of Solar-Wind Turbulence from Two-Point Measurements. *Phys. Rev. Lett.*, *95*, 231101-+. doi: 10.1103/PhysRevLett.95.231101
Matthaeus, W. H., Weygand, J. M., & Dasso, S. (2016, June). Ensemble Space-Time Correlation of Plasma Turbulence in the Solar Wind. *Phys. Rev. Lett.*, *116*(24), 245101. doi: 10.1103/PhysRevLett.116.245101
Mazelle, C., Le Quéau, D., & Meziane, K. (2000). Nonlinear wave-particle interaction upstream from the Earth's bow shock. *Nonlin. Proc. Geophys.*, *7*, 185–190.
Mazets, E. P., Aptekar, R. L., Cline, T. L., Frederiks, D. D., Goldsten, J. O., Golenetskii, S. V., ... Pal'shin, V. D. (2008, June). A Giant Flare from a Soft Gamma Repeater in the Andromeda Galaxy (M31). *Astrophys. J.*, *680*, 545–549. doi: 10.1086/587955
McFadden, J. P., Carlson, C. W., Larson, D., Ludlam, M., Abiad, R., Elliott, B., ... Angelopoulos, V. (2008, December). The THEMIS ESA Plasma Instrument and In-flight Calibration. *Space Sci. Rev.*, *141*, 277–302. doi: 10.1007/s11214-008-9440-2
McFadden, J. P., Phan, T. D., Carlson, C. W., Angelopoulos, V., Glassmeier, K.-H., & Auster, U. (2008, May). Structure of the subsolar magnetopause regions during northward IMF: First results from THEMIS. *Geophys. Res. Lett.*, *351*, L17S09. doi: 10.1029/2008GL033630
Meziane, K., Hull, A. J., Hamza, A. M., & Lin, R. P. (2002, September). On the

bow shock θ_{Bn} dependence of upstream 70 keV to 2 MeV ion fluxes. *J. Geophys. Res.*, *107*, 1243. doi: 10.1029/2001JA005012

Meziane, K., Lin, R. P., Parks, G. K., Larson, D. E., Bale, S. D., Mason, G. M., ... Lepping, R. P. (1999, October). Evidence for acceleration of ions to ~1 MeV by adiabatic-like reflection at the quasi-perpendicular Earth's bow shock. *Geophys. Res. Lett.*, *26*, 2925–2928. doi: 10.1029/1999GL900603

Meziane, K., Mazelle, C., D'Uston, C., Rème, H., Lin, R. P., Carlson, C. W., ... Lepping, R. P. (1997, September). Wind observation of gyrating-like ion distributions and low frequency waves upstream from the earth's bow shock. *Adv. Space Res.*, *20*, 703–706. doi: 10.1016/S0273-1177(97)00459-6

Meziane, K., Mazelle, C., Lin, R. P., Le Quéau, D., Larson, D. E., Parks, G. K., & Lepping, R. P. (2001, April). Three-dimensional observations of gyrating ion distributions far upstream from the Earth's bow shock and their association with low-frequency waves. *J. Geophys. Res.*, *106*, 5731–5742. doi: 10.1029/2000JA900079

Meziane, K., Wilber, M., Lin, R. P., & Parks, G. K. (2003, October). Gyrophase-restricted 100 keV-2 MeV ion beams near the foreshock boundary. *Geophys. Res. Lett.*, *30*, 200000–1. doi: 10.1029/2003GL017592

Miteva, R., Samwel, S. W., & Costa-Duarte, M. V. (2018, February). The Wind/EPACT Proton Event Catalog (1996 - 2016). *Solar Phys.*, *293*, 27. doi: 10.1007/s11207-018-1241-5

Miteva, R., Samwel, S. W., & Krupar, V. (2017, December). Solar energetic particles and radio burst emission. *J. Space Weather Space Clim.*, *7*(27), A37. doi: 10.1051/swsc/2017035

Morioka, A., Miyoshi, Y., Iwai, K., Kasaba, Y., Masuda, S., Misawa, H., & Obara, T. (2015, August). Solar Micro-Type III Burst Storms and Long Dipolar Magnetic Field in the Outer Corona. *Astrophys. J.*, *808*(2), 191. doi: 10.1088/0004-637X/808/2/191

Morioka, A., Miyoshi, Y., Masuda, S., Tsuchiya, F., Misawa, H., Matsumoto, H., ... Oya, H. (2007, March). Micro-Type III Radio Bursts. *Astrophys. J.*, *657*, 567–576. doi: 10.1086/510507

Möstl, C., Miklenic, C., Farrugia, C. J., Temmer, M., Veronig, A., Galvin, A. B., ... Biernat, H. K. (2008, October). Two-spacecraft reconstruction of a magnetic cloud and comparison to its solar source. *Ann. Geophys.*, *26*, 3139–3152. doi: 10.5194/angeo-26-3139-2008

Moullard, O., Burgess, D., Salem, C., Mangeney, A., Larson, D. E., & Bale, S. D. (2001, May). Whistler waves, Langmuir waves and single loss cone electron distributions inside a magnetic cloud: Observations. *J. Geophys. Res.*, *106*, 8301–8314. doi: 10.1029/2000JA900144

Mulligan, T., Russell, C. T., Anderson, B. J., Lohr, D. A., Rust, D., Toth, B. A., ... Gosling, J. T. (1999). Intercomparison of NEAR and Wind interplanetary coronal mass ejection observations. *J. Geophys. Res.*, *1042*, 28217–28224. doi: 10.1029/1999JA900215

Muschietti, L., & Lembège, B. (2013, May). Microturbulence in the electron cyclotron frequency range at perpendicular supercritical shocks. *J. Geophys. Res.*, *118*, 2267–2285. doi: 10.1002/jgra.50224

Muschietti, L., & Lembège, B. (2017, September). Two-stream instabilities from the lower-hybrid frequency to the electron cyclotron frequency: application to the front of quasi-perpendicular shocks. *Ann. Geophys.*, *35*, 1093–1112. doi: 10.5194/angeo-35-1093-2017

Nakwacki, M. S., Dasso, S., Démoulin, P., Mandrini, C. H., & Gulisano, A. M. (2011, November). Dynamical evolution of a magnetic cloud from the Sun to 5.4 AU. *Astron. & Astrophys.*, *535*, A52. doi: 10.1051/0004-6361/201015853

Navarro, R. E., Araneda, J., Muñoz, V., Moya, P. S., F.-Viñas, A., & Valdivia, J. A. (2014, September). Theory of electromagnetic fluctuations for magnetized multi-species plasmas. *Phys. Plasmas*, *21*(9), 092902. doi: 10.1063/1.4894700

Navarro, R. E., Moya, P. S., Muñoz, V., Araneda, J. A., Viñas, A. F., & Valdivia, J. A. (2014, June). Solar Wind Thermally Induced Magnetic Fluctuations. *Phys. Rev. Lett.*, *112*(24), 245001. doi: 10.1103/PhysRevLett.112.245001

Ness, N. F. (1972, January). Interaction of the solar wind with the moon. In *The interplanetary medium: Part ii of solar-terrestrial physics/1970* (pp. 159–205).

Neugebauer, M., & Giacalone, J. (2005, December). Multispacecraft observations of interplanetary shocks: Nonplanarity and energetic particles. *J. Geophys. Res.*, *110*, A12106. doi: 10.1029/2005JA011380

Neugebauer, M., Giacalone, J., Chollet, E., & Lario, D. (2006, December). Variability of low-energy ion flux profiles on interplanetary shock fronts. *J. Geophys. Res.*, *111*, A12107. doi: 10.1029/2006JA011832

Nieves-Chinchilla, T., Colaninno, R., Vourlidas, A., Szabo, A., Lepping, R. P., Boardsen, S. A., ... Korth, H. (2012, June). Remote and in situ observations of an unusual Earth-directed coronal mass ejection from multiple viewpoints. *J. Geophys. Res.*, *117*, 6106. doi: 10.1029/2011JA017243

Nieves-Chinchilla, T., Jian, L. K., Balmaceda, L., Vourlidas, A., dos Santos, L. F. G., & Szabo, A. (2019, July). Unraveling the Internal Magnetic Field Structure of the Earth-directed Interplanetary Coronal Mass Ejections During 1995 - 2015. *Solar Phys.*, *294*(7), 89. doi: 10.1007/s11207-019-1477-8

Nieves-Chinchilla, T., Linton, M. G., Hidalgo, M. A., Vourlidas, A., Savani, N. P., Szabo, A., ... Yu, W. (2016, May). A Circular-cylindrical Flux-rope Analytical Model for Magnetic Clouds. *Astrophys. J.*, *823*, 27. doi: 10.3847/0004-637X/823/1/27

Nieves-Chinchilla, T., Vourlidas, A., Raymond, J. C., Linton, M. G., Al-haddad, N., Savani, N. P., ... Hidalgo, M. A. (2018, February). Understanding the Internal Magnetic Field Configurations of ICMEs Using More than 20 Years of Wind Observations. *Solar Phys.*, *293*, 25. doi: 10.1007/s11207-018-1247-z

Nishida, A. (1994, December). The Geotail mission. *Geophys. Res. Lett.*, *21*(25), 2871–2873. doi: 10.1029/94GL01223

Ogilvie, K. W., Chornay, D. J., Fritzenreiter, R. J., Hunsaker, F., Keller, J., Lobell, J., ... Gergin, E. (1995, February). SWE, A Comprehensive Plasma Instrument for the Wind Spacecraft. *Space Sci. Rev.*, *71*, 55–77. doi: 10.1007/BF00751326

Ogilvie, K. W., Coplan, M. A., Roberts, D. A., & Ipavich, F. (2007, August). Solar wind structure suggested by bimodal correlations of solar wind speed and density between the spacecraft SOHO and Wind. *J. Geophys. Res.*, *112*, A08104. doi: 10.1029/2007JA012248

Ogilvie, K. W., & Desch, M. D. (1997). The wind spacecraft and its early scientific results. *Adv. Space Res.*, *20*, 559–568. doi: 10.1016/S0273-1177(97)00439-0

Ogilvie, K. W., Steinberg, J. T., Fitzenreiter, R. J., Owen, C. J., Lazarus, A. J., Farrell, W. M., & Torbert, R. B. (1996). Observations of the lunar plasma wake from the WIND spacecraft on December 27, 1994. *Geophys. Res. Lett.*, *23*, 1255–1258. doi: 10.1029/96GL01069

Øieroset, M., Lin, R. P., Phan, T. D., Larson, D. E., & Bale, S. D. (2002, October). Evidence for Electron Acceleration up to ∼300 keV in the Magnetic Reconnection Diffusion Region of Earth's Magnetotail. *Phys. Rev. Lett.*, *89*, 195001-+. doi: 10.1103/PhysRevLett.89.195001

Øieroset, M., Phan, T. D., Fujimoto, M., Lin, R. P., & Lepping, R. P. (2001, July). In situ detection of collisionless reconnection in the Earth's magnetotail. *Nature*, *412*, 414–417. doi: 10.1038/35086520

Osman, K. T., Matthaeus, W. H., Hnat, B., & Chapman, S. C. (2012, June). Kinetic Signatures and Intermittent Turbulence in the Solar Wind Plasma. *Phys. Rev. Lett.*, *108*(26), 261103. doi: 10.1103/PhysRevLett.108.261103

Owen, C. J., Lepping, R. P., Ogilvie, K. W., Slavin, J. A., Farrell, W. M., & Byrnes,

J. B. (1996). The lunar wake at 6.8 R_L: WIND magnetic field observations. *Geophys. Res. Lett.*, *23*, 1263–1266. doi: 10.1029/96GL01354
Owens, A., Baker, R., Cline, T. L., Gehrels, N., Jermakian, J., Nolan, T., . . . Post, A. H., Jr. (1995, February). A High-Resolution GE Spectrometer for Gamma-Ray Burst Astronomy. *Space Sci. Rev.*, *71*, 273–296. doi: 10.1007/BF00751333
Owens, M. J., Horbury, T. S., & Arge, C. N. (2010, May). Probing the Large-scale Topology of the Heliospheric Magnetic Field using Jovian Electrons. *Astrophys. J.*, *714*(2), 1617–1623. doi: 10.1088/0004-637X/714/2/1617
Pal'shin, V. D., Charikov, Y. E., Aptekar, R. L., Golenetskii, S. V., Kokomov, A. A., Svinkin, D. S., . . . Tsvetkova, A. E. (2014, December). Konus-Wind and Helicon-Coronas-F observations of solar flares. *Geomagnetism and Aeronomy*, *54*, 943–948. doi: 10.1134/S0016793214070093
Pal'shin, V. D., Hurley, K., Svinkin, D. S., Aptekar, R. L., Golenetskii, S. V., Frederiks, D. D., . . . Ricker, G. (2013, August). Interplanetary Network Localizations of Konus Short Gamma-Ray Bursts. *Astrophys. J. Suppl.*, *207*, 38. doi: 10.1088/0067-0049/207/2/38
Park, J., Caprioli, D., & Spitkovsky, A. (2015, February). Simultaneous Acceleration of Protons and Electrons at Nonrelativistic Quasiparallel Collisionless Shocks. *Phys. Rev. Lett.*, *114*(8), 085003. doi: 10.1103/PhysRevLett.114.085003
Paschmann, G., Papamastorakis, I., Sckopke, N., Haerendel, G., Sonnerup, B. U. O., Bame, S. J., . . . Elphic, R. C. (1979, November). Plasma acceleration at the earth's magnetopause - Evidence for reconnection. *Nature*, *282*, 243–246. doi: 10.1038/282243a0
Phan, T. D., Gosling, J. T., Davis, M. S., Skoug, R. M., Øieroset, M., Lin, R. P., . . . Balogh, A. (2006, January). A magnetic reconnection X-line extending more than 390 Earth radii in the solar wind. *Nature*, *439*, 175–178. doi: 10.1038/nature04393
Pitňa, A., Šafránková, J., Němeček, Z., Franci, L., Pi, G., & Montagud Camps, V. (2019, July). Characteristics of Solar Wind Fluctuations at and below Ion Scales. *Astrophys. J.*, *879*(2), 82. doi: 10.3847/1538-4357/ab22b8
Podesta, J. J., & Borovsky, J. E. (2010, November). Scale invariance of normalized cross-helicity throughout the inertial range of solar wind turbulence. *Phys. Plasmas*, *17*, 112905-+. doi: 10.1063/1.3505092
Podesta, J. J., Roberts, D. A., & Goldstein, M. L. (2006, October). Power spectrum of small-scale turbulent velocity fluctuations in the solar wind. *J. Geophys. Res.*, *111*, A10109. doi: 10.1029/2006JA011834
Podesta, J. J., Roberts, D. A., & Goldstein, M. L. (2007, July). Spectral Exponents of Kinetic and Magnetic Energy Spectra in Solar Wind Turbulence. *Astrophys. J.*, *664*, 543–548. doi: 10.1086/519211
Pohjolainen, S., & Talebpour Sheshvan, N. (2020, March). Cut-off features in interplanetary solar radio type IV emission. *Adv. Space Res.*, *65*(6), 1663–1672. doi: 10.1016/j.asr.2019.05.034
Posner, A., Schwadron, N. A., McComas, D. J., Roelof, E. C., & Galvin, A. B. (2004, October). Suprathermal ions ahead of interplanetary shocks: New observations and critical instrumentation required for future space weather monitoring. *Space Weather*, *2*, S10004. doi: 10.1029/2004SW000079
Pulupa, M., & Bale, S. D. (2008, April). Structure on Interplanetary Shock Fronts: Type II Radio Burst Source Regions. *Astrophys. J.*, *676*, 1330–1337. doi: 10.1086/526405
Raj, A., Phan, T., Lin, R. P., & Angelopoulos, V. (2002, December). Wind survey of high-speed bulk flows and field-aligned beams in the near-Earth plasma sheet. *J. Geophys. Res.*, *107*, 1419. doi: 10.1029/2001JA007547
Raymond, J. C., Thompson, B. J., St. Cyr, O. C., Gopalswamy, N., Kahler, S., Kaiser, M., . . . O'Neal, R. (2000, May). SOHO and radio observa-

tions of a CME shock wave. *Geophys. Res. Lett.*, *27*, 1439–1442. doi: 10.1029/1999GL003669

Reames, D. V. (2000, September). Abundances of Trans-Iron Elements in Solar Energetic Particle Events. *Astrophys. J.*, *540*, L111-L114. doi: 10.1086/312886

Reames, D. V. (2012, September). Particle Energy Spectra at Traveling Interplanetary Shock Waves. *Astrophys. J.*, *757*, 93. doi: 10.1088/0004-637X/757/1/93

Reames, D. V. (2017). *Solar Energetic Particles* (Vol. 932). doi: 10.1007/978-3-319-50871-9

Reames, D. V. (2018, October). Corotating Shock Waves and the Solar-wind Source of Energetic Ion Abundances: Power Laws in A/Q. *Solar Phys.*, *293*, 144. doi: 10.1007/s11207-018-1369-3

Reames, D. V., Cliver, E. W., & Kahler, S. W. (2014, October). Abundance Enhancements in Impulsive Solar Energetic-Particle Events with Associated Coronal Mass Ejections. *Solar Phys.*, *289*, 3817–3841. doi: 10.1007/s11207-014-0547-1

Reames, D. V., & Ng, C. K. (2004, July). Heavy-Element Abundances in Solar Energetic Particle Events. *Astrophys. J.*, *610*, 510–522. doi: 10.1086/421518

Reiner, M. J., Fainberg, J., Kaiser, M. L., & Bougeret, J.-L. (2007, April). Circular Polarization Observed in Interplanetary Type III Radio Storms. *Solar Phys.*, *241*, 351–370. doi: 10.1007/s11207-007-0277-8

Reiner, M. J., & Kaiser, M. L. (1999, August). High-frequency type II radio emissions associated with shocks driven by coronal mass ejections. *J. Geophys. Res.*, *1041*, 16979–16992. doi: 10.1029/1999JA900143

Reiner, M. J., Kaiser, M. L., & Bougeret, J.-L. (2007, July). Coronal and Interplanetary Propagation of CME/Shocks from Radio, In Situ and White-Light Observations. *Astrophys. J.*, *663*, 1369–1385. doi: 10.1086/518683

Reiner, M. J., Kaiser, M. L., Fainberg, J., Desch, M. D., & Stone, R. G. (1996). 2f_p radio emission from the vicinity of the Earth's foreshock: WIND observations. *Geophys. Res. Lett.*, *23*, 1247-+. doi: 10.1029/96GL00841

Reiner, M. J., Kaiser, M. L., Fainberg, J., & Stone, R. G. (1998, December). A new method for studying remote type II radio emissions from coronal mass ejection-driven shocks. *J. Geophys. Res.*, *1032*, 29651–29664. doi: 10.1029/98JA02614

Reiner, M. J., Kaiser, M. L., Karlický, M., Jiřička, K., & Bougeret, J.-L. (2001, December). Bastille Day Event: A Radio Perspective. *Solar Phys.*, *204*, 121–137. doi: 10.1023/A:1014225323289

Reiner, M. J., Kaiser, M. L., Plunkett, S. P., Prestage, N. P., & Manning, R. (2000, January). Radio Tracking of a White-Light Coronal Mass Ejection from Solar Corona to Interplanetary Medium. *Astrophys. J.*, *529*, L53-L56. doi: 10.1086/312446

Reiner, M. J., & MacDowall, R. J. (2015, October). Electron Exciter Speeds Associated with Interplanetary Type III Solar Radio Bursts. *Solar Phys.*, *290*, 2975–3004. doi: 10.1007/s11207-015-0779-8

Richardson, I. G., & Cane, H. V. (2004, September). The fraction of interplanetary coronal mass ejections that are magnetic clouds: Evidence for a solar cycle variation. *Geophys. Res. Lett.*, *311*, L18804. doi: 10.1029/2004GL020958

Richardson, I. G., & Cane, H. V. (2010, June). Near-Earth Interplanetary Coronal Mass Ejections During Solar Cycle 23 (1996 - 2009): Catalog and Summary of Properties. *Solar Phys.*, *264*, 189–237. doi: 10.1007/s11207-010-9568-6

Richardson, I. G., Mays, M. L., & Thompson, B. J. (2018, November). Prediction of Solar Energetic Particle Event Peak Proton Intensity Using a Simple Algorithm Based on CME Speed and Direction and Observations of Associated Solar Phenomena. *Space Weather*, *16*, 1862–1881. doi: 10.1029/2018SW002032

Richardson, J. D., & Paularena, K. I. (2001, January). Plasma and magnetic field correlations in the solar wind. *J. Geophys. Res.*, *106*(1), 239–252. doi: 10

.1029/2000JA000071

Roth, I., & Temerin, M. (1997, March). Enrichment of ^{3}He and Heavy Ions in Impulsive Solar Flares. *Astrophys. J.*, *477*(2), 940–957. doi: 10.1086/303731

Ruffenach, A., Lavraud, B., Owens, M. J., Sauvaud, J.-A., Savani, N. P., Rouillard, A. P., ... Galvin, A. B. (2012, September). Multispacecraft observation of magnetic cloud erosion by magnetic reconnection during propagation. *J. Geophys. Res.*, *117*, 9101. doi: 10.1029/2012JA017624

Russell, I., James M., Bailey, S. M., Gordley, L. L., Rusch, D. W., Horányi, M., Hervig, M. E., ... Merkel, A. W. (2009, March). The Aeronomy of Ice in the Mesosphere (AIM) mission: Overview and early science results. *J. Atmos. Solar-Terr. Phys.*, *71*(3-4), 289–299. doi: 10.1016/j.jastp.2008.08.011

Sadykov, V. M., Kosovichev, A. G., Oria, V., & Nita, G. M. (2017, July). An Interactive Multi-instrument Database of Solar Flares. *Astrophys. J. Suppl.*, *231*, 6. doi: 10.3847/1538-4365/aa79a9

Salem, C., Hubert, D., Lacombe, C., Bale, S. D., Mangeney, A., Larson, D. E., & Lin, R. P. (2003, March). Electron Properties and Coulomb Collisions in the Solar Wind at 1 AU: Wind Observations. *Astrophys. J.*, *585*, 1147–1157. doi: 10.1086/346185

Salem, C., Mangeney, A., Bale, S. D., & Veltri, P. (2009, September). Solar Wind Magnetohydrodynamics Turbulence: Anomalous Scaling and Role of Intermittency. *Astrophys. J.*, *702*, 537–553. doi: 10.1088/0004-637X/702/1/537

Salman, T. M., Winslow, R. M., & Lugaz, N. (2020, January). Radial Evolution of Coronal Mass Ejections Between MESSENGER, Venus Express, STEREO, and L1: Catalog and Analysis. *J. Geophys. Res.*, *125*(1), e27084. doi: 10.1029/2019JA027084

Santolík, O., Gurnett, D. A., Pickett, J. S., Parrot, M., & Cornilleau-Wehrlin, N. (2003, July). Spatio-temporal structure of storm-time chorus. *J. Geophys. Res.*, *108*, 1278. doi: 10.1029/2002JA009791

Santolík, O., Kletzing, C. A., Kurth, W. S., Hospodarsky, G. B., & Bounds, S. R. (2014, January). Fine structure of large-amplitude chorus wave packets. *Geophys. Res. Lett.*, *41*, 293–299. doi: 10.1002/2013GL058889

Santolík, O., Pickett, J. S., Gurnett, D. A., Menietti, J. D., Tsurutani, B. T., & Verkhoglyadova, O. (2010, July). Survey of Poynting flux of whistler mode chorus in the outer zone. *J. Geophys. Res.*, *115*(15), A00F13. doi: 10.1029/2009JA014925

Schiller, Q., Li, X., Blum, L., Tu, W., Turner, D. L., & Blake, J. B. (2014, January). A nonstorm time enhancement of relativistic electrons in the outer radiation belt. *Geophys. Res. Lett.*, *41*, 7–12. doi: 10.1002/2013GL058485

Scholer, M., Ipavich, F. M., Gloeckler, G., Hovestadt, D., & Klecker, B. (1980, January). Upstream particle events close to the bow shock and 200 R_E upstream: ISEE-1 and ISEE-3 observations. *Geophys. Res. Lett.*, *7*(1), 73–76. doi: 10.1029/GL007i001p00073

Schwartz, S. J., & Marsch, E. (1983, December). The radial evolution of a single solar wind plasma parcel. *J. Geophys. Res.*, *88*, 9919–9932. doi: 10.1029/JA088iA12p09919

Share, G. H., Murphy, R. J., White, S. M., Tolbert, A. K., Dennis, B. R., Schwartz, R. A., ... Shea, M. A. (2018, December). Characteristics of Late-phase >100 MeV Gamma-Ray Emission in Solar Eruptive Events. *Astrophys. J.*, *869*, 182. doi: 10.3847/1538-4357/aaebf7

Shodhan, S., Crooker, N. U., Kahler, S. W., Fitzenreiter, R. J., Larson, D. E., Lepping, R. P., ... Gosling, J. T. (2000, December). Counterstreaming electrons in magnetic clouds. *J. Geophys. Res.*, *105*, 27261–27268. doi: 10.1029/2000JA000060

Sibeck, D., Kudela, K., Mukai, T., Nemecek, Z., & Safrankova, J. (2004, December). Radial dependence of foreshock cavities: a case study. *Ann. Geophys.*, *22*,

4143–4151. doi: 10.5194/angeo-22-4143-2004
Sibeck, D. G., Phan, T.-D., Lin, R., Lepping, R. P., & Szabo, A. (2002, October). Wind observations of foreshock cavities: A case study. *J. Geophys. Res.*, *107*, 1271. doi: 10.1029/2001JA007539
Smith, E. J., & Wolfe, J. H. (1976, March). Observations of interaction regions and corotating shocks between one and five AU: Pioneers 10 and 11. *Geophys. Res. Lett.*, *3*(3), 137–140. doi: 10.1029/GL003i003p00137
Sonnerup, B. U. Ö. (1979). Magnetic field reconnection. In *Solar system plasma physics* (Vol. 3, pp. 45–108).
Stansby, D., Horbury, T. S., Chen, C. H. K., & Matteini, L. (2016, September). Experimental Determination of Whistler Wave Dispersion Relation in the Solar Wind. *Astrophys. J. Lett.*, *829*, L16. doi: 10.3847/2041-8205/829/1/L16
Sterken, V. J., Westphal, A. J., Altobelli, N., Malaspina, D., & Postberg, F. (2019, October). Interstellar Dust in the Solar System. *Space Sci. Rev.*, *215*(7), 32. doi: 10.1007/s11214-019-0607-9
Stone, E. C., Frandsen, A. M., Mewaldt, R. A., Christian, E. R., Margolies, D., Ormes, J. F., & Snow, F. (1998, July). The Advanced Composition Explorer. *Space Sci. Rev.*, *86*, 1–22. doi: 10.1023/A:1005082526237
Svinkin, D., Golenetskii, S., Aptekar, R., Frederiks, D., Ridnaia, A., Cline, T., ... Starr, R. (2020, April). Improved IPN error box for GRB 200415A (consistent with the Sculptor Galaxy). *GRB Coordinates Network*, *27595*, 1.
Svinkin, D., Hurley, K., Frederiks, D., Hurley, K., Mitrofanov, I. G., Golovin, D., ... Starr, R. (2020, April). IPN triangulation of GRB 200415A (possible Magnetar Giant Flare in Sculptor Galaxy?). *GRB Coordinates Network*, *27585*, 1.
Svinkin, D. S., Frederiks, D. D., Aptekar, R. L., Golenetskii, S. V., Pal'shin, V. D., Oleynik, P. P., ... Hurley, K. (2016, May). The Second Konus-Wind Catalog of Short Gamma-Ray Bursts. *Astrophys. J. Suppl.*, *224*, 10. doi: 10.3847/0067-0049/224/1/10
Szabo, A., Larson, D., Whittlesey, P., Stevens, M. L., Lavraud, B., Phan, T., ... Pulupa, M. (2020, February). The Heliospheric Current Sheet in the Inner Heliosphere Observed by the Parker Solar Probe. *Astrophys. J. Suppl.*, *246*(2), 47. doi: 10.3847/1538-4365/ab5dac
Takeuchi, T., Araki, T., Luehr, H., Rasmussen, O., Watermann, J., Milling, D. K., ... Nagai, T. (2000, August). Geomagnetic negative sudden impulse due to a magnetic cloud observed on May 13, 1995. *J. Geophys. Res.*, *105*, 18835–18846. doi: 10.1029/2000JA900055
Talebpour Sheshvan, N., & Pohjolainen, S. (2018, November). Visibility and Origin of Compact Interplanetary Radio Type IV Bursts. *Solar Phys.*, *293*, 148. doi: 10.1007/s11207-018-1371-9
Temerin, M., & Roth, I. (1992, June). The Production of 3He and Heavy Ion Enrichments in 3He-rich Flares by Electromagnetic Hydrogen Cyclotron Waves. *Astrophys. J. Lett.*, *391*, L105. doi: 10.1086/186408
Tidman, D. A., & Northrop, T. G. (1968, March). Emission of plasma waves by the Earth's bow shock. *J. Geophys. Res.*, *73*, 1543–1553. doi: 10.1029/JA073i005p01543
Tong, Y., Vasko, I. Y., Pulupa, M., Mozer, F. S., Bale, S. D., Artemyev, A. V., & Krasnoselskikh, V. (2019, January). Whistler Wave Generation by Halo Electrons in the Solar Wind. *Astrophys. J. Lett.*, *870*, L6. doi: 10.3847/2041-8213/aaf734
Tsurutani, B. T., Gonzalez, W. D., Gonzalez, A. L. C., Guarnieri, F. L., Gopalswamy, N., Grande, M., ... Vasyliunas, V. (2006, July). Corotating solar wind streams and recurrent geomagnetic activity: A review. *J. Geophys. Res.*, *111*(A7), A07S01. doi: 10.1029/2005JA011273
Tsurutani, B. T., & Lin, R. P. (1985, January). Acceleration of ¿47 keV ions and ¿2 keV electrons by interplanetary shocks at 1 AU. *J. Geophys. Res.*, *90*(A1), 1–

11. doi: 10.1029/JA090iA01p00001

Tsvetkova, A., Frederiks, D., Golenetskii, S., Lysenko, A., Oleynik, P., Pal'shin, V., ... Aptekar, R. (2017, December). The Konus-Wind Catalog of Gamma-Ray Bursts with Known Redshifts. I. Bursts Detected in the Triggered Mode. *Astrophys. J.*, *850*, 161. doi: 10.3847/1538-4357/aa96af

Turner, D. L., Angelopoulos, V., Morley, S. K., Henderson, M. G., Reeves, G. D., Li, W., ... Rodriguez, J. V. (2014, March). On the cause and extent of outer radiation belt losses during the 30 September 2012 dropout event. *J. Geophys. Res.*, *119*, 1530–1540. doi: 10.1002/2013JA019446

Valdivia, J. A., Toledo, B. A., Gallo, N., Muñoz, V., Rogan, J., Stepanova, M., ... Díaz, M. (2016, November). Magnetic fluctuations in anisotropic space plasmas: The effect of the plasma environment. *Adv. Space Res.*, *58*, 2126–2133. doi: 10.1016/j.asr.2016.04.017

Vandas, M., Fischer, S., Pelant, P., & Geranios, A. (1993, December). Evidence for a spheroidal structure of magnetic clouds. *J. Geophys. Res.*, *98*(A12), 21061–21070. doi: 10.1029/93JA01749

Vandas, M., Geranios, A., & Romashets, E. (2009, August). On expansion of magnetic clouds in the solar wind. *Astrophys. Space Sci. Trans.*, *5*, 35–38. doi: 10.5194/astra-5-35-2009

Vasko, I. Y., Krasnoselskikh, V., Tong, Y., Bale, S. D., Bonnell, J. W., & Mozer, F. S. (2019, February). Whistler Fan Instability Driven by Strahl Electrons in the Solar Wind. *Astrophys. J. Lett.*, *871*, L29. doi: 10.3847/2041-8213/ab01bd

Vasko, I. Y., Kuzichev, I. V., Artemyev, A. V., Bale, S. D., Bonnell, J. W., & Mozer, F. S. (2020, August). On quasi-parallel whistler waves in the solar wind. *Phys. Plasmas*, *27*(8), 082902. doi: 10.1063/5.0003401

Vasko, I. Y., Mozer, F. S., Krasnoselskikh, V. V., Artemyev, A. V., Agapitov, O. V., Bale, S. D., ... Torbert, R. (2018, June). Solitary Waves Across Supercritical Quasi-Perpendicular Shocks. *Geophys. Res. Lett.*, *45*(12), 5809–5817. doi: 10.1029/2018GL077835

Vech, D., Mallet, A., Klein, K. G., & Kasper, J. C. (2018, March). Magnetic Reconnection May Control the Ion-scale Spectral Break of Solar Wind Turbulence. *Astrophys. J. Lett.*, *855*, L27. doi: 10.3847/2041-8213/aab351

Velli, M., Harra, L. K., Vourlidas, A., Schwadron, N., Panasenco, O., Liewer, P. C., ... Maksimovic, M. (2020, September). Understanding the origins of the heliosphere: Integrating observations and measurements from Parker Solar Probe, Solar Orbiter and Other space and ground based observatories. *Astron. & Astrophys.*. (in press) doi: 10.1051/0004-6361/202038245

Verdini, A., Grappin, R., Alexandrova, O., Franci, L., Landi, S., Matteini, L., & Papini, E. (2019, July). Three-dimensional local anisotropy of velocity fluctuations in the solar wind. *Mon. Not. Roy. Astron. Soc.*, *486*(3), 3006–3018. doi: 10.1093/mnras/stz1041

Verdini, A., Grappin, R., Alexandrova, O., & Lion, S. (2018, January). 3D Anisotropy of Solar Wind Turbulence, Tubes, or Ribbons? *Astrophys. J.*, *853*, 85. doi: 10.3847/1538-4357/aaa433

Verscharen, D., Bourouaine, S., & Chand ran, B. D. G. (2013, August). Instabilities Driven by the Drift and Temperature Anisotropy of Alpha Particles in the Solar Wind. *Astrophys. J.*, *773*(2), 163. doi: 10.1088/0004-637X/773/2/163

Verscharen, D., Chandran, B. D. G., Jeong, S.-Y., Salem, C. S., Pulupa, M. P., & Bale, S. D. (2019, December). Self-induced Scattering of Strahl Electrons in the Solar Wind. *Astrophys. J.*, *886*(2), 136. doi: 10.3847/1538-4357/ab4c30

Verscharen, D., Chen, C. H. K., & Wicks, R. T. (2017, May). On Kinetic Slow Modes, Fluid Slow Modes, and Pressure-balanced Structures in the Solar Wind. *Astrophys. J.*, *840*, 106. doi: 10.3847/1538-4357/aa6a56

Verscharen, D., Klein, K. G., & Maruca, B. A. (2019, December). The multi-scale nature of the solar wind. *Living Reviews in Solar Physics*, *16*(1), 5. doi: 10.1007/s41116-019-0021-0

Viñas, A. F., Moya, P. S., Navarro, R., & Araneda, J. A. (2014, January). The role of higher-order modes on the electromagnetic whistler-cyclotron wave fluctuations of thermal and non-thermal plasmas. *Phys. Plasmas*, *21*(1), 012902. doi: 10.1063/1.4861865

von Rosenvinge, T. T., Barbier, L. M., Karsch, J., Liberman, R., Madden, M. P., Nolan, T., ... Walpole, P. (1995, February). The Energetic Particles: Acceleration, Composition, and Transport (EPACT) investigation on the WIND spacecraft. *Space Sci. Rev.*, *71*, 155–206. doi: 10.1007/BF00751329

Vršnak, B., Amerstorfer, T., Dumbović, M., Leitner, M., Veronig, A. M., Temmer, M., ... Galvin, A. B. (2019, June). Heliospheric Evolution of Magnetic Clouds. *Astrophys. J.*, *877*(2), 77. doi: 10.3847/1538-4357/ab190a

Vršnak, B., Aurass, H., Magdalenić, J., & Gopalswamy, N. (2001, October). Band-splitting of coronal and interplanetary type II bursts. I. Basic properties. *Astron. & Astrophys.*, *377*, 321–329. doi: 10.1051/0004-6361:20011067

Šafránková, J., Němeček, Z., Němec, F., Verscharen, D., Chen, C. H. K., Ďurovcová, T., & Riazantseva, M. O. (2019, January). Scale-dependent Polarization of Solar Wind Velocity Fluctuations at the Inertial and Kinetic Scales. *Astrophys. J.*, *870*(1), 40. doi: 10.3847/1538-4357/aaf239

Walker, S. N., Balikhin, M. A., Alleyne, H. S. C. K., Hobara, Y., André, M., & Dunlop, M. W. (2008, March). Lower hybrid waves at the shock front: a reassessment. *Ann. Geophys.*, *26*, 699–707.

Wang, L., Krucker, S., Mason, G. M., Lin, R. P., & Li, G. (2016, January). The injection of ten electron/^{3}He-rich SEP events. *Astron. & Astrophys.*, *585*, A119. doi: 10.1051/0004-6361/201527270

Wang, L., Lin, R. P., & Krucker, S. (2011, February). Pitch-angle Distributions and Temporal Variations of 0.3-300 keV Solar Impulsive Electron Events. *Astrophys. J.*, *727*, 121. doi: 10.1088/0004-637X/727/2/121

Wang, L., Lin, R. P., Krucker, S., & Gosling, J. T. (2006, February). Evidence for double injections in scatter-free solar impulsive electron events. *Geophys. Res. Lett.*, *330*, L03106. doi: 10.1029/2005GL024434

Wang, Y., Shen, C., Liu, R., Liu, J., Guo, J., Li, X., ... Zhang, T. (2018, May). Understanding the Twist Distribution Inside Magnetic Flux Ropes by Anatomizing an Interplanetary Magnetic Cloud. *J. Geophys. Res.*, *123*, 3238–3261. doi: 10.1002/2017JA024971

Whipple, E., & Lancaster, H. (1995, February). International Coordination of Solar Terrestrial Science. *Space Sci. Rev.*, *71*(1-4), 41–54. doi: 10.1007/BF00751325

Wicks, R. T., Alexander, R. L., Stevens, M. L., Wilson III, L. B., Moya, P. S., Viñas, A. F., ... Zurbuchen, T. H. (2016, March). A Proton-cyclotron Wave Storm Generated by Unstable Proton Distribution Functions in the Solar Wind. *Astrophys. J.*, *819*(1), 6. doi: 10.3847/0004-637X/819/1/6

Wicks, R. T., Chapman, S. C., & Dendy, R. O. (2009, January). Spatial Correlation of Solar Wind Fluctuations and Their Solar Cycle Dependence. *Astrophys. J.*, *690*, 734–742. doi: 10.1088/0004-637X/690/1/734

Wicks, R. T., Horbury, T. S., Chen, C. H. K., & Schekochihin, A. A. (2011, January). Anisotropy of Imbalanced Alfvénic Turbulence in Fast Solar Wind. *Phys. Rev. Lett.*, *106*, 045001. doi: 10.1103/PhysRevLett.106.045001

Wicks, R. T., Mallet, A., Horbury, T. S., Chen, C. H. K., Schekochihin, A. A., & Mitchell, J. J. (2013, January). Alignment and Scaling of Large-Scale Fluctuations in the Solar Wind. *Phys. Rev. Lett.*, *110*(2), 025003. doi: 10.1103/PhysRevLett.110.025003

Wicks, R. T., Owens, M. J., & Horbury, T. S. (2010, March). The Variation of Solar Wind Correlation Lengths Over Three Solar Cycles. *Solar Phys.*, *262*, 191–

198. doi: 10.1007/s11207-010-9509-4

Wicks, R. T., Roberts, D. A., Mallet, A., Schekochihin, A. A., Horbury, T. S., & Chen, C. H. K. (2013, December). Correlations at Large Scales and the Onset of Turbulence in the Fast Solar Wind. *Astrophys. J.*, *778*(2), 177. doi: 10.1088/0004-637X/778/2/177

Wild, J. P., Smerd, S. F., & Weiss, A. A. (1963, January). Solar Bursts. *Ann. Rev. Astron. Astrophys.*, *1*, 291–366. doi: 10.1146/annurev.aa.01.090163.001451

Wilson III, L. B. (2010). *The microphysics of collisionless shocks* (Unpublished doctoral dissertation). University of Minnesota.

Wilson III, L. B. (2016, February). Low frequency waves at and upstream of collisionless shocks. In A. Keiling, D.-H. Lee, & V. Nakariakov (Eds.), *Low-frequency Waves in Space Plasmas* (Vol. 216, pp. 269–291). Washington, D.C.: American Geophysical Union. doi: 10.1002/9781119055006.ch16

Wilson III, L. B. (2020, June). Wind WAVES TDSF Dataset. In *Zenodo wind waves tdsf dataset* (Vol. 39, p. 11205). doi: 10.5281/zenodo.3911205

Wilson III, L. B., Cattell, C., Kellogg, P. J., Goetz, K., Kersten, K., Hanson, L., ... Kasper, J. C. (2007, July). Waves in Interplanetary Shocks: A Wind/WAVES Study. *Phys. Rev. Lett.*, *99*, 041101-+. doi: 10.1103/PhysRevLett.99.041101

Wilson III, L. B., Cattell, C. A., Kellogg, P. J., Goetz, K., Kersten, K., Kasper, J. C., ... Meziane, K. (2009, October). Low-frequency whistler waves and shocklets observed at quasi-perpendicular interplanetary shocks. *J. Geophys. Res.*, *114*, A10106. doi: 10.1029/2009JA014376

Wilson III, L. B., Cattell, C. A., Kellogg, P. J., Goetz, K., Kersten, K., Kasper, J. C., ... Wilber, M. (2010, December). Large-amplitude electrostatic waves observed at a supercritical interplanetary shock. *J. Geophys. Res.*, *115*, A12104. doi: 10.1029/2010JA015332

Wilson III, L. B., Cattell, C. A., Kellogg, P. J., Wygant, J. R., Goetz, K., Breneman, A., & Kersten, K. (2011, September). The properties of large amplitude whistler mode waves in the magnetosphere: Propagation and relationship with geomagnetic activity. *Geophys. Res. Lett.*, *38*, 17107. doi: 10.1029/2011GL048671

Wilson III, L. B., Chen, L.-J., Wang, S., Schwartz, S. J., Turner, D. L., Stevens, M. L., ... Goodrich, K. A. (2019a, December). Electron Energy Partition across Interplanetary Shocks. II. Statistics. *Astrophys. J. Suppl.*, *245*(2), 24. doi: 10.3847/1538-4365/ab5445

Wilson III, L. B., Chen, L.-J., Wang, S., Schwartz, S. J., Turner, D. L., Stevens, M. L., ... Goodrich, K. A. (2019b, July). Electron Energy Partition across Interplanetary Shocks. I. Methodology and Data Product. *Astrophys. J. Suppl.*, *243*(1), 8. doi: 10.3847/1538-4365/ab22bd

Wilson III, L. B., Chen, L.-J., Wang, S., Schwartz, S. J., Turner, D. L., Stevens, M. L., ... Goodrich, K. A. (2019c, May). Supplement to: Electron energy partition across interplanetary shocks. In *Zenodo supplementary pdf and two ascii files* (Vol. 28, p. 75806). doi: 10.5281/zenodo.2875806

Wilson III, L. B., Chen, L.-J., Wang, S., Schwartz, S. J., Turner, D. L., Stevens, M. L., ... Goodrich, K. A. (2020a, April). Electron Energy Partition across Interplanetary Shocks. III. Analysis. *Astrophys. J.*, *893*(22), 21. doi: 10.3847/1538-4357/ab7d39

Wilson III, L. B., Chen, L.-J., Wang, S., Schwartz, S. J., Turner, D. L., Stevens, M. L., ... Goodrich, K. A. (2020b, January). Supplement to: Electron energy partition across interplanetary shocks: III. Analysis. In *Zenodo supplementary pdf* (Vol. 36, p. 27284). doi: 10.5281/zenodo.3627284

Wilson III, L. B., Koval, A., Sibeck, D. G., Szabo, A., Cattell, C. A., Kasper, J. C., ... Wilber, M. (2013, March). Shocklets, SLAMS, and field-aligned ion beams in the terrestrial foreshock. *J. Geophys. Res.*, *118*, 957–966. doi: 10.1029/2012JA018186

Wilson III, L. B., Koval, A., Szabo, A., Breneman, A., Cattell, C. A., Goetz, K., … Pulupa, M. (2012, April). Observations of electromagnetic whistler precursors at supercritical interplanetary shocks. *Geophys. Res. Lett.*, *39*, 8109. doi: 10.1029/2012GL051581

Wilson III, L. B., Koval, A., Szabo, A., Breneman, A., Cattell, C. A., Goetz, K., … Pulupa, M. (2013, January). Electromagnetic waves and electron anisotropies downstream of supercritical interplanetary shocks. *J. Geophys. Res.*, *118*, 5–16. doi: 10.1029/2012JA018167

Wilson III, L. B., Koval, A., Szabo, A., Stevens, M. L., Kasper, J. C., Cattell, C. A., & Krasnoselskikh, V. V. (2017, October). Revisiting the structure of low Mach number, low beta, quasi-perpendicular shocks. *J. Geophys. Res.*, *122*(9), 9115–9133. doi: 10.1002/2017JA024352

Wilson III, L. B., Sibeck, D. G., Turner, D. L., Osmane, A., Caprioli, D., & Angelopoulos, V. (2016, November). Relativistic electrons produced by foreshock disturbances observed upstream of the Earth's bow shock. *Phys. Rev. Lett.*, *117*(21), 215101. (Editors' Suggestion) doi: 10.1103/PhysRevLett.117.215101

Wilson III, L. B., Stevens, M. L., Kasper, J. C., Klein, K. G., Maruca, B. A., Bale, S. D., … Salem, C. S. (2018, June). The Statistical Properties of Solar Wind Temperature Parameters Near 1 au. *Astrophys. J. Suppl.*, *236*, 41. doi: 10.3847/1538-4365/aab71c

Winslow, R. M., Lugaz, N., Schwadron, N. A., Farrugia, C. J., Yu, W., Raines, J. M., … Zurbuchen, T. H. (2016, July). Longitudinal conjunction between MESSENGER and STEREO A: Development of ICME complexity through stream interactions. *J. Geophys. Res.*, *121*(7), 6092–6106. doi: 10.1002/2015JA022307

Winter, L. M., & Ledbetter, K. (2015, August). Type II and Type III Radio Bursts and their Correlation with Solar Energetic Proton Events. *Astrophys. J.*, *809*, 105. doi: 10.1088/0004-637X/809/1/105

Wong, H. V. (1970, March). Electrostatic Electron-Ion Streaming Instability. *Phys. Fluids*, *13*, 757–760. doi: 10.1063/1.1692983

Wood, B. E., Wu, C.-C., Lepping, R. P., Nieves-Chinchilla, T., Howard, R. A., Linton, M. G., & Socker, D. G. (2017, April). A STEREO Survey of Magnetic Cloud Coronal Mass Ejections Observed at Earth in 2008–2012. *Astrophys. J. Suppl.*, *229*, 29. doi: 10.3847/1538-4365/229/2/29

Wood, S. R., Malaspina, D. M., Andersson, L., & Horanyi, M. (2015, September). Hypervelocity dust impacts on the Wind spacecraft: Correlations between Ulysses and Wind interstellar dust detections. *J. Geophys. Res.*, *120*, 7121–7129. doi: 10.1002/2015JA021463

Woodham, L. D., Wicks, R. T., Verscharen, D., & Owen, C. J. (2018, March). The Role of Proton Cyclotron Resonance as a Dissipation Mechanism in Solar Wind Turbulence: A Statistical Study at Ion-kinetic Scales. *Astrophys. J.*, *856*, 49. doi: 10.3847/1538-4357/aab03d

Woodham, L. D., Wicks, R. T., Verscharen, D., Owen, C. J., Maruca, B. A., & Alterman, B. L. (2019, October). Parallel-propagating Fluctuations at Proton-kinetic Scales in the Solar Wind Are Dominated By Kinetic Instabilities. *Astrophys. J. Lett.*, *884*(2), L53. doi: 10.3847/2041-8213/ab4adc

Wu, C.-C., & Lepping, R. P. (2015, April). Comparisons of Characteristics of Magnetic Clouds and Cloud-Like Structures During 1995 - 2012. *Solar Phys.*, *290*, 1243–1269. doi: 10.1007/s11207-015-0656-5

Wu, C. S., Winske, D., Papadopoulos, K., Zhou, Y. M., Tsai, S. T., & Guo, S. C. (1983, May). A kinetic cross-field streaming instability. *Phys. Fluids*, *26*, 1259–1267. doi: 10.1063/1.864285

Wu, C. S., Winske, D., Tanaka, M., Papadopoulos, K., Akimoto, K., Goodrich, C. C., … Lin, C. S. (1984, January). Microinstabilities associated with a high Mach number, perpendicular bow shock. *Space Sci. Rev.*, *37*, 63–109. doi:

10.1007/BF00213958

Wygant, J. R., Bonnell, J. W., Goetz, K., Ergun, R. E., Mozer, F. S., Bale, S. D., . . . Tao, J. B. (2013, November). The Electric Field and Waves Instruments on the Radiation Belt Storm Probes Mission. *Space Sci. Rev.*, *179* (1-4), 183–220. doi: 10.1007/s11214-013-0013-7

Xystouris, G., Sigala, E., & Mavromichalaki, H. (2014, March). A Complete Catalogue of High-Speed Solar Wind Streams during Solar Cycle 23. *Solar Phys.*, *289*, 995–1012. doi: 10.1007/s11207-013-0355-z

Zesta, E., & Sibeck, D. G. (2004, January). A detailed description of the solar wind triggers of two dayside transients: Events of 25 July 1997. *J. Geophys. Res.*, *109*, 1201. doi: 10.1029/2003JA009864

Zhang, J., Richardson, I. G., Webb, D. F., Gopalswamy, N., Huttunen, E., Kasper, J. C., . . . Zhukov, A. N. (2007, October). Solar and interplanetary sources of major geomagnetic storms (Dst $\leq$ -100 nT) during 1996-2005. *J. Geophys. Res.*, *112*, A10102. doi: 10.1029/2007JA012321

Zhao, X., Liu, Y. D., Hu, H., & Wang, R. (2019, September). Quantifying the Propagation of Fast Coronal Mass Ejections from the Sun to Interplanetary Space by Combining Remote Sensing and Multi-point In Situ Observations. *Astrophys. J.*, *882* (2), 122. doi: 10.3847/1538-4357/ab379b

Zhao, X. H., Feng, X. S., Feng, H. Q., & Li, Z. (2017, November). Correlation between Angular Widths of CMEs and Characteristics of Their Source Regions. *Astrophys. J.*, *849*, 79. doi: 10.3847/1538-4357/aa8e49

Zhdankin, V., Boldyrev, S., & Mason, J. (2012, December). Distribution of Magnetic Discontinuities in the Solar Wind and in Magnetohydrodynamic Turbulence. *Astrophys. J. Lett.*, *760*, L22. doi: 10.1088/2041-8205/760/2/L22

Zurbuchen, T. H., & Richardson, I. G. (2006, March). In-Situ Solar Wind and Magnetic Field Signatures of Interplanetary Coronal Mass Ejections. *Space Sci. Rev.*, *123* (1-3), 31–43. doi: 10.1007/s11214-006-9010-4

Figure 1.

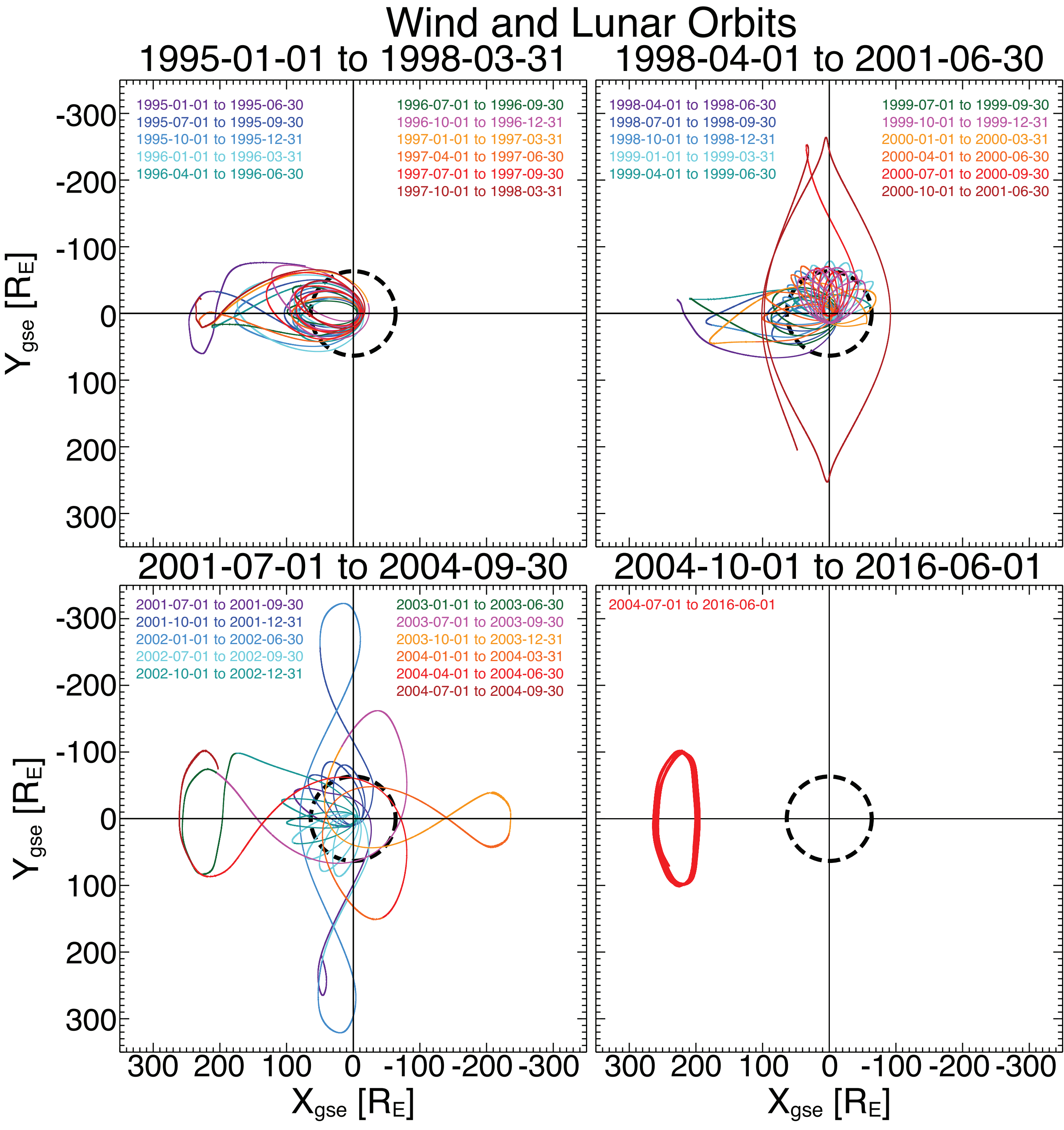

Wind and Lunar Orbits
1995-01-01 to 1998-03-31
1995-01-01 to 1995-06-30
1995-07-01 to 1995-09-30
1995-10-01 to 1995-12-31
1996-01-01 to 1996-03-31
1996-04-01 to 1996-06-30
1996-07-01 to 1996-09-30
1996-10-01 to 1996-12-31
1997-01-01 to 1997-03-31
1997-04-01 to 1997-06-30
1997-07-01 to 1997-09-30
1997-10-01 to 1998-03-31
1998-04-01 to 2001-06-30
1998-04-01 to 1998-06-30
1998-07-01 to 1998-09-30
1998-10-01 to 1998-12-31
1999-01-01 to 1999-03-31
1999-04-01 to 1999-06-30
1999-07-01 to 1999-09-30
1999-10-01 to 1999-12-31
2000-01-01 to 2000-03-31
2000-04-01 to 2000-06-30
2000-07-01 to 2000-09-30
2000-10-01 to 2001-06-30
2001-07-01 to 2004-09-30
2001-07-01 to 2001-09-30
2001-10-01 to 2001-12-31
2002-01-01 to 2002-06-30
2002-07-01 to 2002-09-30
2002-10-01 to 2002-12-31
2003-01-01 to 2003-06-30
2003-07-01 to 2003-09-30
2003-10-01 to 2003-12-31
2004-01-01 to 2004-03-31
2004-04-01 to 2004-06-30
2004-07-01 to 2004-09-30
2004-10-01 to 2016-06-01
2004-07-01 to 2016-06-01
Y_{gse} [R_E]
X_{gse} [R_E]
-300
-200
-100
0
100
200
300

Figure 2.

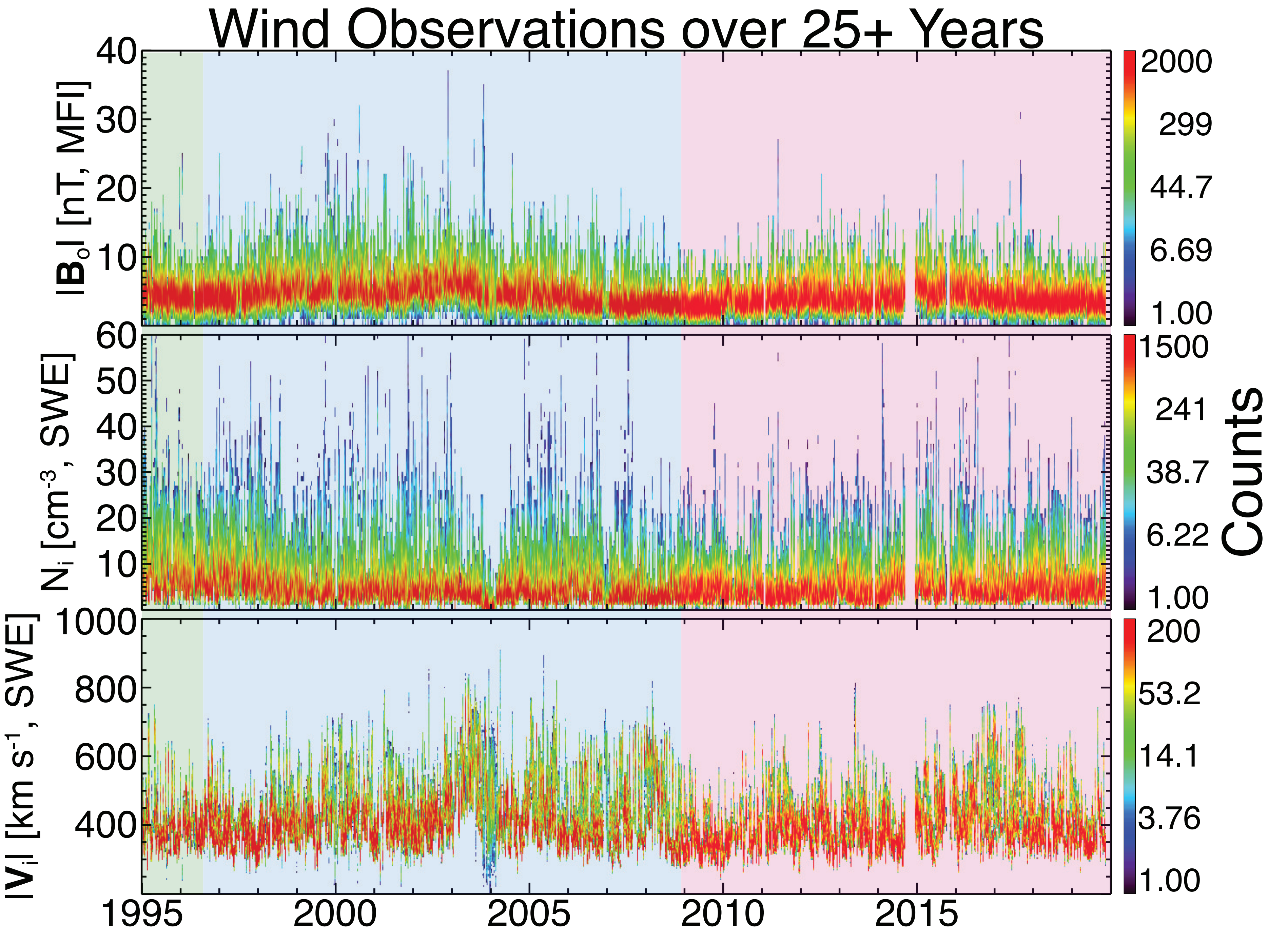

Wind Observations over 25+ Years
|B_o| [nT, MFI]
40
30
20
10
2000
299
44.7
6.69
1.00
N_i [cm^-3, SWE]
60
50
40
30
20
10
1500
241
38.7
6.22
1.00
Counts
|V_i| [km s^-1, SWE]
1000
800
600
400
200
53.2
14.1
3.76
1.00
1995
2000
2005
2010
2015

Figure 3.

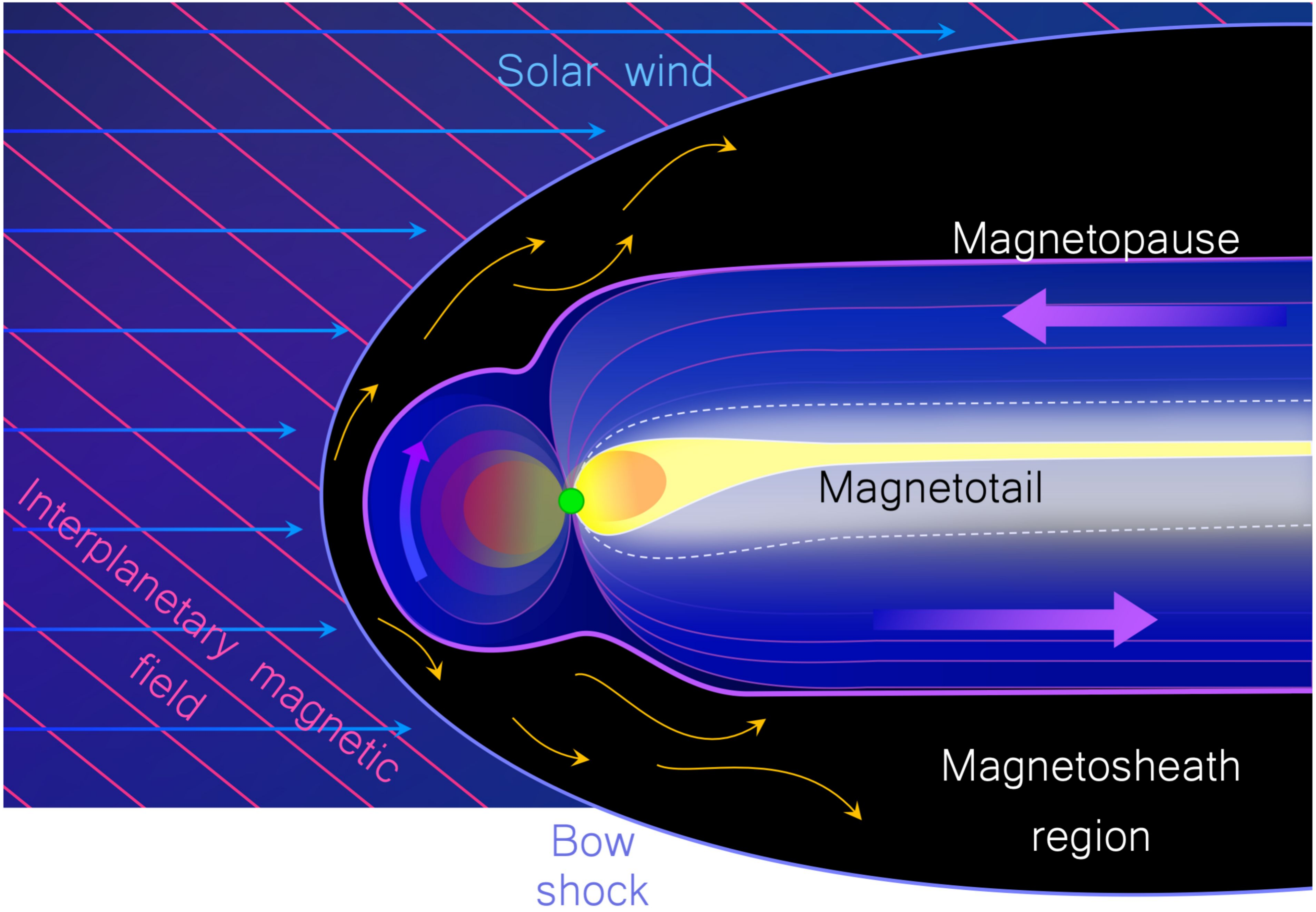
Solar wind
Magnetopause
Magnetotail
Interplanetary magnetic field
Magnetosheath region
Bow shock

Figure 4.

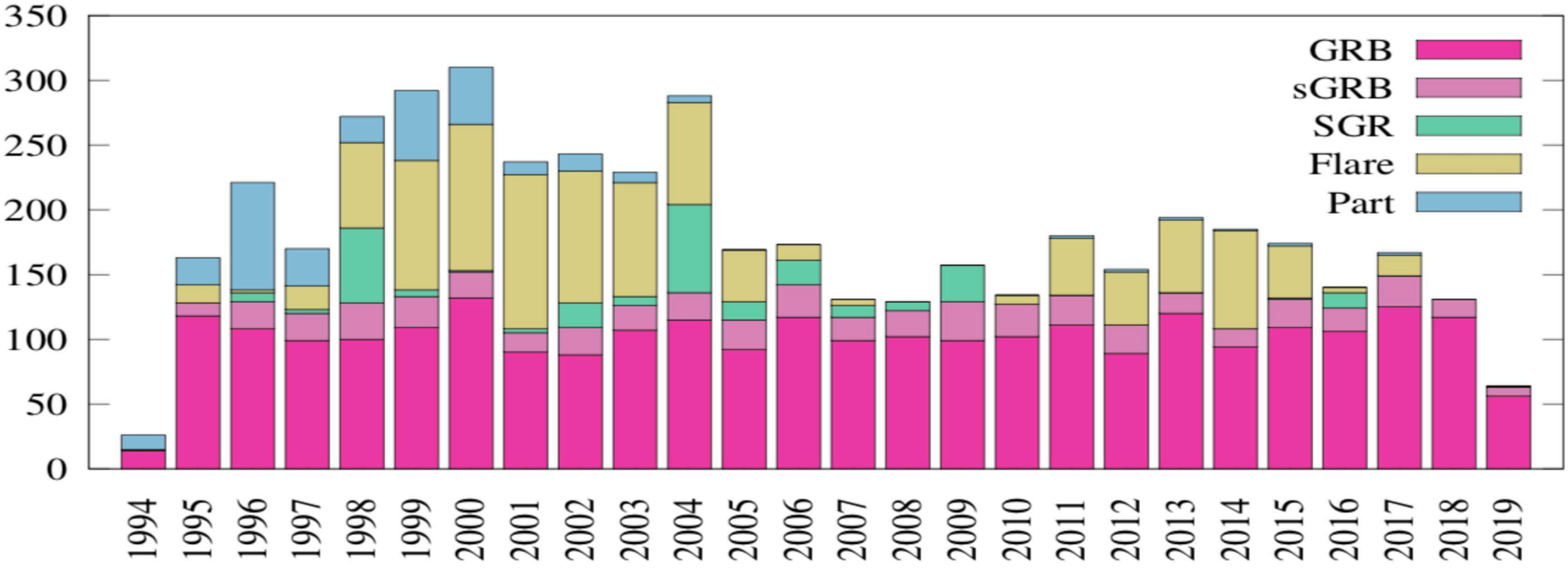

Statistic of ~4700 KW triggers from November 1994 to mid-2019.

Figure 5.

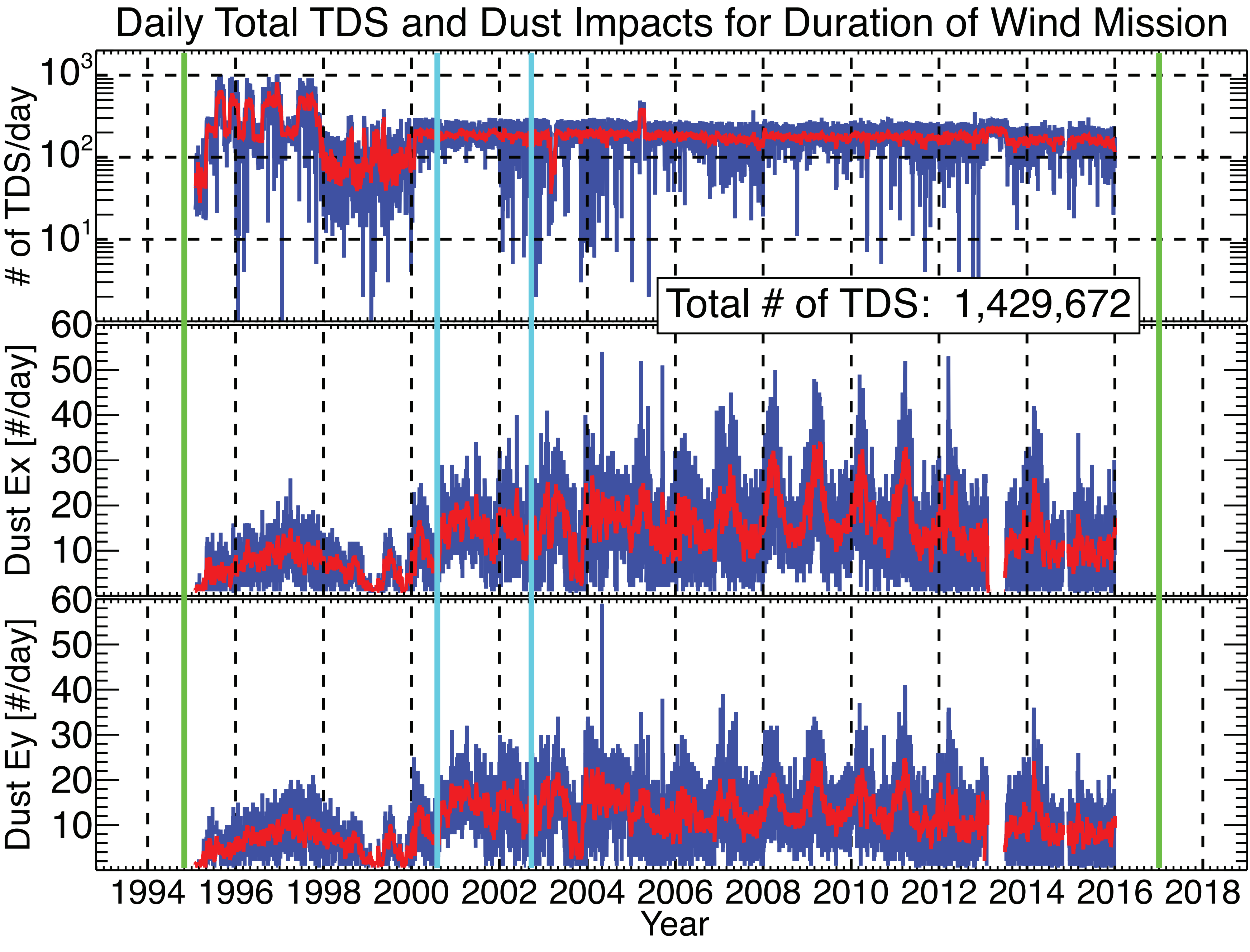

Daily Total TDS and Dust Impacts for Duration of Wind Mission
# of TDS/day
Total # of TDS: 1,429,672
Dust Ex [#/day]
Dust Ey [#/day]
Year

Figure 6.

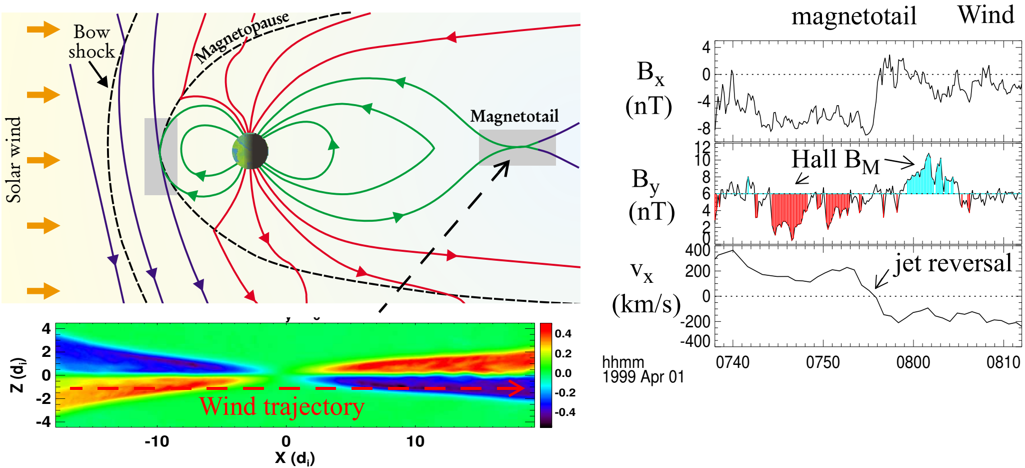

Solar wind
Bow shock
Magnetopause
Magnetotail
Z (d_i)
X (d_i)
Wind trajectory
magnetotail
Wind
Bx (nT)
By (nT)
Hall BM
vx (km/s)
jet reversal
hhmm
1999 Apr 01
0740
0750
0800
0810

Figure 7.

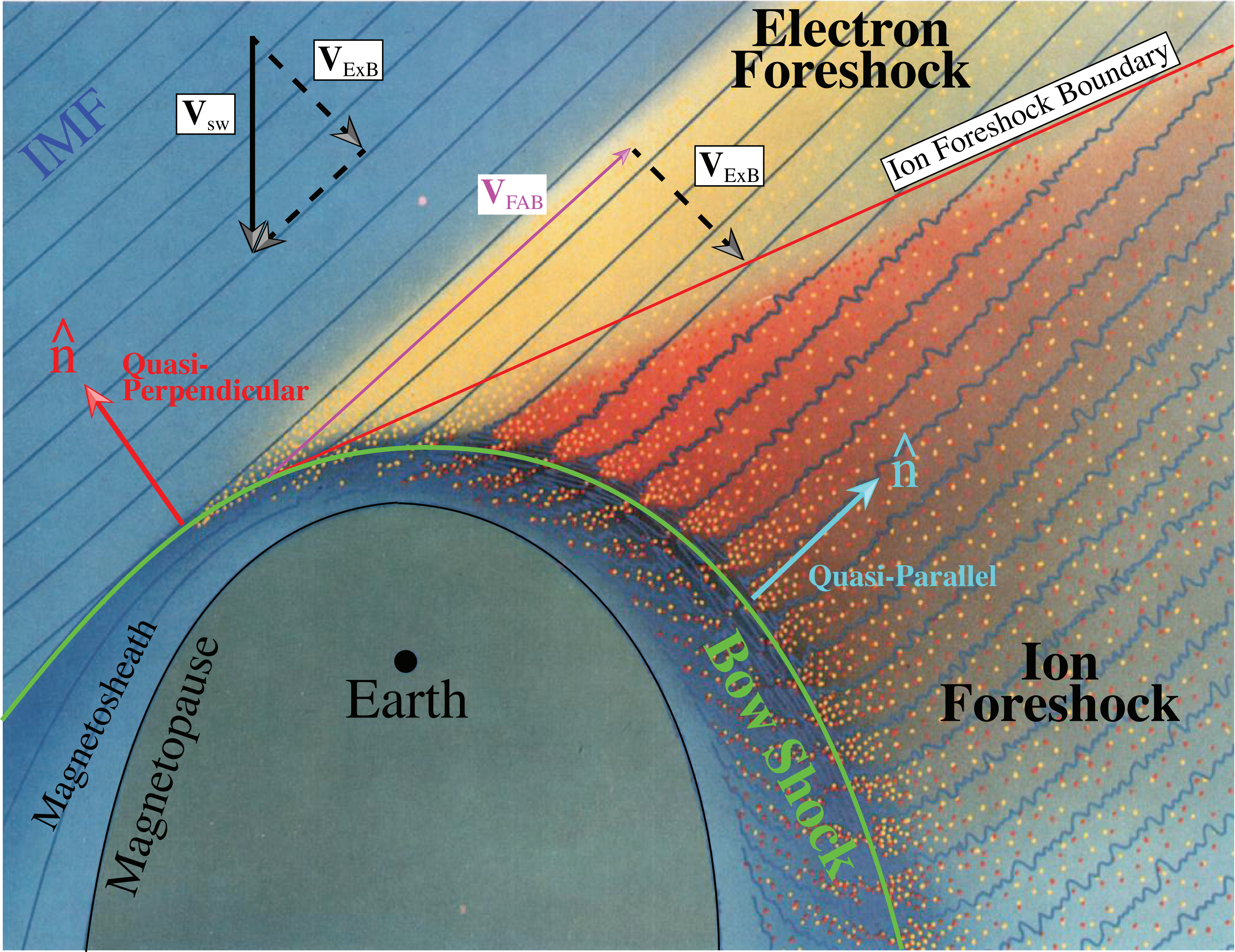

Electron Foreshock
IMF
V_{ExB}
V_{sw}
Ion Foreshock Boundary
V_{FAB}
V_{ExB}
$\hat{n}$
Quasi-Perpendicular
$\hat{n}$
Quasi-Parallel
Earth
Magnetosheath
Magnetopause
Bow Shock
Ion Foreshock

Figure 8.

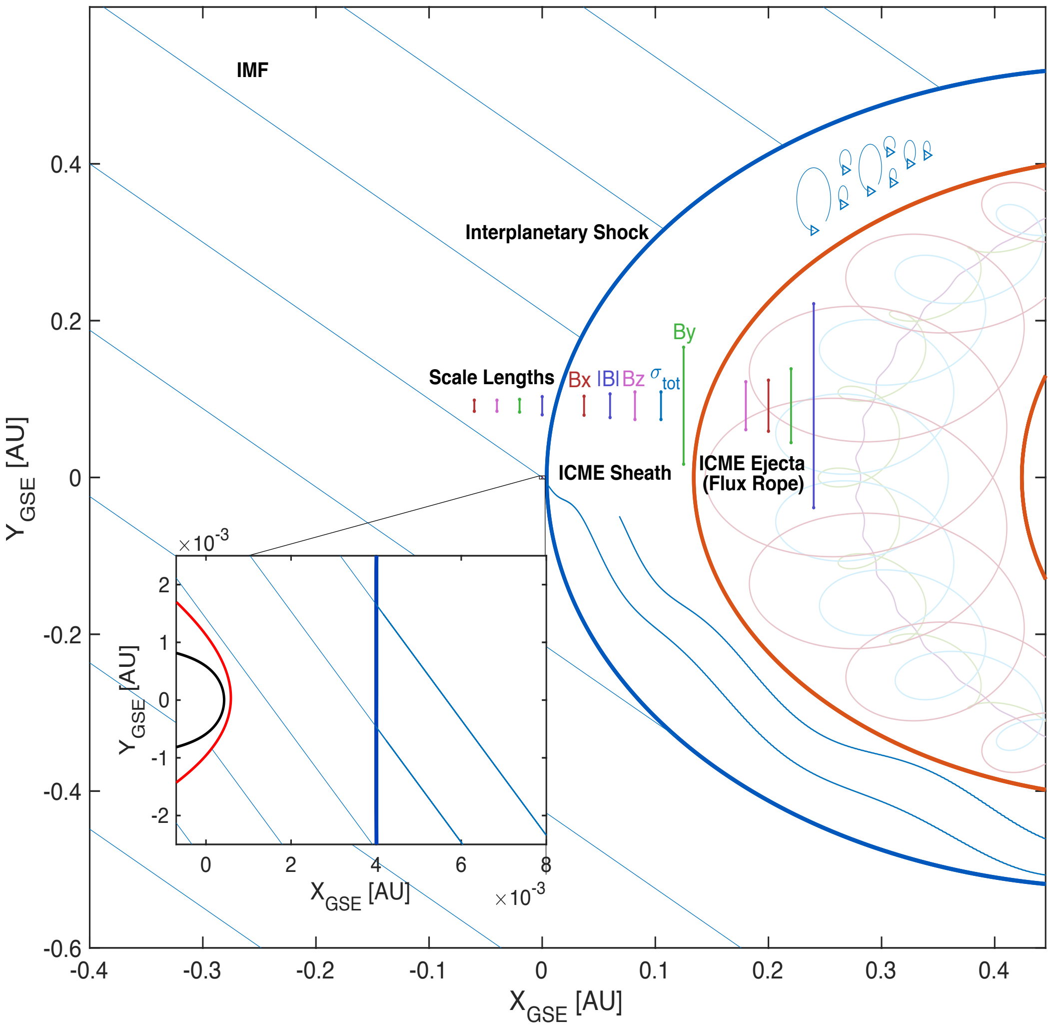
IMF
Interplanetary Shock
Scale Lengths
Bx
|B|
Bz
σ tot
By
ICME Sheath
ICME Ejecta
(Flux Rope)
Y GSE [AU]
X GSE [AU]
×10-3

Figure 9.

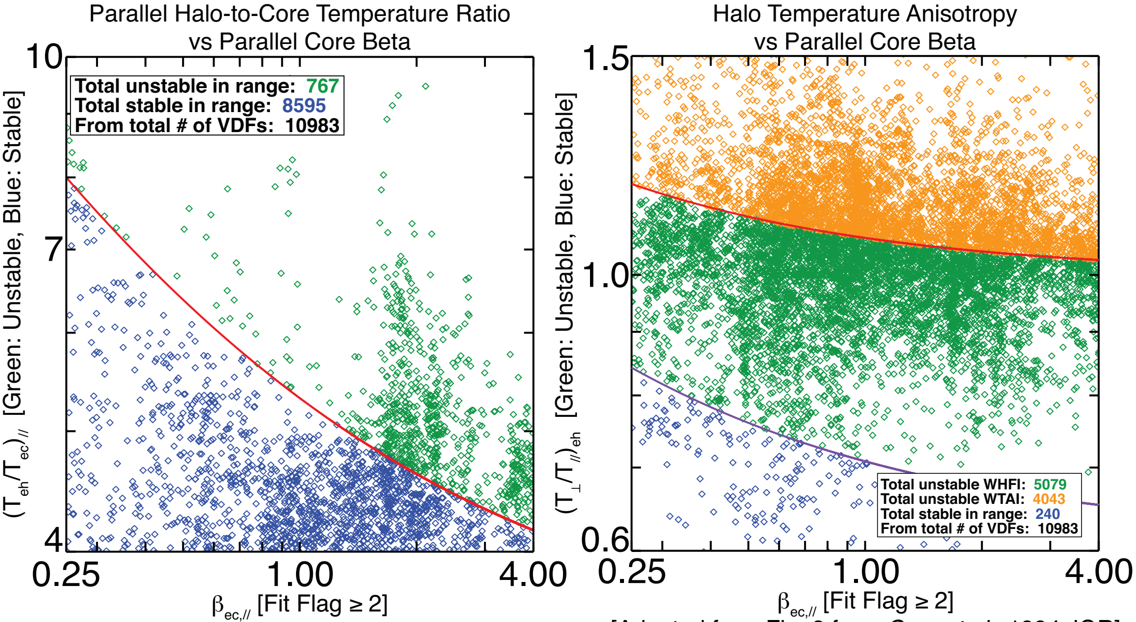

[Adapted from Fig. 7 from *Gary et al.*, 1994 JGR]

[Adapted from Fig. 8 from *Gary et al.*, 1994 JGR]

Figure 10.

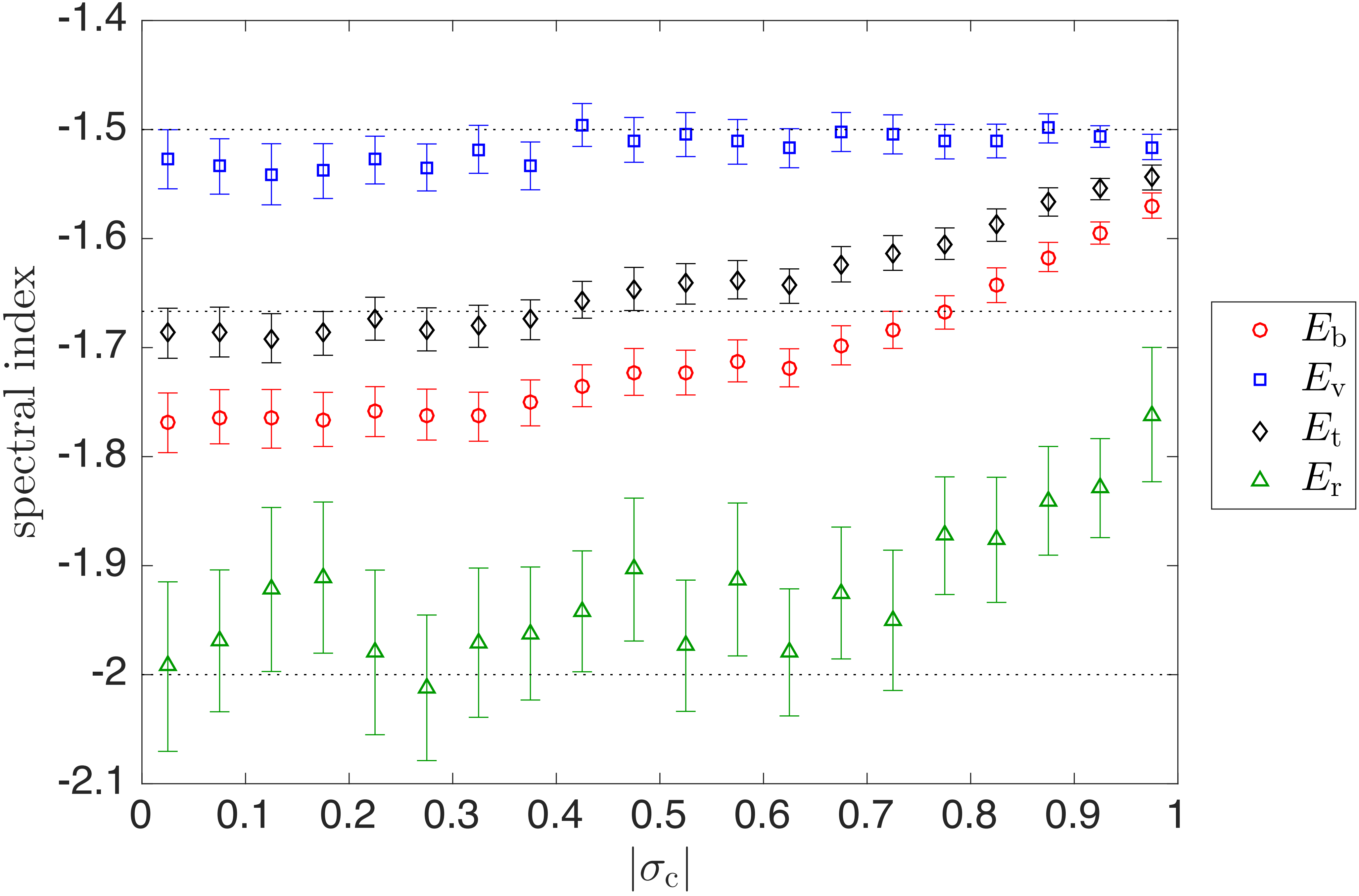

spectral index
-1.4
-1.5
-1.6
-1.7
-1.8
-1.9
-2
-2.1
0
0.1
0.2
0.3
0.4
0.5
0.6
0.7
0.8
0.9
1
$|\sigma_{\rm c}|$
$E_{\rm b}$
$E_{\rm v}$
$E_{\rm t}$
$E_{\rm r}$

Figure 11.

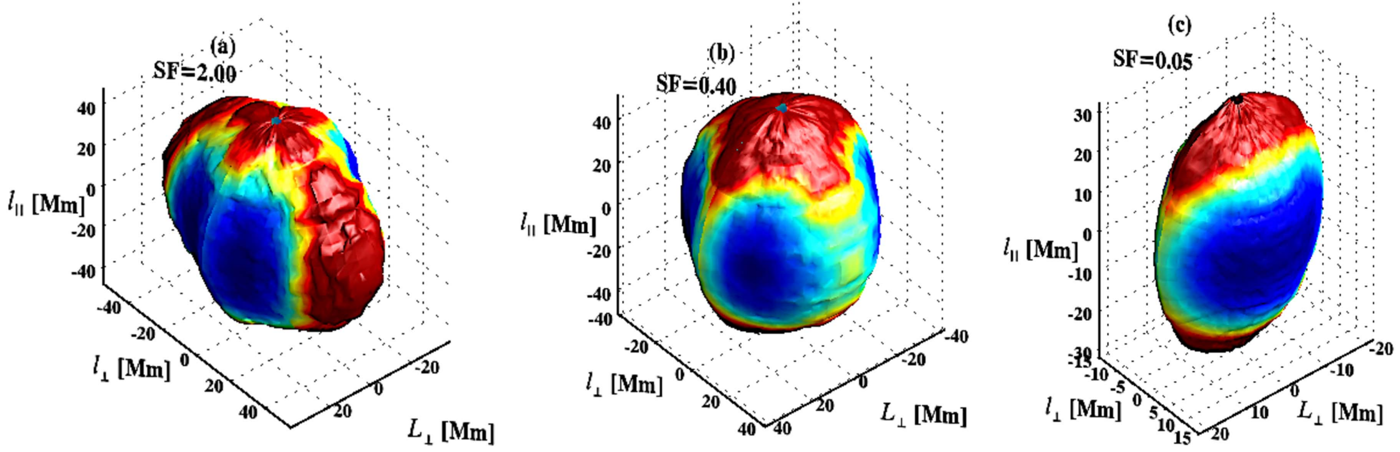

(a)
SF=2.00
$l_{||}$ [Mm]
$l_{\perp}$ [Mm]
$L_{\perp}$ [Mm]
(b)
SF=0.40
$l_{||}$ [Mm]
$l_{\perp}$ [Mm]
$L_{\perp}$ [Mm]
(c)
SF=0.05
$l_{||}$ [Mm]
$l_{\perp}$ [Mm]
$L_{\perp}$ [Mm]

Figure 12.

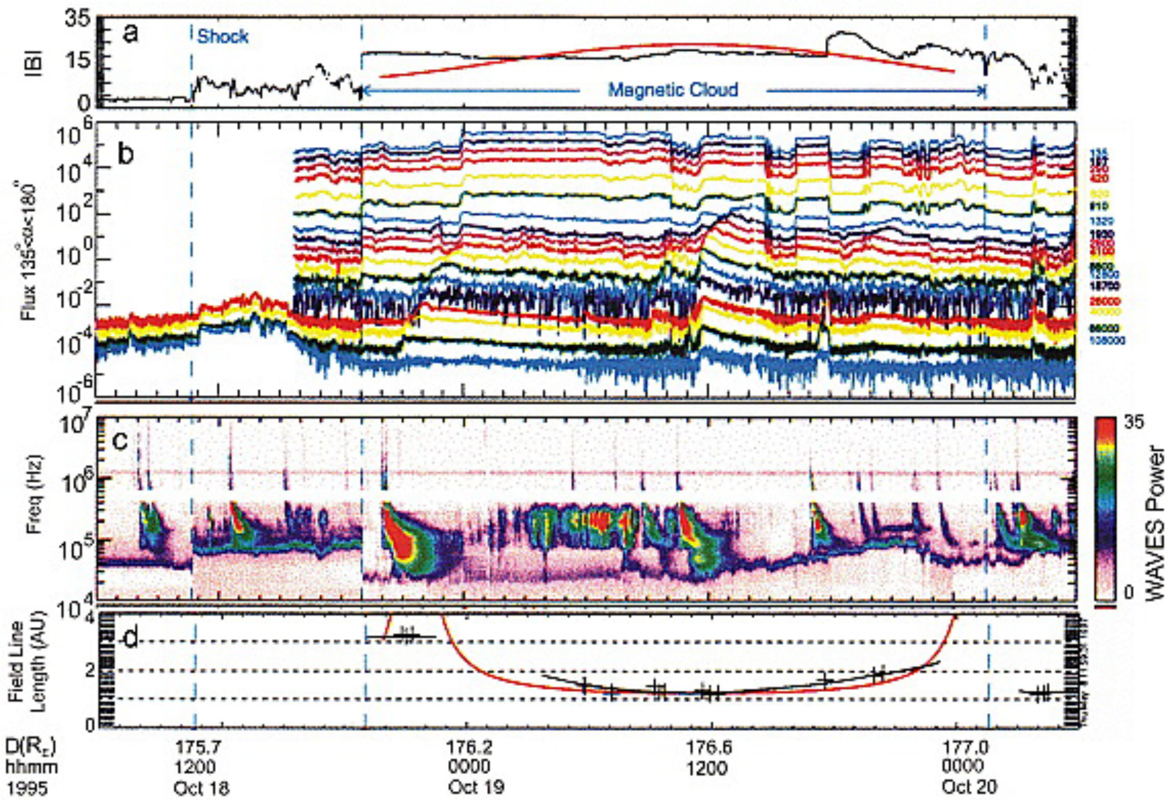

a
|B|
Shock
Magnetic Cloud
b
Flux 135°<α<180°
c
Freq (Hz)
WAVES Power
d
Field Line Length (AU)
D(R_E)
hhmm
1995
175.7
1200
Oct 18
176.2
0000
Oct 19
176.6
1200
177.0
0000
Oct 20

Figure 13.

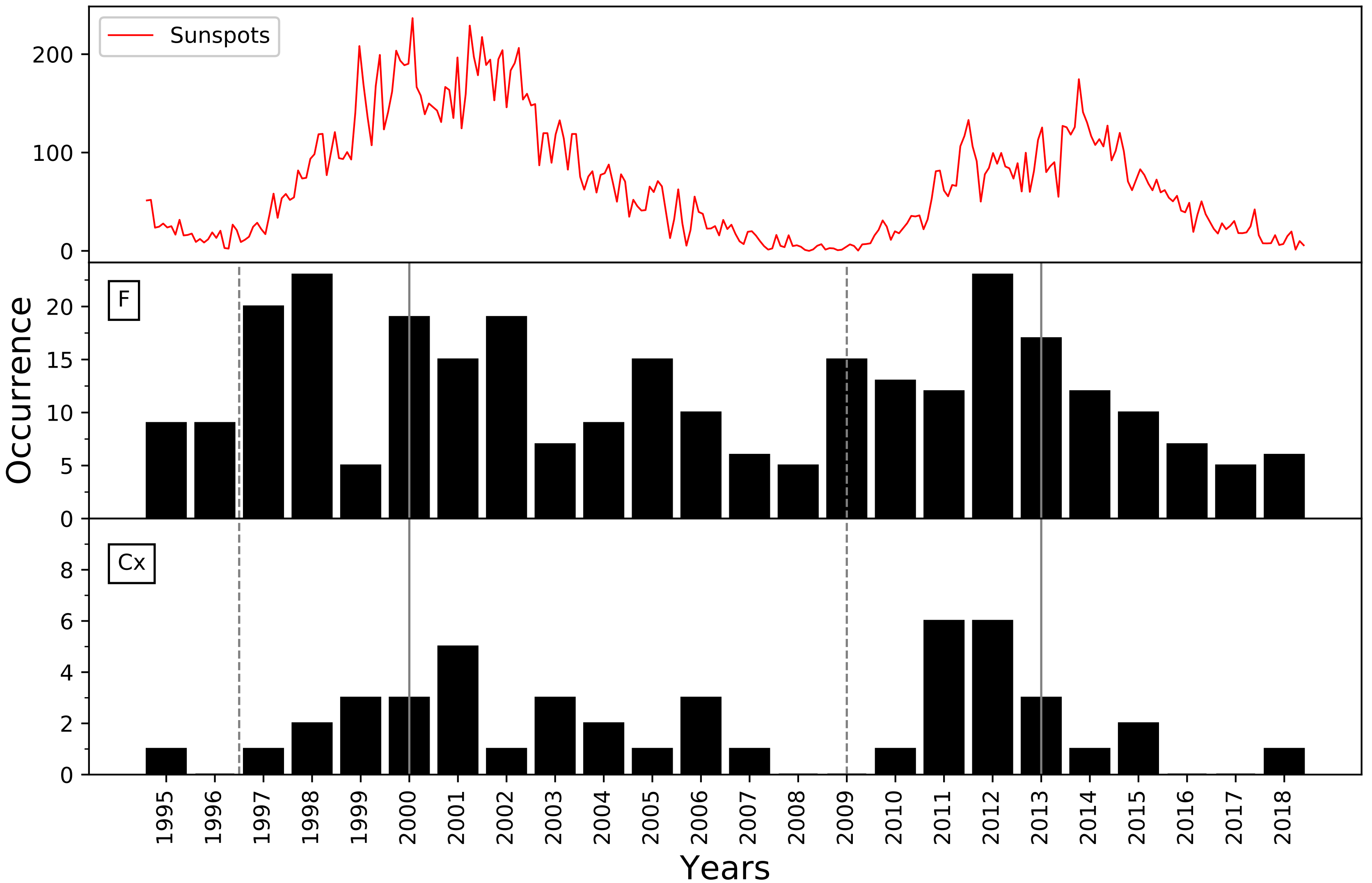

Sunspots
200
100
0
F
Cx
Occurrence
20
15
10
5
0
8
6
4
2
0
1995
1996
1997
1998
1999
2000
2001
2002
2003
2004
2005
2006
2007
2008
2009
2010
2011
2012
2013
2014
2015
2016
2017
2018
Years

Figure 14.

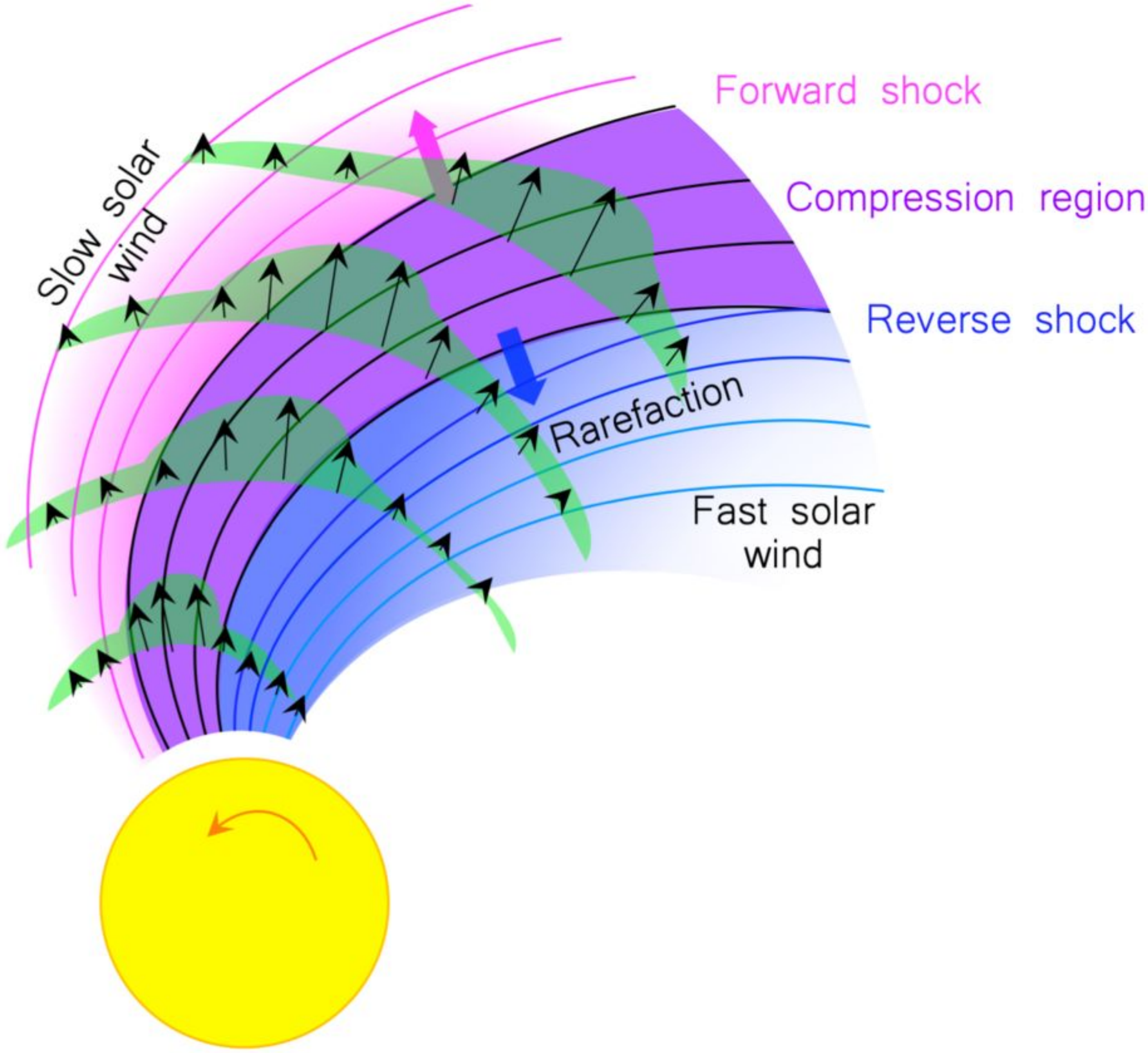
Forward shock
Compression region
Reverse shock
Slow solar wind
Rarefaction
Fast solar wind

Figure 15.

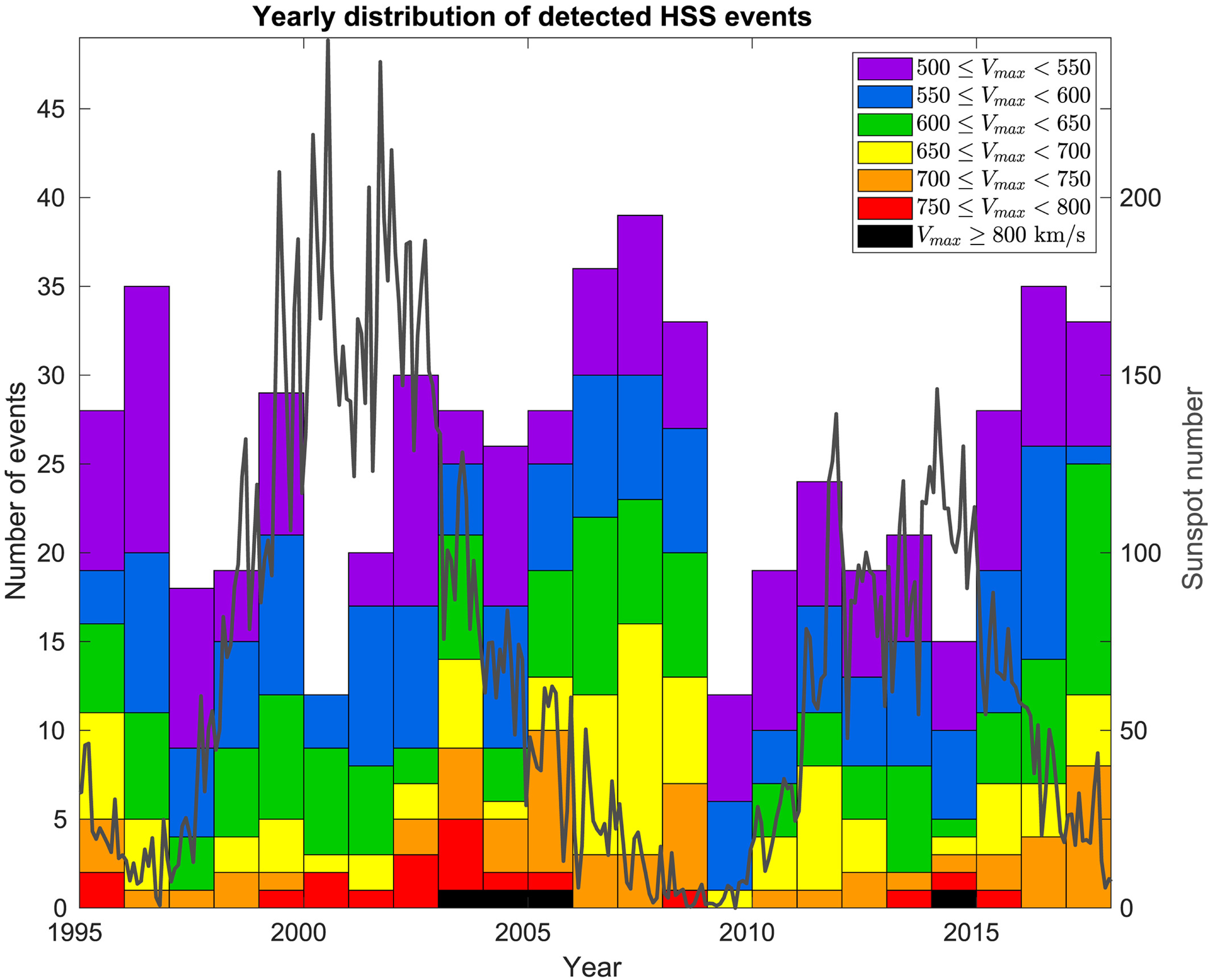

Yearly distribution of detected HSS events
Number of events
Sunspot number
Year
0
5
10
15
20
25
30
35
40
45
0
50
100
150
200
1995
2000
2005
2010
2015
$500 \leq V_{max} < 550$
$550 \leq V_{max} < 600$
$600 \leq V_{max} < 650$
$650 \leq V_{max} < 700$
$700 \leq V_{max} < 750$
$750 \leq V_{max} < 800$
$V_{max} \geq 800$ km/s

Figure 16.

HGI r: 1.09 AU, latitude: 5°, longitude: 227° r: 0.99 AU, latitude: 6°, longitude: 237° r: 0.96 AU, latitude: 7°, longitude: 252°

Figure 17.

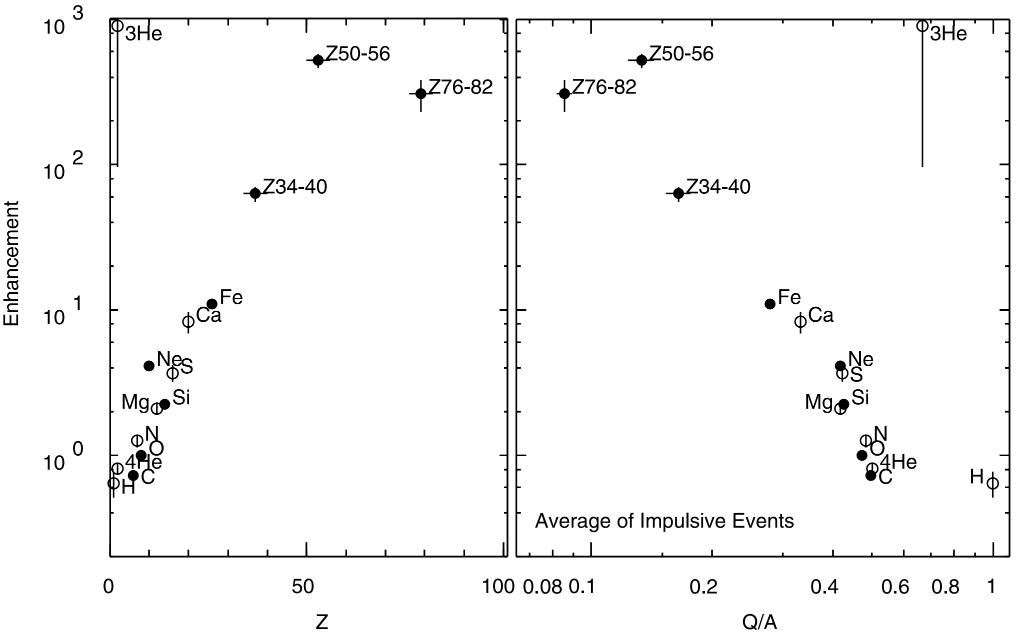
Enhancement
10^3
10^2
10^1
10^0
3He
Z50-56
Z76-82
Z34-40
Fe
Ca
Ne
S
Mg
Si
N
O
4He
C
H
0
50
100
Z
0.08
0.1
0.2
0.4
0.6
0.8
1
Q/A
Average of Impulsive Events

Figure 18.

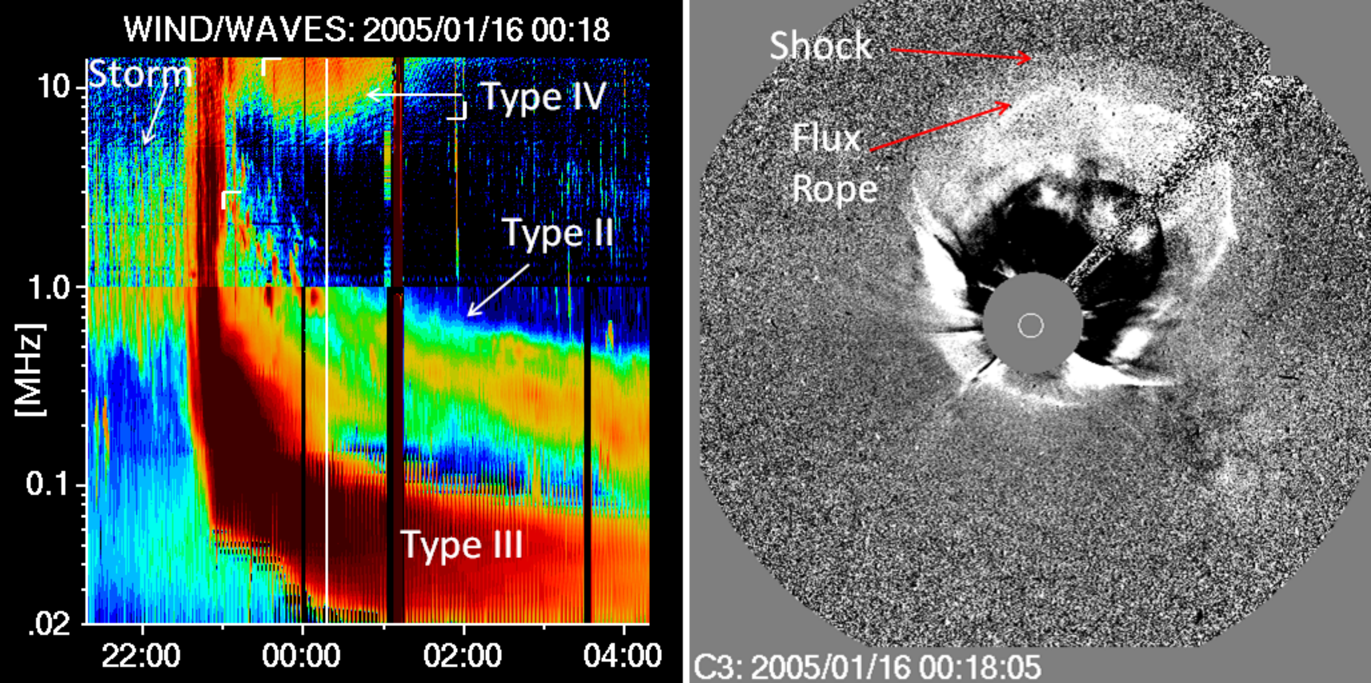
WIND/WAVES: 2005/01/16 00:18
Storm
Type IV
Type II
Type III
10
1.0
0.1
.02
[MHz]
22:00
00:00
02:00
04:00
Shock
Flux
Rope
C3: 2005/01/16 00:18:05

Figure 19.

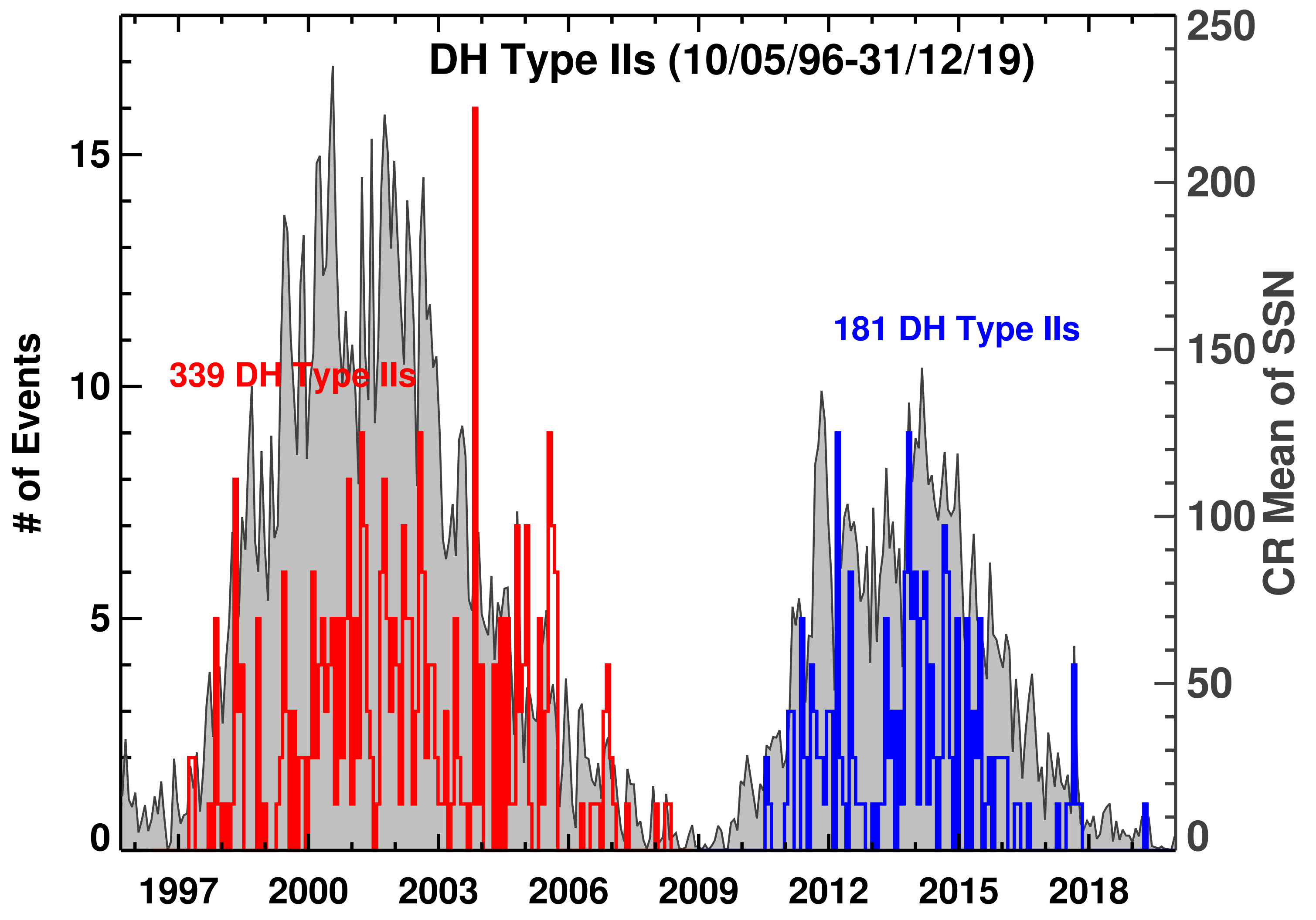
DH Type IIs (10/05/96-31/12/19)
339 DH Type IIs
181 DH Type IIs
# of Events
CR Mean of SSN
0
5
10
15
0
50
100
150
200
250
1997
2000
2003
2006
2009
2012
2015
2018